UNIVERSITÀ DEGLI STUDI DI PADOVA
Sede Amministrativa: Università degli Studi di Padova
Dipartimento di Fisica “G. Galilei”

DOTTORATO DI RICERCA IN FISICA
CICLO XXI

Commissioning of the Silicon Pixel Detector of ALICE and perspectives for beauty production measurement at LHC

Direttore: Ch.mo Prof. Attilio Stella
Tutore: Ch.mo Prof. Giuseppe Viesti
Cotutore: Dott. Andrea Dainese
Cotutore: Dott. Rosario Turrisi

Dottorando: Carlo Bombonati

2 Febbraio 2009

Contents

Introduzione

Esistono forti argomentazioni teoriche che predicono l'esistenza di una transizione di fase, per la materia nucleare, oltre la soglia di denditá di energia critica ≈ 1 GeV/fm^3. In queste condizioni é previsto che i nucleoni perdano la loro individualitá e formino uno stato deconfinato di quark e gluoni chiamato Quark-Gluon Plasma (QGP).

L'indagine sperimentale per il Quark-Gluon Plasma inizió con le collisioni a bersaglio fiso di nuclei pesanti all'AGS ($\sqrt{s_{\mathrm{Au-Au}}} = 4.5$ GeV) e al SPS ($\sqrt{s_{\mathrm{Pb-Pb}}} = 17.3$ GeV). I risultati ottenuti da queste *facility* hanno evidenziato la formazione di uno stato che condivide diverse delle proprietá previste per il Quark-Gluon Plasma.

Il passo successivo nello studio delle proprietá di questo nuovo stato fu la costruzione del primo *collider* di ioni pesanti a BNL, RHIC ($\sqrt{s_{\mathrm{Au-Au}}} = 200$ GeV). I risultati ottenuti a RHIC hanno fornito ulteriori evidenze sperimentali della formazione del Quark-Gluon Plasma. In particolare ha mostrato l'utilitá dei quark pesanti come sonde per il mezzo formatosi in collisioni tra nuclei pesanti ultra-relativistici. I quark pesanti, interagendo on il mezzo tramite l'effetto di perdita d'energia, possono essere studiati per estrarre diversi osservabili.

Con un incremento in energia nel centro di massa,rispetto a RHIC, di un fattore quasi 30, LHC ($\sqrt{s_{\mathrm{Pb-Pb}}} = 5.5$ TeV) é la nuova frontiera per lo studio del QGP. Il netto aumento di energia significa produrre goccie di QGP piućalde e piulongeve. Questo permette un migliore confronto tra i risultati sperimentali e le stime teoriche. Inoltre il nuovo regime energetico apre la possibilitá di usare il quark beauty, assime al quark charm, come sonda sperimentale. Questo permetterá anche un confronto tra la produzione di beauty e di charm che, ci si attende, possa fornire informazioni sul meccanismo di perdita d'energia.

ALICE[1] é l'esperimento dedicato al programma di ioni pesanti al LHC. Tra le sue caratteristiche vi é la presenza di un rivelatore di vertice, l'Inner Tracking

---

[1] A Large Ion Collider Experiment

System (ITS). Ció consente di separare con precisione le traccie primarie da quelle secondarie, consentendo quindi di distenguere la produzione di charm da quella di beauty. In altre parole consente di studiare il mezzo sfruttando due diverse sonde sperimentali ($M_c \approx 1.2$ GeV/c^2 e $M_b \approx 4.8$ GeV/c^2).

Il Silicon Pixel Detector (SPD) costituisce i due strati piú interni dell'ITS. Lo SPD, con la sua alta granularitá, alta risoluzione e con il suo piccolo raggio determina la risoluzione sul vertice e sul parametro d'impatto dell'ITS. Il suo design, la sua costruzione ed il suo *commissioning* sono dunque di cruciale importanza per lo studio dei quark pesanti ad ALICE.

L'attivitá svolta nell'ambito della presente tesi é stata mirata alla preparazione per lo studio della produzione di beauty. Ha perció incluso la costruzione dei settori, il *tuning* dell'impianto di raffreddamento ed il *commissioning* dell'SPD. Piú in dettaglio:

- Assemblaggio dei sensori a *pixel* sul supporto di fibra di carbonio. Dato il suo ruolo come tracciatore, l'assemblaggio dell'SPD richiede l'impiego di specifiche procedure per assicurare un'alta precisione.

- *Tuning* e funzionamento del sistema di raffreddamento dell'SPD. La dissipazione dell'SPD é di circa 1.5 kW. Questo vuol dire che, senza raffreddamento, la temperatura dei sensori aumenterebbe alla velocita' di circa 1°C/s. L'impianto di raffreddamento é quindi di vitale importanza per il funzionamento del rivelatore.

- Sviluppo di un set di strumenti per il monitoraggio dell'allineamento dell'ITS ed, in particolare, dell'SPD. Il misallineamento del rivelatore dev'essere valutato ed riportato nel software della geometria per ottimizzare la risoluzione spaziale. Questa operazione viene fatta utilizzando dei programmi dedicati. Per controllare i risultati ottenuti da questi programmi e per valutare la risoluzione spaziale del rivelatore, é stato sviluppato uno strumento software apposito.

- Valutazione sulla possibilitá di usare i decadimenti semi-elettronici del beauty per lo studio del QGP, con particolare riferimento alle problematiche inerenti ai primi run ad LHC (identificazione degli elettroni e misallineamento). Gli studi di simulazione riportati qui sono mirati alla valutazione delle performance di ALICE per la misura del fattore di modifica nucleare ($R_{\rm AA}$) e dell'anisotropia azimutale (v_2) degli elettroni provenienti da decadimenti del beauty. Inoltre, sfruttando precedenti studi sulla produzione del charm, é stato possibile stimare la sensitivita' per la dipendenza dalla massa della perdita d'energia partonica.

Introduction

There are compelling theoretical arguments that point to the existence of a phase transition, for strongly-interacting matter, at a critical energy density of about 1 GeV/fm^3. At such extreme conditions it is predicted that the nucleons lose their individuality and form a deconfined state of quarks and gluons called Quark-Gluon Plasma (QGP).

The experimental search for the Quark-Gluon Plasma started with the fixed target heavy ion collisions experiments at the AGS ($\sqrt{s_{\mathrm{Au-Au}}} = 4.5$ GeV) and SPS ($\sqrt{s_{\mathrm{Pb-Pb}}} = 17.3$ GeV). They have suggested the formation of a state of matter that shares many of the expected properties of the theoretical Quark Gluon Plasma.

The next step in the study of the properties of this new state of matter was the construction of the first dedicated ultra-relativistic heavy ion collider at BNL, RHIC ($\sqrt{s_{\mathrm{Au-Au}}} = 200$ GeV) RHIC has provided further evidence for the long-sought Quark-Gluon Plasma and a number of new observables. In particular, its results have shown the usefulness of hard partons as probes for the medium formed in relativistic heavy-ion collisions. Energetic partons, interacting with the medium through a QCD energy loss mechanism, can be used to evaluate some of the properties of the QGP.

With an increase in centre-of-mass energy, with respect to RHIC, of a factor almost 30, LHC ($\sqrt{s_{\mathrm{Pb-Pb}}} = 5.5$ TeV) is the new frontier for the study of the quark-gluon plasma. The drastic increase in energy means that LHC will create hotter and longer-lived drops of QGP matter, therefore enabling a better comparison between data and theory. The increase in energy will open the possibility to use the beauty quark as an experimental probe along with the charm. Moreover, the comparison between the behaviour of the charm and beauty quarks is expected to provide valuable information on the underlying mechanism of partonic energy loss.

ALICE[2] is the dedicated heavy ion experiment at LHC. Among its characteristics is the presence of an Inner Tracking System (ITS). Which brings the possibility to precisely separate primary from secondary tracks allowing to disentangle the production of charm and beauty. This means the possibility to investigate the medium using two different ($M_c \approx 1.2$ GeV/c^2 and $M_b \approx 4.8$ GeV/c^2) probes.

The Silicon Pixel Detector (SPD) constitutes the innermost two layers of the ITS. The SPD, with its high granularity, high spatial resolution and small radius, determines the vertex and impact parameter resolution of the ITS. Its design, construction and commissioning are therefore of crucial importance for the heavy quark studies at ALICE.

The activities carried out within the present work were aimed at the preparation for heavy quarks measurements, thus including the construction and commissioning of the SPD. More in detail, they can be summarised in the following:

- Assembly of the silicon pixel sensors on the carbon fibre support. Given its role as a precision tracker, the assembly of the SPD requires the use of specific procedures to ensure a high degree of accuracy.

- Tuning and maintenance of the cooling system of the SPD. The SPD power dissipation is of about 1.5 kW. This means that, without cooling, the temperature of the sensors would rise at about 1°C/s. The cooling system is thus of vital importance for the operation of the detector.

- Development of a set of tools for the monitoring of the alignment procedures of the ITS and, in particular of the SPD. The misalignment of the detector must be accounted for in the software description of the geometry in order to optimize the spatial resolution. The matching of the geometry with the data is done using software procedures. A dedicated set of tools has been developed to control the results of this phase and to evaluate the resolution of the detector.

- Study of the possibility of using semi-electronic decays of beauty particles for the investigation of the QGP, with an emphasis on the specific issues of the first LHC runs (electron PID and misalignment). The simulation studies reported here are devoted to assess ALICE performance in measuring the nuclear modification factor and the elliptic flow of electrons from

---

[2] A Large Ion Collider Experiment

beauty decays. Moreover, using previous studies on the charm production measurement, it has been possible to estimate the sensitivity to the mass dependence of the partonic energy loss.

Chapter 1

Heavy-ion collisions at high energy: study of QCD in extreme conditions

The aim of heavy ion collisions at high energy is to study quantum chromodynamics (QCD) in extreme conditions of high density and temperature. Even before QCD had been established as the fundamental theory of strong interactions, it had been argued that the basic properties of hadronic matter must lead to some form of critical behaviour at high temperature and/or density [1].

In the QCD framework, the quarks are considered to be "confined" in hadrons. This refers to the experimental fact that no free quarks have been observed. The fact that quantum chromodynamics should be confining is not derived from the fundamental properties of the theory, but is taken as a postulate. Intuitively, confinement is due to the force-carrying gluons having colour charge. As any two electrically-charged particles separate, the electric force between them decreases quickly, allowing (for example) electrons to become unbound from nuclei. At variance, as two quarks separate, the gluon field forms strings of colour charge, which tend to bring the quarks together as if they were some kind of rubber band. Because of this behaviour, the colour force experienced by the quarks in the direction to hold them together, remains constant, regardless of their distance from each other.

Since a hadron has a finite size of ≈ 1 fm^3 (e.g. for protons), if the density is increased beyond 1 hadron/fm^3 it is expected that the hadrons will begin to overlap and their individuality to be confused [2]. In other words there is a limit to the density (and, thus, to the temperature) of a hadronic system beyond which hadrons start to ‘superimpose’.

At such extreme conditions of density (or temperature), matter, due to the observation that QCD is an asymptotically free theory[1], is no longer made of hadrons but rather of “free” quarks. This simple picture is confirmed by lattice QCD calculations [3]. Such calculations predict that at a critical temperature of ≈ 170 MeV, corresponding to an energy density $\varepsilon_c \approx 1$ GeV/fm^3, nuclear matter undergoes a phase transition to a deconfined state of quarks and gluons. In addition, chiral symmetry is approximately restored and quark masses are reduced from their effective values in hadronic matter to their bare ones (from hundreds MeV/c^2 to few MeV/c^2). Since the colour charge of the quarks and gluons is expected to be screened (due to the high colour-charge density environment) this state is called Quark-Gluon Plasma (QGP) [4], in analogy with electromagnetic plasmas.

The only tool to study deconfined matter in the laboratory is provided by ultra-relativistic heavy-ion collisions, where one expects to attain an energy density higher than the critical value ε_c, thus making the QCD phase transition the only one predicted by the Standard Model that is within experimental reach. The main objective of heavy-ion physics is to explore the phase diagram of strongly interacting matter, to study the phase transition and the physics of the Quark-Gluon Plasma state. However, the system created in heavy-ion collisions undergoes a fast dynamical evolution from the extreme initial conditions to the diluted final hadronic state. The understanding of this fast evolving system is a theoretical challenge which goes far beyond the exploration of equilibrium QCD.

In this chapter, after a brief summary on some of the most relevant theoretical results (Section 1.1), will be shown the experimental techniques used to study hot and dense nuclear matter (Section 1.2) and some of their (Sections 1.3 and 1.4) results. The chapter will close with some perspectives for the upcoming heavy-ion program at LHC (Section 1.5).

1.1 The Physics of hot and dense matter

1.1.1 The QCD phase diagram

Simple thermodynamical considerations and QCD calculations have led us to believe that strongly interacting matter exists in different states. Its behaviour, as a function of the baryonic chemical potential[2] μ_B (a measure of the baryonic density) and of the temperature T, is shown in the phase diagram reported in Fig. 1.1. At low temperatures and for $\mu_\mathrm{B} \approx 1$ GeV (that corresponds to the nuclear density), is found ordinary matter. Increasing the energy density of the system, by "compression" (i.e. increasing μ_B) or by "heating" (i.e. increasing T), a hadronic gas phase is reached in which nucleons interact and form pions, excited states of the proton and of the neutron (Δ resonances) and other hadrons.

Increasing the temperature of the system even further, a phase transition to a

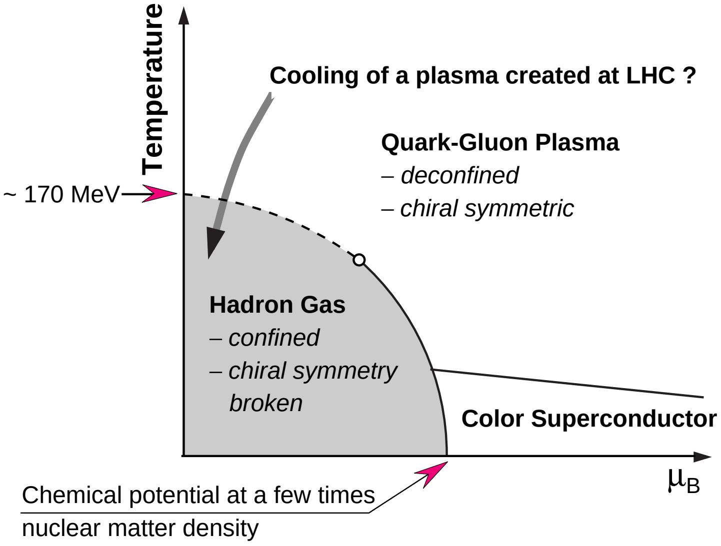

Figure 1.1: *The phase diagram of QCD.*

---

[1] Asymptotic freedom is the property of some gauge theories in which the interaction between the particles, such as quarks, becomes arbitrarily weak at ever shorter distances, i.e. length scales that asymptotically converge to zero (or, equivalently, energy scales that become arbitrarily large).

[2] The baryonic chemical potential μ_B of a system is defined as the change in energy of the system when the total baryonic number N_B (baryons - antibaryons) is increased (or decreased) by one unit: $\mu_\mathrm{B} = \mathrm{d}E/\mathrm{d}N_B$.

deconfined QGP is predicted: the density of partons (quarks and gluons) becomes so large that the confinement of quarks in hadrons disappears because the concept of hadron becomes meaningless. For the case of a vanishing baryon chemical potential, the critical temperature is estimated to be $T_{\rm c} \approx 150 - 200$ MeV [3, 9].

The transition to the QGP phase is of the first-order[3] for values of the baryon chemical potential larger than ≈ 400 MeV [10,11]. For lower values, the transition is believed to be a crossover.

At high values of the baryon chemical potential, but low values of the temperature, nuclear matter consist of an extremely dense, degenerate Fermi gas of interacting quarks. The high density and the interaction among the quarks can lead to the formation of quark–quark pairs which determine a colour superconducting phase. Such state has been predicted to form in the core of neutron stars [12, 13].

The phase transition can be reached along different "paths" on the ($\mu_{\rm B}$, T) plane. In the primordial Universe, the transition QGP-hadrons, from the deconfined to the confined phase, took place at $\mu_{\rm B} \approx 0$ (the global baryonic number was approximately zero) as a consequence of the expansion of the Universe and of the decrease of its temperature (path downward along the vertical axis) [14]. The region investigated by relativistic heavy ion collisions is close to the critical point for the CERN-SPS facility and lower, both in T and $\mu_{\rm B}$, for the BNL-AGS. Instead, the BNL-RHIC facility explores the region of the crossover transition. The CERN-LHC will explore the region at even higher T and lower $\mu_{\rm B}$ with respect to BNL-RHIC, in a more baryon-free environment.

1.1.2 Lattice QCD results

Equilibrium and phase transitions involve quarks and gluons interacting on a large distance scale in a thermal medium. Because of the increasing strength of QCD interactions with the distance, such phenomena cannot be treated using perturbative methods.

---

[3] Phase transitions are classified according to the type of the discontinuity of the free energy (F) as a function of the temperature. A first-order transition is characterised by a discontinuity of $\partial F/\partial T$ (e.g. Bose-Einstein condensation and ice sublimation). Second-order transitions are characterised by a discontinuity of $\partial^2 F/\partial T^2$ (e.g. ferromagnetic transition, superconductor transition and super-fluid transition). Crossover transitions have no discontinuities and no clear separation between phases (e.g. water phase transition beyond critical point, $T \geq 647.096$ K and $p \geq 22.064$ MPa).

The formulation of QCD on a discrete rather than continuous space-time naturally introduces a momentum cut off, which regularises the theory. In this formulation space-time is represented as a crystalline lattice: vertexes connected by lines. Quarks may reside only on vertexes and gluons can only travel along lines. For a realistic representation one should reduce the spacing between vertexes to zero, or to the Planck length. As this is computationally impossible, lattice QCD calculations often involve analysis at different lattice spacings to determine the lattice-spacing dependence, which can then be extrapolated to the continuum. Despite such difficulties several interesting results have been obtained, as summarised in the following.

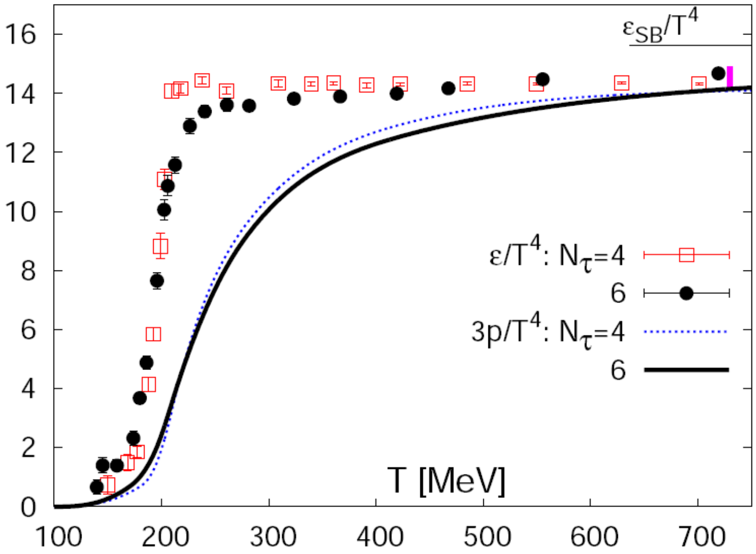

Figure 1.2: *Lattice results for energy density (dots) and pressure (lines) with two different cut-off (*$N_\tau = 4, 6$*) and with almost physical quark mass values (the pion mass is about* 220 MeV*) [9].*

The critical temperature calculations (for the case of realistic quark masses and vanishing μ_B) depends on the treatment of the quark masses, on the cut-off value of the calculations and observable used to identify the transition but the value appears to lie in the range $T_c = (185 - 195)$ MeV [9, 15]. If one considers the system to be made up of massless, non-interacting particles, it is possible to write the energy density as:

$$\varepsilon = [\frac{7}{8} \cdot (n_{dof}^{quarks} + n_{dof}^{antiquarks}) + n_{dof}^{gluons}] \frac{\pi^2}{30} T^4 = \frac{37\pi^2}{30} T^4 \tag{1.1}$$

where the degrees of freedom for flavour, spin, $q/\overline{q}$ and colour have been considered. It is possible to write a similar formula for the pressure.

$$3p = [2(n_{colour}^2 - 1) + \frac{7}{2} n_{colour} n_{flavour}] \frac{\pi^2}{30} T^4 \tag{1.2}$$

In Fig. 1.2 the results of recent lattice QCD calculations for energy density (ε) and pressure (p) are shown. The first feature to notice is the rapid increase of $\frac{\varepsilon}{T^4}$ at $T \approx 200$ MeV. This is explained as an increase in the degrees of freedom (see Eq. 1.1) from $n_{dof} = 3$ for a pion gas to $n_{dof} = 95/2$ (for 3 quark flavour) in the deconfined phase, where the additional colour and flavour degrees of freedom become available. Looking also at the $\frac{3p}{T^4}$ one should notice that the transition around T_{c} is not sharp but rather of the crossover type. One last feature is the asymptotic value of the energy density that remains about 10% below the Stefan-Boltzmann limit (for an ideal gas of non-interacting particles). This is explained as due to residual interactions among the quarks and gluons.

In vacuum, quarks dress themselves with partons of the "sea" to form the constituent quarks that make up hadrons. As a result, the bare quark mass $m_q \approx 0$ is replaced by a constituent quark mass $M_q \approx 300$ MeV. In a hot medium, this dressing melts and $M_q \to 0$. Since the QCD Lagrangian for $m_q = 0$ is chirally symmetric, $M_q \neq 0$ implies spontaneous chiral symmetry breaking. The quark mass shift $M_q \to 0$ thus corresponds to chiral symmetry restoration. Lattice calculations confirmed this picture and showed that deconfinement and chiral symmetry restoration occur at approximately the same temperature [16].

It was shown that the QCD transition is chiral-symmetry restoring as well as deconfining. This in turn has consequences for the in-medium properties of both light- and heavy-quark bound states. The present results are shown in Fig.1.3/ The heavy-quark potential, starts to show an appreciable temperature dependence for $T > 0.6T_{\mathrm{c}}$. With increasing temperature it becomes easier to separate heavy quarks to infinite distance. Already at $T \simeq 0.9T_{\mathrm{c}}$, the free-energy difference for a heavy-quark pair separated by a distance similar to the J/ψ radius ($r_\psi \sim 0.2$ fm) and a pair separated to infinity is only 500 MeV, which is compatible with the average thermal energy of a gluon ($\sim 3T_{\mathrm{c}}$). The $\mathrm{c\overline{c}}$ bound states are thus expected to dissolve close to T_{c}.

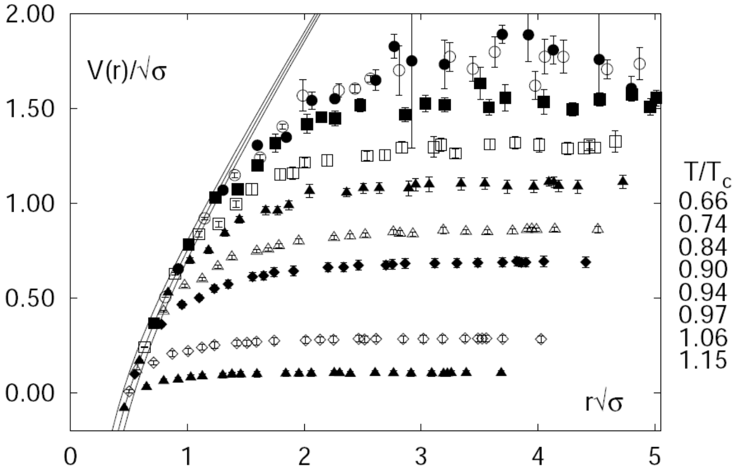

Figure 1.3: *Heavy-quark QCD potential for a 3-flavour QGP versus the quark-antiquark separation (where σ is the string tension). The different points correspond to lattice culations with different temperatures [16].*

1.2 Ultra-relativistic heavy-ion collisions

In 1975 J.C. Collins and M.J. Perry proposed that the conditions of the interior of neutron stars would reach a state of asymptotically free quarks [2].

In the '80s the interest over this possible state of matter gave birth to several 'low-energy' experiments, mainly at the GSI SIS facility ($1-2$ GeV per nucleon) and the Dubna JINR (^{12}C beam with a momentum of 4.5 GeV/c per nucleon).

The step-up in energy (and therefore, initial temperature) came in 1986 with the opening of the BNL-AGS ($\approx 6-15$ GeV per nucleon) heavy ion program (at first with Si beams and, from 1992 on, with Au beams) and of the CERN-SPS (with a momentum of $20-200$ GeV/c per nucleon) heavy ion program (at first with O and S beams then, from 1994 on, with Pb and In beams).

The CERN-SPS experiments used S beams (NA34, NA35, NA38 and NA80), Pb beams (NA44, NA45/CERES, NA49, NA50, NA52/NWMASS, WA97/NA57 and WA98), and In beams (NA60) [20–26, 28–31]. An important milestone of the CERN-SPS era was the announcement, in 2000, of the discovery of a new state of matter featuring many of the characteristics of the theoretically predicted Quark-Gluon Plasma [5]. The results of SPS will be discussed more in detail in

Section 1.3.

After this "discovery", a whole range of opportunities to study the QGP properties, opened. The first facility with this aim was BNL-RHIC with Au–Au colliding beams at $\sqrt{s_{\rm NN}} = 200$ GeV. BNL-RHIC began taking data in 2000 and produced a wealth of exciting results, some of which will be discussed more in detail in Section 1.4.

The next step into the understanding of the QGP is the CERN-LHC collider. It will soon provide Pb–Pb collisions at $\sqrt{s_{\rm NN}} = 5.5$ TeV opening a new era for the field, in which particle production will be dominated by hard processes in a baryon-free environment, and the energy densities will possibly be high enough to treat the generated quark-gluon plasma as an ideal gas (Section 1.5). .

1.2.1 The dynamics of heavy-ion collisions

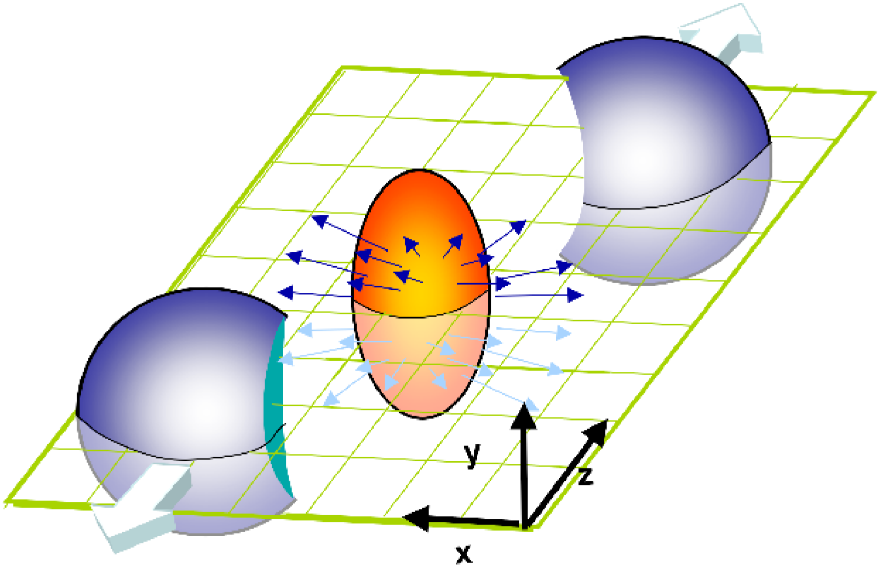

Figure 1.4: *Schematic representation of a heavy-ion collision.*

The hot and dense fireballs created in relativistic heavy-ion collisions undergo thermalisation, cooling by expansion, hadronisation, chemical and thermal freeze-out in a pattern that strongly resembles the evolution of the Universe after the Big Bang. A major difference is, however, the much smaller size of the heavy-ion fireball and its much (by about 18 orders of magnitude) faster dynamical evolution when compared with the Big Bang. This complicates the theoretical analysis of the experimental observations. A heavy-ion collision is depicted in Fig. 1.4. Its main stages can be summarised as:

1. Two disk-like nuclei approach each other, Lorentz contracted along the beam direction by a factor $\gamma = E_{beam}/M$ (where E_{beam} is the beam energy per nucleon and $M = 0.94$ GeV is the nucleon mass, such that $\gamma \approx 110$ for heavy ions at RHIC and ≈ 3000 at the LHC at their respective top energies). The partonic density in the nucleus can reach the point where the gluons saturate the available phase space. When the saturation occurs the nucleus behaves like a wall of colour charge, a Colour Glass Condensate (CGC) [7].

2. After impact, hard collisions with large momentum transfer $Q \gg 1$ GeV between quarks, antiquarks or gluons (partons) inside the nucleons of the two nuclei produce secondary partons with large transverse momenta p_{t}, this hard scattering happens at early times $\approx 1/Q \approx 1/p_{\mathrm{t}}$.

3. The remnants of the original nuclei, called "spectator nucleons", fly along the beam line. The nucleons that do not survive the collision (called "participants") form the so called "fireball". The name "fireball" is due to the high energy of the system and its rapid expansion (estimated with HBT[4] techniques to be $\approx 0.5\,c$). If the energy and density of the fireball are high enough, it can form a "droplet" of Quark Gluon Plasma. Soft collisions with small momentum exchange $Q \ll 1$ GeV produce many more particles somewhat later and thermalize the QGP after about 1 fm/c (at the SPS). The resulting thermalized QGP fluid expands hydrodynamically and cools approximately adiabatically.

4. As the fireball cools down the available energy is insufficient to alter the specie of the particles and the QGP converts to a gas of hadrons (chemical freeze-out). The hadrons continue to interact quasi-elastically, further accelerating the expansion and cooling of the fireball until thermal freeze-out.

---

[4] The Hanbury-Brown and Twiss (HBT) correlation effect was originally used to determine source sizes for both laboratory and stellar sources. Correlations of identical pions were shown to be sensitive to source dimensions in proton-antiproton collisions. For a modern review of the use of HBT in heavy-ion physics see [8].

> The chemical composition of the hadron gas is fixed during the hadronisation process and remains basically unchanged afterwards. Unstable hadrons decay and the stable decay products stream freely towards the detector.

By studying the behaviour of the matter created in the heavy-ion collisions it is possible to explore the phase structure and phase diagram of strongly interacting matter. Where proton-proton physics aims at an understanding of the elementary degrees of freedom and fundamental forces at the shortest distances, the heavy-ion program focuses on the condensed matter aspects of bulk material whose constituents interact with each other through these forces. The difference between this kind of condensed matter physics and the traditional one is that, for the QGP case, the fundamental interaction is mediated by the strong rather than the electromagnetic force. The coupling strength of the strong interaction gets bigger rather than smaller at large distances, leading us to expect a completely new type of phase structure. Indeed, strongly interacting matter appears to behave like a liquid ("quark soup") at high temperature and like a gas ("hadron resonance gas") at low temperature, contrary to intuition. On the other hand, the QGP state, with its unconfined colour charges, has similarities with electrodynamic plasmas whose dynamical behaviour is controlled by the presence of unconfined electric charges. For example, both feature Debye screening of electric (colour) fields (see [6]). The main differences are that QGP temperatures are about a factor 1000 higher, and that particle densities are about a factor 10^9 larger, than their counterparts in the hottest and densest electrodynamic plasmas.

1.3 Experimental results from SPS

The energy density, at the time of local thermal equilibration, can be determined using the Bjorken estimate [17]:

$$\varepsilon = \left(\frac{\mathrm{d}N_{\mathrm{h}}}{\mathrm{d}y}\right)_{y=0} \times \frac{w_{\mathrm{h}}}{\pi R_{\mathrm{A}}^2 \tau_0} \tag{1.3}$$

where $(\mathrm{d}N_{\mathrm{h}}/\mathrm{d}y)_{y=0}$ specifies the number of hadrons emitted per unit of rapidity[5] at mid-rapidity and w_{h} their average energy in the direction transverse to the beam axis. The effective initial volume is determined in the transverse plane by

---

[5] The longitudinal rapidity of a particle with four-momentum $(E, \vec{p})$ is defined as $y = \frac{1}{2} \ln\left(\frac{E+p_z}{E-p_z}\right)$, being z the direction of the beam(s).

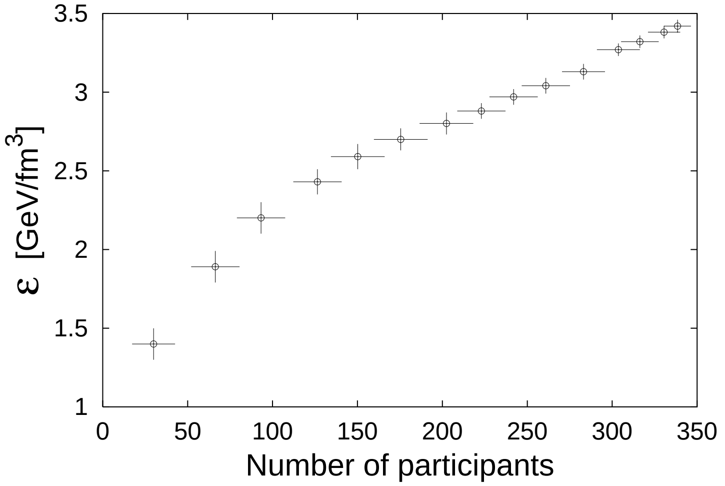

Figure 1.5: *The energy density in Pb–Pb collisions at the SPS as measured by NA50 [29].*

the nuclear radius R_A, and longitudinally by the formation time τ_0 of the thermal medium.

The energy density was measured in Pb–Pb collisions at $\sqrt{s_\mathrm{NN}} = 17$ GeV at the SPS by the NA50 experiment [29]. In Fig. 1.3 ε is plotted as a function of the centrality of the collision, determined by the number of participant nucleons; it covers the range from 1 to 3.5 GeV/fm^3. Lattice calculations, as already mentioned, give for the energy density at deconfinement, $\varepsilon(T_\mathrm{c})$, values around or slightly below 1 GeV/fm^3. This means that, for central collisions, the initial conditions at the SPS are well above the predicted requirements for a phase transition to occur.

1.3.1 J/ψ suppression

In a medium of charged particles, the interaction of one charge will be reduced or cancelled out by the surrounding charges. This effect is known as Debye screening, and while originally defined for electromagnetic plasmas, it has been extended to plasmas of colour charge as well in a paper by T. Matsui and H. Satz in 1986 [6]. In the Plasma Phase, where the colour charges are liberated, the colour interaction potential between two quarks is expected to be screened for distances beyond a screening length λ_D ("Debye length"), similarly to what happens in the case of

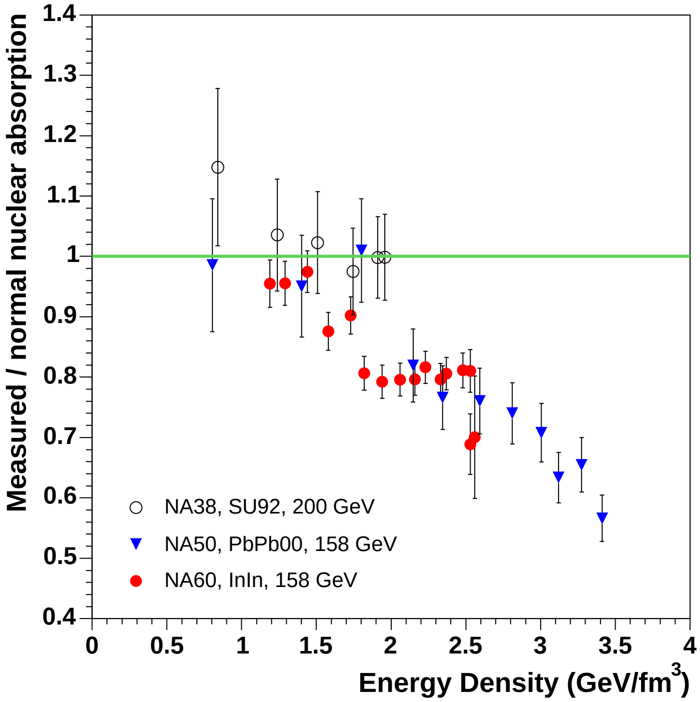

Figure 1.6: *The ratio of measured J/ψ suppression over the expected suppression from nuclear absorption (inferred from p–A collisions) as a function of the energy density, as measured by NA38, NA50 and NA60 [29, 30].*

the Debye screening in an electromagnetic plasma[6]. Hadrons with a radius $r > \lambda_D$ will therefore not bind in the QGP phase. In particular, charmonium ($c\bar{c}$) and bottonium ($b\bar{b}$) states with a radius $r > \lambda_D$ cannot be produced at this stage: the Q and $\overline{Q}$ quarks lose their correlation and follow independent trajectories. What makes quarkonium states particularly interesting is that heavy quarks can only be produced at the onset of the collision, in a high energy interaction between

---

[6] In an electromagnetic plasma, the potential of a charge is screened by the field of the electrons that surround it:

$$\Phi(r) = \frac{Z\,e}{r}\,e^{-\frac{r}{\lambda_D}}$$

with

$$\lambda_D = \sqrt{\frac{kT}{4\pi\,n_0 e^2}}$$

where n_0 is the density of electrons in the plasma two energetic partons. Later, when the energy is redistributed among the many hundreds of produced particles, no collision in the system can involve enough energy to allow for heavy quark production any more. Therefore, as long as the $\mathrm{Q\overline{Q}}$ yield per event is so low that the probability of later combining an uncorrelated $\mathrm{Q\overline{Q}}$ pair at the hadronisation stage is negligible (as it is at SPS energies) the only chance of producing a bound quarkonium state would be shortly after the pair is produced. Debye screening prevents this, leading to a suppression in the yield of quarkonia in the final state.

This effect was observed by the NA50 and NA60 experiments: in Fig. 1.6 the ratio of measured suppression and expected suppression from normal nuclear effects (estimated from p–p, p–A and S–U collisions) as a function of the energy density (related to the centrality of the collision[7]) [29,30]. The additional suppression, clearly visible for central Pb–Pb and In–In collisions ($\varepsilon > 2 - 2.5$ GeV/fm^3) is interpreted as due to the fact that, in the high colour-charge density environment of a QGP, the strong interaction between the two quarks of the $\mathrm{c\bar{c}}$ pair is screened and the formation of their bound state is consequently prevented.

1.3.2 Enhancement of strange baryon production

In the QGP, the chiral symmetry restoration decreases the threshold for the production of a $\mathrm{s\bar{s}}$ pair from twice the constituent mass of the s quark, ≈ 600 MeV, to twice the bare mass of the s quark, ≈ 300 MeV, which is less than half of the energy required to produce strange particles in hadronic interactions. In the QGP multi-strange baryons can be produced by statistical combination of strange (and non-strange) quarks, while in an hadronic gas they have to be produced through a chain of interactions that increase the strangeness content in steps of one unit. For this reason an hyperon enhancement growing with the strangeness content was indicated as a signal for QGP formation.

This effect was first predicted by J. Rafelski and B. Müller in 1982 [18] and it was, indeed, observed by the WA97/NA57 experiment [31]. In Fig. 1.7 one can see that the production of strange and multi-strange baryons increases by 10 times and more (up to 20 times for the Ω) in central Pb–Pb collisions in comparison to p–Be, where the QGP is not expected to be produced. As predicted, the enhancement $\mathcal{E}$ is increasing with the strangeness content: $\mathcal{E}(\Lambda) < \mathcal{E}(\Xi) <$

---

[7] The centrality of a collision is defined as the distance, in the transverse plane, between the centres of the two nuclei b, usually expressed as a percentage of the total inelastic cross section.

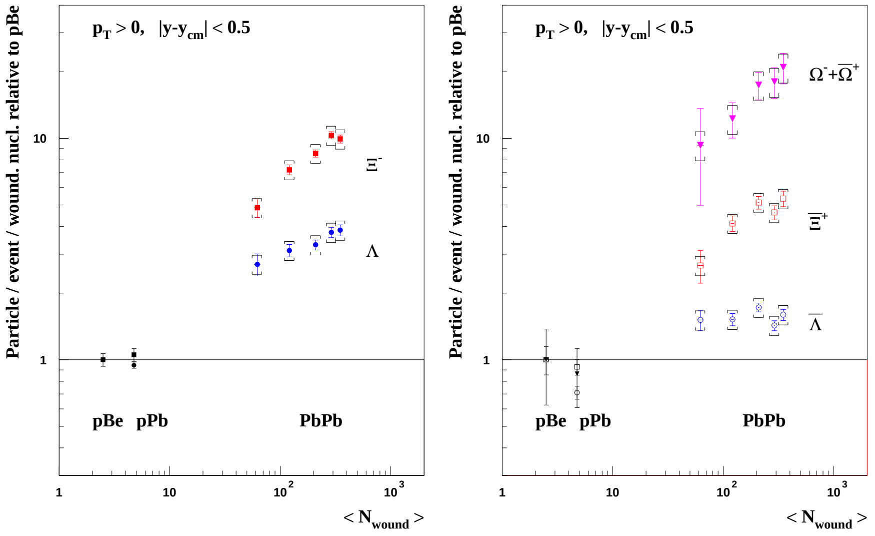

Figure 1.7: *Strange baryon production in Pb–Pb per participant nucleon, normalised to the ratio from p–Be, as a function of the number of participant nucleons, as measured by NA57 at the SPS [31].*

$\mathcal{E}(\Omega)$.

1.3.3 Dileptons excess

Among the earliest suggestions [19] for QGP signatures has been the appearance of an enhanced radiation of dileptons (and/or photons) in the intermediate-mass region, 1.5 GeV $< M_{ll} <$ 3 GeV i.e., well above the light vector mesons ρ, ω and ϕ but below the J/ψ resonances. The importance of this region resides on the facts that, on one hand, low-energy hadronic processes (such as $\pi\,\pi$ annihilation or Dalitz decays) are sufficiently suppressed, and, on the other hand, hard processes (in particular Drell-Yan annihilation), which prevail in the high-mass region $M \geq 4$ GeV, increase rather slowly towards smaller M and thus may be "over-shined" by thermal radiation.

At the CERN-SPS, intermediate-mass dilepton spectra have been measured in the dimuon mode by the NA38/NA50 [23], HELIOS–3 [24] and, more recently, NA60 [28] collaborations. In central collisions of heavy nuclei all experiments found factors of 2-3 enhancement over the extrapolation of known sources from proton-induced collisions, given by primordial Drell-Yan annihilation as well as semileptonic decays of associatedly produced charmed D ($\overline{D}$) mesons. All observations can consistently be interpreted in terms of thermal radiation from the fireball.

Also the CERES experiment [21] has found an enhancement in the low-mass dielectron spectra ($M < M_{\phi}$). This excess was found to be present in S–Au collisions at $\sqrt{s_{\mathrm{NN}}} = 19.4$ GeV and Pb–Pb collisions at $\sqrt{s_{\mathrm{NN}}} = 17.3$ GeV. This excess is interpreted in terms of thermal production by $\pi^{+}\pi^{-}$ annihilation from the dense hadronic gas created in nuclear collisions together with a ρ in-medium modification (a broadening of ρ spectral shape or a ρ-mass shift due to chiral symmetry restoration).

1.4 Experimental results from RHIC

The Relativistic Heavy Ion Collider (RHIC) in Brookhaven began operation during summer 2000. With a factor 10 increase in the centre-of-mass energy with respect to the SPS, $\sqrt{s_{\mathrm{NN}}}$ up to 200 GeV, the produced collisions are expected to be well above the phase transition threshold. Moreover, in this energy regime, the so-called ‘hard processes’ (production of energetic partons, $E >$ 3-5 GeV, out of the inelastic scattering of two partons from the colliding nuclei) have a significantly larger cross section and they become experimentally accessible.

1.4.1 Elliptic flow

Collective flow is driven by pressure gradients and thus provides access to the equation of state (EOS) $p(\varepsilon)$ (p is the thermodynamic pressure, ε is the energy density, and the net baryon density μ_B is small enough at RHIC energies that its influence on the EOS can be neglected). For the case of an ideal fluid, the acceleration of the fluid is controlled by the speed of sound $c_s = \sqrt{\frac{\partial p}{\partial \varepsilon}}$ which determines the fluid reaction to the pressure or energy density gradients.

Lattice QCD data show that c_s^2 decreases from about 1/3 at $T > 2\,T_{\mathrm{c}}$ by almost a factor 10 close to T_{c}, rising again to around 0.16–0.2 in the hadron gas phase below T_{c}. The finally observed collective flow transverse to the beam direction reflects a (weighted) average of the history of $c_s(T)$ along the cooling trajectory explored by the fireball medium. Different aspects of the final flow pattern weight this history differently. The azimuthally averaged “radial flow”

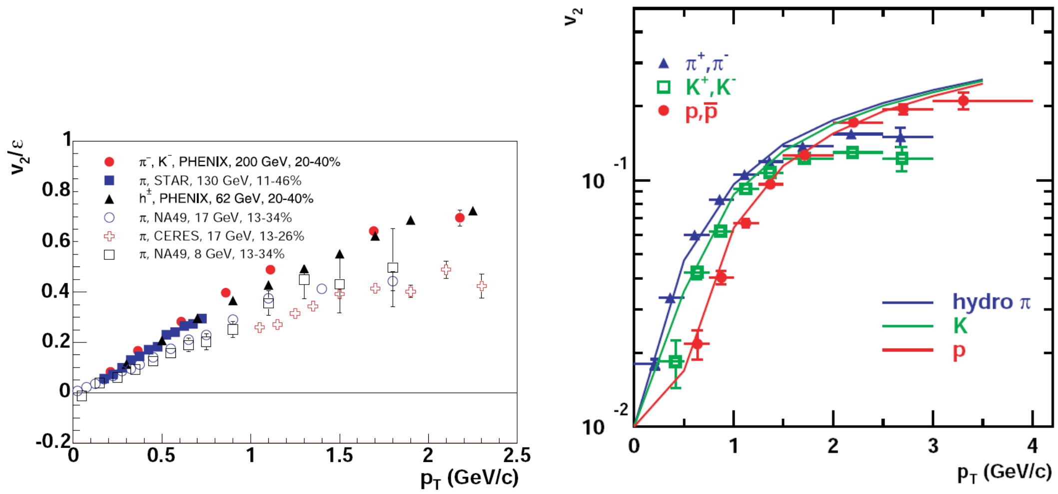

Figure 1.8: Left: v_2 *divided by the eccentricity* (ϵ) *for mid-central collisions at RHIC (filled symbols) and SPS (open symbols). Dividing by eccentricity removes to first order the effect of different centrality selections across the experiments.* Right: *Elliptic flow for pions, kaons and protons produced in minimum-bias collisions at RHIC compared to hydro calculations [33].*

receives contributions from all expansion stages, due to persistent pressure gradients between the fireball interior and the outside vacuum. Flow anisotropies are generated mostly during the hot early collision stages. They are driven by spatial anisotropies of the pressure gradients due to the initial spatial deformation of the nuclear reaction zone. This deformation decreases with time as a result of anisotropic flow, since the matter accelerates more rapidly, due to larger pressure gradients, in the direction where the fireball was initially shorter. With the disappearance of pressure gradient anisotropies, the driving force for flow anisotropies vanishes, and due to this "self-quenching" effect the elliptic flow saturates early. If the fireball expansion starts at sufficiently high initial temperature, it is possible that all elliptic flow is generated before matter reaches T_c and hadronizes. In this case (which it is expected to be realised in heavy-ion collisions at the LHC) elliptic flow is a clean probe of the EOS of the QGP phase.

Usually the azimuthal particle distributions are studied by analysing the differential production cross-sections in terms of a Fourier decomposition:

$$\frac{dN}{p_\mathrm{t}\,dp_\mathrm{t}\,dy\,d\phi} = \frac{1}{2\pi}\frac{dN}{p_\mathrm{t}\,dp_\mathrm{t}\,dy}\{1 + \sum_{i=1} 2v_i[i(\phi - \Psi_{RP})]\},$$

$$v_n(y, p_\mathrm{t}, b) = \langle \cos[n(\phi - \Psi_{RP})] \rangle$$

where Ψ_{RP} is the reaction plane[8] angle, y is the particle rapidity, b is the impact parameter of the collision and v_i are the Fourier coefficients. The lowest order Fourier terms are the so called direct flow (v_1) and elliptic flow (v_2).

The scaling of the elliptic flow with eccentricity (left panel of Fig. 1.8) for low p_t shows that v_2 is tied to the spatial asymmetry of non–central collisions. This indicates that a high level of collectivity is present at a early stage of the collision.

Each particle species has its own v_2 coefficient, characterizing the elliptic azimuthal deformation of its momentum distribution. In Fig. 1.8 (right panel) v_2 is shown as a function of transverse momentum for a variety of hadron species with different masses, ranging from the pions to the protons, along with hydrodynamic model calculation based on an ideal fluid.

As it can be seen in Fig. 1.8 (right panel), in this domain the data show excellent agreement with ideal fluid dynamical predictions, including the hydrodynamically predicted rest mass dependence of v_2 (at the same p_t, heavier hadrons show less elliptic flow). Ideal fluid dynamics thus gives a good description of the collective behaviour of the bulk of the fireball matter.

It must be emphasised that the ideal hydrodynamic prediction of $v_2(p_\mathrm{t})$ is essentially parameter free: all model parameters (initial conditions and decoupling temperature) are fixed in central collisions where $v_2 = 0$, and the only non-trivial input for non-central collisions is the initial geometric source eccentricity as a function of impact parameter. Originally, this eccentricity was computed from a geometric Glauber model (see [32]). The experimental data fully matches the theoretical prediction from ideal fluid dynamics, leaving very little room for viscosity, which would reduce the theoretical value for the elliptic flow. This is the cornerstone of the "perfect fluid" paradigm for the QGP that has emerged from the RHIC data.

However, recently suggested alternate models for the initial state, for example the Colour Glass Condensate, can give initial eccentricities that are up to 30%

---

[8] The "reaction plane" is defined by the beam direction and the distance of the two colliding nuclei.

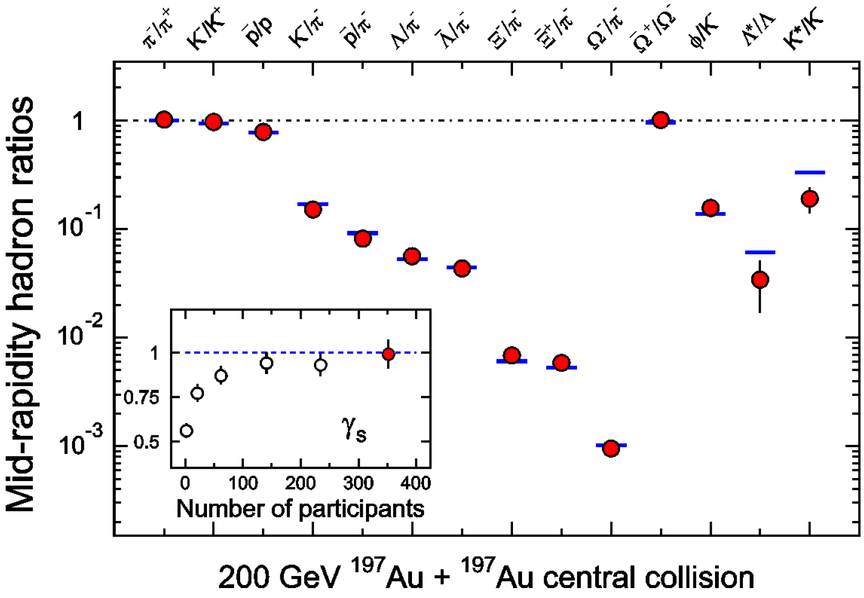

Figure 1.9: *Ratios of* p_t*-integrated mid-rapidity yields for different hadron species measured in STAR for central Au–Au collisions at* $\sqrt{s_\mathrm{NN}} = 200$ GeV*. The horizontal bars represent statistical model fits to the measured yield ratios for stable and long-lived hadrons. The variation of* γ_s *with centrality is shown in the inset, including the value (leftmost point) from fits to yield ratios measured by STAR for* 200 GeV *p–p collisions. Taken from [76].*

larger than the Glauber model values. Furthermore, the first ideal fluid calculations used an incorrect chemical composition during the late hadronic stage of the collision. Once corrected, this increased the theoretical prediction for $v_2(p_\mathrm{t})$ for pions by another 30%. If both these effects are included, the measured $v_2(p_\mathrm{t})$ reaches only about 2/3 of the ideal fluid limit, opening some room for viscous effects in the fireball fluid.

1.4.2 Hadron ratios

Fig. 1.9 compares STAR measurements of hadron yield ratios for central Au–Au collisions to statistical model fits. The observed hadron ratios give information about the chemical composition of the fireball when it reaches the chemical freeze–out. The plot clearly shows that the hadron yield ratios measured in Au–Au collisions at RHIC can be described extremely well using a thermal model with just two parameters: a chemical decoupling temperature $T_{chem} = 163 \pm 4$ MeV and a small baryon chemical $\mu_B = 24 \pm 4$ MeV. In central and semi-central collisions the phase space for strange quarks is fully saturated: if one generalises the thermal fit to include a strangeness saturation factor[9] γ_s one finds $\gamma_s = 0.99 \pm 0.07$. In peripheral collisions (with less than 150 participating nucleons), γ_s is found to drop, approaching a value around 0.5 in p–p collisions, reflecting the canonical strangeness suppression in such collisions (see [76]). This suppression is removed in central Au–Au collisions. In contrast to γ_s (see Fig. 1.9), the chemical decoupling temperature T_{chem} is found to be completely independent of collision centrality. So, at freeze–out, all Au–Au collisions are well described by a thermalized hadron resonance gas in relative chemical equilibrium with respect to all types of inelastic as long as the total number of strange valence quark–antiquark pairs is conserved.

1.4.3 Hard probes: binary scaling and jet quenching

Due to the transient nature of the matter created in high energy nuclear collisions, external probes cannot be used to study its properties. However, the dynamical processes that produce the bulk medium also produce energetic particles through hard scattering processes. The interaction of these energetic particles with the medium provides a class of unique, penetrating probes that are analogous to the method of computed tomography in medical science. For $p_{\mathrm{t}} > 5$ GeV/c the observed hadron spectra in Au–Au collisions at RHIC exhibit the power-law falloff in cross section with increasing p_{t} that is characteristic of perturbative QCD hard-scattering processes. The parameters of this power–law behaviour vary systematically with collision centrality, in ways that reveal important properties of the matter traversed by these penetrating probes.

Binary scaling

When dealing with high–energy nuclear collisions it is important to understand if the yields in proton-nucleus and nucleus-nucleus can be considered as the result of independent collisions between the point–like constituent of the nucleons. If

---

[9] The strangeness saturation factor is defined as: $\gamma_s = e^{\frac{\mu_{\langle s+\bar{s}\rangle}}{T}}$ where $\mu_{\langle s+\bar{s}\rangle}$ is the chemical potential for strange quarks. γ_s is a measure of the chemical saturation of strangeness with $\gamma_s < 1$ meaning under-saturation and $\gamma_s = 1$ saturation, i.e. chemical equilibrium.

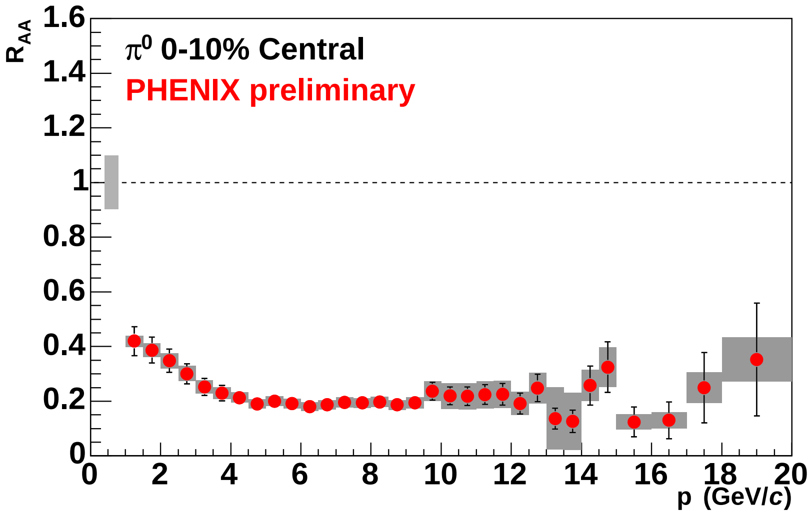

Figure 1.10: *Nuclear modification factor as a function of transverse momentum for* π^0 *from* 200 GeV *central Au–Au collisions as measured by PHENIX [77].*

this is the case, the production should scale from p–p yields with a coefficient, N_{coll}, that is the average number of binary nucleon–nucleon inelastic collisions.

Several effects can contribute to a deviation from binary scaling. They are generally divided into two classes:

- *initial state effects*, such as nuclear shadowing (described in Section 1.5.4), that could affect the hard cross section in a way which depends on the size and energy of the colliding nuclei, but not on the medium formed in the collision;

- *final state effects*, induced by the medium, that can change the yields and/or the kinematic distributions (e.g. $p_{\rm t}$ and rapidity) of the produced hard partons; a typical example is the partonic energy loss; these final state effects depend on the properties (gluon density, temperature and volume) of the medium and they can therefore provide information on such properties.

The modifications to the binary scaling can be estimated measuring the nuclear modification factor, R_{AA}, defined as:

$$R_{AA}(p_{\mathrm{t}}, \eta) = \frac{\frac{d^2 N^P_{AA}}{dp_{\mathrm{t}}\, d\eta}}{\langle N_{coll} \rangle \times \frac{d^2 N^P_{NN}}{dp_{\mathrm{t}}\, d\eta}}$$

where dN^P_{AA} is the yield of a particle P in a nucleus–nucleus collision and dN^P_{NN} is the same yield in a nucleon–nucleon collision. If the yield of the process scales with the number of collisions, one expects $R_{AA} = 1$.

Fig. 1.10 shows the nuclear modification factor for π^0 from 200 GeV central Au–Au collisions as measured by PHENIX. What is seen is that high p_{t} particles in central Au–Au collisions are suppressed by a factor ≈ 5 relative to the binary scaling expectations. Conventional nuclear effects cannot account for the suppression. Furthermore, the suppression is not seen in d–Au collisions but is unique to Au–Au collisions, proving experimentally that it results not from nuclear effects in the initial state, but rather from the final state effect of hard scattered partons or their fragmentation products in the dense medium generated in Au–Au collisions.

High-p_{t} suppression and parton energy loss

One can use fast partons, created in primary collisions between quarks or gluons from the two nuclei, to probe the early dense stage of the medium. Such hard partons, emitted with high transverse momenta p_{t} , fragment into a spray of hadrons in the direction of the parton, forming a jet.

The rate for creating such jets can be factored into a hard parton-parton cross section, described by perturbative QCD, a soft structure function describing the probability to find a parton to scatter off inside a nucleon within the colliding nuclei, and a soft fragmentation function describing the fragmentation of the scattered parton into hadrons. The structure and fragmentation functions are universal and can be measured in deep inelastic e–p scattering (DIS) and in p–p collisions. Nuclear modifications of the structure function can be measured in DIS of electrons on nuclei. Jets thus form a calibrated, self-generated probe which can be used to explore the fireball medium tomographically. The medium will affect the hard parton along the path from its production point to where it exits the fireball. If the parton is sufficiently energetic, it will exit the medium before it can begin to fragment into hadrons. The difference in jet production rates or, more generally, in the rates for producing high-p_{t} hadrons from jet fragmentation in Au–Au and pp collisions can be calculated in terms of the density of scatterers in the

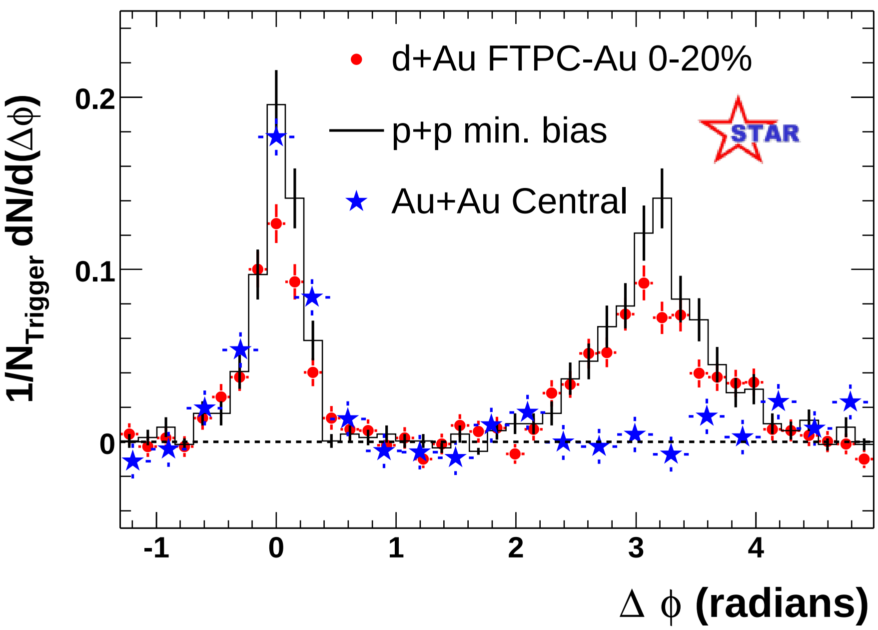

Figure 1.11: *Azimuthal correlations of charged particles relative to a high–p_t trigger particle. At $\Delta\,\phi = 0$ there is peak relative to the trigger jet and at $\Delta\,\phi = \pi$ there should be the peak relative to the counter–jet [76].*

medium, multiplied with a perturbatively calculable cross section (if the parton has sufficiently high energy to justify a perturbative approach), and integrated along the path of the jet. This integrated product of density times cross section characterises the opacity of the medium. Since the probe is coloured and interacts through colour exchange, it is sensitive to density of colour charges resolvable at the scale of its Compton wave length. Such density will be higher in a colour-deconfined QGP than in a cold nucleus where quarks and gluons are confined inside the nucleons.

It was Bjorken [34] who first suggested that partons traversing bulk partonic matter might undergo significant energy loss, with observable consequences on the parton subsequent fragmentation into hadrons. More recent theoretical studies have demonstrated that the elastic parton scattering contribution to energy loss first contemplated by Bjorken is likely to be negligible with respect to gluon radiation induced by passage through the matter [35]. Such effect would manifest by a significant softening and broadening of the jets resulting from the fragmentation of partons that traverse substantial lengths of matter containing a high density of partons. This evidence is called "jet quenching".

Fig. 1.11 shows STAR measurements of the azimuthal distribution of hadrons with $p_{\mathrm{t}} > 2$ GeV/c relative to a trigger hadron with $p_{\mathrm{t}}^{trig} > 4$ GeV/c. A hadron pair drawn from a single jet will generate an enhanced correlation at $\Delta\phi \approx 0$, as observed for p–p, d–Au and Au–Au. A hadron pair drawn from back-to-back jets will generate an enhanced correlation at $\Delta\phi \approx \pi$, as observed for p–p and for d–Au with somewhat broader width than the near-side correlation peak. However, the back-to-back dihadron correlation is strikingly, and uniquely, absent in central Au–Au collisions, while for peripheral Au–Au collisions the correlation appears quite similar to that seen in p–p and d–Au. If the correlation is indeed the result of jet fragmentation, the suppression is again due to final state effects of hard-scattered partons or their fragmentation products in the dense medium generated in Au–Au collisions.

While the away–side correlations of energetic hadrons with the trigger one are depleted, the away–side correlations between *soft* hadrons ($p_{\mathrm{t}} < 1.5$ GeV/c) and the trigger hadron are enhanced. The energy lost by the fast parton travelling away from the trigger hadron and through the medium re–appears in the form of additional soft hadrons, with a distribution of transverse momenta similar to that of the medium itself: as the Au–Au collisions become more central, the average transverse momenta $\langle p_{\mathrm{t}} \rangle$ of the extra hadrons emitted into the away-side hemisphere are observed to approach the $\langle p_{\mathrm{t}} \rangle$ of the entire collision event.

While large effects have been observed and the phenomenon of jet quenching in dense matter has been firmly established, precision data in a larger-p_{t} range are needed to fully explore the jet quenching phenomena and their connection to properties of the dense matter. The region $2 < p_{\mathrm{t}} < 6$ GeV/c has significant contributions from non-perturbative processes other than vacuum fragmentation of partons, perhaps revealing novel hadronisation mechanisms.

Coalescence

Because of its non-perturbative nature, hadronisation has so far been treated only phenomenologically based on the statistical model, the duality model, or the coalescence model. In coalescence model, hadrons are formed from quarks that are close in phase space. As a result, baryons with momentum p_{t} are produced from quarks with momenta $\sim p_{\mathrm{t}}/3$, while mesons with same momentum are from

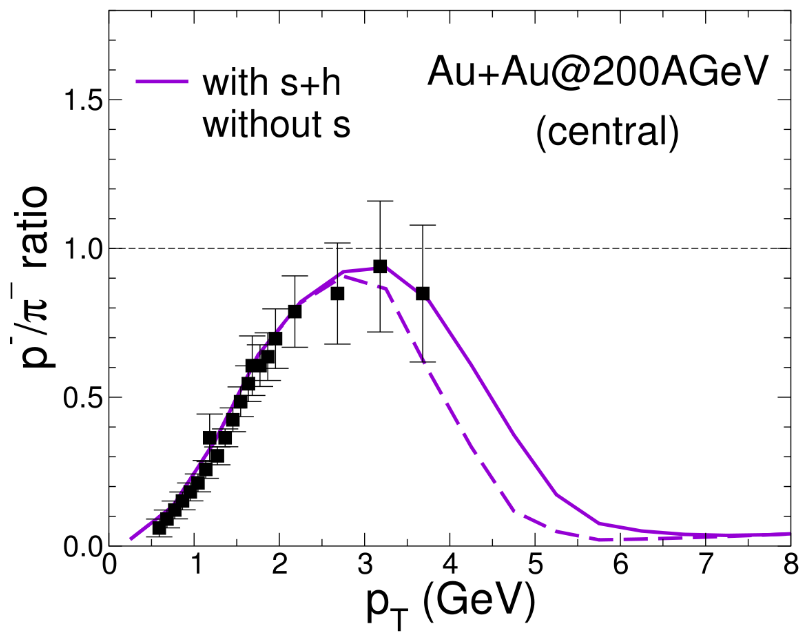

Figure 1.12: *Antiproton to pion ratio in Au+Au collisions at* $\sqrt{s_{\mathrm{NN}}} = 200$ GeV. *Solid and dashed curves are results with and without contribution to antiproton from coalescence of thermal partons [37].*

quarks with momenta $\sim p_{\mathrm{t}}/2$. Since the transverse momentum spectra of quarks decrease with p_{t}, production of high momentum baryons from quark coalescence is more favoured than mesons. This is opposite to the fragmentation process where baryon production is penalised with respect to mesons as more quarks need to be produced from the vacuum, leading to a typical p/π ratio of ~ 0.2. Results on $\overline{p}/\pi$ ratio are shown in Fig. 1.12 together with data from PHENIX.

1.5 Perspectives for LHC

The Large Hadron Collider will provide nuclear collisions at a centre-of-mass energy 30 times higher than at RHIC, opening a new era for the field, in which particle production will be dominated by hard processes, and the energy densities will possibly be high enough to treat the generated quark–gluon plasma as an ideal gas.

These qualitatively new features will allow to address the task of the LHC heavy ion programme: a systematic study of the properties of the quark–gluon plasma state.

1.5.1 Running strategy

The LHC is expected to run essentially in the same yearly mode as the SPS, starting with several months of p–p running followed at the end of each year by several weeks of heavy-ion collisions. For rate estimates, all LHC experiments use an effective time per year of 10^7 s for p–p and 10^6 s for heavy-ion operation.

The initial LHC running programme foresees [107]:

- Test runs at $\sqrt{s} = 10$ TeV
- Regular p–p runs at $\sqrt{s} = 14$ TeV (luminosity: $3 \times 10^{30}\,\mathrm{cm}^{-2}\,s^{-1}$)
- 1-2 years with Pb–Pb runs at $\sqrt{s_{\mathrm{NN}}} = 5.5$ TeV (luminosity $10^{27}\,\mathrm{cm}^{-2}\,s^{-1}$)
- 1 year with p–Pb runs at $\sqrt{s_{\mathrm{NN}}} = 8.8$ TeV (luminosity: $8 \times 10^{28}\,\mathrm{cm}^{-2}\,s^{-1}$)

The uncertainties in the initial conditions for heavy-ion collisions at the LHC translate into significant ambiguities for separating initial from final-state medium effects. A main motivation for a nucleon–nucleus run is to alter the relative importance of initial and final state medium effects, thus allowing for a better separation between them. p–A (or d–A) collisions will provide, together with the p–p results, a compulsory benchmark for the interpretation of the A–A data.

1.5.2 Bulk particle production

The average charged-particle multiplicity per rapidity unit (rapidity density $\mathrm{d}N_{\mathrm{ch}}/\mathrm{d}y$) is the first accessible observable which can provide valuable informations. On the theoretical side, it fixes a global property of the medium produced in the collision. Since it is related to the attained energy density, it enters the calculation of most other observables. Another important 'day-one' observable is the total transverse energy, per rapidity unit at mid-rapidity. It determines how much of the total initial longitudinal energy is converted to transverse debris of QCD matter. On the experimental side, the particle multiplicity fixes the main unknown in the detector performance; the charged-particle multiplicity per unit rapidity largely determines the accuracy with which many observables can be measured.

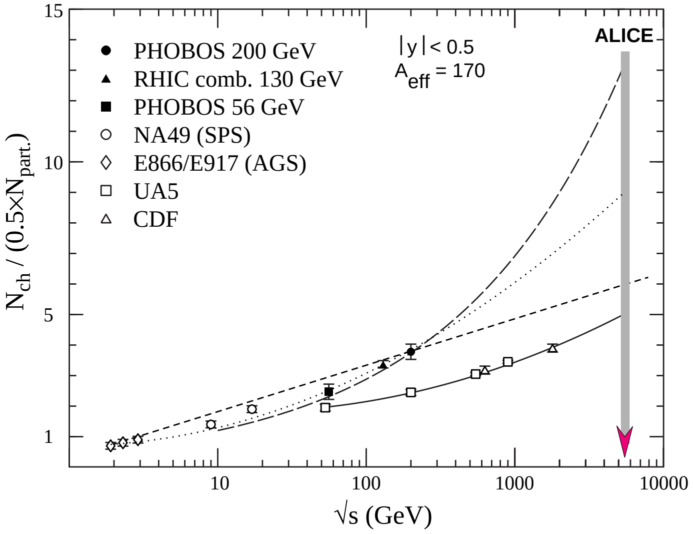

Figure 1.13: *Charged-particle rapidity density per participant pair as a function of centre-of-mass energy for A–A and p–p collisions. Experimental data for p–p collisions are overlaid by the solid line. The dashed line is a fit* $0.68 \ln(\sqrt{s}/0.68)$ *to all the nuclear data. The dotted curve is* $0.7 + 0.028 \ln^2 s$*. It provides a good fit to data below and including RHIC, and predicts* $N_{\rm ch} = 9 \times 170 = 1500$ *at LHC. The long dashed line is an extrapolation to LHC energies using the saturation model [38]. Taken from [107].*

There is no first principle calculation of $\mathrm{d}N_{\rm ch}/\mathrm{d}y$ starting from the QCD Lagrangian, since particle production is dominated by soft non-perturbative QCD. Therefore, the large variety of available models of heavy ion collisions gives a wide range of predicted multiplicities. Before RHIC, the predictions for the LHC reached up to more than 8000 charged particles per unit of rapidity. The multiplicity measured at RHIC, $\mathrm{d}N_{\rm ch}/\mathrm{d}y \simeq 650$ at $\sqrt{s_{\rm NN}} = 200$ GeV, is about a factor 2 lower than what was predicted by most models. As it can be seen from Figure 1.13, the multiplicity at the LHC is not expected to be larger than 3000-4000 charged particles per unit of rapidity. An approximate prediction for the LHC taken directly from the figure is $\mathrm{d}N_{\rm ch}/\mathrm{d}y \approx 13 \times A_{eff} = 2200$.

Table 1.1: *Comparison of the parameters characterising central nucleus–nucleus collisions at different energy regimes.*

Parameter		SPS	RHIC	LHC
$\sqrt{s_{\mathrm{NN}}}$	[GeV]	17	200	5500
$\mathrm{d}N_{\mathrm{ch}}/\mathrm{d}y$		400	650	$\simeq 2500$
Initial temperature	[MeV]	200	350	> 600
Energy density	[GeV/fm^3]	3	> 15	120
Freeze-out volume	[fm^3]	few 10^3	few 10^4	few 10^5
Life-time	[fm/c]	< 2	2-4	> 10

1.5.3 A new domain?

Starting from the estimates of the charged multiplicity many parameters of the medium produced in the collision can be inferred. Table 1.1 presents a comparison of the most relevant parameters for SPS, RHIC and LHC energies [38].

At the LHC, the high energy in the collision centre of mass is expected to determine a large energy density and an initial temperature at least a factor 2 larger than at RHIC. This high initial temperature extends also the life-time and the volume of the deconfined medium, since it has to expand while cooling down to the freeze-out temperature, which is ≈ 170 MeV (it is independent of $\sqrt{s}$, above the SPS energy). In addition, the large expected number of gluons favours energy and momentum exchanges, thus considerably reducing the time needed for the thermal equilibration of the medium. To summarise, the LHC will produce *hotter, larger and longer-living* 'drops' of QCD plasma than the present heavy ion facilities.

The key advantage in this new 'deep deconfinement' scenario is that the quark–gluon plasma studied by the LHC experiments will be much more similar to the quark–gluon plasma that can be investigated from a theoretical point of view by means of lattice QCD.

As mentioned, lattice calculations are mostly performed for a baryon-free system ($\mu_{\mathrm{B}} = 0$). In general, $\mu_{\mathrm{B}} = 0$ is not valid for heavy ion collisions, since the two colliding nuclei carry a total baryon number equal to twice their mass number. However, the baryon content of the system after the collision is expected to be concentrated rather near the rapidity of the two colliding nuclei. Therefore, the larger the rapidity of the beams, with respect to their centre of mass, the lower the baryo-chemical potential in the central rapidity region. The rapidities of the beams at SPS, RHIC and LHC are 2.9, 5.3 and 8.6, respectively. Clearly, the LHC is expected to be much more baryon-free than RHIC and SPS and, thus, closer to the conditions simulated in lattice QCD.

Heavy ion collisions at the LHC access not only a quantitatively different regime of much higher energy density but also a qualitatively new regime, mainly for two reasons. First because high-density parton distributions are expected to dominate particle production. That means the number of low-energy partons (mainly gluons) in the two colliding nuclei is, therefore, expected to be so large as to produce a significant shadowing effect (described in the next Section) that suppresses the inelastic scatterings with low momentum transfer. Second because at the LHC energies hard processes should contribute significantly to the total A–A cross section. This opens up the possibility to use heavy flavour as an experimental tool for a detailed characterisation of the QGP medium. Heavy flavour will be the subject of the next chapter.

1.5.4 Parton distribution functions

In the inelastic collision of a proton (or, more generally, nucleon) with a particle, the Bjorken x variable is defined as the fraction of the proton momentum carried by the parton that enters the hard scattering process. The distribution of x for a given parton type (e.g. gluon, valence quark, sea quark) is called Parton Distribution Function (PDF) and it gives the probability to pick up a parton with momentum fraction x from the proton.

The LHC will allow to probe the parton distribution functions of the nucleon and, in the case of proton–nucleus and nucleus–nucleus collisions, also their modifications in the nucleus, down to unprecedented low values of x.

High-density parton distributions will determine particle production. The LHC heavy-ion programme accesses a novel range of Bjorken-x values as shown in figure 1.14 where the relevant x ranges of the highest energies at SPS, RHIC and LHC with the heaviest nuclei are compared.

The extension of the x range down to $\sim 10^{-4}$ at the LHC means, in a very simplified picture, that a large-x parton in one of the two colliding Pb nuclei 'sees' the other incoming nucleus as a superposition of $\approx$ A $\times$ $1/10^{-4}$ $\approx$ 10^6

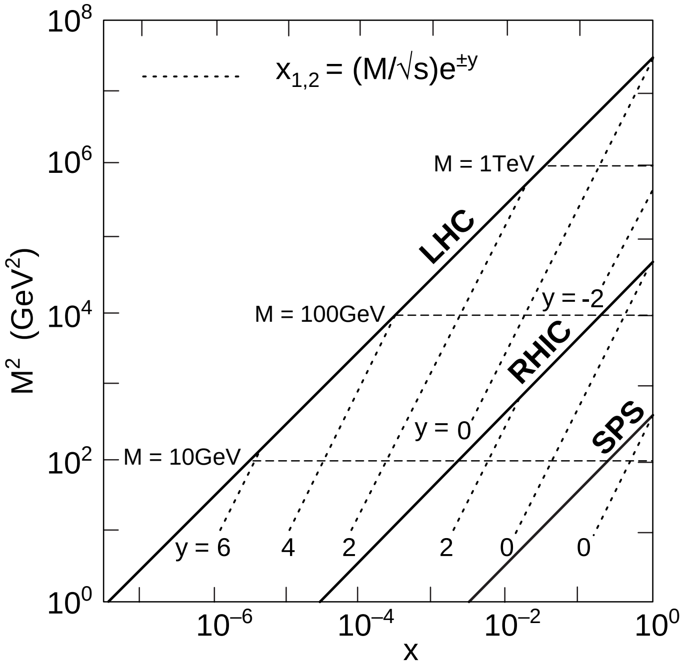

Figure 1.14: *The range of Bjorken x and M^2 relevant for particle production in nucleus–nucleus collisions at the top SPS, RHIC, and LHC energies. Lines of constant rapidity are shown for LHC, RHIC and SPS [107].*

gluons. These gluons are so many that the lower-momentum ones tend to merge together: two gluons with momentum fractions x_1 and x_2 merge in a gluon with momentum fraction x_1+x_2 ($g_{x_1}g_{x_2} \to g_{x_1+x_2}$). As a consequence of this ‘migration towards larger values of x, that does not affect only gluons but all partons, the nuclear parton densities are depleted in the small-x region (and slightly enhanced in the large-x region) with respect to the proton parton densities.

This phenomenon is known as “nuclear shadowing effect” and it has been experimentally studied in electron–nucleus Deep Inelastic Scattering (DIS) in the range $5 \cdot 10^{-3} < x < 1$ [44]. However, no data are available in the x range covered by the LHC and the existing data provide only weak constraints for the gluon PDFs, which do not enter the measured structure functions at leading order.

As will be shown in the following Chapters, this effect will complicate the comparison between experimental data and theoretical calculations in the low transverse momentum region.

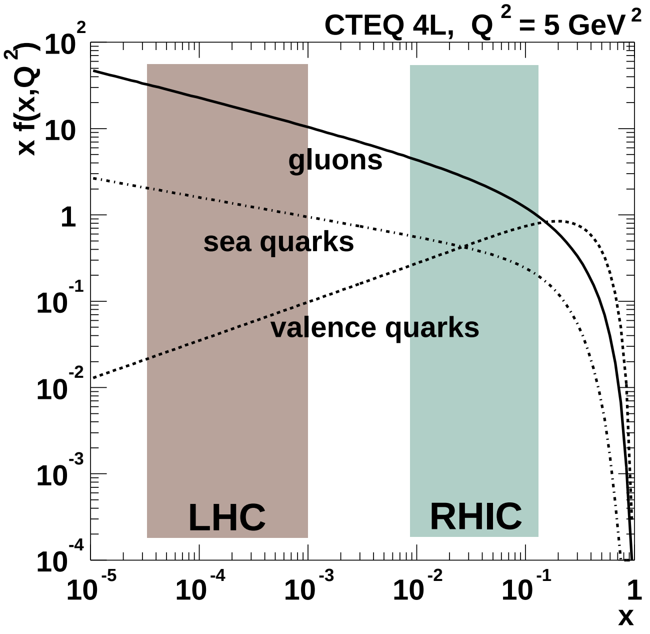

Figure 1.15: *Parton distribution functions in the proton, in the CTEQ 4L parametrisation, for* $Q^2 = 5$ GeV^2*. Taken from [193].*

Chapter 2

Heavy quarks in heavy-ion collisions

Heavy flavour quarks (charm and beauty) are of particular interest for the study of the dense medium formed in heavy-ion collisions. In particular, for the high energy collisions (proton–proton and Pb–Pb) that will take place at LHC, the key features are the following:

- Heavy quarks will be produced in abundance. With a predicted factor 100 of increase in the yield for $b\bar{b}$ pairs at LHC with respect to RHIC, beauty production will be measurable with good precision.
- Being produced mainly in initial hard scattering processes, their production yield does not depend on the properties of the medium. Therefore heavy quarks are a "clean" experimental probe for the study of medium effects.
- Heavy quarks are interesting probes for the medium created in the collisions since they interact with it via partonic energy loss and their long decay time implies that they experience the entire evolution of the fireball.
- The measurement of charm and beauty production in proton–proton and proton–nucleus collisions, besides providing the necessary baseline for the study of medium effects in nucleus–nucleus collisions, is of great intrinsic interest, as a test of both perturbative and non-perturbative sectors of QCD in a new energy domain.

Section 2.1 reviews the calculation for the production of charm and beauty in proton–proton (2.1.1) and Pb–Pb (2.1.2) collisions at LHC. Section 2.2 describes some of the experimental observables related with the heavy quarks and Section 2.3 summarises some of the experimental results obtained with the study of heavy quarks.

2.1 Heavy flavour production at LHC

Heavy quarks are produced in the early stage of the collision in primary partonic scatterings with large virtuality Q and, thus, on temporal and spatial scales, $\Delta\tau \sim \Delta r \sim 1/Q$, which are sufficiently small for the production to be unaffected by the properties of the medium, in the case of nucleus–nucleus collisions. In fact, the minimum virtuality $Q_{\rm min} = 2\,M_Q$ in the production of a $Q\overline{Q}$ pair implies a space time scale of $\sim 1/(2\,M_Q) \simeq 1/2.4~\mathrm{GeV}^{-1} \simeq 0.1$ fm (for charm), to be compared to the expected lifetime of the QGP phase at the LHC, > 10 fm. Thus, the initially-produced heavy quarks experience the full collision history.

Given the large virtualities that characterise the production of heavy quarks, it is safe to assume that the baseline cross section in nucleon–nucleon collisions can be calculated in the framework of collinear factorisation and perturbative QCD (pQCD). The general lines followed for the cross section calculations in proton–proton collisions and the results and theoretical uncertainties at LHC energies are described [106, 107].

2.1.1 Proton-proton collisions

Given the heavy quark large mass ($M_{\rm b} \approx 4.8~\mathrm{GeV}/c^2 > M_{\rm c} \approx 1.2~\mathrm{GeV}/c^2 > \Lambda_{QCD} \approx 200~\mathrm{MeV}/c^2$) [127] their production can be described by a perturbative approach (pQCD). Using the factorisation theorem one can write the single-inclusive differential cross section for the production of a heavy flavour hadron H_Q as:

$$\begin{aligned} \mathrm{d}\sigma^{\mathrm{NN}\to \mathrm{H}_Q X}(\sqrt{s_{\rm NN}}, M_Q, \mu_{\rm F}^2, \mu_{\rm R}^2) \;=\; & \sum_{i,j=q,\overline{q},g} f_i(x_1,\mu_{\rm F}^2) \otimes f_j(x_2,\mu_{\rm F}^2) \otimes \\ & \mathrm{d}\hat{\sigma}^{ij\to Q(\overline{Q})\{k\}}(\alpha_{\rm s}(\mu_{\rm R}^2), \mu_{\rm F}^2, M_Q, x_1 x_2 s_{\rm NN}) \otimes \\ & D_Q^{\mathrm{H}_Q}(z, \mu_{\rm F}^2)\,, \end{aligned} \tag{2.1}$$

where, Q is the heavy quark (either charm or beauty), M_Q is its mass, $\hat{p}_{\rm t}$ its transverse momentum and H_Q its resulting hadron. The sum runs over all subprocesses that lead to the heavy flavoured hadron. The formula is made up of different terms:

- $f_i(x_i, \mu_F^2)$ is the parton distribution function, the probability of finding a quark or a gluon i with a momentum fraction x_i of the nucleon. The PDFs are evolved with the virtuality Q^2 up to the factorisation scale μ_F using the DGLAP equations [42].
- $\frac{\mathrm{d}\hat{\sigma}}{\mathrm{d}\hat{p}_\mathrm{t}}(ij \to Q(\overline{Q}))$ is the partonic cross section. Given the high mass of the quarks involved ($M_\mathrm{b} > M_\mathrm{c} > \Lambda_{QCD}$) it is related to interactions of partons at high Q^2. This means that it can be computed by perturbative QCD. It is a function of the heavy quark mass (M_Q), of the parton-parton centre of mass energy squared ($x_1 x_2 s$) and of the quark transverse momentum ($\hat{p}_\mathrm{t}$). Using the pQCD approach, the cross section can be calculated as a power expansion of α_s. It has been calculated up to next-to-leading order (NLO, see Ref. [43]), that corresponds to $O(\alpha_s^3)$).
- $D_Q^{H_Q}(z, \mu_F^2)$ is the fragmentation function, that represents the probability for the heavy quark Q to hadronize as a specific hadron H_Q with a momentum fraction $z = p_{H_Q}/p_Q$. This is usually extracted by fitting a phenomenological model to fragmentation data in e^+e^-.

The following paragraphs outline the status of the cross section calculations in nucleon–nucleon collisions [106].

The existing data on total charm production cross section in p–p and p–A collisions[1] up to ISR energies are compared in Fig. 2.1 with NLO calculations [47]. In Fig. 2.2 a NLO calculation from Ref. [50] is compared to the data in p$\overline{\mathrm{p}}$ collisions from UA1, CDF and D0, for which the b quark production cross section integrated for $p_\mathrm{t} > p_\mathrm{t}^\mathrm{min}$ is given. These measurements are taken in the central rapidity region ($|y| < 1.5$ for UA1, $|y| < 1$ for CDF and D0). All the calculations have been performed using the following values for the heavy quark masses (M_c, M_b) and for the factorisation and renormalisation scales (μ_F, μ_R):

$$M_\mathrm{c} = 1.2 \text{ GeV} \qquad\qquad \mu_F = \mu_R = 2\,\mu_0 \tag{2.2}$$

for charm, and

$$M_\mathrm{b} = 4.75 \text{ GeV} \qquad\qquad \mu_F = \mu_R = \mu_0 \tag{2.3}$$

---

[1] The p–A results were scaled according to the number of binary nucleon–nucleon collisions, in order to obtain the equivalent cross section in p–p.

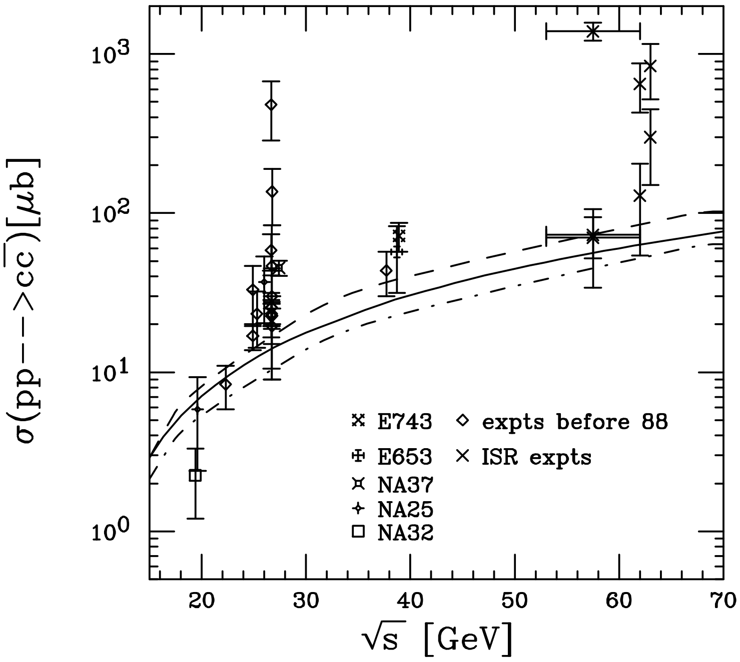

Figure 2.1: *Total charm production cross section from p–p and p–A measurements compared [107] to NLO calculations [47] with MRS D-' (solid), MRST HO (dashed) and MRST LO (dot-dashed) parton distributions.*

for beauty; $\mu_0 = \sqrt{(p^2_{\mathrm{t,Q}} + p^2_{\mathrm{t,\overline{Q}}})/2 + M^2_Q}$ is approximately equal to the transverse mass of the produced heavy quarks.

For both charm and beauty the theory describes the present data reasonably well.

The results for LHC energies ($\sqrt{s} = 5.5$, 8.8 and 14 TeV) are reported in Table 2.1. These values are obtained using the NLO pQCD calculation implemented in the program HVQMNR [100] and two sets of parton distribution functions, MRST HO [39] and CTEQ 5M1 [40], which include the small-x HERA results. The difference due to the choice of the parton distribution functions is relatively small ($\sim$ 20-25% at 5.5 TeV, slightly lower at 14 TeV).

The dependence on the PDF set represents only a part of the error on the theoretical estimate. An evaluation of the theoretical uncertainties was done by varying the M_{c} (M_{b}), μ_F and μ_R parameters and is reported in [51]. At LHC energies, the theoretical uncertainties span a factor $\sim$ 2-3 in the total production

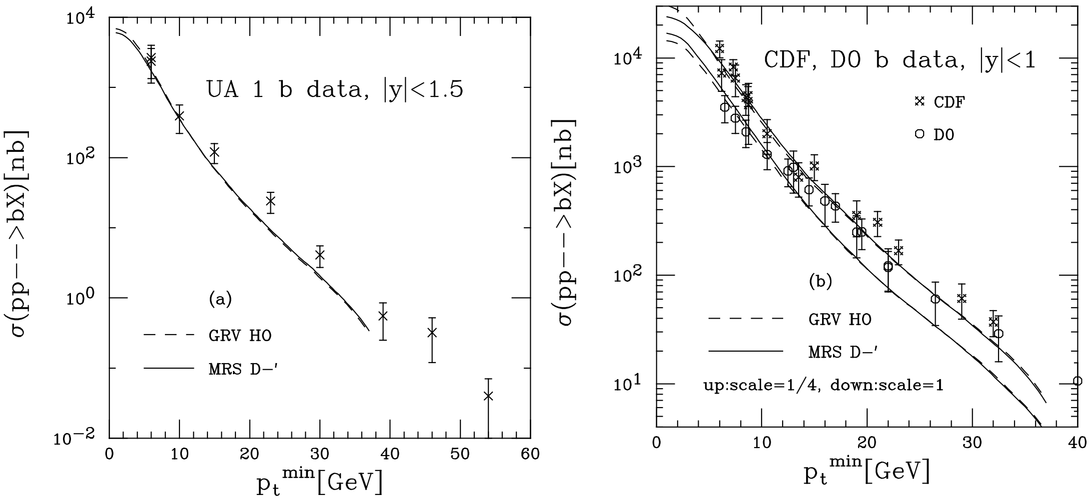

Figure 2.2: *Comparison with b quark production cross section integrated over* $p_t > p_t^{\min}$ *from (a) UA1 [48] and (b) CDF and D0 [49]. The NLO calculations are with MRS D-' (solid) and GRV HO (dashed) parton distributions.*

cross section of both charm and beauty quarks.

Yields in proton–proton collisions at $\sqrt{s} = 14$ TeV

Using a proton–proton inelastic cross section $\sigma_{\rm pp}^{\rm inel} = 70$ mb at 14 TeV [107] and the average heavy flavour cross sections in the last row of Table 2.1, the yields

Table 2.1: *NLO calculation [100] for the total* $\rm c\overline{c}$ *and* $\rm b\overline{b}$ *cross sections in p–p collisions at 5.5, 8.8 and 14* TeV*, using the MRST HO and CTEQ 5M1 parton distribution functions.*

	$\sigma_{\rm pp}^{\rm c\overline{c}}$[mb]			$\sigma_{\rm pp}^{\rm b\overline{b}}$[mb]		
$\sqrt{s}$	5.5 TeV	8.8 TeV	14 TeV	5.5 TeV	8.8 TeV	14 TeV
MRST HO	5.9	8.4	10.3	0.19	0.28	0.46
CTEQ 5M1	7.4	9.6	12.1	0.22	0.31	0.55
Average	6.6	9.0	11.2	0.21	0.30	0.51

for the production of $Q\overline{Q}$ pairs are:

$$N_{\rm pp}^{Q\overline{Q}} = \sigma_{\rm pp}^{Q\overline{Q}} \Big/ \sigma_{\rm pp}^{\rm inel}. \tag{2.4}$$

Thus 0.16 $\rm c\overline{c}$ pairs and 0.0072 $\rm b\overline{b}$ pairs per event was obtained.

2.1.2 Nucleus-nucleus collisions

If no nuclear effects are taken into account, a nucleus–nucleus collision can be considered, for hard processes, as a superposition of independent nucleon–nucleon (NN) collisions. Thus, the cross section for such processes in heavy-ion collisions can be calculated using a simple geometrical extrapolation from pp collisions, i.e. assuming that the hard cross section scales from pp to nucleus–nucleus collisions proportionally to the number of inelastic nucleon–nucleon collisions (binary scaling).

Nuclear effects, such as nuclear shadowing, broadening of the parton intrinsic transverse momentum ($k_{\rm t}$) in the nucleon, in-medium parton energy loss, as well as possible enhancements due to additional production in the medium, can modify this geometrical scaling from p–p to nucleus–nucleus collisions. Such effects are, indeed, what one want to measure. Nuclear shadowing can be accounted for by recalculating the hard cross section in elementary nucleon–nucleon collisions with nuclear-modified parton distribution functions and extrapolating to the nucleus–nucleus case.

Cross sections and yields in Pb–Pb collisions at $\sqrt{s_{\rm NN}} = 5.5$ TeV

For the calculation of the yields was used the EKS98 parametrisation [52] of nuclear shadowing (see [106]). The centrality dependence of the shadowing is weak for collisions in the considered centrality range (up to 10% of $\sigma^{\rm inel}$) [53] and is neglected here. The reduction of the cross section due to shadowing amounts to about 35% for $\rm c\overline{c}$ pairs and to about 15% for $\rm b\overline{b}$ pairs (beauty production corresponds to larger values of x, less affected by the shadowing suppression).

Table 2.2 reports the charm and beauty total cross sections and yields per NN collision (with and without shadowing) at $\sqrt{s_{\rm NN}} = 5.5$ TeV, as calculated with the HVQMNR program, and the extrapolated values for Pb–Pb collisions, as obtained from binary scaling [106]. The values shown correspond to the average of the results obtained with MRST HO and CTEQ 5M1 parton distribution functions.

Table 2.2: *Total cross sections and yields for charm and beauty production in NN and Pb–Pb collisions at* $\sqrt{s_{\rm NN}} = 5.5$ TeV*. The effect of shadowing is shown as the ratio* $C_{\rm shad}$ *of the cross section calculated with and without the modification of the parton distribution functions. Taken from [106].*

	Charm	Beauty
$\sigma^{Q\overline{Q}}_{\rm NN}$ [mb] *w/o shadowing*	6.64	0.21
$\sigma^{Q\overline{Q}}_{\rm NN}$ [mb] *w/ shadowing*	4.32	0.18
$C_{\rm shad}$	0.65	0.84
$\sigma^{Q\overline{Q}}_{\rm Pb-Pb}$[b] ($5\%\sigma^{inel}$)	45.0	1.79
$N^{Q\overline{Q}}_{\rm Pb-Pb}$ ($5\%\sigma^{inel}$)	115.0	4.56

Table 2.3: *Summary table of the production yields and of the average magnitude of nuclear shadowing in pp, pPb, and Pb–Pb collisions. Taken from [106].*

	Charm			Beauty		
System	pp	pPb	Pb–Pb	pp	pPb	Pb–Pb
Centrality	min.-bias	min.-bias	centr. (5%)	min.-bias	min.-bias	centr. (5%)
$\sqrt{s_{\rm NN}}$	14 TeV	8.8 TeV	5.5 TeV	14 TeV	8.8 TeV	5.5 TeV
$N^{Q\overline{Q}}$/ev	0.16	0.78	115	0.0072	0.029	4.56
$C_{\rm shad}$	1	0.80	0.65	1	0.90	0.84

Cross sections and yields in pPb collisions at $\sqrt{s_{\rm NN}} = 8.8$ TeV

Using A = 208 and $\sigma^{\rm inel}_{\rm p-Pb} = 1.9$ barn [107], the yield of $Q\overline{Q}$ pairs per minimum-bias collision is:

$$N^{Q\overline{Q}}_{\rm p-Pb} = \sigma^{Q\overline{Q}}_{\rm NN} \cdot 0.109\ {\rm mb}^{-1}. \tag{2.5}$$

As for the Pb–Pb case, the effect of nuclear shadowing was accounted for by using the EKS98 parametrisation [52].The effect is lower for pPb, since one of the colliding nuclei is a proton: the reduction of the cross sections due to nuclear shadowing is about 20% for charm and about 10% for beauty.

A summary of the production yields and of the average magnitude of nuclear shadowing in the three considered colliding systems is presented in Table 2.3.

2.2 Heavy flavour as probes

2.2.1 Parton energy loss for heavy quarks

While traversing the dense matter produced in nucleus–nucleus collisions, the initially-produced hard partons lose energy, mainly on account of multiple scatterings and medium-induced gluon radiation, and become quenched. An intense theoretical activity has developed around the subject [56–60]. Here is summarised the general lines of the so-called “BDMPS” model [57, 58]. In a simplified picture, an energetic parton produced in a hard collision undergoes, along its path in the dense medium, multiple scatterings in a Brownian-like motion with mean free path λ, which decreases as the medium density increases. In this multiple scattering process, the gluons in the parton wave function pick up transverse momentum $k_{\rm t}$ with respect to its direction and they may eventually ‘decohere’ and be radiated.

The scale of the energy loss is set by the characteristic energy of the radiated gluons, which depends on L and on the properties of the medium:

$$\omega_c = \hat{q}\, L^2/2 \tag{2.6}$$

where $\hat{q}$ is the transport coefficient of the medium, defined as the average transverse momentum squared transferred to the projectile per unit path length, $\hat{q} = \langle k_{\rm t}^2 \rangle_{\rm medium}/\lambda$ [61].

In the case of a static medium, the distribution of the energy ω of the radiated gluons (for $\omega \ll \omega_c$) is of the form:

$$\omega \frac{{\rm d}I}{{\rm d}\omega} \simeq \frac{2\,\alpha_{\rm s}\, C_{\rm R}}{\pi} \sqrt{\frac{\omega_c}{2\omega}} \tag{2.7}$$

where $C_{\rm R}$ is the QCD coupling factor (Casimir factor), equal to 4/3 for quark–gluon coupling and to 3 for gluon–gluon coupling. The integral of the energy distribution up to ω_c estimates the average energy loss of the parton:

$$\langle \Delta E \rangle = \int_0^{\omega_c} \omega \frac{{\rm d}I}{{\rm d}\omega} {\rm d}\omega \propto \alpha_{\rm s}\, C_{\rm R}\, \omega_c \propto \alpha_{\rm s}\, C_{\rm R}\, \hat{q}\, L^2\,. \tag{2.8}$$

The average energy loss is: proportional to $\alpha_{\mathrm{s}}\, C_{\mathrm{R}}$ and, thus, larger by a factor $9/4 = 2.25$ for gluons than for quarks; proportional to the transport coefficient of the medium; proportional to L^2; independent of the initial parton energy E. It is a general feature of all parton energy loss calculations [56–64] that the gluon energy distribution (2.7) does not depend on E. Depending on how the kinematic bounds are taken into account, the resulting ΔE is then independent [57, 58] or logarithmically dependent on E [62–64]. However, there is always an intrinsic dependence of the radiated energy on the initial energy, determined by the fact that the former cannot be larger than the latter, $\Delta E \leq E$. As discussed in Ref. [66], this effectively results in reducing the difference between quark and gluon average energy losses and in changing the L dependence from quadratic to approximately linear. Moreover, since a consistent theoretical treatment of the finite-energy constraint is at present lacking in the BDMPS framework, approximations have to be adopted, thus introducing uncertainties in the results [66, 72].

The transport coefficient is proportional to the density of the scattering centres and to the typical momentum transfer in gluon scattering off these centres. A review of the estimates for the value of the transport coefficient in media of different densities can be found in Ref. [65]: the estimate is $\hat{q}_{\mathrm{cold}} \simeq 0.05~\mathrm{GeV}^2/\mathrm{fm}$ for cold nuclear matter and, for a QGP formed at the LHC with energy density $\epsilon \sim 50$–$100~\mathrm{GeV}/\mathrm{fm}^3$, $\hat{q}$ may be as large as $100~\mathrm{GeV}^2/\mathrm{fm}$.

The medium-induced energy loss of heavy quarks was first studied in Refs. [55, 67]. Subsequently, in Ref. [54] it was argued that for heavy quarks, because of their large mass, the radiative energy loss should be lower than for light quarks. The predicted consequence of this effect was an enhancement of the ratio of D mesons to pions (or light-flavoured hadrons in general) at moderately-large (5–10 GeV/c) transverse momenta, with respect to that observed in the absence of energy loss.

Heavy quarks with moderate energy, i.e. $m/E > 0$, propagate with a velocity $\beta = \sqrt{1 - (m/E)^2}$ significantly smaller than the velocity of light, $\beta = 1$. As a consequence, in the vacuum, gluon radiation at angles Θ smaller than the ratio of their mass to their energy $\Theta_0 = m/E$ is suppressed[2] [68]. The relatively depopulated cone around the heavy-quark direction with $\Theta < \Theta_0$ is called the 'dead cone'.

In Ref. [54] the dead-cone effect is assumed to characterise also in-medium

---

[2] A term $(\Theta^2 + \Theta_0^2)^{-2}$ governs the angular dependence of the propagator of the gluon-radiation process $Q \to Qg$.

gluon radiation, and the energy distribution of the radiated gluons (2.7), for heavy quarks, is estimated to be suppressed by a factor:

$$\omega \frac{\mathrm{d}I}{\mathrm{d}\omega}\bigg|_{\mathrm{Heavy}} \bigg/ \omega \frac{\mathrm{d}I}{\mathrm{d}\omega}\bigg|_{\mathrm{Light}} = \left[1 + \frac{\Theta_0^2}{\Theta^2}\right]^{-2} = \left[1 + \left(\frac{m}{E}\right)^2 \sqrt{\frac{\omega^3}{\hat{q}}}\right]^{-2} \equiv F_{\mathrm{H/L}}(m/E, \hat{q}, \omega)\,, \tag{2.9}$$

where the expression for the characteristic gluon emission angle [54] $\Theta \simeq (\hat{q}/\omega^3)^{1/4}$ has been used. The dead-cone suppression factor $F_{\mathrm{H/L}}$ in Eq. (2.9) increases (less suppression) as the heavy-quark energy E increases (the mass becomes negligible) and it decreases at large ω, indicating that the high-energy part of the gluon radiation spectrum is drastically suppressed by the dead-cone effect.

A detailed calculation of the radiated-gluon energy distribution $\omega\,\mathrm{d}I/\mathrm{d}\omega$ in the case of massive partons [69] confirms the qualitative feature of lower energy loss for heavy quarks, although the effect is found to be quantitatively smaller than that derived with the dead-cone approximation of Ref. [54]. A comparison of the results obtained in the two cases for the D meson suppression in central Pb–Pb collisions at the LHC can be found in Ref. [70]. Calculation results published in Ref. [71] and based on the BDMPS formalism (modified for massive partons according to Ref. [69]) and on a Glauber-model description of the collision geometry, indicate the *heavy-to-light ratios* at the LHC as promising new observables to test the partonic mechanism expected to underlie jet quenching. The heavy-to-light ratios for D and B mesons, $R_{\mathrm{D}/h}$ and $R_{\mathrm{B}/h}$, are defined as the ratio of the nuclear modification factors of the heavy flavoured mesons to that of light flavoured hadrons (h):

$$R_{\mathrm{D(B)}/h}(p_{\mathrm{t}}) = R_{\mathrm{AA}}^{\mathrm{D(B)}}(p_{\mathrm{t}}) / R_{\mathrm{AA}}^{h}(p_{\mathrm{t}}) = \frac{\mathrm{d}^2 N_{\mathrm{AA}}^{\mathrm{D(B)}}/\mathrm{d}p_{\mathrm{t}}\mathrm{d}y}{\mathrm{d}^2 N_{\mathrm{pp}}^{\mathrm{D(B)}}/\mathrm{d}p_{\mathrm{t}}\mathrm{d}y} \bigg/ \frac{\mathrm{d}^2 N_{\mathrm{AA}}^{h}/\mathrm{d}p_{\mathrm{t}}\mathrm{d}y}{\mathrm{d}^2 N_{\mathrm{pp}}^{h}/\mathrm{d}p_{\mathrm{t}}\mathrm{d}y}\,. \tag{2.10}$$

Heavy-to-light ratios are suggested to be sensitive to the colour-charge and to the mass dependence of medium-induced parton energy loss [71], as illustrated in Fig. 2.3 where $R_{D/h}(p_{\mathrm{t}})$ and $R_{B/h}(p_{\mathrm{t}})$ are shown, without and with the effect of the c and b masses, for the transport coefficient range $\hat{q} = 25$–$100~\mathrm{GeV}^2/\mathrm{fm}$, expected for central Pb–Pb collisions at the LHC on the basis of the R_{AA}^{h} values measured at RHIC [73, 75] (the curves for the much lower value $\hat{q} = 4~\mathrm{GeV}^2/\mathrm{fm}$ are reported as well for comparison).

- For D mesons (see upper panels of Fig. 2.3 for $M_{\mathrm{c}} = 0,\ 1.2$ GeV) the effect of the charm mass is expected to be small and limited to the range $p_{\mathrm{t}} <$

10 GeV/c, where initial-state effects, like shadowing, or final-state effects other than parton energy loss, like in-medium hadronisation, may prevent a clear analysis of heavy-to-light ratios. For higher transverse momentum ($10 \leq p_{\rm t} \leq 20$ GeV/c), charm quarks would behave essentially like massless quarks. However, since at LHC energy light-flavoured hadron yields are dominated by gluon parents, $R_{{\rm D}/h}$ would be enhanced with respect to unity as a consequence of the larger colour charge (reflected in the Casimir factor $C_{\rm R}$) of gluons relative to quarks. Therefore, $R_{{\rm D}/h}$ would be a sensitive probe of the colour-charge dependence of parton energy loss.

- For B mesons (see lower panels of Fig. 2.3 for $M_{\rm b} = 0,\ 4.8$ GeV), in contrast, the heavy-to-light ratio would be strongly enhanced due to the large b mass even in the range $10 \leq p_{\rm t} \leq 20$ GeV/c, thus providing a sensitive test of the mass dependence of parton energy loss.

2.2.2 Azimuthal dependence of heavy quark production

The azimuthal anisotropy of particle production in non-central events is regarded as a powerful tool to study the early stage of nucleus–nucleus collisions (see [107]). The spatial anisotropy of the almond-shaped nuclear overlap region in the initial stage is expected to be transferred into momentum anisotropy in the final state. A non-zero v_2 also for heavy quarks would support partonic level thermalisation and very high density at the early stage of the collision. A recent measurement of the v_2 of electrons from heavy flavour (mainly charm) decays by the PHENIX Collaboration [74], that will be further discussed in Section 2.3.2, favours a scenario in which the charm quark has a similar v_2 to lighter quarks. At the LHC, the large cross section for heavy-quark production will allow the direct measurement of charm and beauty mesons v_2, not only in the intermediate $p_{\rm t}$ region up to $6-8$ GeV/c, where the parton coalescence mechanism is expected to be relevant, but possibly also at higher momenta, where hadronisation should take place via fragmentation out of the medium. The high-$p_{\rm t}$ hard partons (or heavy quarks) should not thermalize in the medium and, thus, they should not acquire the large elliptic flow induced by collective pressure effects. Their azimuthal anisotropy in non-central collisions should instead be mainly determined by the path-length dependence of QCD energy loss in the geometrically-asymmetric dense medium.

In summary, depending on the considered momentum range, the measurement of the D and B mesons azimuthal anisotropy v_2 probes (a) the degree of

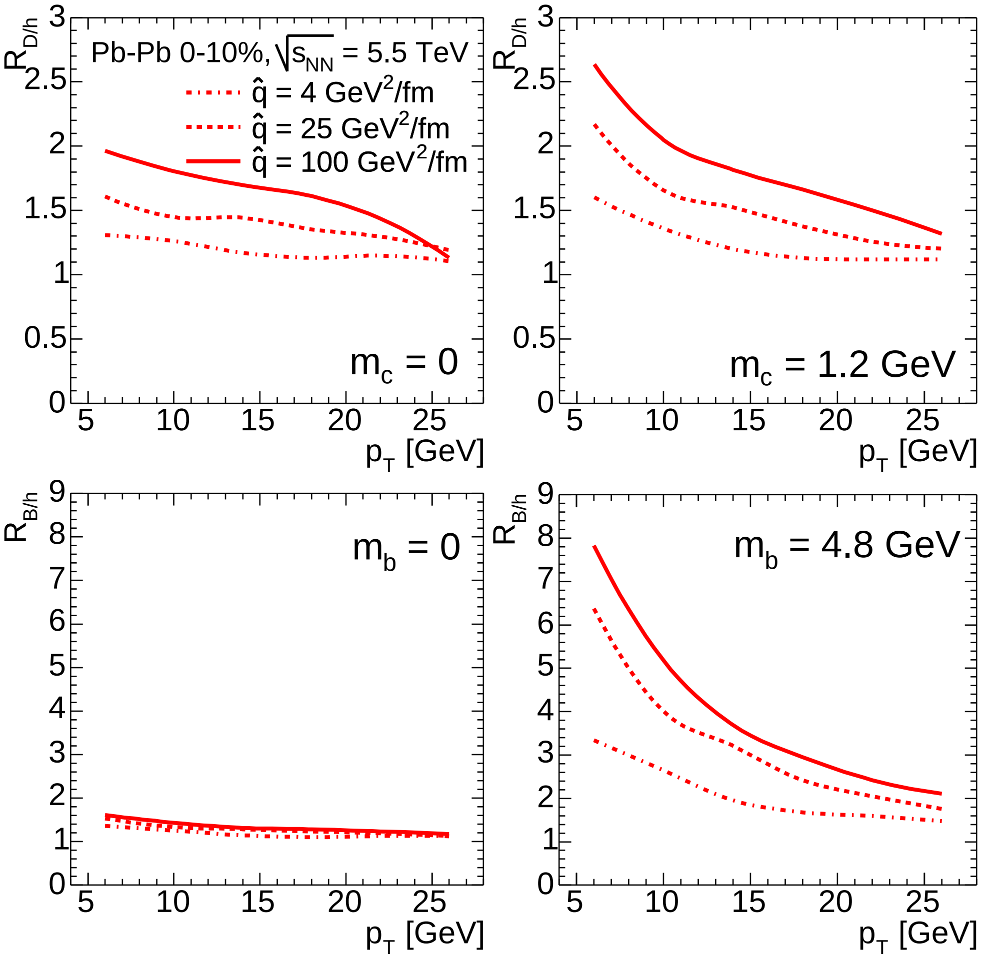

Figure 2.3: *Heavy-to-light ratios, Eq. (2.10), for D mesons (upper plots) and B mesons (lower plots) for the case of a realistic heavy quark mass (plots on the right) and for a case study in which the quark-mass dependence of parton energy loss is neglected (plots on the left). From Ref. [71].*

thermalisation of charm and beauty quarks in the expanding medium, at low and intermediate momenta ($\leq$ 7 GeV/c); (b) the in-medium path-length dependence of heavy-quark energy loss in the almond-shaped partonic system, at higher momenta ($\geq$ 7 GeV/c).

2.3 Current experimental results

2.3.1 Heavy flavour at Tevatron

Among the first measurements of b cross-section in hadronic collisions starts with UA1 at the p$\overline{\text{p}}$ ($\sqrt{s}$ = 630 GeV) collider [84]. The data were compared with theoretical predictions [85, 86], showing good agreement, within the rather large (±40%) theoretical (a full NLO QCD calculation including all mass effects) uncertainty [85, 86].

After UA1, the first published data from CDF [87] appeared as a surprise. CDF collected a sample of 14 ± 4 fully reconstructed $B^{\pm} \to \psi\, K^{\pm}$ decays, leading to $\sigma(\text{p}\overline{p} \to bX) = 6.1 \pm 1.9_{stat} \pm 2.4_{syst}\ \mu b$ for CDF versus a theoretical prediction of $1.1 \pm 0.5\ \mu b$.

Theoretical work to explain the apparent contradiction between the success of the NLO theory at 630 GeV and the problems at 1.8 TeV concentrated on possible effects induced by the different range of x probed at the two energies, PDF uncertainties and large small-x effects, but no conclusive solution was found.

CDF expanded the set of measurements, including final states with inclusive ψ and ψ' [88] and inclusive leptons [89], summarised in fig.2.4.

The measurement of the b cross section from the inclusive charmonium decays turned out later to be incorrect due to an erroneous estimate of the prompt b production rates. The data on inclusive leptons, while high compared to the central value of the theoretical prediction, were nevertheless consistent with its upper value, and in any case within 1 σ.

Increased statistics in run I allowed CDF to improve its measurement of fully reconstructed exclusive decay modes, leading to the measurements in fig. 2.5. For this measurement CDF used 19 pb^{-1} of data. The cross section was still high compared to the central value of the theoretical prediction (data/theory = 1.9 ± 0.3), but this was already a marked improvement over the first measurement from run 0, when this ratio was equal to 6.1.

The same data, when compared to theoretical predictions obtained a couple of years later using the same QCD calculations, but up-to-date sets of input PDFs (MRST [90] with $\alpha_s(m_Z) = 0.1175$, and CTEQ5M [91] with $\alpha_s(m_Z) = 0.118$), gave very good agreement. The crucial difference was the change in the value of the QCD coupling strength as extracted from global PDF fits. The fits used in the CDF 1995 publication (MRSD0 [92] did not include HERA data and had

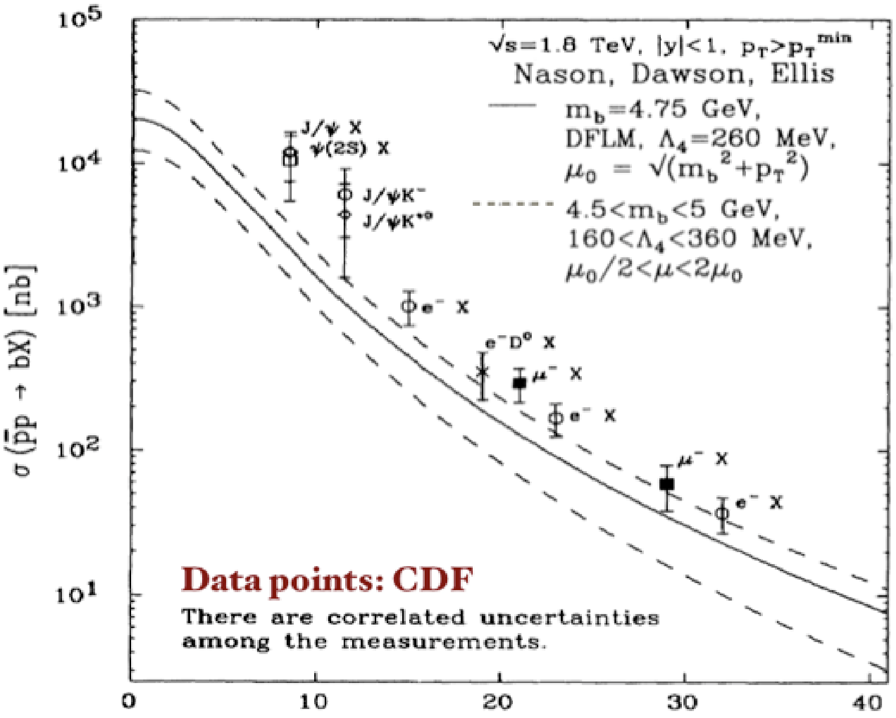

Figure 2.4: *CDF data from inclusive ψ, ψ' and lepton final states, compared to NLO QCD calculations [88, 89].*

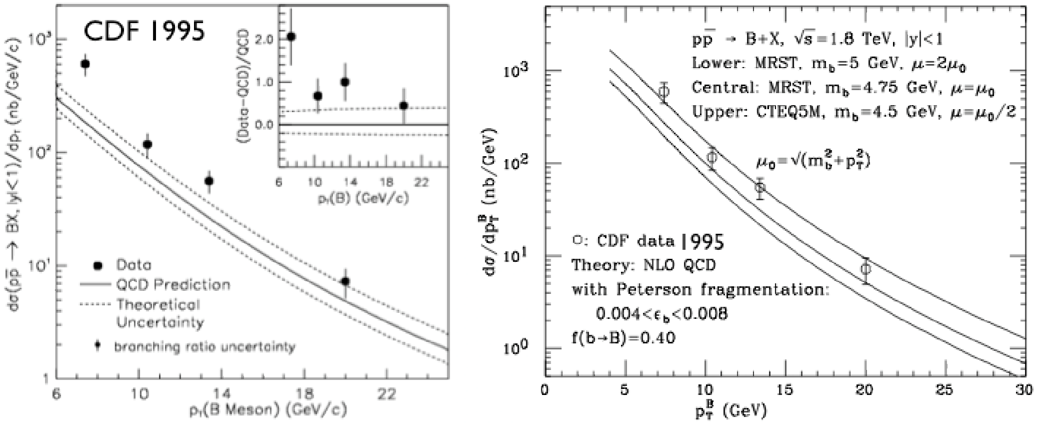

Figure 2.5: *Evolution of data over theory with improved PDFs. The data on both plots are the same. Taken from [94].*

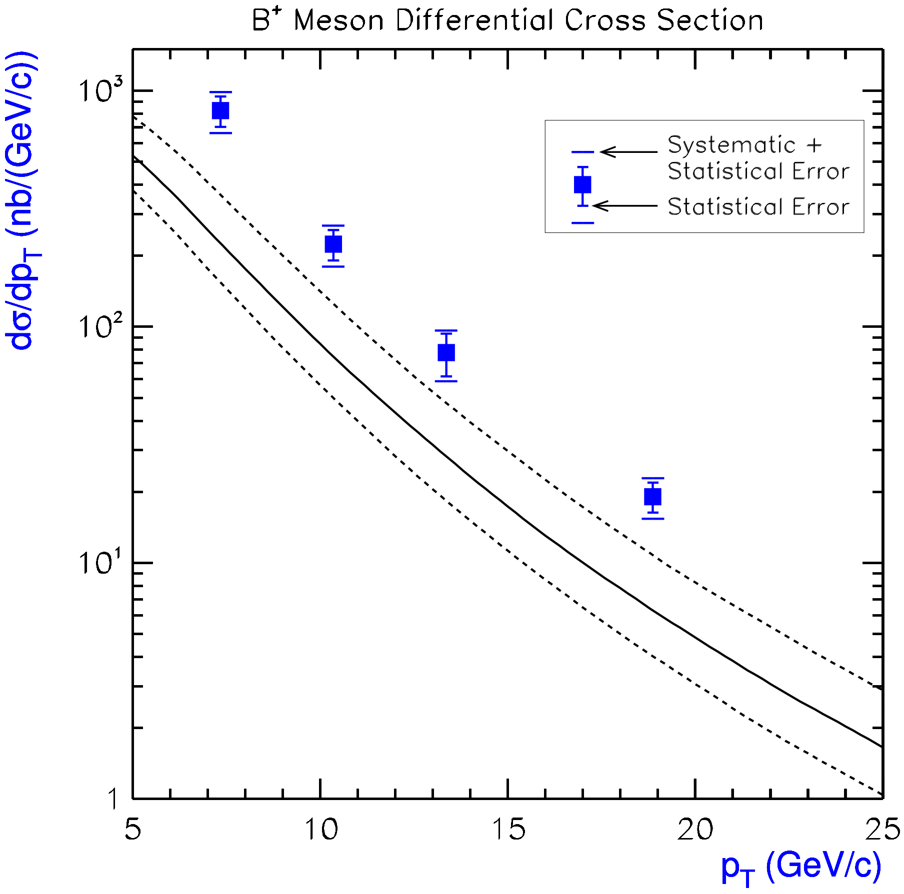

Figure 2.6: *Final CDF analysis of run I exclusive-decay data, compared to the CDF evaluation of the NLO QCD prediction with MRST PDFs and Peterson fragmentation [95].*

$\alpha_s(m_Z) = 0.111$, significantly lower than what was estimated from LEP, namely $\alpha_s(m_Z) \approx 0.120$. This 10% difference, when evolved to the scales of relevance to b production, becomes much more significant, especially because b rates grow like α_s^2.

While the improvements in the PDF fits were reducing the difference between data and theory, a new CDF measurement from the full sample of run I exclusive B decays in the range 6 GeV $< p_{\rm t} <$ 20 GeV appeared in 2001 [95], and is shown here in Fig. 2.6. The total rate turned out to be 50% larger than in the previous 1995 publication [93]: $\sigma(p_{\rm t}(B+) > 6 \text{ GeV}, |y| < 1) = 3.6 \pm 0.6mb$, compared to the previous $2.4 \pm 0.5mb$, a change in excess of 2σ . The ratio between data and the central value of the theory prediction was quoted as 2.9 ± 0.5: a serious disagreement was back.

On the other side of the Tevatron ring, the D0 experiment started presenting the first b cross section measurements in 1994. The first preliminary results were in good agreement with QCD estimates. They were eventually published, after significant changes, in [97]. The results from a larger dataset of $6.6pb^{-1}$ appeared in [98], where ψ dimuons were added. They showed a clear increase over the preliminary analysis, but were still consistent with the QCD expectations. The same data set underwent further analysis, and eventually appeared few years later in [99]. After this new analysis the data were significantly higher than QCD, and higher than in 1996, especially in view of the fact that in the meantime the theory predictions had increased by almost a factor of 2 as a result of the use of new PDF sets. This evolution underscores the difficulty in performing these measurements, and indicates that it was not just the theory that was having difficulties in coming to grips with the problem.

With the advent of the run II several improvement took place in the ability to trigger on very low p_{t}^{b} events, allowing for a measurement down to $p_{\mathrm{t}}^{b} \approx 0$, although still in the limited rapidity range $|y_b| < 0.6$. On the theoretical side a new tool had become available, namely Fixed-Order at Next-to-Leading-Log (FONLL) calculations (for some recent results see [101] and for charm [102]).

The comparison of the run II data with the theoretical calculations is given in Fig. 2.7, which shows the data with the prediction for the spectrum of J/ψ from H_b decays. After almost 15 years of improvements on the experimental and theoretical tools, the data now lies well within the uncertainty band, and are in very good agreement with the theoretical predictions (FONLL).

2.3.2 Heavy flavour at RHIC

Due to the low cross section at RHIC energy, the results from RHIC are (almost) only for the charm quark. At RHIC, open charm analysis is done by detecting D mesons either through their semi-leptonic decays or via hadronic channels. The latter is the cleanest signal, nevertheless it is more difficult to reconstruct without a dedicated vertex detector.

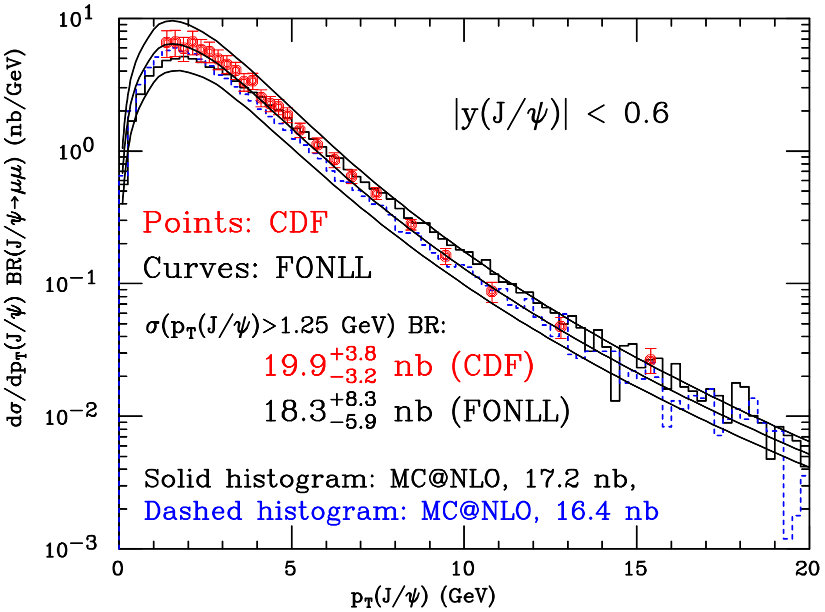

Figure 2.7: *CDF J/ψ spectrum from B decays. The theory band represents the FONLL systematic uncertainties. Two MC@NLO predictions are also shown (histograms). Data from [96].*

Proton-proton collisions

Fig. 2.8 (panel a) shows the invariant differential cross section for electrons coming from heavy flavour (mostly charm) decays as measured by the PHENIX experiment [79]. All background sources, such as Dalitz decays[3] and photon convertions, were subtracted. The data are compared with FONLL calculations in fig. 2.8 (panel a). In Fig. 2.8 (panel b) the ratio of the data over the FONLL calculation is shown. The ratio seems to be constant (for $p_t > 2$ GeV/c) and to be ≈ 1.7.

While the PHENIX data are quite in agreement with the FONLL calculations, STAR data are about a factor 4 above than the prediction.In spite of a large disagreement on non-photonic electron production, the FONLL calculations reproduce quite well the shape of STAR data [80].

---

[3] $\pi^0 \to e^+ e^- \gamma$

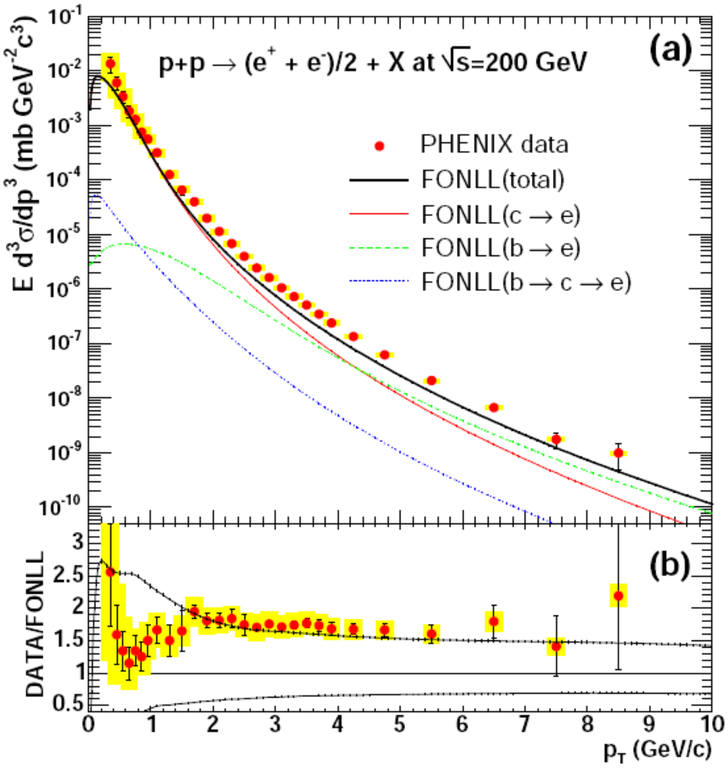

Figure 2.8: (a) *Invariant differential cross section of electrons from heavy flavour decays in p–p collisions at RHIC. The curves are FONLL calculations and the dots are data from PHENIX.* (b) *Ratio of the data and the FONLL calculation. The two curves show the theoretical upper and lower limit of the FONLL calculation. The error bars (bands) represent the statistical (systematic) errors [79].*

Gold-Gold collisions

The charm cross section measurements in Au–Au collisions are shown in Fig. 2.9 for the STAR experiment. The charm spectrum can be measured down to $p_{\mathrm{t}} \approx$ 0.2 GeV using muons and direct D meson measurements, thus covering the 95% of the total charm cross section.

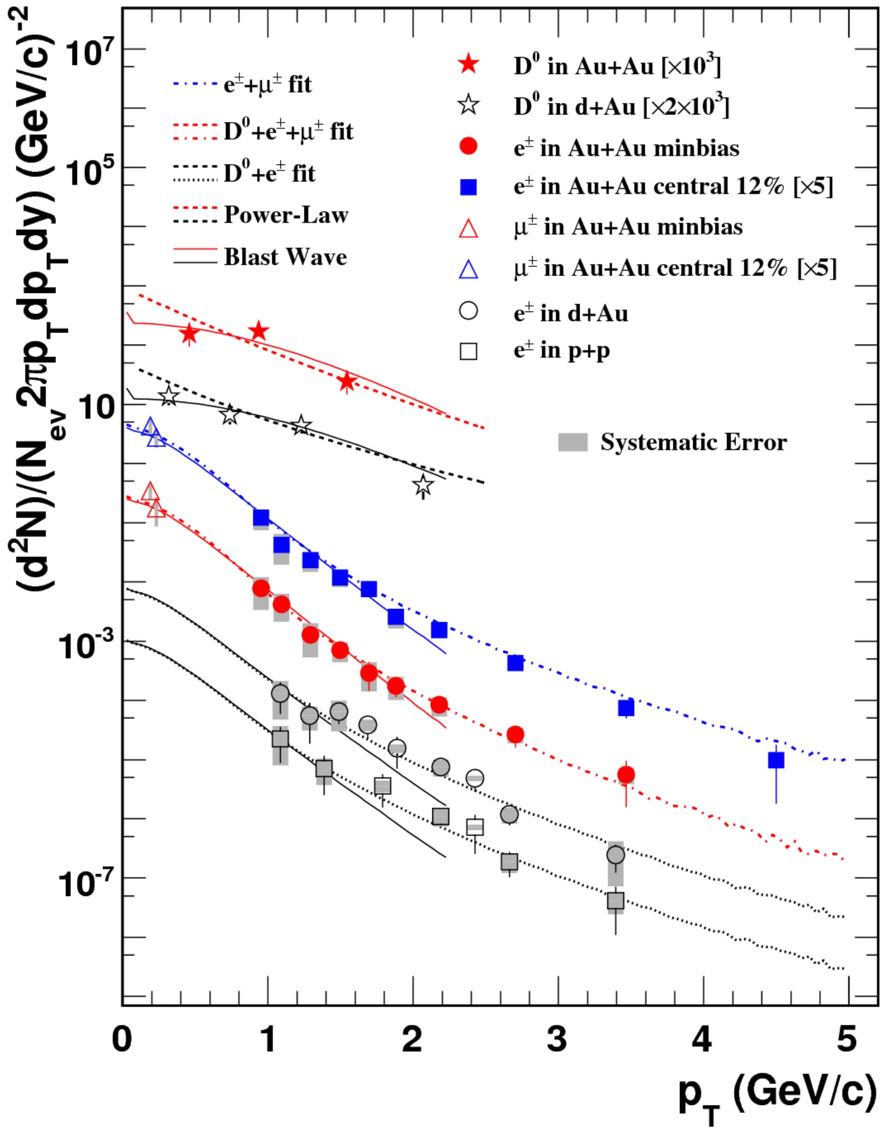

Figure 2.9: *Open charm reconstruction summary from STAR:* p_t *distributions for* D^0 *mesons, for charm-decayed muons, and for non-photonic electrons. The overall magnitude of the cross-section in d–Au and Au–Au is about 4–5 times larger than NLO calculations [81].*

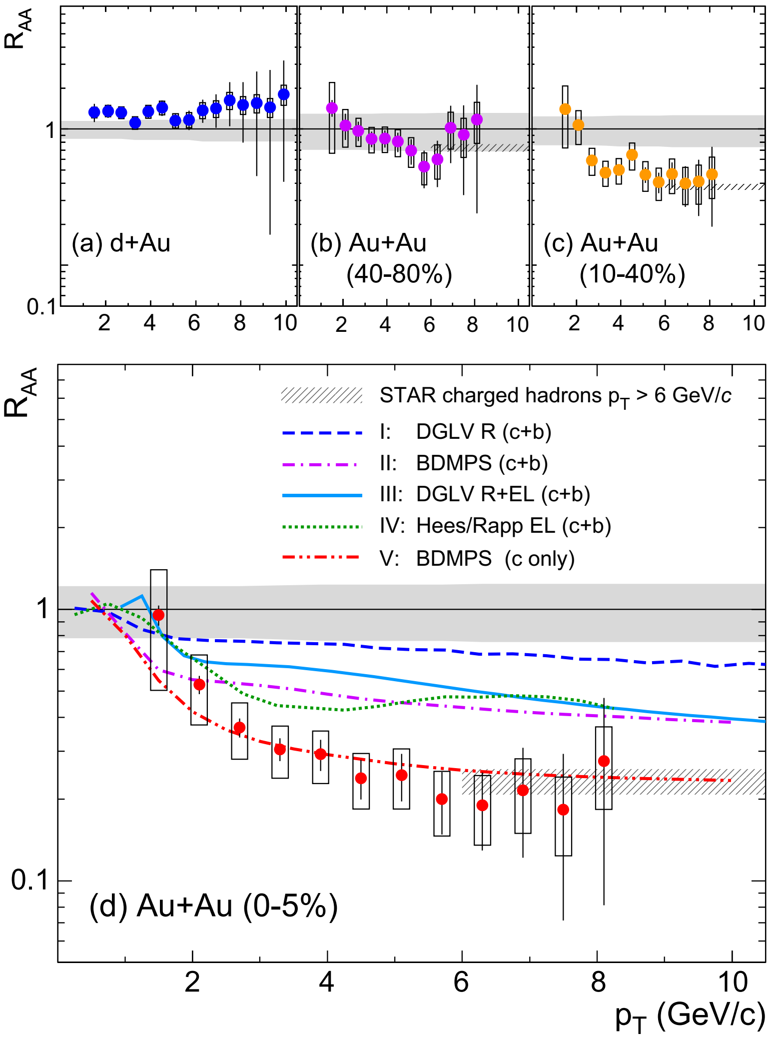

Figure 2.10: Upper panel: *the nuclear modification factor,* $R_{\rm AA}$ *for* $d - Au$ *and semi-peripheral* $Au - Au$ *collisions at* $\sqrt{s_{\rm NN}} = 200$ GeV. Lower panel: $R_{\rm AA}$ *for central* $Au - Au$ *collisions. The data is from the STAR experiment [80], for more details on the theoretical curves, see the text.*

Suppression of non-photonic electrons

The nuclear modification factor (R_{dAu})for d–Au collisions is shown in the upper panel of Fig. 2.10 and it is consistent with binary scaling plus a moderate Cronin enhancement.

Since in d–Au collisions a suppression of the nuclear modification factor is not

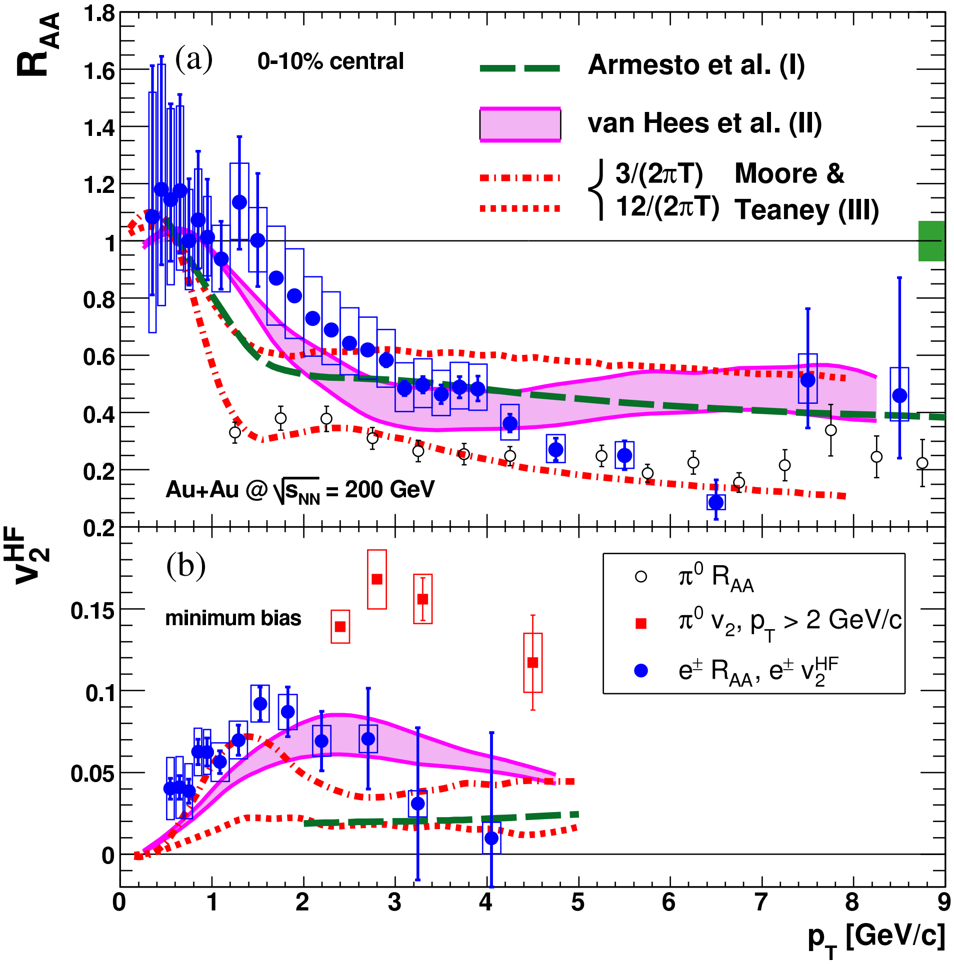

Figure 2.11: Top: R_{AA} *for heavy flavour electrons in central collisions (0–10%) compared with* π^0 *data and theoretical calculations.* Bottom:) v_2 *for heavy flavour electrons in minimum bias collisions compared with* π^0 *data and the same theoretical calculation as above. The data is from the PHENIX experiment [83], for more details on the theoretical curves, see the text.*

observed, it was argued that the observed suppression in Au–Au at high p_t could be related to final-state effects, like parton energy loss in the medium created in the heavy-ion collision.

The R_{AA} of non-photonic electrons measured by STAR and PHENIX are shown in Fig. 2.10 and 2.11 respectively as a function of the transverse momentum.

The STAR data are compared to five energy loss calculations in Fig. 2.10. Calculation "I" uses the radiative energy loss with few hard scattering, including bottom quark and assuming an initial gluon density of $\mathrm{d}N_g/\mathrm{d}y = 1000$. Calculation "II" uses the BDMPS radiative energy loss via multiple soft collisions with a transport coefficient of $\hat{q} = 14$ GeV^2/fm. Calculations "I" and "II" both overestimate the observed R_{AA}. This discrepancy may indicate significant collisional energy loss for heavy quarks. Calculation "III" is a prediction that includes both radiative and collisional energy loss for charm and bottom quarks [103]. Calculation "IV" uses a heavy-quark energy loss based on elastic scattering mediated by resonance excitations of B and D mesons [104]. The calculation that appears to better represent the data is the "V". It is the same of Curve "II" (BDMPS with radiative energy loss) but for D mesons decay only.

PHENIX data for the R_{AA} of single electrons are shown in the top panel of Fig. 2.11, compared with the calculations "IV" (now called "II") and "V" (now called "I") described before. A model based on the diffusion coefficient (see [105]), is also compared to the data. Using this model, the data suggest that only a small diffusion coefficient and viscosity are needed. This in turn seems to indicate that the matter formed at RHIC is a nearly perfect fluid.

Non-photonic electrons azimuthal anisotropy

From the study of non-photonic single electrons and from the comparison with theoretical models, there are indications of charm elliptic flow v_2 for $p_{\mathrm{t}} < 2$ GeV, compatible with the v_2 from lighter quarks. In addition, as can be seen from the lower panel of Fig. 2.11, for PHENIX data, the v_2 seems to decrease at high p_{t}. The model based on elastic collisions and resonance scatterings [104] (shown as the shaded area in the figure) is in good agreement with the data. Other calculations based on radiative energy loss (dashed line) or on transport properties of the medium fail in describing the v_2.

Conclusions

To summarise, the main conclusion that can be drawn from the results obtained from charm measurements at RHIC are the following:

- Charm cross section has been measured (both in d–Au and Au–Au) and, while there are some discrepancies between STAR and PHENIX, the charm yield scales with the number of binary collisions.

- Non-photonic electron suppression in Au–Au is very large when compared to the expectations from radiative energy loss, which seem to work well for light quark hadrons.

- Non photonic electron v_2 supports the picture of an early thermalization: if the c quark has a collective behaviour, like elliptic flow, it must have been thermalized but its time scale is of the order $\approx 1/M_Q$. Moreover, fitting the data for v_2 with a model based on a diffusion parameter suggests that the matter formed in Au–Au collisions is a near-perfect fluid.

One of the main sources of uncertainty on the charm measurements at RHIC is the contamination from beauty decays. To separate beauty and charm decays a vertex detector is needed. ALICE at LHC makes use of the increase in the cross section for beauty (w.r.t RHIC) and of the Inner Tracking System to separate and study the decays of beauty hadrons. Chapter 3 will describe the ALICE experiment and its Inner Tracking System, with an emphasis on the Silicon Pixel Detector since it is the most critical sub-system for the vertexing performance. Chapter 4 will be dedicated to the assembly, the operation and the commissioning of the SPD. Chapter 5 will deal with the problems related with the alignment of the Inner Tracking System and its effect on the detector performance. Finally, Chapter 6 will analyse some of the results that can be obtained with the ALICE apparatus for the beauty measurement in the semi-electronic decay channel.

Chapter 3

The ALICE experiment

The first ideas of a general-purpose, heavy-ion detector at the LHC were expressed in a workshop at the end of 1990 [108]. The ALICE concept ([107]) evolved via the Expression of Interest [109] and a Letter of Intent [110] towards the Technical Proposal [111] and its Addenda [112–114]. The experiment was approved in 1997 and the designs of the different detector systems are described in detail in a number of Technical Design Reports [115–126]. The expected detector performance and the physics reach, based on detailed simulations, are summarised in the Physics Performance Report [106, 107].

ALICE consists of a central barrel part, which measures hadrons, electrons, and photons, and a forward muon spectrometer. Its overall dimensions are $16{\times}16{\times}26$ m^3 with a total weight of approximately 10,000 t.

The central part covers polar angles from 45° to 135° and is embedded in a large solenoid magnet reused from the L3 experiment at LEP. From the inside out, the barrel contains an Inner Tracking System (ITS) of six planes of high-resolution silicon pixel (SPD), drift (SDD), and strip (SSD) detectors, a cylindrical Time-Projection Chamber (TPC), three particle identification arrays of Time-of-Flight (TOF), Ring Imaging Cherenkov (HMPID) and Transition Radiation (TRD) detectors, and two electromagnetic calorimeters (PHOS and EMCal). All detectors except HMPID, PHOS, and EMCal cover the full azimuth.

The forward muon arm (polar angles 2°–9°) consists of an arrangement of absorbers, a large dipole magnet, and fourteen planes of tracking and triggering chambers. Several smaller detectors (ZDC, PMD, FMD, T0, V0) for global event characterisation and triggering are located at small angles. An array of scintillators (ACORDE) on top of the L3 magnet is used to trigger on cosmic rays.

As discussed in Chapter 2, beauty quarks are promising probes for the study of the QGP. One possible strategy to measure the beauty quark production is using electron-tagged tracks with a displacement with respect to the primary collision vertex. This approach is favoured by the large semi-electronic branching ratio (b.r. $\approx$ 10% [127]) and by the significant mean proper decay length ($c\tau \approx 500$ μm) of beauty hadrons. The ALICE experiment has been designed also in view of exploiting these features. The central barrel ($|\eta| < 0.9$) provides good capabilities for electron identification in the Transition Radiation Detector and in the Time Projection Chamber, coupled to precise tracking and vertexing in the TPC and in the silicon detectors (pixels, drifts and strips) of the Inner Tracking System.

In the present chapter the ALICE experimental setup will be briefly described, concentrating on the sub-detectors that are crucial for the beauty detection via single electrons: ITS, TPC and TRD.

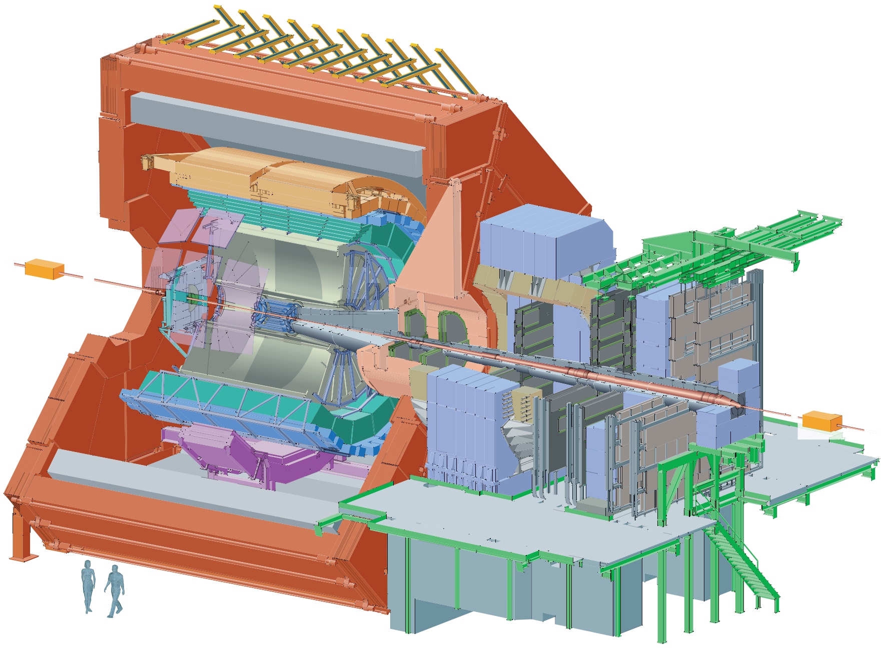

Figure 3.1: *ALICE schematic layout.*

Table 3.1: *Dimensions and characteristics of the ITS detectors.*

Layer	Type	r [cm]	$\pm z$ [cm]	Rad. Length [%]	Channels
1	pixel	3.9	14.1	1.14	3 276 800
2	pixel	7.6	14.1	1.14	6 553 600
3	drift	15.0	22.2	1.13	43 008
4	drift	23.9	29.7	1.26	90 112
5	strip	38.0	43.1	0.83	1 148 928
6	strip	43.0	48.9	0.86	1 459 200

3.1 Inner Tracking System

The ITS surrounds the beam pipe, for which it provides the mechanical support so that no relative movement will take place during operation. The beam pipe is a 800 μm-thick beryllium cylinder of 6 cm outer diameter, coaxial with the ITS detector layers. As shown schematically in Fig. 3.2 the ITS consists of six cylindrical layers of silicon detectors. The two innermost layers are based on silicon pixel technology and constitute the Silicon Pixel Detector (SPD). They are located at radii 3.9 and 7.6 cm. The two middle layers are based on silicon drift technology (the Silicon Drift Detector, SDD). They are located at radii 15 and 23.9 cm. The two outer layers are based on silicon strip technology and constitute the Silicon Strip Detector (SSD). They are located at radii 38 and 43 cm.

The ITS covers the rapidity range of $|\eta| < 0.9$ for all vertexes located within the length of the interaction diamond ($\pm 1\sigma$, i.e. ± 5.3 cm, at nominal LHC energy, along the beam direction). The number, position and segmentation of the layers were optimised for efficient track finding and high impact-parameter resolution. In particular, the outer radius is determined by the necessity to match tracks with those from the TPC, and the inner radius is the minimum allowed by the radius of the beam pipe. The first layer has a more extended pseudo-rapidity coverage ($|\eta| < 1.98$) to provide, together with the Forward Multiplicity Detectors, continuous coverage for the measurement of charged-particles multiplicity. The detectors and front-end electronics are held by lightweight carbon–fibre structures. The geometrical dimensions and the technology used in the various layers of the ITS are summarised in Table 3.1.

The main tasks of the Inner Tracking System (ITS) are to localise the primary

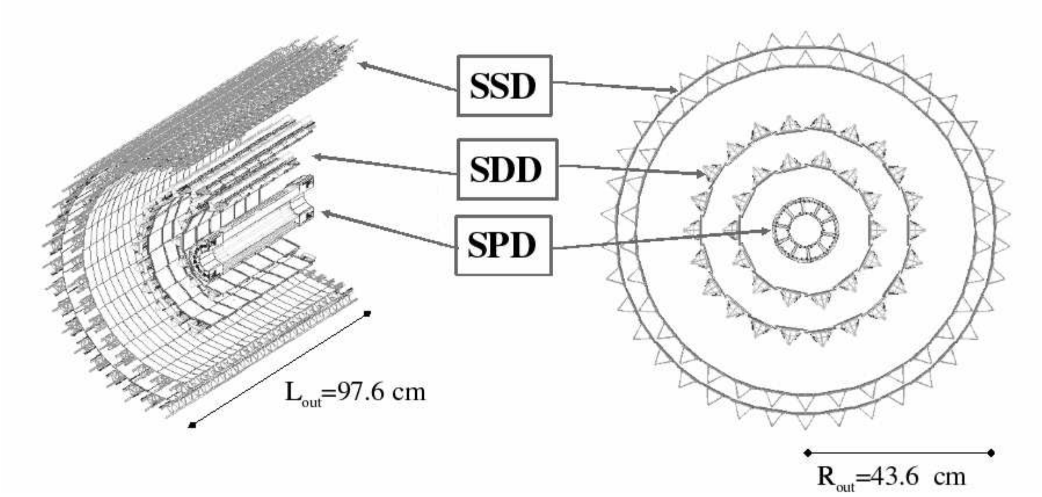

Figure 3.2: *Layout of the ITS.*

vertex with a resolution better than 100 μm, to improve the momentum and angle resolution for particles reconstructed by the Time-Projection Chamber, to reconstruct the secondary vertexes from the decays of hyperons and D and B mesons, to track and identify particles with momentum below 200 MeV/c, and to reconstruct particles traversing dead regions of the TPC. The ITS therefore contributes to practically all physics topics addressed by the ALICE experiment, as discussed in detail in [107]. In the following In view of the items presented in the next two Chapters, in the following will be described in detail the three sub-detectors of the ITS. The performance for the impact parameter resolution will be presented in Chapter 5.

3.1.1 The Silicon Pixel Detector

The Silicon Pixel Detector is the innermost detector of the ALICE set-up and it is composed of two layers. It is a fundamental element for the determination of the position of the primary vertex as well as for the measurement of the impact parameter of secondary tracks originating from the weak decays of strange, charm, and beauty particles [107]. The SPD will operate in a region where the track density could be as high as 50 tracks/cm^2, and in relatively high radiation levels: in the case of the inner layer, the integrated levels (10 years, standard running scenario) of total dose and fluence are estimated to be $\approx$ 2.7 kGy and

$\approx 3.5 \times 10^{12}$ n/cm^2 (1 MeV neutron equivalent), respectively [128]. The SPD design implements several specific solutions to minimise the material budget. The average material traversed by a straight track perpendicular to the detector surface is $\approx 1\% \, X_0$ per layer.

The actual sensitive element is a two-dimensional matrix of reverse-biased silicon detector diodes bump-bonded to readout chips. Each diode is connected through a conductive solder bump to a contact on the readout chip corresponding to the input of an electronics readout cell. The readout is binary: in each cell, a threshold is applied to the pre-amplified and shaped signal and the digital output level changes when the signal is above a set threshold. This technique had already been successfully applied in the WA97 and NA57 experiments at CERN [129]. The basic detector module is the half-stave (HS). Each half-stave consists of two ladders, one Multi-Chip Module (MCM) and one high density aluminium/polyimide multi-layer interconnect. The ladder consists of a silicon sensor matrix bump bonded to 5 front-end chips. The sensor matrix includes 256×160 cells measuring 50 μm ($r\phi$) by 425 μm (z). Longer sensor cells are used in the boundary region to ensure coverage between readout chips. The sensor matrix has an active area of 12.8 mm ($r\phi$) $\times$ 70.7 mm (z). The front-end chip reads out a submatrix of 256 ($r\phi$) $\times$ 32 (z) detector cells. The thickness of the sensor is 200 μm, the smallest that can be achieved with an affordable yield in standard processes. The thickness of the readout chip is 150 μm; the readout wafers are thinned after bump deposition, before bump bonding. The two ladders are attached and wire bonded to the high density aluminium/polyimide interconnect (pixel bus). A 200 μm clearance between the short edges allows for dicing tolerances and ease of assembly. The pixel bus carries data/control bus lines and power/ground planes. The multi-chip-module, wire bonded to the pixel bus and located at the end of the half-stave, controls the front-end electronics and is connected to the off-detector readout system via optical fibre links.

The ALICE pixel readout chip includes many operation parameters that are remotely adjustable. The on-chip global registers include 42 8-bit DACs that adjust current and voltage bias references, L1 trigger delay, global threshold voltage, and leakage current compensation. In each pixel cell a 3-bit register allows individual tuning of the threshold; there is also provision to enable the test pulse input and to mask the cell. All configuration parameters are controlled through the JTAG bus via the digital PILOT chip.

Each pixel chip generates a pulse (Fast-OR) whenever a pixel cell (or a group

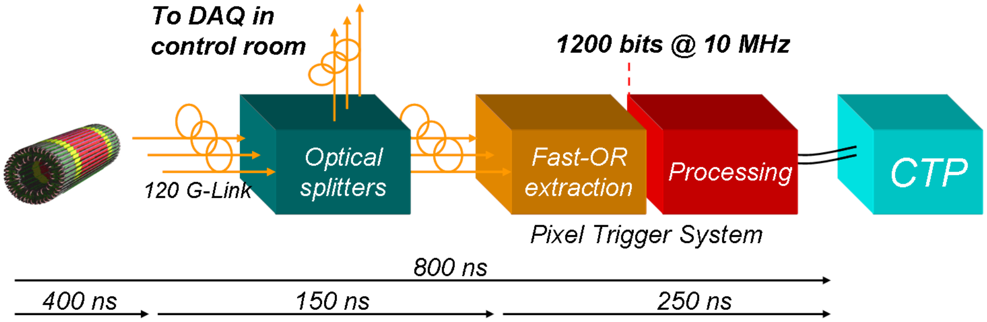

Figure 3.3: *Layout of the pixel trigger system architecture.*

of them) detects a particle signal above threshold. The Fast-OR is used to self-trigger the front-end in test mode and to implement a prompt physics trigger. The Fast-OR signals of the 10 chips on each of the 120 half-staves are read by the PILOT chip ([130–132]) and transmitted every 100 ns on the 120 optical links that are also used for the data readout. The Fast-OR allows the implementation of a unique prompt trigger capability. The pre-processed Fast-OR data can be used to contribute to the Level 0 trigger decision in the ALICE Central Trigger Processor (CTP). The Fast-OR output is synchronised with the 10 MHz pixel system clock, hence the signal is effectively integrated over 100 ns corresponding to 1 bunch-crossing in the case of operation with heavy ions, or 4 consecutive bunch-crossings in proton–proton operation. All 120 half-staves are synchronised to the same integration period covering the same set of bunch-crossings in order to limit this ambiguity when all Fast-OR signals are simultaneously processed and to minimise the latency. In the ALICE trigger system, the bunch-crossing ambiguity can be resolved by considering the coincidence between the pixel trigger signal and the ALICE V0 detector signal. A full description of the pixel trigger system is given in [133]. The pixel trigger system architecture is shown in Fig. 3.3.

The SPD barrel is structured as follows. Two half-staves are attached head-to-head along the z direction to a carbon-fibre support sector (CFSS), with the MCMs at the two ends, to form a stave. Each sector supports six staves: two on the inner layer and four on the outer layer. Fig. 3.4 shows the layout of two sectors. Ten sectors are then mounted together around the beam pipe to close the full barrel. In total, the SPD (60 staves) includes 240 ladders with 1200 chips for a total of 9.8×10^6 cells. The inner (outer) SPD layer is located at an average distance of 3.9 cm (7.6 cm) from the beam axis.

The power dissipated in the front-end electronics is ≈ 1.35 kW. The cooling system is of the evaporative type and is based on C_4F_{10}. The sectors are equipped with cooling capillaries embedded in the sector support and running underneath the staves (one per stave). The heat transfer from the front-end chips is assured with high thermal conductivity grease. The SPD barrel is surrounded by an Al-coated carbon-fibre external shield to prevent radiation of heat towards the SDD layers. Figure 3.5 shows one half-barrel assembled and ready to be integrated in the pixel mechanics.

In Chapter 4 the assembly procedure of the half-staves on the CFSS will be detailed. The cooling system and its working principles will also be illustrated.

3.1.2 The Silicon Drift Detector

The Silicon Drift Detectors [118] are the two intermediate layers of the ITS, where the charged particle density is expected to reach up to 7 cm^{-2}. They have good multitrack capability and provide two out of the four $\mathrm{d}E/\mathrm{d}x$ samples needed for the ITS particle identification.

The ALICE SDDs were produced from very homogeneous high-resistivity (3 kΩcm) 300 μm thick Neutron Transmutation Doped (NTD) silicon [134]. As shown in Fig. 3.6, they have a sensitive area of $70.17(r\phi)\times 75.26(z)$ mm^2 and a total area of 72.50×87.59 mm^2. The sensitive area is split into two drift regions by the central cathode strip to which a HV bias of -2.4 kV is applied. In each drift region, and on both detector surfaces, 291 p^+ cathode strips, with 120 μm pitch, fully deplete the detector volume and generate a drift field parallel to the wafer surface. To keep the biasing of the collection region independent on the drift voltage, a second bias supply of -40 V is added. The overall detector performance, when averaged over its entire area, does not depend significantly on the applied bias voltage in a fairly large range from -1.65 kV to -2.4 kV, so the precise value of bias voltage to be applied during long term operation is to be adapted to the specific running conditions. To improve the detector reliability, all the drift and guard regions have their own built-in voltage dividers. Their total power dissipation is 1 W per detector and is removed by an appropriate air circulation system. Each drift region has 256 collection anodes with 294 μm pitch and three rows of 33 MOS charge injectors (20×100 μm^2 each) to monitor the drift velocity which depends on temperature: $v_{\text{drift}} \propto T^{-2.4}$, [135], which gives a

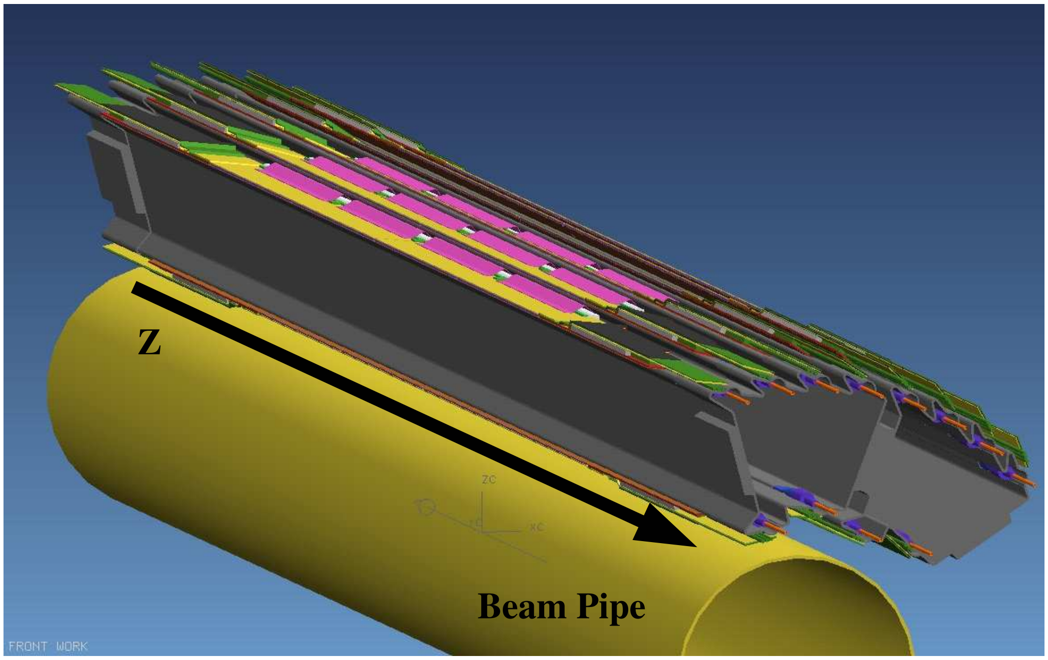

Figure 3.4: *Layout of two assembled carbon-fibre support of the Si-pixel staves around the beam pipe.*

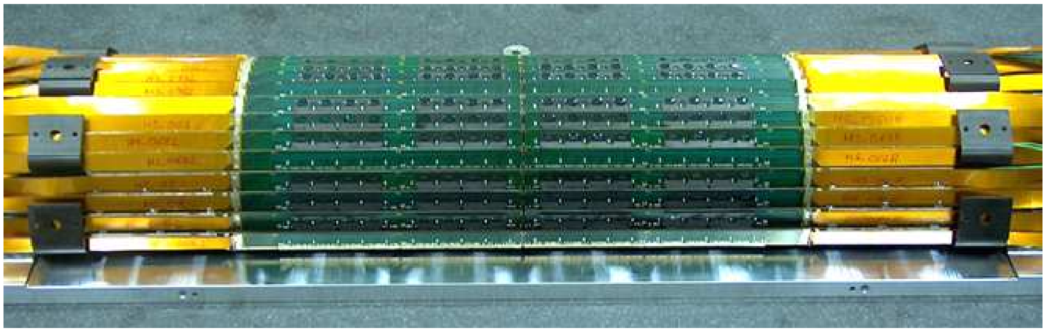

Figure 3.5: *Half barrel assembled on reference table.*

0.8%/K variation at room temperature.

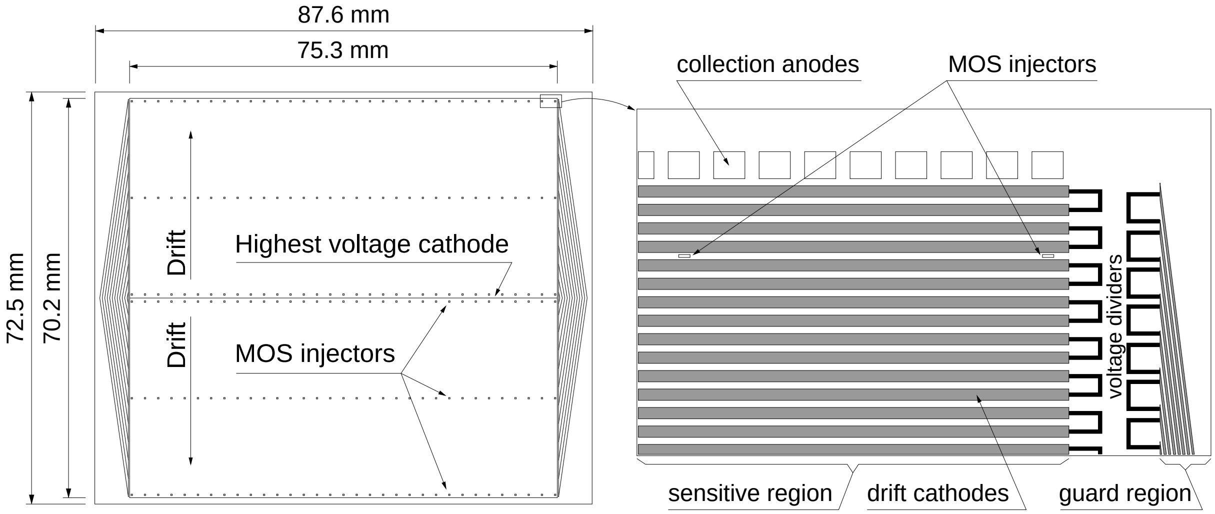

Figure 3.6: *Layout of the ALICE SDD. The sensitive area is split into two drift regions by the central, highest voltage, cathode. Each drift region has one row of 256 collection anodes and three rows of 33 charge injectors for monitoring the drift velocity. Drift and guard regions have independent built-in voltage dividers.*

A SDD module consists of one silicon drift detector and two front-end hybrids, each connected to the corresponding end-ladder LV board. A micro-cable, specially designed to carry high voltage (up to over 2.4 kV), connects the detector to the HV end-ladder board. All the assembly and test steps were performed in-house [136].

The SDDs modules are mounted on linear structures called ladders. There are 14 ladders with six modules each on layer 3, and 22 ladders with eight modules each on layer 4. Modules and ladders are assembled to have an overlap of the sensitive areas larger than 580 μm in both $r\phi$ and z directions. This ensures full angular coverage for vertexes located within the interaction diamond, ± 5.3 cm, and for $p_{\mathrm{t}} > 35\mathrm{MeV}/c$.

In Fig.3.7 the completely assembled SDD detectors are shown, prior to insertion in the SSD detectors, together with a CAD drawing of the SDD layers, showing ladders from both layers and the support cones.

The space precision along the drift direction ($r\phi$), as obtained during beam tests of full-size prototypes, is better than 38 μm over the whole detector surface.

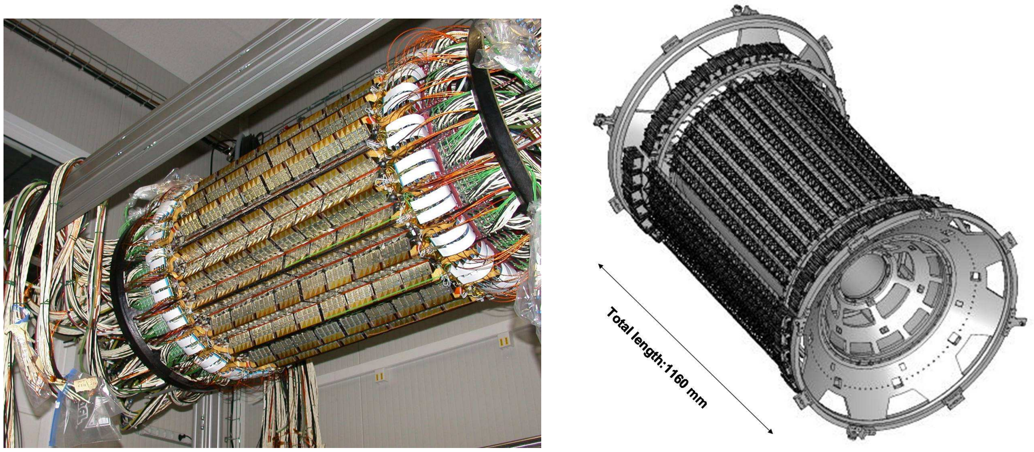

Figure 3.7: Left: *The SDD detector completely assembled, ready to be integrated with the Silicon Strips.* Right: *The CAD design of the SDD layers, showing the support cones and the ladders of the two layers.*

The precision along the anode axis (z) is better than 30 μm over 94% of the detector surface and reaches 60 μm close to the anodes, where a fraction of clusters affects only one anode. The average values are 35 μm and 25 μm respectively [137]. The detection efficiency is larger than 99.5% for amplitude thresholds as high as 10 times the electronic noise. The coordinate along the drift direction ($r\phi$) is obtained by measuring the drift time of the electrons. In Chapter 5 the calibration of the SDD sensors will be detailed.

3.1.3 The Silicon Strip Detector

The outer layers of the ITS are crucial for the matching of tracks from the TPC to the ITS. They provide a two dimensional measurement of the track position. In addition they provide $\mathrm{d}E/\mathrm{d}x$ information to assist particle identification for low-momentum particles. The system is optimised for low mass in order to minimise multiple scattering.

Both outer layers use double sided Silicon Strip Detectors [138]. The detection modules [139] consist of one sensor each, connected to two hybrids with six HAL25 [140] chips each. All interconnections between the sensor and the electronics in the detection module are made using aluminium on polyimide cables (micro-cables) [141]. Minimisation of the material budget of the mechanical support for the detection modules is achieved by using linear Carbon Fibre Composite (CFC) material [142] for all support structures in the active volume. The cooling system is also optimised [143, 144] in line with the zero heat balance required for all ALICE detectors. The application of 300 μm thick CFC with high thermal conductivity as miniature motherboards [144] (stiffeners) significantly reduces the material needed for the support and cooling of the front-end chips [144]. The modules are assembled on ladders [142] of the same design as those supporting the SDD. These ladders are one module wide and up to 25 modules long along the beam direction. The 72 ladders, carrying a total of 1698 modules, are mounted on CFC support cones in two concentric cylinders. For each layer the ladders are mounted in two slightly different radii such that full azimuthal coverage is obtained. The modules are cooled by water running through two thin (40 μm wall thickness) phynox[1] tubes along each ladder [144, 145].

The electronic signals from the modules are AC-coupled and buffered in custom made electronics, the EndCap Modules (ECM) [146] located at each end of each ladder. The analogue to digital conversion of the signals performed in the Front-End ReadOut Modules (FEROM) [147] located outside the ALICE magnet. The technology of each component was chosen corresponding to the radiation environment and magnetic field in which they need to operate. The segmentation of the power, cooling and readout system avoids failure of significant parts of the system due to a single point failure. Down to the level of the front-end chips malfunctioning components can be isolated to maintain system integrity. A detailed description of the SSD system design can be found in [118].

The sensors are 300 μm thick and they have 768 strips on each side with a pitch of 95 μm. The stereo angle is 35 mrad which is a compromise between stereo view and reduction of ambiguities resulting from high particle densities. The stereo angle is obtained by defining strips with an angle of 7.5 mrad with respect to the sensor short edge on the p-side and with an angle of 27.5 mrad on the n-side. Sensors are mounted with the strips nearly parallel to the magnetic field in order to optimise the resolution in the bending direction. The sensor p-side (n-side) of layer 5 (layer 6) faces the interaction region. This results in four almost

---

[1] Phynox, UNS R30003, (Elgiloy) is a hardenable alloy on a cobalt basis (40% Co, 20% Cr, 16% Ni and 7% Mo). Its mechanical strength may exceed 2000 N/mm^2, after hardening. It is non-magnetic, very resistant to corrosion (better than any other stainless steel) and temperature resistant (with a coefficient of expansion of about 12.5 μm/m $^\circ$ C).

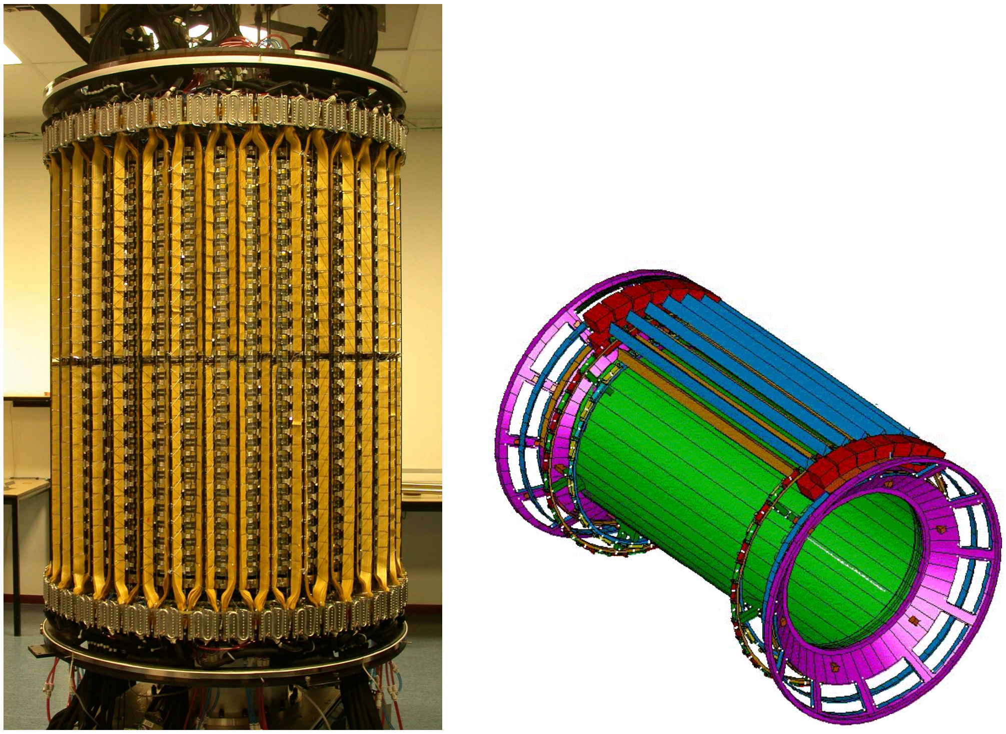

Figure 3.8: Left: *The SSD detector completely assembled, ready to be integrated in the TPC.* Right: *The CAD design of the SSD layers.*

equally spaced strip orientations in the two layers, which significantly reduces the number of ambiguities seen by the tracking software.

The chips are glued directly on the stiffener which provides a thermal conductivity about 1.3 times better than copper while keeping the multiple scattering to a minimum (about 0.03% X_0). Each stiffener is connected to the cooling tubes by small aluminium clamps. The flex consists of two layers of 30 μm thick aluminium traces on a 20 μm thick polyimide foil. These layers are glued together and the electrical connections between them are made using single point tape automated bonding (spTAB) [148]. The flex hosts power lines as well as digital and analogue lines for driving and reading the chips. The decoupling capacitors and transmission line termination resistors are soldered onto the flex.

The detection modules are connected to the Front-End ReadOut Module (FEROM) [147] by means of the endcap modules [146]. These modules are placed at both ends of each ladder. The main task of the Front-End ReadOut Module is to digitise the 2.6 million analogue samples from the front-end modules, keeping up with the trigger rate in ALICE. This is achieved by digitising the signals from each of the 1698 detection modules in parallel.

3.2 Time-Projection Chamber

The Time-Projection Chamber (TPC) [121] is the main tracking detector of the central barrel and is optimised to provide, together with the other central barrel detectors, charged-particle momentum measurements with good two-track separation, particle identification, and vertex determination [121].

The phase space covered by the TPC in pseudo-rapidity is $|\eta| < 0.9$ for tracks with full radial track length (matches in ITS, TRD, and TOF detectors); for reduced track length (at reduced momentum resolution), an acceptance up to about $|\eta| = 1.5$ is accessible. The TPC covers the full azimuth (with the exception of the dead zones, $\approx 10\%$). A large p_{t} range is covered from low p_{t} of about 0.2GeV/c up to 100 GeV/c with good momentum resolution.

In proton–proton runs, the memory time of the TPC is the limiting factor for the luminosity due to the ~ 90 μs drift time. At a proton–proton luminosity of about 5×10^{30} cm^{-2}s^{-1}, with a corresponding interaction rate of about 350 kHz, 'past' and 'future' tracks from an average of 60 proton–proton interactions are detected together with the triggered event; the detected multiplicity corresponds to about 30 minimum-bias p–p events. The total occupancy, however, is lower by more than an order of magnitude than in Pb–Pb collisions, since the average proton–proton multiplicity is about a factor 10^3 lower than the Pb–Pb multiplicity for central collisions [111]. Tracks from pile-up events can be eliminated because they point to the wrong vertex.

The detector is made of a large cylindrical field cage (see Fig. 3.9, top panel), filled with 90 m^3 of Ne/CO$_2$/N$_2$ (90/10/5), in which the primary electrons are transported over a distance of up to 2.5 m on either side of the central electrode to the end plates. Multi-wire proportional chambers with cathode pad readout are mounted into 18 trapezoidal sectors at each end plate.

Field Cage

The field cage is based on a design with a central high-voltage electrode and two opposite axial potential dividers which create a highly uniform electrostatic field in the common gas volume (see Fig. 3.9, top panel). The central electrode is a stretched aluminised Mylar foil of 22 μm thickness to satisfy the requirement of minimal material near 90° relative to the beam direction. The electrical potential in the drift region is defined by aluminised Mylar strips wound around 18 inner and outer support rods. The rods are aligned with the dead zones in-between the readout chambers. Because of the $Ne/CO_2/N_2$ gas mixture used in the TPC, the field cage is operated at high voltage gradients, of about 400 V/cm, with a high voltage of 100 kV at the central electrode, which results in a maximum drift time of about 90 μs.

An insulating gas envelope of CO_2 in containment vessels surrounds the field cage. The field cage and containment volumes are each constructed from two concentric cylinders, sealed by the end plate on either side. To provide high structural integrity against gravitational and thermal loads while keeping the material budget low, composite materials were used. Hence the mechanical stability and precision is guaranteed to be about 250 μm.

The drift gas $Ne/CO_2/N_2$ (90/10/5) is optimised for drift speed, low diffusion, low radiation length and hence low multiple scattering, small space-charge effect, and ageing and stability properties. Mixtures containing CH_4 and CF_4 were rejected due to their ageing properties. The N_2 admixture improves the quenching and allows higher maximum gas gains [149]. The drawback of Ne/CO_2 is that this mixture is a “cold” gas, with a steep dependence of drift velocity on temperature [150]. For this reason, the TPC is aiming for a thermal stability with $\Delta T \leq 0.1$ K in the drift volume, see below.

The gas system circulates and purifies the gas mixture, with very low fresh gas injection. The pressure follows the ambient pressure. The CO_2 and N_2 fractions are kept stable to 0.1%, necessary to ensure stable drift velocity and gas gain of the readout chambers. The O_2 impurity as achieved with a reduced flow during commissioning is extrapolated to be about 1 ppm or lower in the final installation in the cavern, limiting the signal reduction due to attachment for the maximum drift length of 2.5 m to $< 5\%$.

Readout Chambers

The readout chambers instrument the two end plates of the TPC cylinder with an overall active area of 32.5 m^2 [151–153]. The chambers are multi-wire proportional chambers with cathode pad readout. Because of the radial dependence of the track density, the readout is segmented radially into two readout chambers with slightly different wire geometry adapted to the varying pad sizes mentioned below. The radial range of the active area is from 84.8 cm to 132 cm (and from 134.6 cm to 246.6 cm) for the inner (and outer) chamber, respectively. In order to optimise the active area it was built larger than the openings of the end plate. To achieve this

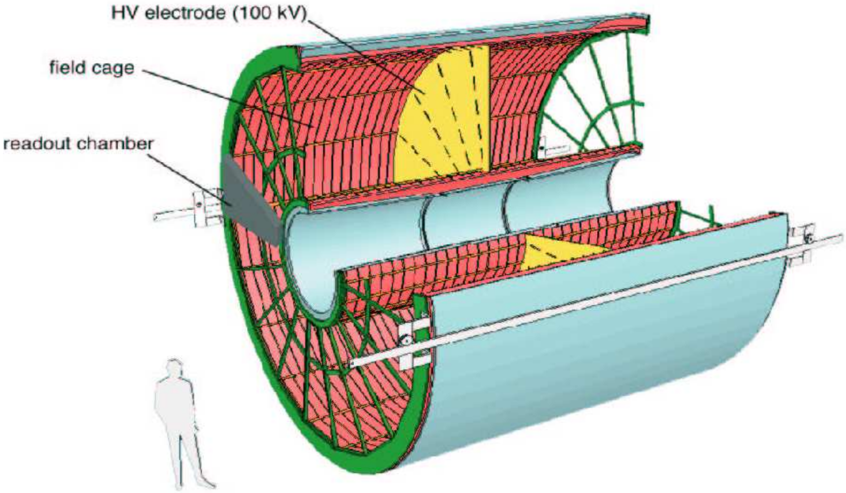

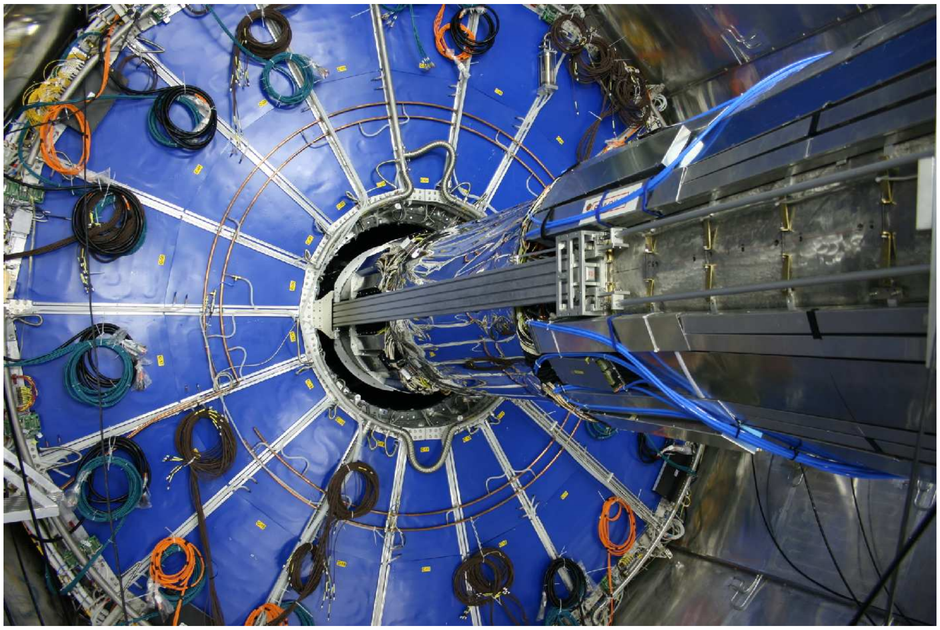

Figure 3.9: Top: *Schematic layout of the TPC.* Bottom:*Photo of the TPC in the spaceframe, seen from the muon absorber side, at the "parking position" which allows access to the ITS. The ITS is supported by temporary rails that are finally removed.*

design the readout chamber were mounted from the inside. This was accomplished with a mounting tool that allowed insertion of a chamber through the end plates into the field cage, rotating and positioning of the chamber once inside, and finally engaging the chamber in its proper orientation with the mount points on the end plate from inside. The inactive areas between neighbouring inner chambers are aligned with those between neighbouring outer chambers. Such an arrangement optimises the momentum precision for detected high-momentum tracks but has the drawback of creating cracks in the acceptance: in about 10% of the azimuthal angle the detector is non-sensitive. The readout chambers are made of standard wire planes, i.e. they consist of a grid of anode wires above the pad plane, a cathode wire plane, and a gating grid.

To keep the occupancy as low as possible and to ensure the necessary $\mathrm{d}E/\mathrm{d}x$, position and two-track resolution, there are about 560 000 readout pads of three different sizes: 4×7.5 mm^2 in the inner chambers, 6×10 mm^2 and 6×15 mm^2 in the outer chambers.

The TPC field cage, which weighs 8 t including the end plates and readout chambers, occupies the central opening of the spaceframe. The TPC has been mounted inside the spaceframe on a rail system, with 4 feet gliding on Teflon. In the installation phase of the ITS and beam line, and possibly in future service periods, the TPC is partially retracted from the spaceframe by about 5 m to a "parking position", allowing access to the area around the interaction point (see Fig. 3.9).

In Chapter 6 the PID performance of the TPC will be discussed.

3.3 Transition Radiation Detector

The main purpose of the ALICE Transition Radiation Detector (TRD) [123] is to provide electron identification in the central barrel for momenta above 1 GeV/c. Below this momentum electrons can be identified via specific energy loss measurement in the TPC. Above 1 GeV/c transition radiation (TR) from electrons passing a radiator can be exploited in concert with the specific energy loss in a suitable gas mixture to obtain the necessary pion rejection capability. In conjunction with data from the ITS and the TPC it is possible to study the production of light and heavy vector-meson resonances and the dilepton continuum both in proton–proton as well as in Pb–Pb collisions. Exploiting the excellent impact parameter resolution of the ITS it is furthermore possible to reconstruct open charm and open beauty in semi-leptonic decays.

The TRD was designed to derive a fast trigger for charged particles with high momentum. It is part of the Level 1 trigger and can significantly enhance the recorded Υ-yields, high-$p_{\rm t}$ J/ψ, the high-mass part of the dilepton continuum as well as jets. The design parameters of the TRD are the following:

Pion rejection capability This is governed by the signal-to-background ratio in the measurement of J/ψ production and its $p_{\rm t}$ dependence. This led to the design goal for the pion rejection capability of a factor 100 for momenta above 1 GeV/c in central Pb–Pb collisions [113]. The measurement of the lighter vector-mesons and the determination of the continuum between the J/ψ and the Υ will only be feasible when this level of rejection can be reached.

Position and momentum resolution It is crucial to be able to match to the TPC in order to exploit the combined momentum resolution leading to an overall mass resolution of about 100 MeV/c^2 at the Υ-mass (for B = 0.4 T). The required pointing accuracy for electrons needs to be on the level of a fraction of a TPC pad. The anticipated momentum resolution of the TRD of 3.5 (4.7)% at 5 GeV/c (depending on multiplicity) will crucially determine the sharpness of the trigger threshold in $p_{\rm t}$ as well as the capability to reject fake tracks.

Radiation length It has to be minimised in order to reduce Bremsstrahlung leading to incorrect momentum determination or loss of electrons and to reduce photon conversions resulting in increased occupancy as well as incorrect matching.

Detector granularity In the bending direction this is governed by the desired momentum resolution and in longitudinal direction by the need to correctly identify and track electrons through all layers of the detector even at the largest

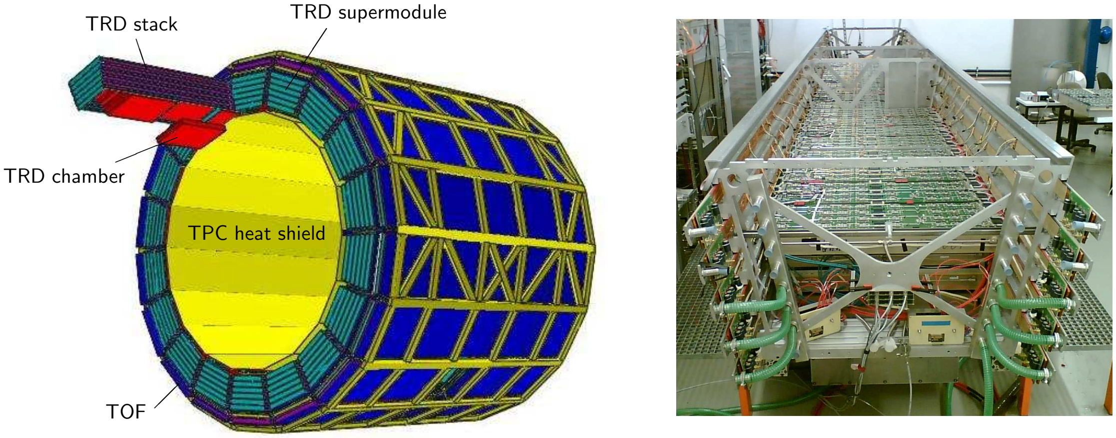

Figure 3.10: *Left panel: Schematic drawing of the TRD layout in the ALICE space frame. Shown are 18 super modules each containing 30 readout chambers (red) arranged in five stacks of six layers. One chamber has been displaced for clarity. On the outside the TRD is surrounded by the Time-Of-Flight (TOF) system (dark blue). On the inside the heat shield (yellow) towards the TPC is shown. Right panel: Super module during assembly with the first three layers installed.*

anticipated multiplicities. For the desired quality of the reconstructed dilepton pair signal (mostly dictated by the tracking efficiency) this leads to pads with an average area of about 6 cm^2, a tracking efficiency of 90% can thus be achieved for single tracks.

Including secondary particles this leads to a maximum occupancy of 34% at the highest simulated multiplicity density of $\mathrm{dN_{ch}/d}\eta = 8000$.

The final design of the TRD is depicted in Fig. 3.10. The TRD consists of 540 individual readout detector modules. They are arranged into 18 super modules (right panel of Fig. 3.10) each containing 30 modules arranged in five stacks along z and six layers in radius. In longitudinal (z) direction the active length is 7 m, the overall length of the entire super module is 7.8 m, its total weight is 1650 kg.

Each detector element consists of a carbon fibre laminated Rohacell/polypropylene fibre sandwich radiator of 48 mm thickness, a drift section of 30 mm thickness, and a multi-wire proportional chamber section (7 mm) with pad readout. The pad planes are supported by a honeycomb carbon-fibre sandwich back panel (22 mm). While very light, the panel and the radiator provide enough mechanical rigidity of the chamber to cope with overpressure up to 1 mbar to ensure a deformation of less than 1 mm. The entire readout electronics is directly mounted on the back panel of the detector. Including the water cooling system the total thickness of a single detector layer is 125 mm. In the bending plane ($r\phi$) each pad row consists of 144 pads. The central chambers consist of 12, all others of 16 pad rows. This leads to an overall channel count of 1.18×10^6. The total active area subtended by the pads is 716 m^2.

In Chapter 6 the PID performance of the TRD will be discussed.

3.4 Time-Of-Flight

The Time-Of-Flight (TOF) detector [122] is a large area array that covers the central pseudo-rapidity region ($|\eta| \leq 0.9$) for Particle IDentification (PID) in the intermediate momentum range, below about 2.5 GeV/c for pions and kaons, up to 4 GeV/c for protons, with a π/K and K/p separation better than 3σ [106,154]. The TOF, coupled with the ITS and TPC for track and vertex reconstruction and for $\mathrm{d}E/\mathrm{d}x$ measurements in the low-momentum range (up to about 1 GeV/c), will provide event-by-event identification of large samples of pions, kaons, and protons. In addition, at the inclusive level, identified kaons will allow invariant mass studies, in particular the detection of open heavy-flavoured states and vector-meson resonances such as the ϕ meson ([106,111,154,155]).

To fulfil the aforementioned tasks a large-coverage TOF detector, operating efficiently, with an good intrinsic response and an overall occupancy not exceeding the 10–15% level at the highest predicted charged-particle density of $\mathrm{d}N/\mathrm{d}\eta = 8000$ was required; see [106]. This led to the current design with more than 10^5 independent TOF channels. Since a large area had to be covered, a gaseous detector was chosen.

The detector covers a cylindrical surface of polar acceptance $|\theta - 90°| < 45°$. It has a modular structure corresponding to 18 sectors in ϕ and to 5 segments in z direction (see Fig. 3.4).

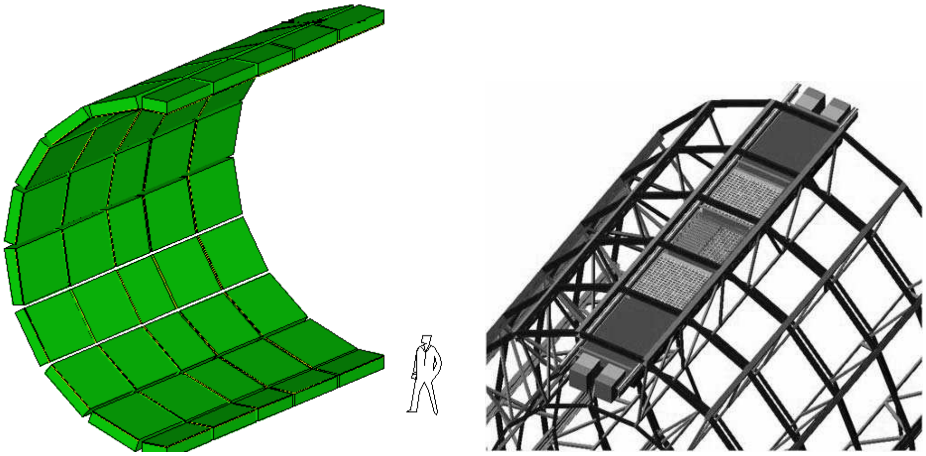

Figure 3.11: *Layout of the TOF detector (*left*) and of a single TOF sector (supermodule), consisting of 5 modules inside the space frame (*right*).*

3.5 PHOton Spectrometer

The PHOton Spectrometer (PHOS, [107, 116]) is a high-resolution electromagnetic spectrometer covering a limited acceptance domain at central rapidity. The main physics objectives are the test of thermal and dynamical properties of the initial phase of the collision extracted from low p_t direct photon measurements and the study of jet quenching through the measurement of high-p_t π^0 and γ-jet correlations.

The high particle multiplicity in nuclear collisions requires a dense, highly segmented calorimeter with small Molière radius at a large distance from the interaction point in order to keep the cell occupancy at a manageable level of about $10-20\%$. A good energy and position resolution improves the signal to background ratio for meson identification, in particular at low p_t where the combinatorial background is very large. The identification of photons requires high discrimination power against charged hadrons, neutrons and anti-neutrons.

To meet the required performance, PHOS is designed as a single-arm high-resolution high-granularity electromagnetic spectrometer consisting of a highly segmented electromagnetic calorimeter (PHOS) and a Charged-Particle Veto (CPV) detector. PHOS is subdivided into five independent PHOS+CPV units, called PHOS modules. It is positioned on the bottom of the ALICE setup at a distance of 460 cm from the interaction point. After its final installation it will cover approximately a quarter of a unit in pseudo-rapidity, $-0.12 \leq \eta \leq 0.12$, and 100° in azimuthal angle.

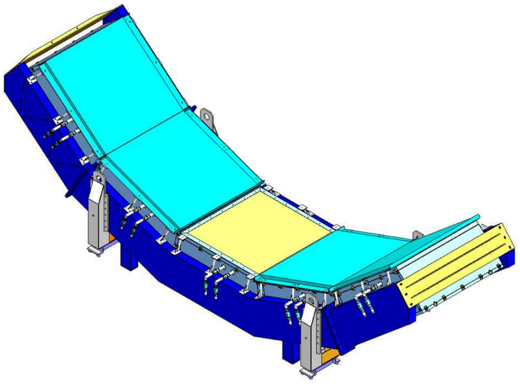

Figure 3.12: *Layout of 5 PHOS modules.*

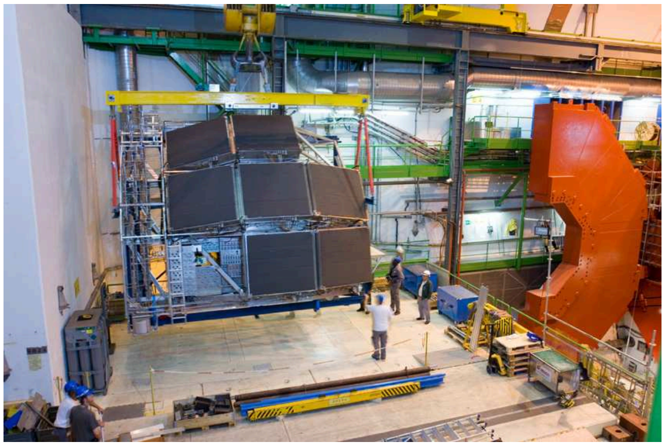

Figure 3.13: *View of the seven modules of the HMPID mounted on the cradle.*

3.6 High-Momentum Particle IDentificaton

The High-Momentum Particle Identification Detector (HMPID) [115], is dedicated to inclusive measurements of identified hadrons at p_{t} >1 GeV/c. The aim is to enhance the PID capability of ALICE by enabling identification of charged hadrons beyond the momentum interval attainable through energy-loss (in ITS and TPC) and time-of-flight measurements (in TOF). The detector was optimised to extend the useful range for π/K and K/p discrimination, on a track-by-track basis, up to 3 GeV/c and 5 GeV/c, respectively. The HMPID was designed as a single-arm array with an acceptance of 5% of the central barrel phase space. The geometry of the detector was optimised with respect to the particle yields in p–p and heavy-ion collisions at LHC energies, and with respect to the large opening angle required for two-particle correlation measurements, see Section 6.3 of [106]. In addition the identification of light nuclei and anti-nuclei (d, t, ^{3}He, α) at high transverse momenta in the central rapidity region can also be performed with the HMPID [159].

The HMPID is based on Ring Imaging Cherenkov (RICH) counters and consists of seven modules of about 1.5×1.5 m^2 each, mounted in an independent support cradle (Fig. 3.13) [160]. The cradle is fixed to the spaceframe at the two o'clock position.

3.7 ElectroMagnetic Calorimeter

The construction of a large ElectroMagnetic Calorimeter (EMCal) [114] began in 2008 with the aim to enable ALICE to explore in detail the physics of jet quenching (interaction of energetic partons with dense matter) over the large kinematic range accessible in heavy-ion collisions at the LHC [107]. The EMCal is a large Pb-scintillator calorimeter located adjacent to the ALICE magnet coil at a radius of $\sim$ 4.5 metres from the beam line. It covers $|\eta| \leq 0.7$ and $\Delta\phi = 107°$, and is positioned approximately opposite in azimuth to the ALICE Photon-Spectrometer (PHOS) calorimeter. The overall design of the EMCal was heavily influenced by its location within the ALICE L3 magnet. Figure 3.14 shows a schematic integration drawing of the end view of the ALICE central barrel.

The choice of a large-acceptance, moderate-resolution electromagnetic calorimeter provides a cost-effective pathway into jet physics in ALICE. The EMCal increases the electromagnetic calorimeter coverage of ALICE by nearly an order of magnitude. It provides a fast and efficient trigger (L0, L1) for hard jets, photons and electrons, allowing ALICE to exploit fully the luminosity of the LHC. The EMCal also measures the neutral energy component of jets, enabling full jet reconstruction in all collision systems, from proton–proton to Pb–Pb. The combination of the EMCal, the excellent ALICE charged particle tracking capabilities, and the modest ALICE magnetic-field strength, is a preferred configuration for jet reconstruction in the high-background environment of heavy-ion collisions, allowing the optimisation of background rejection while preserving the crucial jet-quenching signals at moderate transverse momentum.

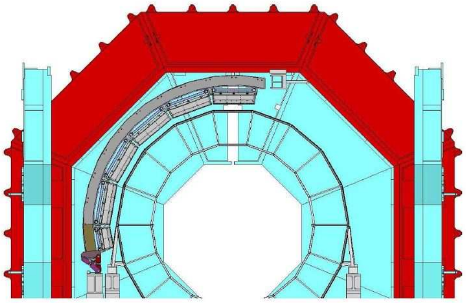

Figure 3.14: *Schematic integration drawing of the end view of the ALICE central barrel.*

3.8 Muon Arm

Muon detection is performed in the pseudo-rapidity region $-4.0 < \eta < -2.5$ by the muon spectrometer. With this detector, the complete spectrum of heavy-quark vector-mesons resonances (i.e. J/ψ, ψ', Υ, Υ' and Υ''), as well as the ϕ meson, will be measured in the $\mu^+\mu^-$ decay channel. The simultaneous measurement of all the quarkonia species with the same apparatus will allow a direct comparison of their production rate as a function of different parameters such as transverse momentum and collision centrality. In addition to vector mesons, the unlike-sign dimuon continuum up to masses around 10 GeV/c^2 will be measured. Since at LHC energies the continuum is expected to be dominated by muons from the semi-leptonic decay of open charm and open beauty, it will be possible to study the production of open (heavy) flavour with the muon spectrometer. Heavy-flavour production in the region $-2.5 < \eta < -1$ will be accessible through measurement of $e - \mu$ coincidences, where the muon is detected by the muon spectrometer and the electron by the TRD.

The layout of the muon spectrometer is shown in Figs. 3.15 and 3.16. The spectrometer consists of the following components: a passive front absorber to absorb hadrons and photons from the interaction vertex; a high-granularity tracking system of 10 detection planes; a large dipole magnet; a passive muon-filter wall, followed by four planes of trigger chambers; an inner beam shield to protect the chambers from primary and secondary particles produced at large rapidities.

The front absorber, whose length is 4.13 m, is located inside the solenoid magnet. The fiducial volume of the absorber is made predominantly out of carbon and concrete to limit small-angle scattering and energy loss by traversing muons. The spectrometer is shielded throughout its length by a dense absorber tube surrounding the beam pipe. The tube (beam shield) is made of tungsten, lead and stainless steel. While the front absorber and the beam shield are sufficient to protect the tracking chambers, additional protection is needed for the trigger chambers. For this reason the muon filter, i.e. an iron wall 1.2 m thick is placed after the last tracking chamber, in front of the first trigger chamber.

The tracking chambers were designed to achieve a spatial resolution of about 100 μm, necessary for an invariant-mass resolution of the order of 100 MeV/c^2 at the Υ mass [161,162]. In addition they have to be able to operate at a hit density of about $5{\times}10^{-2}$ cm^{-2} expected in central Pb–Pb collisions. area of about 100 m^2. All these requirements were fulfilled by the use of cathode pad chambers. They

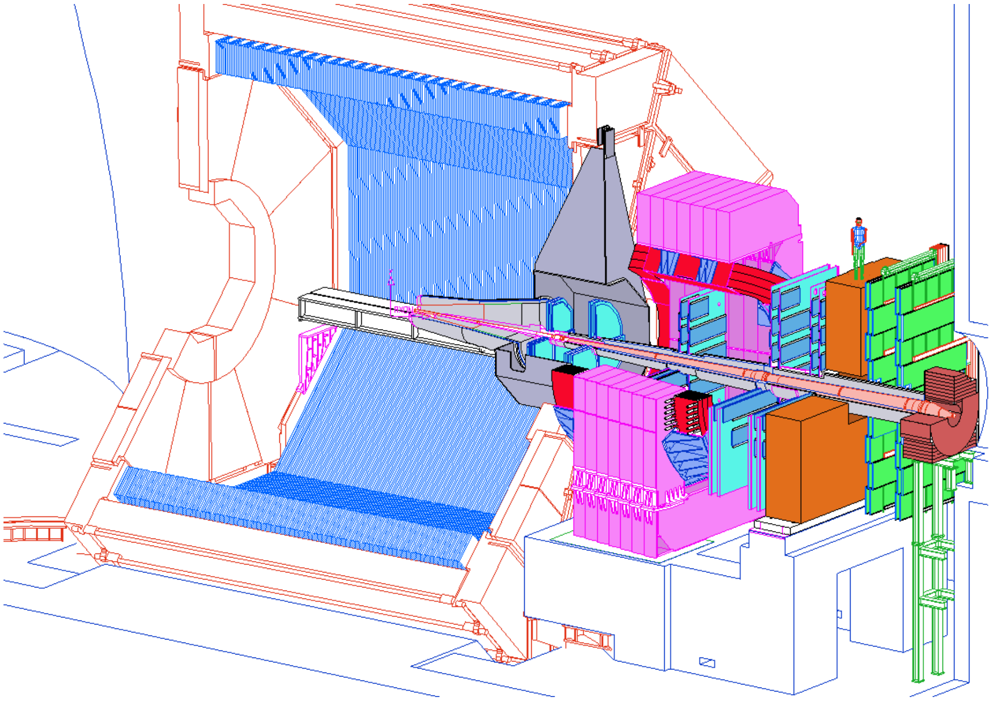

Figure 3.15: *Layout of the muon spectrometer.*

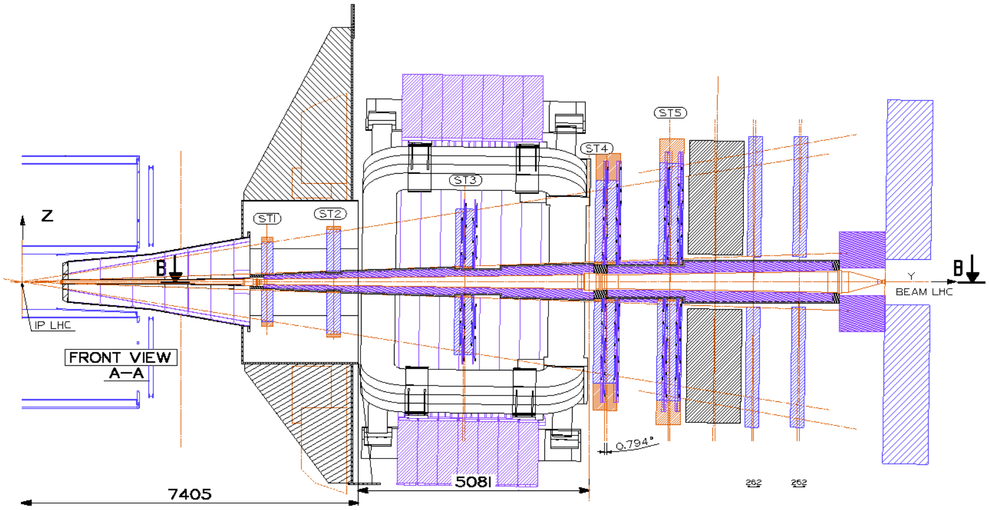

Figure 3.16: *Muon spectrometer longitudinal section; according to the adopted numbering scheme station 1 (ST1) is the closest to the central barrel.*

are arranged in five stations: two are placed before, one inside and two after the dipole magnet. Each station is made of two chamber planes. Each chamber has two cathode planes, which are both read out to provide two-dimensional hit information

The dipole magnet [163] is placed 7 m from the interaction vertex, at some 10 cm distance from the L3 solenoid. The size (free gap between poles 3.5 m, height of the yoke 9 m, total weight about 900 t) is defined by the requirements on the angular acceptance of the spectrometer.

Chapter 4

Silicon Pixel Detector: from assembly to commissioning

In this chapter the final stage of the assembly and the commissioning of the SPD will be described. As already discussed in the previous chapter, the reconstruction of heavy flavour decays requires good vertexing and PID capabilities. Given the large mean proper decay length of beauty hadrons, one of the most crucial detector performance figures will be the track impact parameter resolution. To achieve the required spatial precision a detector with the following features is needed: as close as possible to the primary vertex of the collision; low material budget to minimise multiple scattering; high granularity, in order to cope with the high multiplicity environment of heavy-ion collisions. The SPD was designed to fulfil these requirements.

Particular care has been dedicated to the design and assembly procedures to keep as high as possible the mechanical precision. The assembly procedure, in particular, must be well controlled to avoid large misalignments between the actual detector and the design geometry. Most techniques devoted to the correction of the detector misalignments work well for “small” displacements. Therefore, the precision of the assembly procedure of the detector has a direct impact on its final performance.

Another important design feature, common to all modern tracking detectors is the cooling system. Given the power dissipation of the electronics and the stringent requirements on the material budget, the design and operation of the cooling system play a crucial role on the operation of the detector.

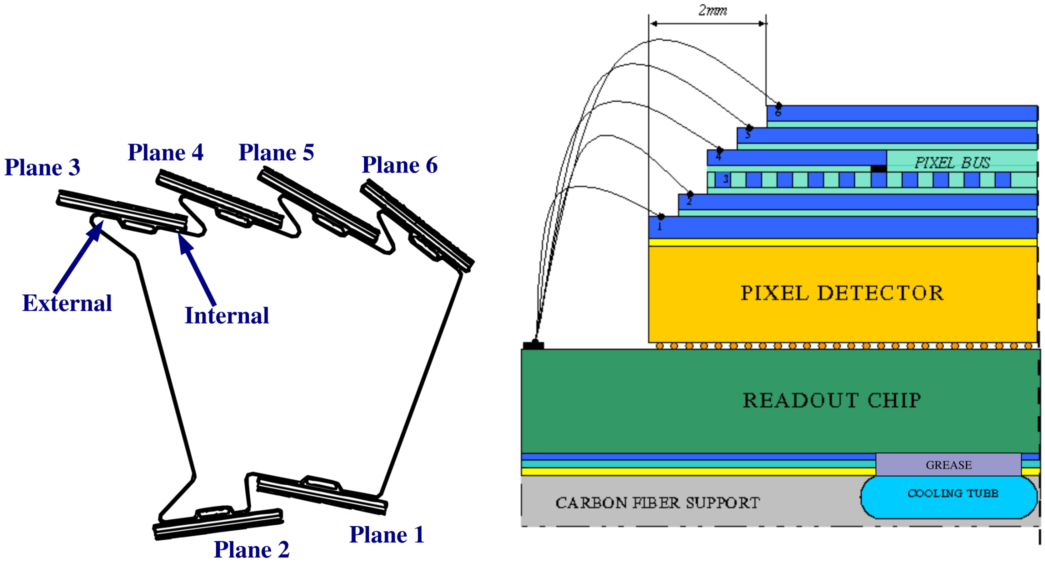

Figure 4.1: Left: *Transverse view of the layout of a carbon fibre support sector and its numbering scheme for the assembly.* Right: *Layout of the cross section of a mounted half-stave.*

4.1 SPD assembly

The structure of the SPD was illustrated in detail in Section 3.1.1. Here “sector assembly” means the system of procedures that range from the construction of the sector support to the assembly of the SPD barrel. The phases of the “sector assembly” performed by the INFN ALICE Padova group are:

- design and construction of the Carbon Fibre Sector Support (CFSS);
- design and construction of the cooling system (cooling ducts, capillaries and collectors);
- installation of the cooling lines on the CFSS;
- assembly of the sector (i.e. installation of the half-staves on the CFSS).

4.1.1 Tools and components

Carbon-Fibre Sector Support (CFSS)

The CFSS is the mechanical support structure of the Silicon Pixel Detector. The left panel of Fig. 4.1 shows the layout of a CFSS and its numbering scheme for the assembly. The shape of the CFSS is such to allow a partial overlap of the coverage of single staves in the first layer, while the turbo geometry on the second layer has been chosen in order to optimise the angle of incidence of positive charged particles (i.e. as close as possible to 90°). The shape has also been designed to maximise the stiffness of the support with respect to transversal distortions and it has been fully realised by the Padova Mechanical Engineering Service. The actual construction of all the CFSSs was done at the INFN LNL laboratory using a dedicated autoclave and custom designed tools.

The CFSS are made by a composite obtained winding two layers of unidirectional high-modulus, 100 μm-thick carbon fibre tapes, with fibres parallel and perpendicular to the beam axis, around an Anticorodal mandrel and interposed with a resin cured at high temperature. In order to obtain a good surface finishing quality metallic counter-mandrels are also used. The carbon fibre layers are then cooked in an autoclave at 1.5 bar and 120 °C. After the cooking, the CFSS was extracted and sanded in order to remove loose fibres. The CFSS then has a Parylene deposition (about 10 μm thick) in order to increase the electrical insulation and to also avoid the accidental release of debris from the CFSS surface. After the Parylene deposition the CFSS is ready to be equipped with the cooling system. This includes: the capillaries (Fig. 4.2, top) the phynox cooling ducts (Fig. 4.2, middle), and the collector boxes (Fig. 4.2, bottom). The first step is to put a thin layer of thermal grease in the empty cave of the CFSS planes. The grease improves the thermal contact between the cooling duct and the carbon fibre, thus improving the cooling uniformity. The grease also acts as "glue" ensuring a higher mechanical stability of the cooling duct. After the deposition of the grease, the cooling ducts are put in place and the capillaries are soldered to the ducts. At this point, the sector is ready to be assembled with its half-staves. After the half-staves are glued (see the next sections), the collector boxes are soldered to the capillaries. All the procedures were done in the LNL Clean Laboratory and special precautions were taken to avoid introducing dust or grease in the cooling ducts and capillaries.

The wall thickness of the CFSS is about 200 μm in the sensitive region in-

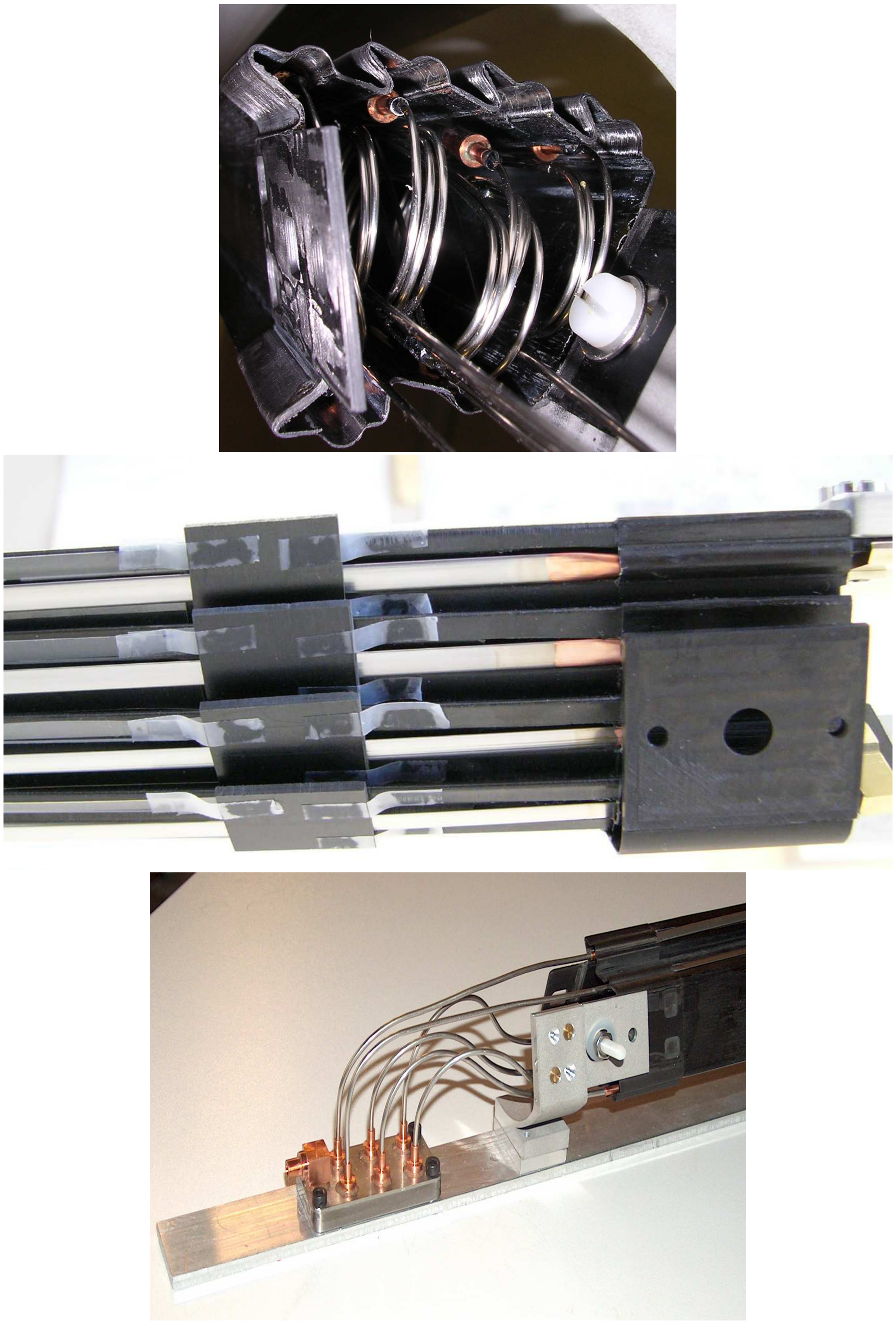

Figure 4.2: *The cooling system of the sectors.* Top: *In-going capillaries (0.5 mm inner diameter, 550 mm length) are winded in spiral shape and placed inside the carbon fibre support.* Middle: *The phynox ducts (40* µm *wall thickness) are placed inside the caves of the carbon fibre supports, thermal contact is ensured by a thermal grease.* Bottom: *Out-going capillaries are soldered to distribution boxes.*

creasing to 600 μm at the ends in order to allow the positioning of the mechanical references and of the components needed for the global assembly of the sectors. The global thickness of the support end-sections is locally increased to 1.8 mm in the connections area, in order to allow for an adequate pin length. All the coupling pins and pin seats are made of carbon fibre in order to minimise the material budget.

The CFSS design provides a direct thermal contact (mediated and improved by a thermal grease) between the cooling duct and the silicon chip back-plane. Fig. 4.1 (right panel) shows the cross section of a half-stave mounted on the CFSS. This allows to maximise the thermal coupling between the stave and the cooling system and to avoid problems of anisotropic heat conductivity typical of carbon fibre structures. The global and local deformations of the CFSS are expected to be of the order of a few μm in the service conditions.

The CFSS qualification is performed by means of a 3D survey machine, with software that allows direct comparison with the 3D CAD model of the components. The planarity, the angular distortion and the difference between the nominal and the measured dimensions are within tolerances. Since the half-stave structure is a combination of materials with a non-negligible mismatch of thermal expansion coefficients, the half-staves are firmly attached to the stiff carbon-fibre structure by means of UV glue dots and carbon-fibre clips. Possible deformations do not exceed 10 μm (in any direction) with stresses well within acceptable limits. Further details can be found in [165].

The SPD Barrel Sector Assembly System (BSAS)

The Clean Laboratory, operated by the Alice Pixel Group of INFN Padova, is equipped with a JOHANSSON TOPAZ Measuring Machine. A Barrel Sector Assembly System (BSAS) dedicated to the assembly of the half-staves on the Carbon Fibre Support has been built and is in operation since the beginning of 2005. Its components are mounted directly on the working plane of the TOPAZ machine. The majority of the assembly tasks are performed by using stepping motors, computer-controlled by two NATIONAL INSTRUMENTS PCI-7334 Motion Control Cards hosted on a P4 computer running WINDOWS XP, and by two modules NI MID-7604 4 Axis Integrated Stepper Drive. The control software has been developed under LabView. The main components of the BSAS are:

- The Rotating Sector Support (RSS);

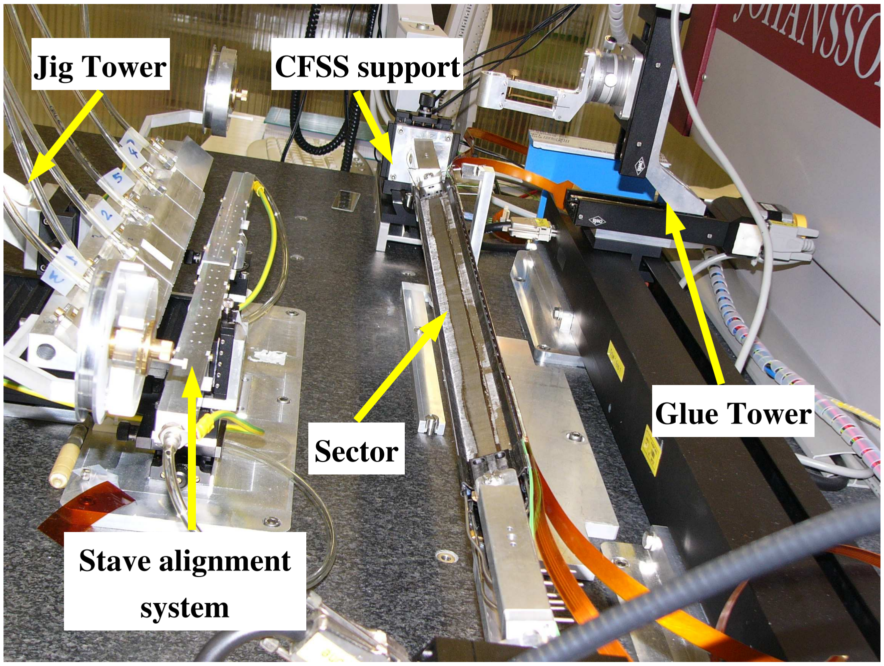

Figure 4.3: *Layout of the SPD Barrel Sector Assembly System.*

- The Stave Alignment System (SAS)
- The Grease and Glue Tower (GGT);
- The Stave Jig Tower (SJT).

The schematics of the BSAS are reported in Fig. 4.3. All the BSAS components have been calibrated before the whole assembly procedure The components of the BSAS are briefly described in the following sections.

The Rotating Sector Support (RSS)

The Rotating Sector Support is used to align and rotate the CFSS, already equipped with cooling ducts, mounted on two removable forks. The alignment of the first plane, out of the six that will hold the Staves in each sector, is performed on the measuring machine by acting on micrometric screws that control the forks positions. The alignment is relative to the TOPAZ working plane. Once the first plane is aligned, all other planes are selected by rotating the CFSS with a computer-controlled stepping motor (mod. DMT-6b). The angular precision of

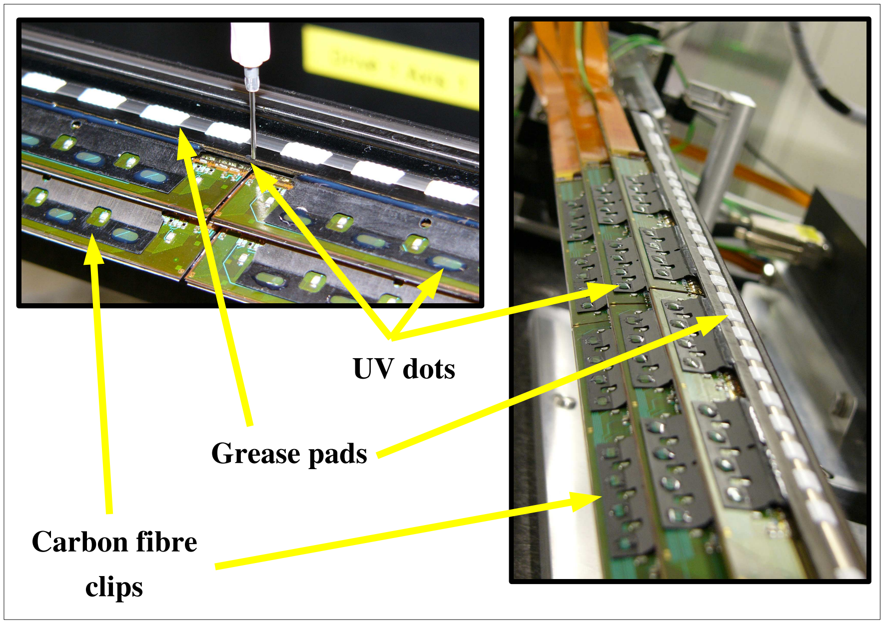

Figure 4.4: *In the upper plane of the CFSS, thermal grease pads on the cooling duct and UV dots are visible. Such material is dispensed before the assembly of the half-staves. In the lower CFSS planes, several already assembled half-staves are shown. The half-staves are attached to the CFSS with carbon fibre clips and UV glue dots.*

the software-controlled positioning is better than 6×10^{-4} $(\Delta\theta/\theta)$. After this automated positioning, a fine adjustment of the planarity of each CFSS plane with respect to the reference plane is performed manually. The reproducibility of the angular position after a full rotation cycle among the six stave planes has been measured to be within 3.2 μrad.

The Stave Alignment System (SAS)

The Stave Alignment System is used to adjust the relative distance and the planarity of the two half-staves. Two half-staves are positioned with the grounding foils on two separate surfaces, mechanically connected, where they are retained by a vacuum system. Micrometric movements are used to control their position with respect to the TOPAZ machine reference plane. The TOPAZ machine measuring head and an additional optical head are used to control the alignment.

The Stave Jig Tower (SJT)

The Stave Jig Tower is used to transfer the complete Stave from the SAS to the CFSS, to position it and to hold it in place on the CFSS during the gluing phase. The jig position is controlled by two motorised slits along the vertical z-axis (LIMES 200) and the y-axis (LIMES 250), perpendicular to the mounting plane. The typical precision was found to be better than 20μm with respect to the nominal position.

The part of the jig that holds the stave is made by six independent parts, each with its own independent, computer controlled vacuum system. Two out of the three jig portions that hold each half-stave are centred on the two ladders and the third one on the Multi-Chip Module (MCM) housing the auxiliary electronic components. Such a jig design allows the dismounting of a single part without releasing the entire half-stave. This feature is essential for the gluing procedure described below.

The Grease & Glue Tower (GGT)

As the name implies, the fundamental task of the Grease and Glue Tower is to distribute the thermal grease in a proper pattern that will ensure a good thermal contact between the half-staves and the cooling duct. For the first sector it was also used to distribute the UV glue used to fix the half-staves directly to the CFSS or, in some positions, to fix the carbon fibre clips.

The tower allows precise positioning of the working head all along the CFSS length (600 mm along the x-axis) as well as along the vertical z-axis (60 mm, mod LM60) and the y-axis (100 mm, mod LM100). As for the previous components, all individual movements of GGT have been calibrated. In addition, tests have been performed to verify the overall accuracy and reproducibility of the positioning of the needle of the glue syringe. Such tests have demonstrated that the overall accuracy is within 100 μm along the 600 mm long movement (x-axis) and within 20 μm for the y and z-axis. The GGT is equipped with a syringe for the thermal grease and a syringe for the UV glue, both of them can be equipped with different needles according to the need. The glue dispenser I&J Fisnar DD305 and the UV lamp EXFO Lite 3000 are used.

Gluing compounds for the barrel sector assembly

In the past, the ALICE Padova team performed a study of the compounds to be used in the assembly of the SPD. The main initial requirements were a good thermal contact between the half-staves and the cooling ducts, the possibility to remove an underperforming half-stave without damaging the entire sector, and the radiation hardness.The best solution has been found using two different compounds: a thermal grease for the thermal contact and a UV curable glue for the mechanical attachment of the staves on the support.

As far as the UV glue is concerned, the Norland NEA 123 resin has been tested with very good results. The high viscosity of this glue allows dispensing it both on the top and on the bottom of the object to be assembled, depending on the specific mounting steps [166]. In the case of the thermal compound, several candidates have been evaluated, by measuring the thermal conductivity of a thin layer (about 100 μm), and studying the mechanical properties and the radiation hardness. To test the radiation hardness, the four best candidates have been irradiated at LNL by using 27 MeV protons up to a fluence of 5×10^{12} protons/cm^2. This irradiation is equivalent to the dose of about 500 kRad, as expected for the SPD detector in 10 years of running at LHC [167]. Results from the irradiation tests were satisfactory for all samples [168]. Consequently the selection of the thermal grease was made looking also to the general properties of the materials. The AOS 52029 thermal grease has been finally selected.

4.1.2 Procedure

As far as the assembly of the SPD sectors is concerned, the main steps of the procedure can be summarised as follow:

- a CFSS, equipped with the cooling ducts, is placed on its support as shown in Fig. 4.3. It is then aligned parallel to the working reference frame of the JOHANSSON TOPAZ measuring machine. Then, the plane to be mounted is aligned. Fig 4.5 shows a typical example of the measurement on the plane after alignment. The two sets of measurements “internal” and “external” are relative to the position of the cooling duct (see Fig. 4.1).

- two half-staves are placed on the “stave alignment system” (see Fig. 4.3) then they are aligned to form a Stave. As stated before the typical precision of this operation is of around 20 μm. Once aligned the Stave is picked up

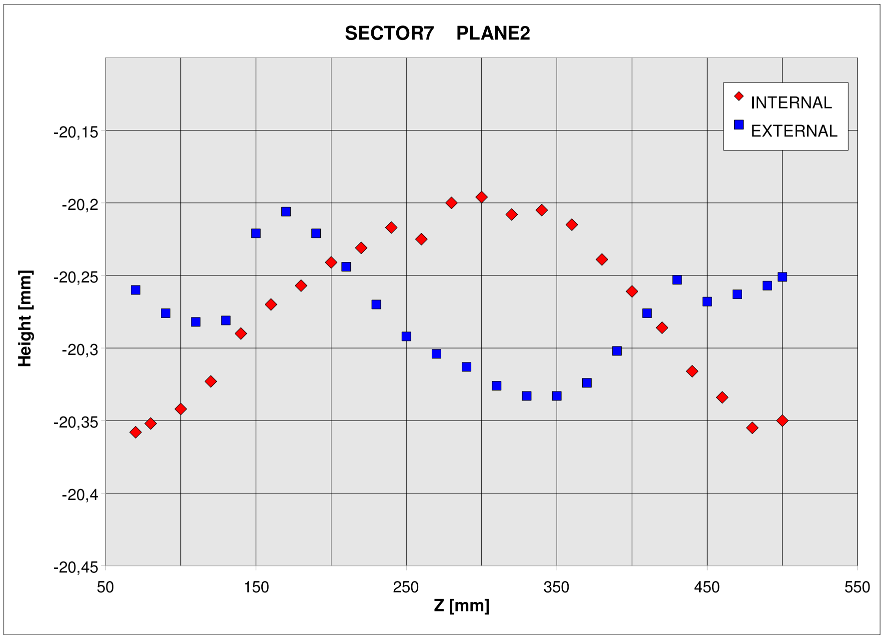

Figure 4.5: *Example of the planarity measurements of the CFSS for a plane of Sector 7. The Z axis is the coordinate along the sector. The Y axis is the height of the fibre referred to an arbitrary point.*

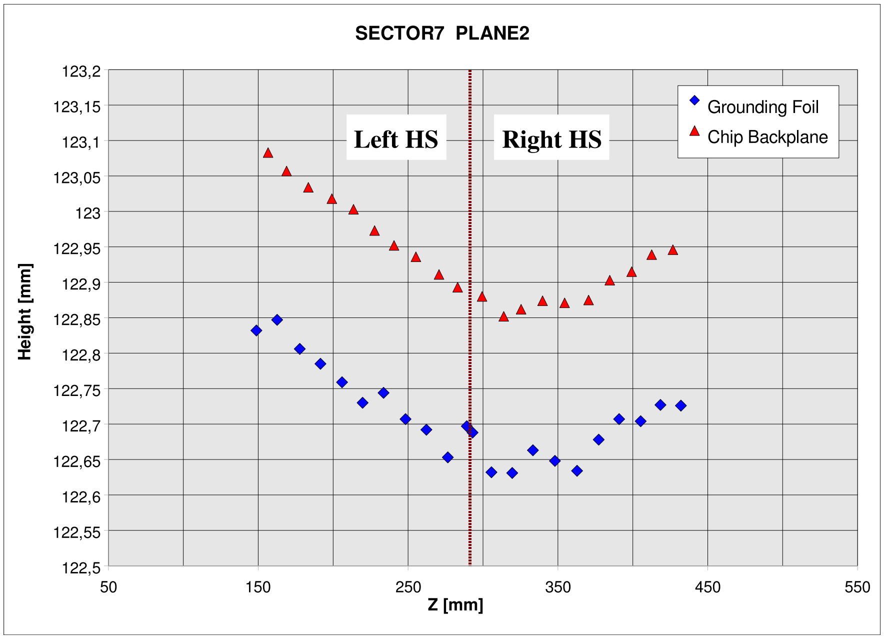

Figure 4.6: *Example of the planarity measurements for a stave of Sector 7 just before moving it into the final position. The Z axis is the coordinate along the sector. The Y axis is the depth of the stave referred to an arbitrary point.*

by the arm of the Jig tower using a vacuum holding tool. Fig 4.6 shows a typical example of the measurement of the planarity of the stave. The planarity of the stave is not critical as it, once pressed in position, will adapt to the shape of the fibre.

- a thin layer (about 200 μm) of thermal grease is dispensed in rectangular pads on the cooling duct as shown in the Fig. 4.4, each pad corresponds to the back side of an ALICE1LHCb readout chip. The amount of grease dispensed in every pad is calculated on the shape of the fibre and the stave (Fig. 4.5 and 4.6) to optimise the thermal contact between the cooling duct and the chip backplane. The amount of grease can be precisely controlled by changing the speed of the GGT. After the deposition of the thermal grease the operator puts a set of UV glue dots along the external edge of the plane (for plane 2 and 6 this is done on both edges).
- the aligned Stave is laid on the prepared plane. Its descent is carefully monitored by measuring a set of reference points after each movement. Finally the Stave is glued to the CFSS by curing the UV glue dots. The upper part of the stave is fixed using carbon fibre clips, to protect the wire-bonding and to ensure a good mechanical stability, as shown in figure 4.4.

4.1.3 Results

The assembly protocol has been extensively tested during the first quarter of 2005, including the Quality Control HS tests that were performed in Padova when the HS arrived from the Bari production plan and after the mounting on the CFSS. Moreover, a specific reworkability test has been performed demonstrating the possibility of dismounting a specific HS without damage for the rest of the Sector and for the dismounted detector.

The assembly of the whole SPD barrel was completed in 2007 with a yield of 100% (all accepted half-staves were assembled on the CFSS without any loss or damage).

4.2 Cooling

The major contribution to the on-detector power dissipation is due to front-end chips: they generate a nominal heat load of ≈ 23 W in each stave. In operation,

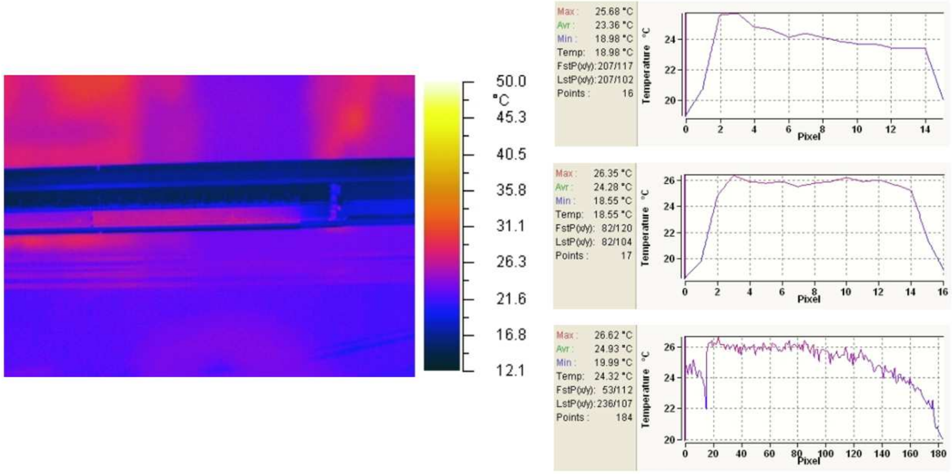

Figure 4.7: Left: *infrared image of an SPD half-stave during operation.* Right: *temperature profiles - transversal across the ladders (top two plots) and longitudinal along the full half-stave (bottom plot).*

if a sudden failure of the cooling were to occur, the temperature at the half-stave would increase at a rate of 1 °C/s. Continuous monitoring and a fast, reliable safety interlock on each half-stave are therefore mandatory. They are based on Pt1000 temperature transducers mounted on the pixel bus, next to the pixel chips. Two daisy chains of 5 transducers each (interleaved positions) provide redundant measurements of the average temperature. One chain is read out in the MCM, the other is hard-wired to the remote interlock system, based on a programmable logic controller (PLC) that is part of the detector control and safety system. Temperature values are logged. If the temperature reaches a preset threshold, the low-voltage power supply is promptly switched off by the safety interlock and an alarm is generated.

The design of the cooling system was driven by several constraints, such as: low material budget, fluid chemical stability, minimal temperature gradients, cooling duct temperature above the dew point, leak tightness of the system and fluid dielectricity. Several possible solutions based on different coolants were considered [169]. The final choice of an evaporative system with C_4F_{10} as coolant was found to fulfil all the requirements.

The cooling ducts are obtained using phynox tubes with a wall thickness of 40 μm and an initial diameter of 2.6 mm, squeezed down to flat profile with an

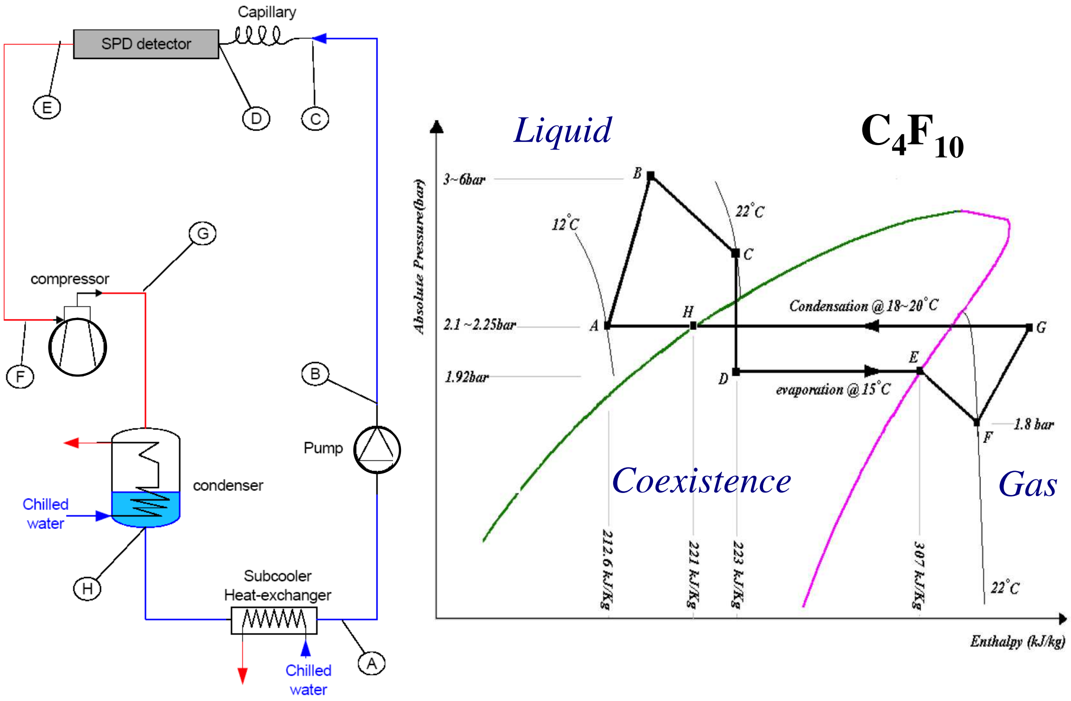

Figure 4.8: Left: *Simplified layout of the cooling plant.* Right: *Layout of the cooling cycle.*

overall thickness of 600 μm in the thin dimension. On the inlet side they are equipped with long (550 mm) CuNi capillaries (500 μm of diameter) winded in a spiral shape. On the outlet side they are equipped with CuNi pipes that go directly to a distribution box. The cooling tubes and the CuNi capillaries and pipes are produced at MEDELEC MINIMECA (Lausanne, Switzerland). Each sector is equipped with cooling collectors (i.e. "distribution box"), made of stainless steel, at the two ends, one functioning as an inlet and the other as an outlet for the whole sector. The parts for the cooling collectors were made in Italy by CINEL and the brazing in vacuum was done at CERN. All materials used in the cooling circuitry have been chosen to be long-term corrosion-resistant. Also each part is individually tested again leaks by He-leak detection. The test is repeated after each soldering/assembly step. Each sector is certified leakless (at 10^{-8} mbar l/s level).

In the final test, detectors are turned on at nominal power. An infrared (IR) camera is used to measure the temperature distribution on the external part of the pixel matrix (i.e. the bus), on the MCM and on the power extenders (copper–polyimide laminates). The average operating temperature of the half-staves is in the range of 25 °C to 30 °C. The temperature profile measured on a half-stave with the IR camera is shown in Fig. 4.7. The temperature does not exceed 35 °C and the local variations are limited to a few °C.

As shown in Fig. 4.8 (right), the C_4F_{10} follows a Joule-Thomson cycle (rapid expansion at constant enthalpy and subsequent evaporation). Each stave is put in thermal contact with the cooling duct mounted in a groove on the CFSS by a thermal grease layer (see Section 4.1.1). The liquid C_4F_{10} (Fig. 4.8, point A) is overcooled and compressed by a pump (point B) then it is brought to the coexistence phase (points C-D) inside the cooling duct by a pressure drop in the path along the capillaries.Heat abduction through phase transition (points D-E) takes place inside the cooling tube at 15–18 °C (1.9–2.0 bar). A compressor raises then the pressure pushing the gas towards a condenser (points F-G), where the liquid phase is re-established (point H) by heat transfer with cold water (≈ 6 °C).

The cooling conditions can be controlled by regulating the pressure of the liquid going in the detector (P_{liq}) and of the vapour coming out from the detector (P_{gas}). P_{liq} regulates the amount of liquid that flows into the detector and P_{gas}, since it sets the coexistence condition of the mixed phase, the evaporation rate inside the cooling duct.

The cooling plant has been installed inside the ALICE experimental hall in November 2007. Soon after, the system has been started for the first "turn-on" test in December 2007. Since then, a performance lower than expected has been found. A few half-staves ($\approx 12\%$) had to be left out from the test because they always exceeded the maximum allowed temperature. The issue has been identified in the higher than expected temperature of the C_4F_{10} liquid in the region close to the SPD. Indeed, due to technical reasons, the layout of the cooling hydraulics in the experimental hall underwent some modifications which resulted in a variation of the conditions of the fluid at the SPD input. The necessary modification to the system have already been implemented and are ready to be tested.

4.3 Commissioning

The ten sectors were first assembled into two half-barrels of five sectors each. After being tested, they have been mounted around the beam pipe. The TPC and the rest of the ITS (SDD and SSD) were moved to their final positions and the electrical and hydraulic connections were completed and tested. The integration of the SPD in the ALICE experimental hall was completed at the end of June 2007. In the meantime, all the software structure, i.e. Detector Control System (DCS), Experimental Control System (ECS) and Data Acquisition (DAQ), were finalised and tested, along with the installation and testing of the off-detector electronics.

A series of calibration and cosmic runs for the ALICE commissioning started in December 2007. The SPD was initially set up with the configuration files produced during the half-stave characterisation. After that an Oracle DataBase, the SPD Construction DataBase (CDB), was provided to store the new configurations. Fig. 4.9 shows the very first tracked muon from a cosmic-ray event in the SPD (February 2008). The two lower plots in Fig. 4.9 were taken from the online monitor that was used to check the general status of the data taking with the SPD.

During the commissioning the uniformity matrix response was measured with the internal pulser to determine the noisy and not responding pixels as well as the operating temperature of each half-stave. A fine tuning of the programmable DAC settings was done to lower as much as possible the power consumption keeping the same level of performance. The main DAC adjustments are the ones which determine the pixel chip high and middle reference voltages and the one that sets the preamplifier bias current.

Stable data taking with the required performance was achieved with 106 half-staves out of 120 total (88.3%) in the first test phase. Most of the missing half-staves will be recovered in the second test phase, after the Winter 2008/2009 break. The average operating temperature of the half-staves has stabilised at 28° C, after fine-tuning the cooling system. This value is close to the design one (25° C) and significant improvements are expected after the completion of the foreseen modifications (see 4.2).

The number of dead pixel measured during the half-stave characterisation was $\approx 0.01\%$ while the number of masked pixels in the working half-staves is $\approx 5 \times 10^{-3}\%$ (one pixel in 20,000). These figures are likely to change because: a) the number of noisy pixels is strongly configuration-dependent and b) the measurement of dead pixels is not complete yet due to insufficient statistic. All the readout electronics and power supply modules were installed and are now operational. The SPD readout time was measured at $\approx 320\ \mu$s.

In May 2008 the commissioning of the pixel trigger system began. It required

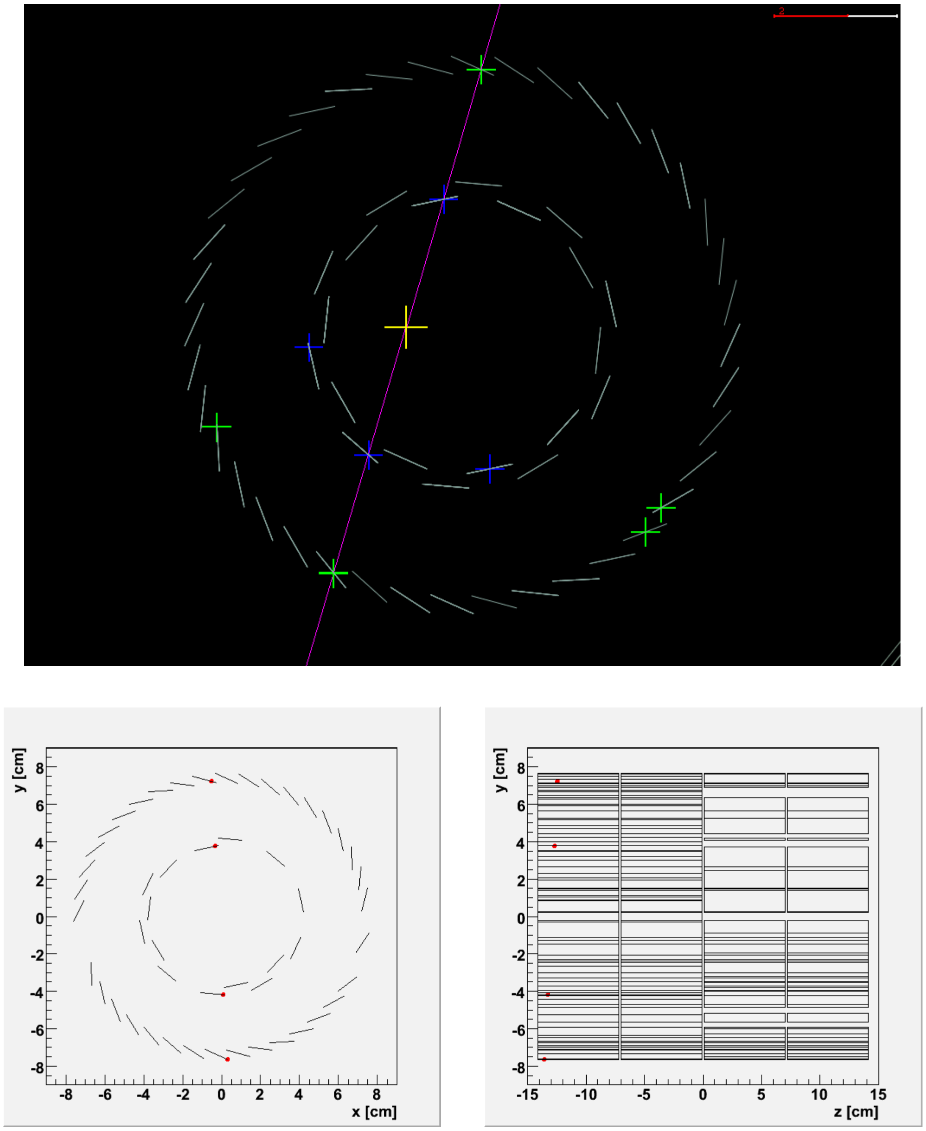

Figure 4.9: Top: *First tracked muon from a cosmic-ray event in the SPD.* Bottom: *One of the first cosmic tracks as seen by the SPD online monitor (MOOD [170]). The track is shown from the front view (left) and from the side view of the SPD (right).*

dedicated DACs tuning for the SPD Fast-OR circuitry. At present 923 out of 1200 chips are included in the Fast-OR logic ($\approx$ 88% of available half-staves). In the beginning a manual procedure to tune the four Fast-OR DACs was used. This was needed in order to understand the system and to build the basis of a fully automatic procedure. It is now under development and will be integrated in the configuration runs. The pixel trigger is crucial for the SPD commissioning and, in general, for the ALICE central tracker alignment (i.e. the ITS and TPC) using cosmic tracks. Thanks to an on-board Field-Programmable Gate Array (FPGA), the algorithms of the pixel trigger can be programmed. The pixel trigger has several implemented algorithms that can be software selected. The default algorithm used during the commissioning was the so-called “top-bottom-outer-layer”: a trigger is generated if the cosmic track generates one hit in the outer layer of the top half-barrel and one hit in the outer layer of the bottom half-barrel. Since May 2008 more than 100,000 reconstructed cosmic tracks were collected by the ITS with the SPD as trigger. The trigger rate ranged from 0.08 Hz to 0.18 Hz, depending on the number of half-staves participating in the trigger logic. The values found are in agreement with the expected rate measured by L3 at LEP. The tracks from cosmic rays with four points in the SPD layers (there are $\approx$ 45,000 with 4 points and $\approx$ 55,000 with 3 points) are used for the alignment of the SPD itself. The alignment of the ITS (and in particular of the SPD) will be the subject of the next Chapter.

On June 15 ALICE was in its standard mode of taking data from cosmic rays. At this same time the CERN LHC was conducting a high intensity injection test sending 4 bunches of 4×10^{10} protons (spaced by 500 ns) through the TI2 injection line into the TED (beam dump) $\approx$ 80 m upstream of ALICE. All of these protons interacted with the beam stopper. A number of muons were produced and travelled through the beam stop and were detected by the SPD. The signals generated by these muons are shown in Fig. 4.10. Since these muons are travelling nearly parallel with the surface of the sensitive volumes, there are many more hits produced then muons.

Since June, from the data collected by the SPD (and its pixel trigger) the multiplicity of the beam in different conditions was extracted. This information was used by LHC Machine Team as a quick feedback to adjust the beam parameters.

Fig. 4.11 shows one of the very first beam-gas events seen by the ITS as it appears in the ALICE event display. Now the SPD is essentially ready for the first collisions and it is expected to achieve its nominal performance after few additional commissioning runs.

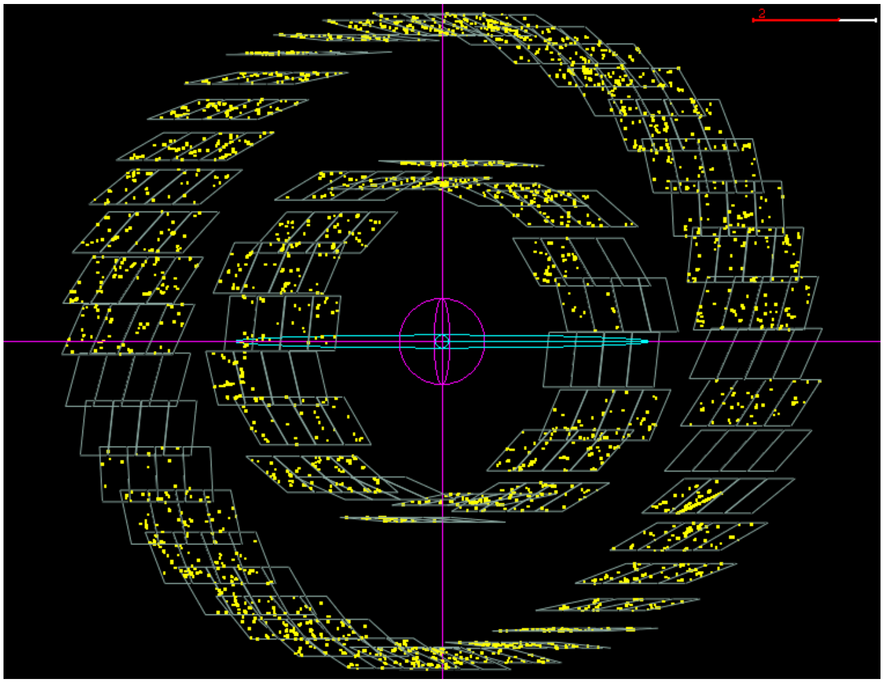

Figure 4.10: *June 15, 2008 the first artificial event at LHC: a muon shower from the stopping of a test beam.*

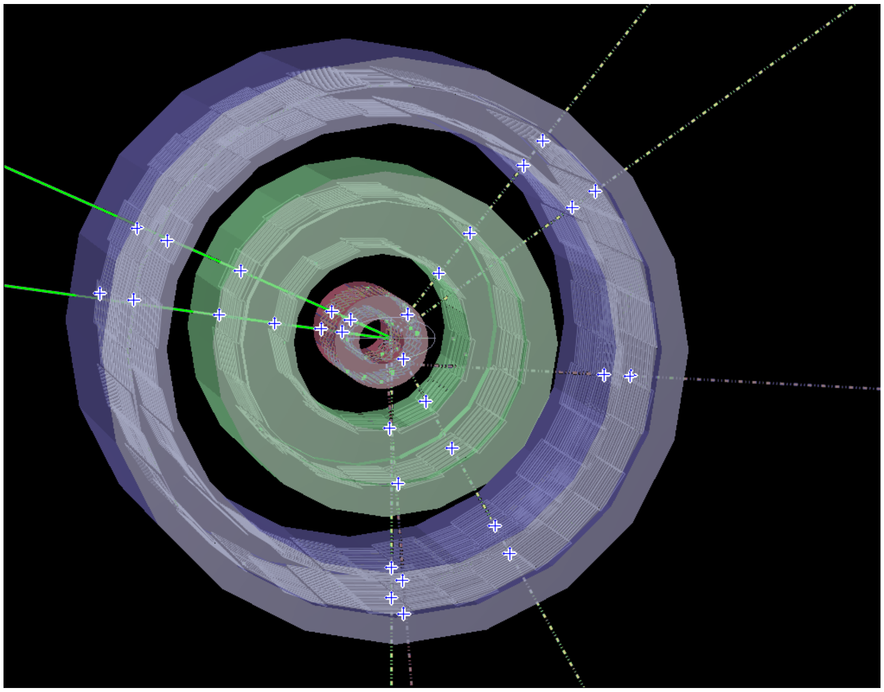

Figure 4.11: *One of the first beam gas events as seen by the ITS (September 12, 2008).*

Chapter 5

Inner Tracking System: vertexing performance and alignment

Secondary vertexes are the signature of the (weak) decays of particles containing strangeness, charm or beauty. The identification of these decays is particularly challenging in the case of open charm and open beauty hadrons that have mean proper decay lengths of $\sim$ 100-500 μm, namely D^0 ($c\tau \simeq$ 123 μm), D$^+$ ($c\tau \simeq$ 315 μm) and B mesons ($c\tau \sim$ 500 μm) [127].

The most effective constraint for the selection of such particles is the presence of one or more tracks that are displaced from the interaction (primary) vertex. The variable allowing to evaluate the displacement of a track is its *impact parameter*, which is the distance of closest approach of the reconstructed particle trajectory to the primary vertex. The impact parameter projection in the transverse plane, $d_0(r\phi)$, is defined as:

$$d_0(r\phi) \equiv q \cdot \left[R - \sqrt{(x_V - x_C)^2 + (y_V - y_C)^2} \right], \tag{5.1}$$

where q is the sign of the particle charge, R and (x_C, y_C) are the radius and the centre of the track projection in the transverse plane (which is a circle) and (x_V, y_V) is the position of the primary vertex in the transverse plane. The impact parameter is attributed a sign in order to ease the identification of specific topologies. The z projection of the impact parameter, $d_0(z)$, is defined as:

$$d_0(z) \equiv z_{\text{track}} - z_V, \tag{5.2}$$

where z_{track} is the z position of the track after it has been propagated to the distance of closest approach in the transverse plane, and z_V is the position of the primary vertex along the beam direction.

For both the $r\phi$ and z projections, the impact parameter resolution has a contribution due to the track position resolution and a contribution due to the uncertainty on the primary vertex position:

$$\sigma(d_0) = \sigma_{\text{track}} \oplus \sigma_{\text{vertex}}. \tag{5.3}$$

Therefore, it is crucial to achieve a very good resolution ($<$ 50-60 μm) not only on the track position at the vertex, but also on the position in $r\phi$ of the primary vertex itself.

For heavy ion collisions at the LHC, the transverse beam size is very small and the primary vertex position is know for a given run with an uncertainty of only $\simeq$ 10 μm. This uncertainty is negligible and, therefore, the resolution on $d_0(r\phi)$ corresponds with the resolution on the track position.

In the case of the proton–proton runs, since the beams have to be defocused to reduce the luminosity, the *a priori* information on the vertex position might be extremely poor ($\sigma \approx$ 150 μm) and an event-by-event reconstruction of all the three coordinates is mandatory in order to fulfil the resolution requirements stated above. A detailed description of the vertex finding procedure can be found in Ref. [183,184] for the Pb–Pb case and in Ref. [185] for the proton–proton case. Given its importance, in Section 5.1 some results for the track impact parameter resolution, under different conditions, will be shown.

Any silicon tracking system is an assembly of several separate modules, whose positions are displaced, with respect to the ideal case, during the assembly and integration of the different detector components [171,172]. In addition these components can move slightly in time due to mechanical stresses or to thermal and magnetic field effects. Such misalignments can considerably worsen the resolution of the track (σ_{track}) and even the tracking efficiency (if the misalignments are large enough to affect the tracking algorithm). A worsening of the track resolution directly affects the resolution on impact parameter and, for the case of proton–proton collisions, the resolution on the position of the primary vertex (since it will be reconstructed using the tracks). Therefore, to achieve the nominal design resolution, the misalignment of the detector must be measured and corrected for. Two methods to tackle this problem will be described in Sect. 5.2.

Table 5.1: *Summary of the resolutions for the ITS detectors. The local coordinates are defined in Fig. 5.8*

Loc. Coord.	SPD	SDD	SSD
X [μm]	12	28	20
Y [μm]	0	0	0
Z [μm]	120	20	830

5.1 Track impact parameter resolution

5.1.1 Impact parameter resolution in Pb-Pb collisions

The resolutions are shown in Fig. 5.1 as a function of the track transverse momentum. The resolution in $r\phi$ (z) is 65 (170) μm at $p_{\mathrm{t}} = 1$ GeV/c and 12 (40) μm at $p_{\mathrm{t}} = 20$ GeV/c. The large difference between the two projections reflects the different spatial resolutions in the $r\phi$ and z directions of the detectors in the ITS. Table 5.1 summarises the spatial performances for the detectors of the ITS. The resolutions are reported in the local coordinates of the sensors (see Fig. 5.8), where local X corresponds to "$r\phi$" and the local Z is parallel to global Z. The local Y is the axis perpendicular to the sensor.

Particle type dependence

For low momenta, the main contribution to the impact parameter resolution is due to the multiple scattering, which depends on $1/\beta$ [127]. Consequently, for a given p_{t}, the resolution itself is worse for heavier particles, that have lower velocity β. Figure 5.2 presents the resolutions for electrons ($e^{\pm}$), pions ($\pi^{\pm}$), kaons ($\mathrm{K}^{\pm}$) and protons (p and $\overline{\mathrm{p}}$). For $p_{\mathrm{t}} > 1$ (1.5) GeV/c the resolutions for kaons (protons) are the same as for pions.

The separation at low p_{t} between pions and electrons is not well defined, because the latter can suffer from energy loss due to the bremsstrahlung process; even if the probability is quite low ($\sim 1\%$ at $p_{\mathrm{t}} = 1$ GeV/c), this spoils both the momentum and the impact parameter resolution.

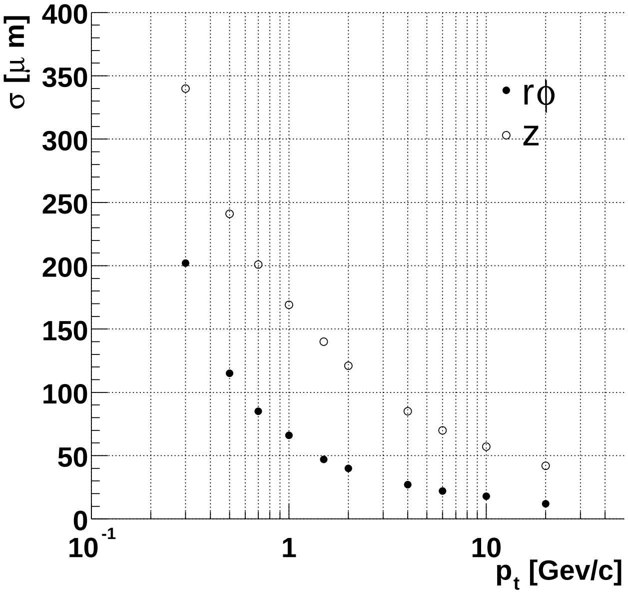

Figure 5.1: *Impact parameter resolutions for primary charged pions reconstructed in the TPC and in the ITS (with 6 clusters in the ITS) in central Pb–Pb collisions (*$\mathrm{d}N_{\mathrm{ch}}/\mathrm{d}y = 6000$*). From [193].*

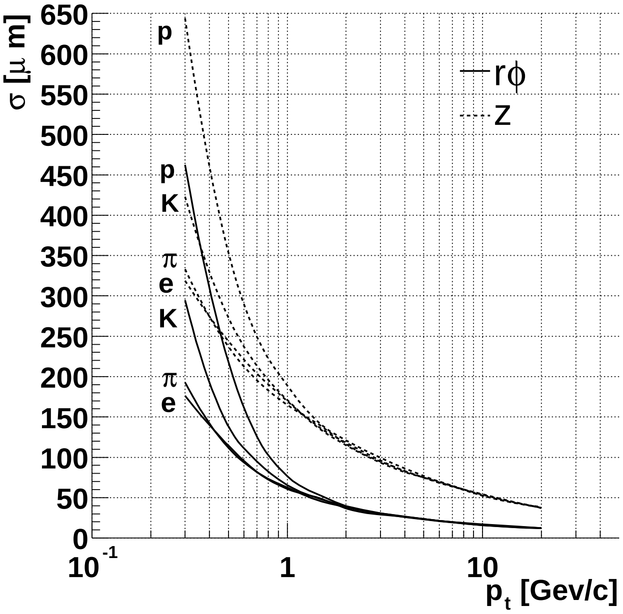

Figure 5.2: *Impact parameter resolutions for electrons, pions, kaons and protons as a function of the transverse momentum. From [193].*

5.1.2 Impact parameter resolution in p-p collisions

Given the results presented in the former section, in proton–proton the impact parameter resolution has a significant contribution from the uncertainty on the primary vertex position, which is, on average, about one order of magnitude larger than in the Pb–Pb case.

The resolution on the track position in the transverse plane (the main contribution to the impact parameter resolution) is essentially the same in proton–proton and in Pb–Pb if 6 ITS clusters are required (Fig. 5.3).

The aim of the measurement of the tracks impact parameter is the identification of one or more displaced tracks with respect to the interaction vertex. Therefore, in pp collisions, the following strategy for the measurement of the impact parameter was adopted: the impact parameter of a given track j is estimated as the distance of closest approach of the track j to the vertex position obtained by excluding the track j from the vertex reconstruction. In fact, if the track j was included in the reconstruction, it would bias the vertex position, leading to a systematic underestimation of the impact parameter. This effect is shown in Fig. 5.4, where the following distributions are compared for primary pions with $p_\mathrm{t} \approx 1$ GeV/c: impact parameter using true vertex position (solid), impact parameter using vertex estimated from all tracks (dashed), impact parameter using vertex estimated from all tracks but j (dotted).

The algorithm for vertex reconstruction in proton–proton collisions allows the measurement of the impact parameter projection in the bending plane with a resolution that is not substantially worse than the track position resolution for low and medium transverse momentum tracks, in particular for tracks produced in high-multiplicity events. To this respect, one must keep in mind that events with heavy flavour production have a multiplicity which is larger than the mean multiplicity in proton–proton minimum-bias events.

For high-momentum tracks the achieved impact parameter resolution is roughly twice the track position resolution. However, this is not a drastic improvement, since, at high p_t, the background to heavy flavour particles is almost negligible and, therefore, the selection based on the impact parameter is not as crucial as it is for low-momentum particles.

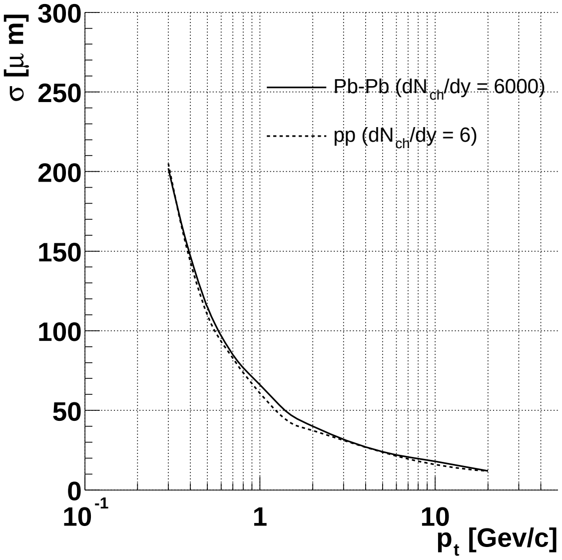

Figure 5.3: *Resolution on the track position in the transverse plane in Pb–Pb and in pp for pions. From [193].*

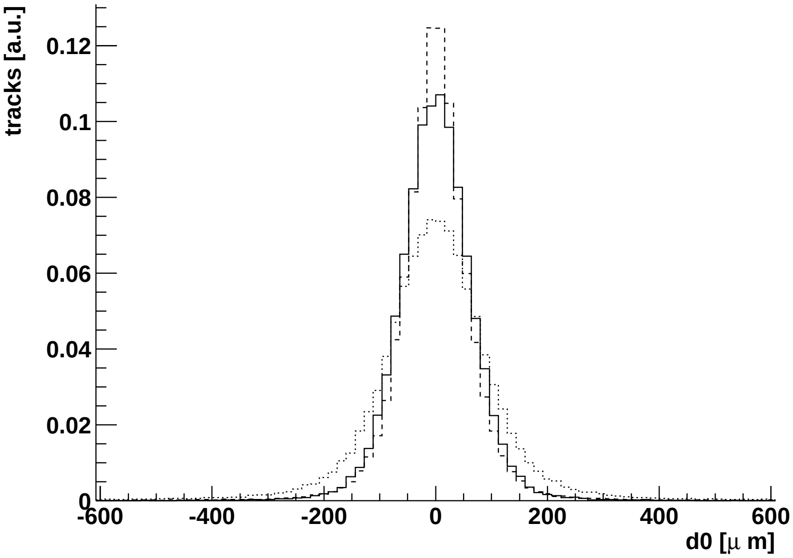

Figure 5.4: *Distributions of the impact parameters for primary pions with* $p_t \approx 1$ GeV/c *obtained: using true vertex position (solid), using vertex estimated from all tracks in the event (dashed), using vertex estimated from all tracks but the current one (dotted). From [193].*

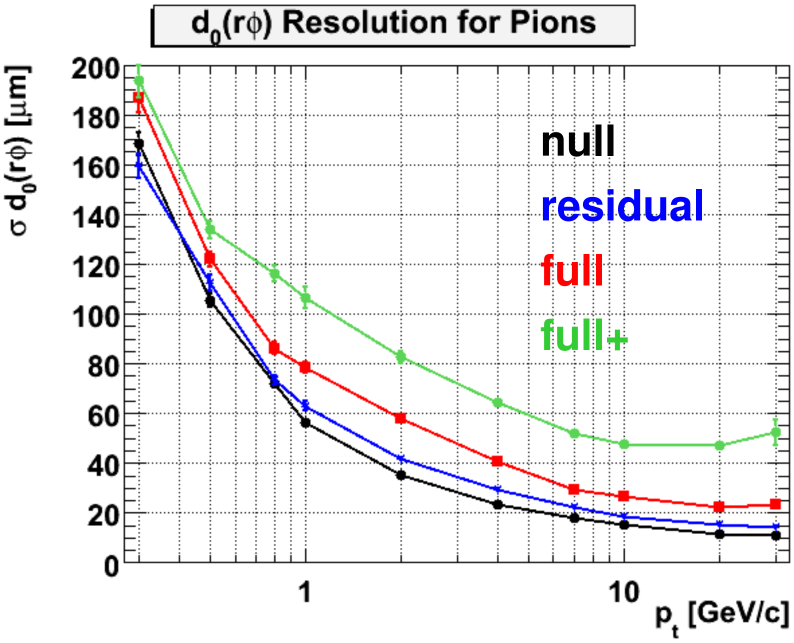

Figure 5.5: *Impact parameter resolution for different scenarios of misalignment (see text).*

5.1.3 Impact parameter resolution including misalignments

The results shown until now were obtained for the case of an "ideal detector", that is one free from mechanical imperfection. To have an estimate of the effect of possible misalignments on the impact parameter, two scenarios were prepared. The "full misalignment" scenario is the one expected in the initial analysis of the data from cosmic muons. It has been estimated from expected mechanical imprecision. It is actually set to 20-45 μm at the sensor level and higher at the ladder or layer level ($\approx$ 100 μm). The "full+" misalignment scenario was estimated using the "worst case" values from the mechanical tolerances of the ITS. The "residual misalignment" scenario is the expected misalignment left after applying the realignment procedure(s). The target is to reach a $\approx$ 20% (or better) degradation of the resolution. A summary of the shifts for the various misalignment scenarios is listed in Tab. 5.2. Those numbers should be compared with the resolutions of the detectors that are summarised in Tab. 5.1. The effects on the impact parameter resolution are shown in Fig. 5.5. The results were obtained by reconstructing

Table 5.2: *Summary of the misalignment scenarios for the ITS sensors. The values are for the local coordinates.*

Scenario		SPD	SDD	SSD
Residual	[μm]	$10_X \times 10_Y \times 20_Z$	$20_X \times 20_Y \times 20_Z$	$15_X \times 15_Y \times 100_Z$
Full	[μm]	$20_X \times 20_Y \times 20_Z$	$45_X \times 45_Y \times 45_Z$	$30_X \times 30_Y \times 100_Z$
Full+	[μm]	$30_X \times 30_Y \times 30_Z$	$70_X \times 70_Y \times 70_Z$	$45_X \times 45_Y \times 150_Z$

misaligned events using the ideal geometry.

5.2 Alignment of the Inner Tracking System

The task of aligning the ALICE ITS is particularly challenging also due to the very large number of degrees of freedom. The numbers of sensitive volumes are 240 for the SPD, 260 for the SDD, 1698 for the SSD, for a total of 2198 alignable sensitive volumes. That translates into 13188 degrees of freedom.

The general strategy for the alignment of the ITS is to use data from cosmic-ray muons (data taking began in February 2008), beam-gas events and the first proton–proton collisions. The procedure will make use of data without the magnetic field at first. Later on, the data with magnetic field will be included in the analysis. This allows the selection of high-momentum tracks, that are less influenced by multiple scattering, and therefore they give more precise results. The outline of the alignment program is as follows:

1. The first step is to align the "internal" misalignment of the SPD. The procedure begins with the SPD because it is the sub-detector with the highest statistics (due to the pixel Fast-OR) and because it is used to refit the tracks that will be used to align the other sub-detectors.

2. The next step is to align the layers that are easier to calibrate. This means the SPD and the SSD but also the z coordinate of the SDD can be included early to improve the resolution in z (see Tab. 5.1).

3. Once the SPD and SSD are aligned, it is possible to proceed with the global alignment of the ITS and the TPC (already internally aligned).

4. Finally, the drift coordinate ($r\phi$) of the SDD can be included. This is left for last since the calibration of the SDD needs time and there is an interplay between the alignment and the calibration.

Two independent methods, based on track-to-measured-points residuals minimisation, have been prepared for the internal alignment of the ITS. The first method uses the Millepede approach [173], where a global fit to all residuals is performed, extracting all the misalignment parameters simultaneously. The second method performs a (local) minimisation for each single module and accounts for module correlations by iterating the procedure until convergence is reached.

The MILLEPEDE approach

In the ALICE software Millepede was implemented by the muon spectrometer group and, recently, the code has been adapted to the ITS. It is a method to solve the linear least squares problem with a simultaneous fit of all global (alignment) and local (track) parameters, irrespectively of the number of local parameters. A practical limit for the number of global (alignment) parameters is about ten thousands. Main requirement of this approach is that the measured value, the residual, i.e. the deviation between the fitted and measured data, can be well approximated with a linear function of the alignment (d_i) and track (δ_i) parameters. In formula:

$$z_i = y_i - (\sum_j \alpha_j \, \delta_{ij} + \sum_k \alpha_k \, d_k)$$

where z_i is the residual and y_i is the measurement. The internal Millepede procedure is summarised in the following:

- Initialisation from a configuration file (list of modules to be aligned, constraints, starting geometry);
- Calculation for each track of the local and global derivatives at each hit and filling of the corresponding local equations;
- Local (track) fits;
- Global (alignment parameters) fit.

The results (see [174, 175]) for the Millepede approach will be shown in the next Sections.

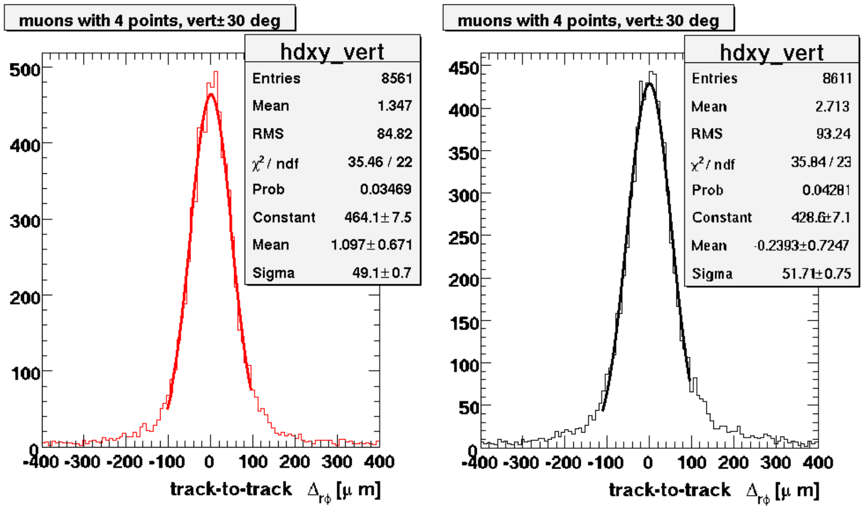

Figure 5.6: *Track-to-track distance at Y=0 for the SPD realigned with Millepede (left) and realigned with the Iterative method (right). The tracks were required to have 4 points in the SPD layers.*

Iterative approach

The idea of the iterative approach is to perform a minimisation for each single module and to account for module correlations by iterating the procedure until convergence is reached. A fit of the track points, excluding the point on the module under study, will be not affected by the module misalignment itself. The residuals are then used to estimate the alignment parameters afterwards, through the construction of a χ^2 function of the alignment parameters and the subsequent minimisation of the χ^2. Since the fit results are affected by the misalignments of all the modules, as many tracks as possible must be used in order to "sum up" to zero the correlations for the modules considered. An iterative procedure is then needed in order to estimate the realignment parameters for all the modules. For this method, a good starting point is to provide all the mechanical survey information together with some initial condition points.

This method has been developed by the ALICE Padova group, on an existing framework within the AliROOT code. It has now reached a level of precision comparable with the Millepede approach (see [176]). Fig. 5.6 shows the comparison between Millepede and the Iterative approach for the realignment of the SPD.

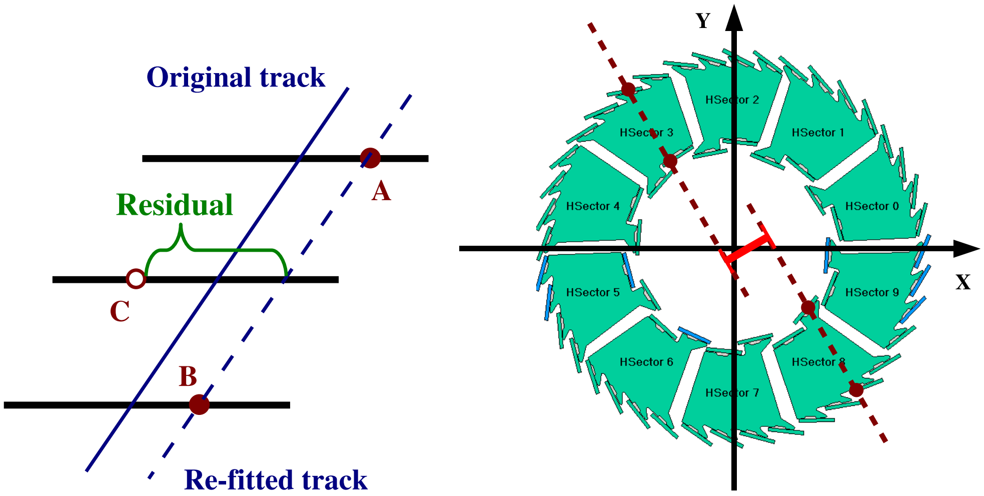

Figure 5.7: Left: *Schematic representation of the measurement of a residual (see text).* Right: *Schematic representation of the "track-to-track distance at $Y = 0$" observable (see text).*

5.2.1 ITS alignment monitoring using the residuals

Both realignment methods are intrinsically "blind": they optimise the system without taking into account the actual situation of the mechanics. Therefore a tool to check the results of the alignment procedure was needed. The observables used to check the quality of the realignment are the distributions of the residuals.

The procedure consists in considering a track (see left panel of the Fig. 5.7), excluding a point (point "C" in Fig. 5.7), refitting the track using the leftover points (points "A" and "B" in Fig. 5.7). The distance, on the sensor plane, between the excluded point and the refitted track is called "residual". The residual is defined in three different projections:

$$\begin{array}{rll} \textbf{RPHI}: & Res(\phi) & = \frac{\phi_{trk}-\phi_{pt}}{|\phi_{trk}-\phi_{pt}|}\sqrt{(X_{trk}-X_{pt})^2+(Y_{trk}-Y_{pt})^2} \\ \textbf{X}: & Res(X) & = (X_{trk}-X_{pt}) \\ \textbf{Z}: & Res(Z) & = (Z_{trk}-Z_{pt}) \end{array}$$

Where X, Y, Z, ϕ are the coordinates as shown in Fig. 5.8 (left panel). The subscript "pt" stands for the coordinates of the considered point. The subscript "trk" stands for the coordinates of the intersection between the refitted track and

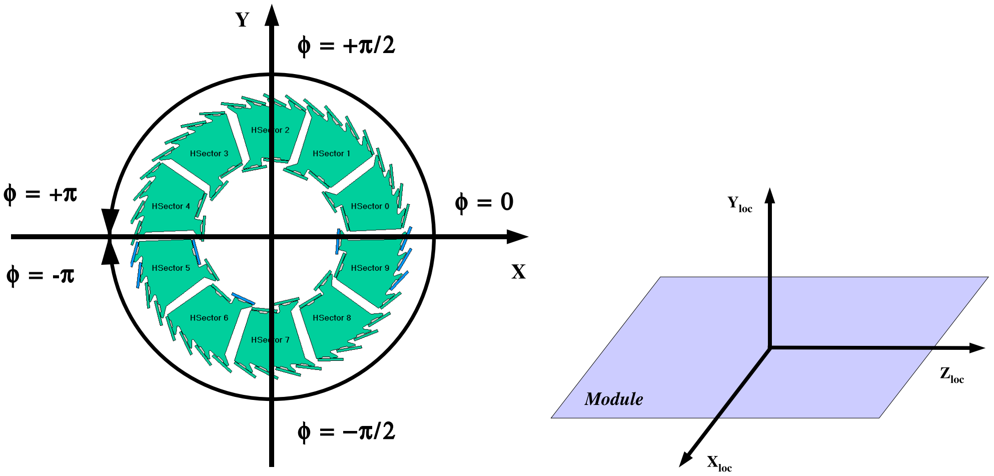

Figure 5.8: Left: *Global reference system of the ITS shown with the SPD. The X-axis points toward the inside of the LHC ring and the Z-axis is along the beam line.* Right: *Local reference system as seen from a sensitive module. The Z-axis is along the beam line and parallel to the global Z-axis.*

the module of the considered point. Since most of the tracks from cosmic rays will be almost parallel to the Y-axis, most of the clusters will be on the modules around $|\phi| \approx \pi/2$ (see Fig. 5.9). This means that, at least in the initial phase, the Y coordinate will not be an interesting observable since the most populated modules are the ones less sensitive to shifts in Y.

The extraction of the residual has been implemented in the AliITSResidualsAnalysis class in AliROOT. The class input is the file that contains the information of the tracks and their points (AliTrackPoints), from the standard reconstruction.

The three main parameters to set, for extraction of the residuals, are:

- the list of volumes that are to be used for refitting the tracks
- the list of volumes where the residuals are to be calculated
- the minimum number of points to use for refitting the tracks

Since there are 2198 selectable volumes, several methods for creating the lists of volumes from general criteria are provided. The most common selection criteria are:

- “SPD top half-barrel versus bottom half-barrel”. In this case the refitting is done using the points on the top Half-Barrel of the SPD and the residuals are extracted for the volumes in the lower Half-Barrel. This selection is most commonly used to check the internal realignment of the SPD.
- “SPD versus SSD”. In this case the refitting is done using the points in the SPD and the residuals are extracted for the volumes of the SSD. This selection is used, after the realignment of the SPD, to check the alignment of the SSD.
- “SPD and SSD versus SDD”. In this case the refitting is done using the points in the SPD and SSD. The residuals are extracted for the SDD. This selection is used for the time zero calibration of the SDD (see Sect. 5.2.2).

Another variable used to evaluate the quality of the alignment procedure is the so-called “track-to-track distance at Y = 0”, that is shown in the right panel of Fig. 5.7. A single track can be separated in two different tracks by fitting the points with $Y > 0$ (upper half) and the points with $Y < 0$ (bottom half). The distance, in X, of the two halves, measured in the plane with $Y = 0$, is the “track-to-track distance at Y = 0”.

5.2.2 ITS alignment monitoring results

Alignment of the SPD

The statistics of tracks from cosmic rays collected from June to October 2008 is of about 95,000 good events. Of which about 45,000 have 4 clusters in the SPD and 50,000 have 3 clusters in the SPD. Fig. 5.9 shows the distribution of the clusters in the transverse plane of the ITS for all events.

Fig. 5.10 shows the track to track distance in the $Y = 0$ plane for the SPD, before and after the Millepede realignment procedure, compared with the same results from simulated data with no misalignment. In the case of the cosmic data after the realignment the distribution can be fitted with a gaussian that has a standard deviation (“sigma”) of 56 μm. For the case of simulated data the distribution has a sigma of 43 μm. The expected value, for straight tracks passing close the centre of the SPD, for the spread of the distribution of the track-to-track distance is:

$$\sigma^2_{\Delta x} = 2\,\frac{(r^2_{SPDout} + r^2_{SPDin})}{(r_{SPDout} - r_{SPDin})^2}\,\sigma^2_{spatial}$$

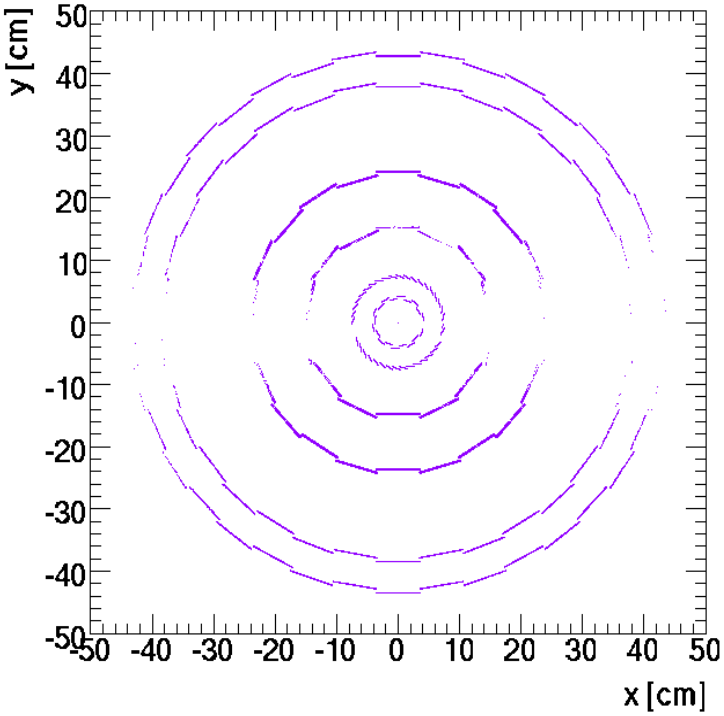

Figure 5.9: *Distribution of the clusters in the ITS, seen in the transverse plane, for the full cosmic run of 2008.*

Where $\sigma_{\Delta x}$ is the sigma of the distribution of the track-to-track distance at $Y = 0$, $\sigma_{spatial}$ is the spatial resolution of the detector, r_{SPDout} is the radius of the outer layer of the SPD and r_{SPDin} is the radius of the inner layer of the SPD. Thus a spatial resolution of 11 μm is obtained for the case of the simulated data. Since no misalignment was introduced in the simulation, this value reflects the intrinsic resolution of the detector (for the local X coordinate, 12 μm). For the real data, the spatial resolution is of 15 μm. This value has to be compared with the expected resolution for the residual misalignment, that is about 20% larger than the intrinsic resolution, about 14.4 μm. Therefore the Millepede procedure already realigns the SPD (in the local X coordinate) down to the level of the residual misalignment.

Since the detector is made of different and interconnected parts, the implementation of Millepede done by the ALICE Padova group follows a hierarchical procedure. The alignment procedure begins with the SPD following the order:

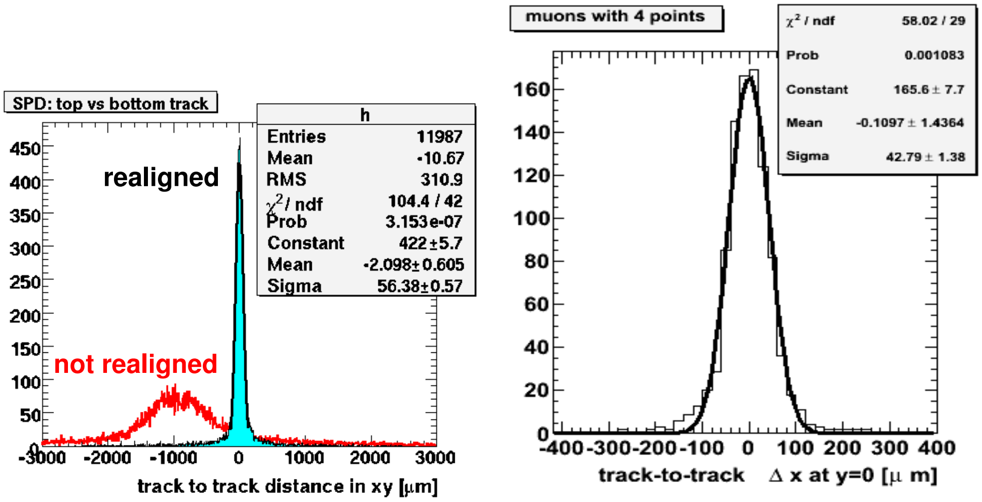

Figure 5.10: Left: *Track-to-track distance at* $Y = 0$*, for the SPD, before and after the Millepede realignment procedure.* Right: *Track-to-track distance at* $Y = 0$*, for the SPD, using simulated data with no misalignment.*

$Sectors \rightarrow Staves \rightarrow Half - Staves \rightarrow Ladders$ and then moves on to the SSD layers. It is interesting to check the track-to-track distance at $Y = 0$ after every step. This is shown in Fig. 5.11. The alignment of the sectors centres the distribution at zero. The single largest improvement comes with the alignment of the staves This means that the larges misalignments are at the level of the staves.

The track-to-point residuals were analysed using the residuals-based monitoring procedure described before. Fig. 5.12 shows the distributions of the the residuals in RPHI and global X for the bottom half of the SPD with the tracks re-fitted in the top half of the SPD. The structures in the residuals are due to the misalignment of the staves: every stave contributes differently to the distribution. Fig. 5.13 shows the same distributions after the Millepede realignment: they present a single peak with a sigma of ≈ 70 μm (for the residuals in X on the inner layer), depending on the range of the fit. This value is close to the expected value for the case of residual misalignment, ≈ 60 μm.

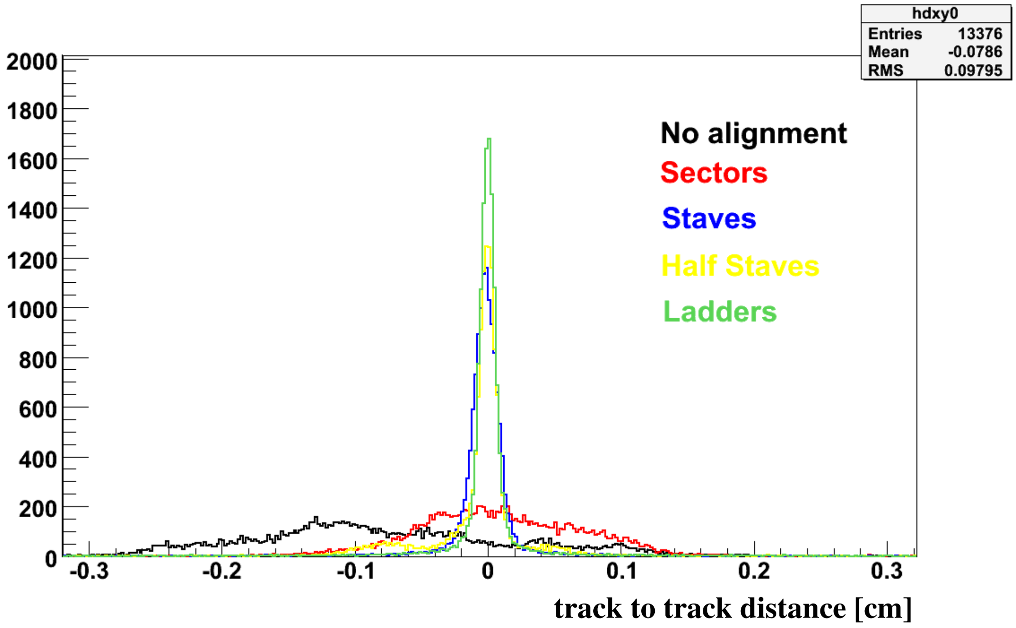

Figure 5.11: *Track-to-track distance at* $Y = 0$*, for the SPD, during the various steps of the Millepede realignment.*

Alignment of the SSD

To extract the residuals for the SSD, the tracks were fitted using the volumes of the SPD aligned with Millepede. Fig. 5.14 shows the results for the residuals in RPHI and X. The distribution before realignment presents a peculiar structure with two peaks in X and a single peak in RPHI . While the source of this feature is still under investigation, the important result is that Millepede is able to correctly account for the misalignment, as it can be seen from Fig. 5.15.

Time calibration of the SDD

The SDD uses the drift time to extract the local X coordinate of the cluster. While the drift velocity can be measured using the MOS injectors present on every SDD sensor (see Chapter 3, Section 3.1.2), the time offset, t_0 (which results from cable length, delays etc.), should be extracted from the reconstructed clusters. One possible method makes use of the residuals between the reconstructed track position and the cluster coordinates. One method to estimate the time offset is

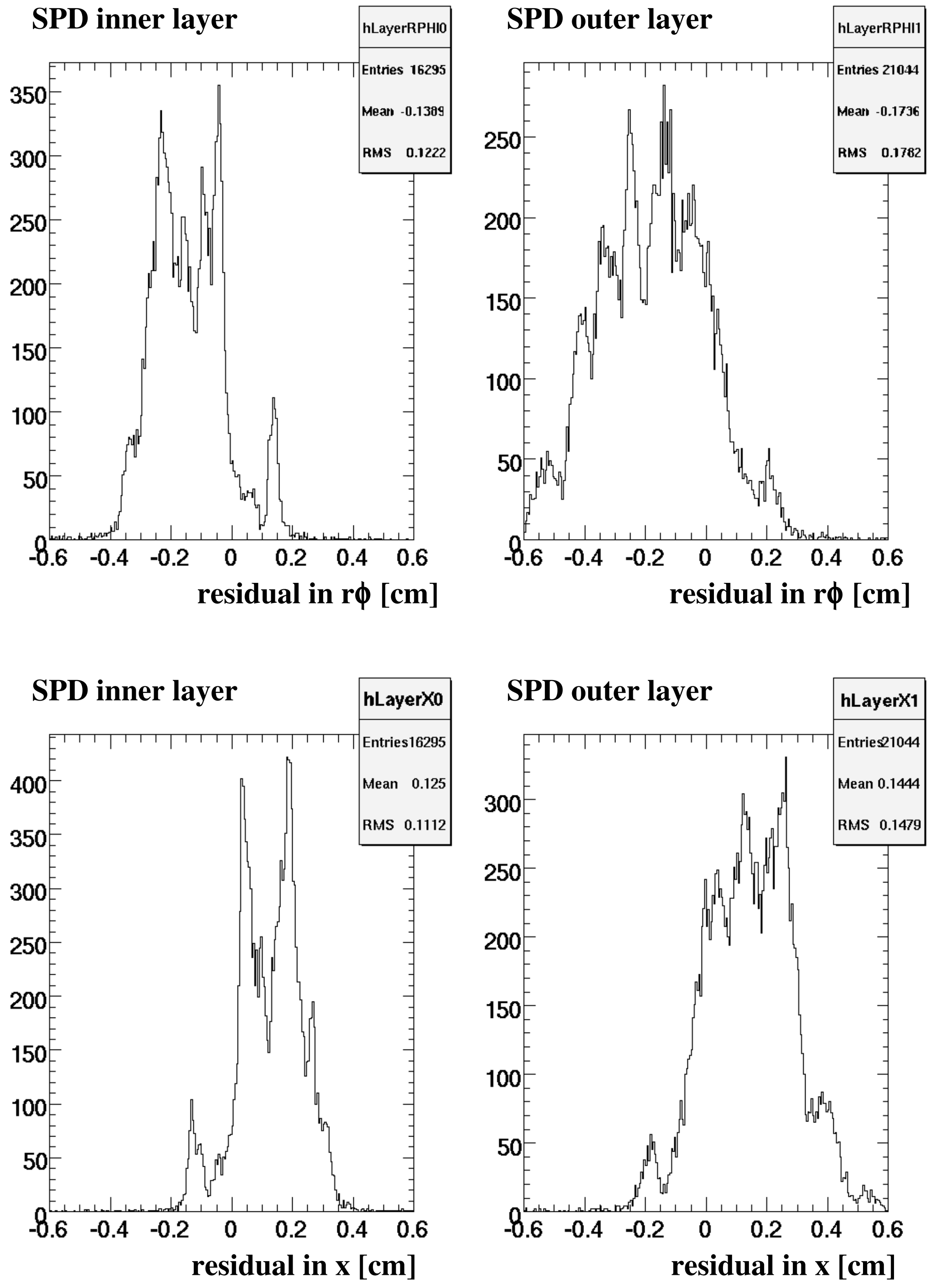

Figure 5.12: *Residuals for the SPD inner layer (left side) and outer layer (right side). The refitting was done using the top Half-Barrel of the SPD and the residuals are shown for the bottom Half-Barrel.*

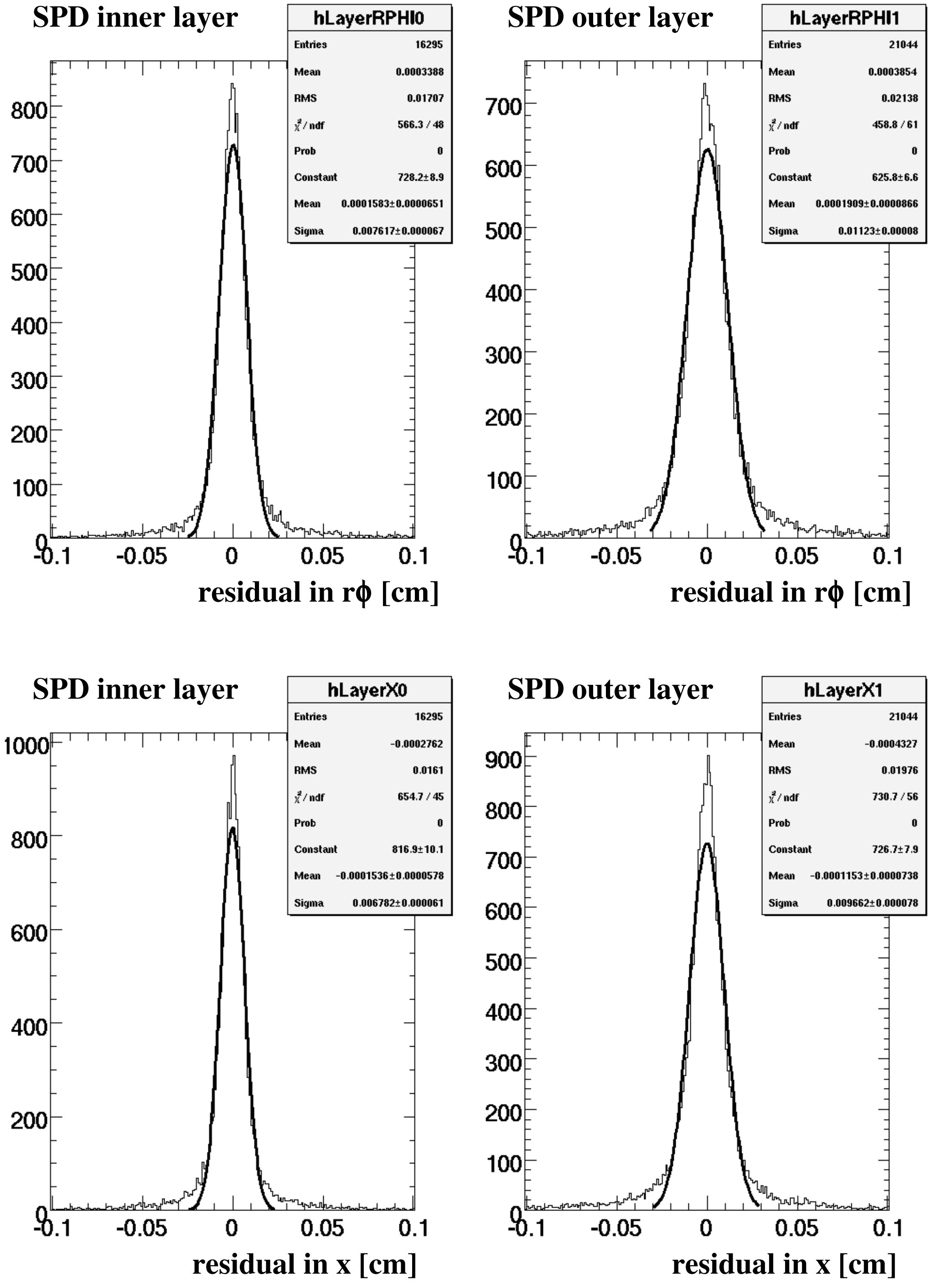

Figure 5.13: *Residuals for the SPD inner layer (left side) and outer layer (right side) after the realignment with Millepede. The refitting was done using the top Half-Barrel of the SPD and the residuals are shown for the bottom Half-Barrel.*

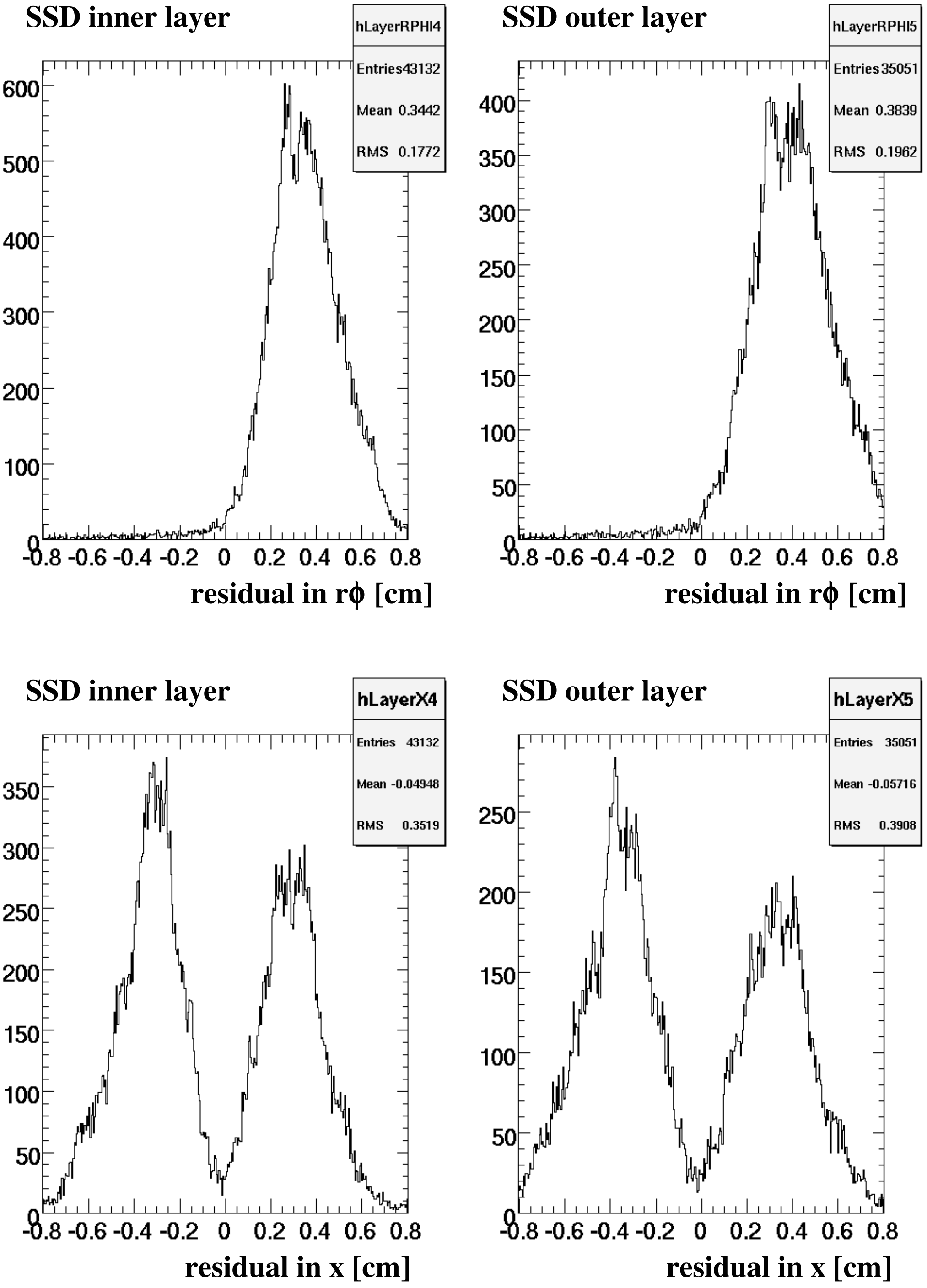

Figure 5.14: *Residuals for the SSD inner layer (left side) and outer layer (right side). The refitting was done using the clusters on the SPD and the residuals are shown for the SSD.*

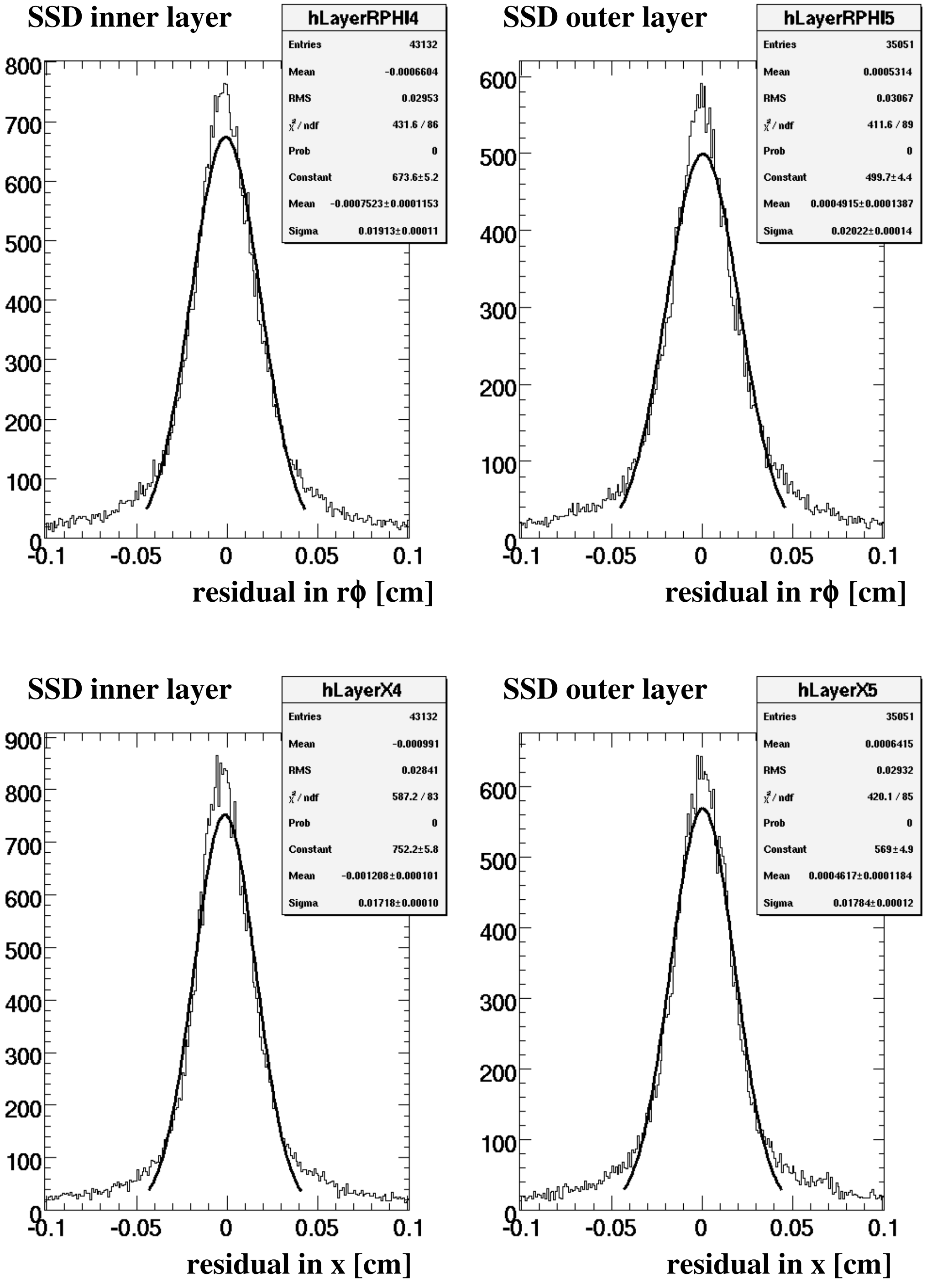

Figure 5.15: *Residuals for the SSD inner layer (left side) and outer layer (right side) after the realignment with Millepede. The refitting was done using the clusters on the SPD and the residuals are shown for the SSD.*

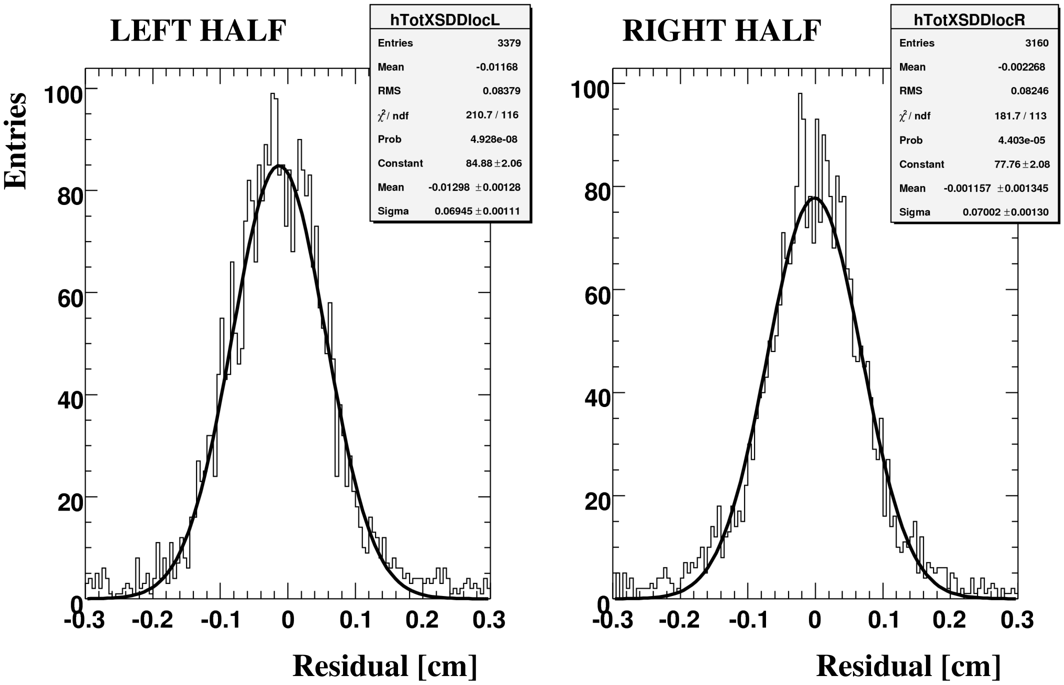

Figure 5.16: *Residual distributions (in local X) for the upper and lower halves of the SDD sensors (the results are for global* $Z > 0$ *only).*

using the residuals. As was shown in Chapter 3 (Fig. 3.6), the SDD is divided into two drift regions that are usually called "left half" ($X_{loc} > 0$) and "right half" ($X_{loc} < 0$). Since the electrons in the two halves drift in opposite directions, a miscalibration in the time measurement will introduce a shift of the peak of the residuals distribution equal and opposite signed in the two sides. By measuring the peak position in the two halves of each sensor one obtains:

$$\frac{\Delta X_{peak}}{2} = v_{drift}\, t_0 \qquad \Rightarrow \qquad t_0 = \frac{\Delta X_{peak}}{2\, v_{drift}}$$

where ΔX_{peak} is the difference between the peak positions of the distribution of the residuals in the two halves, v_{drift} is the drift velocity and t_0 is the time offset. The drift velocity is of the order of 6.6 μm/ns with significant differences between different modules due to several factors, among them geometrical position in the ITS, dopant concentration and temperature. This is the reason why, to extract the t_0, v_{drift} is measured on a module-by-module basis. Fig. 5.16 shows an example of this procedure. The residuals were obtained fitting the tracks with the points from the SPD and SSD. Both the SPD and SSD were realigned with Millepede. It can be seen that the sigma of the fits is quite large (700 μm), this is due not only to the geometrical misalignment but also to the way the tracks are triggered. Since the readout frequency of the Fast-OR of the SPD is 10 MHz, and this induces a time jitter of 100 ns. That, for a $v_{drift} \approx 6.6$ μm/ns, means a spread of 660 μm. The work on the SDD time calibration is presently in progress. For recent development refer to [177, 178].

Future perspectives

Since the present statistics collected from cosmic rays already allows to align the central part of the ITS, the next step would be to use proton–proton collisions. For the AliITSResidualsAnalysis framework this presents some difficulties. The first is that most of the proton–proton events will have the magnetic field turned on while the AliITSResidualsAnalysis framework was initially designed for straight tracks. The propagation and the extraction of the residuals for curved track has been successfully tested and it will be addressed in the next Section. The second problem is that a track from a proton–proton collision crosses the ITS in 6 points while a track from a cosmic event crosses the ITS in 12 points. This reduces the possible selections of the sets of volumes to fit the track (e.g. the case of "SPD top half-barrel versus bottom half-barrel"). Alternative solutions to give a full understanding of the alignment with tracks from proton–proton collisions are presently under investigation.

5.3 Results for cosmic runs with magnetic field

During the cosmic runs, about 1400 tracks were collected with the magnetic field from the central magnet turned on. Of these, 750 were with a field of +0.5 T and 710 with a field of −0.5 T. To check the results for the curved tracks several changes had to be made. The Kalman filter [179] fits to a straight line, so it cannot be used with curved tracks. The results were obtained using the Riemann fitter [180], which is the dedicated fitter for curved tracks. Since, in the transverse plane the track is a circle, at least three volumes must be be used to fit the track.

In the procedure used to test the AliITSResidualsAnalysis framework, the following configuration was used: the SSD and the outer layer of the SPD to fit

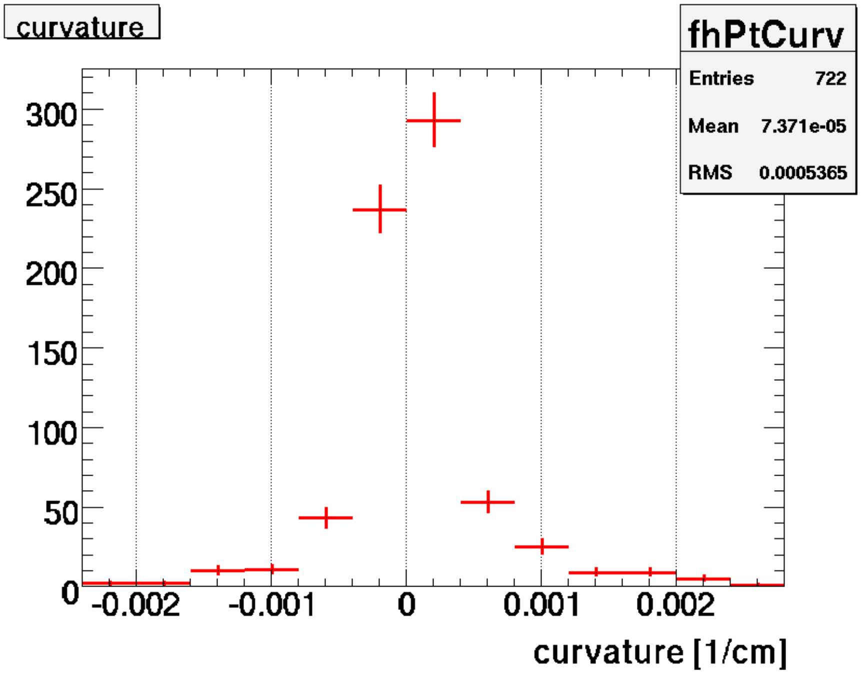

Figure 5.17: *Distribution of track curvature for the events with* $B = +0.5$ T*.*

the tracks and the inner layer of the SPD to extract the residuals, or the SSD and the inner layer of the SPD to fit the tracks and the outer layer of the SPD to extract the residuals. At least 4 points were required in the fit.

In the case of no magnetic field, the sigma of the residuals distribution is of 20 μm and 26 μm for residuals in X and RPHI, respectively. In the case of $B = +0.5$ T, the sigma of the residuals distribution is of 21 μm and 26 μm for residuals in X and RPHI, respectively. This allows to conclude that the AliITSResidualsAnalysis can handle curved tracks and that the magnetic field does not introduce additional misalignments (for a more detailed discussion see [181]).

Since the AliITSResidualsAnalysis is able to calculate the residuals with curved tracks, it is also possible to extract the curvature from the tracks. This is shown in Fig. 5.17. As expected for muons from cosmic rays (i.e. from the interaction of a proton), the number of positive charged tracks is larger than the number of negative charged tracks. Knowing the magnetic field, from the curvature can be deduced the distribution in transverse momentum. This is shown in Fig. 5.18 for positive and negative tracks. For comparison, Fig. 5.19 shows the same distribu-

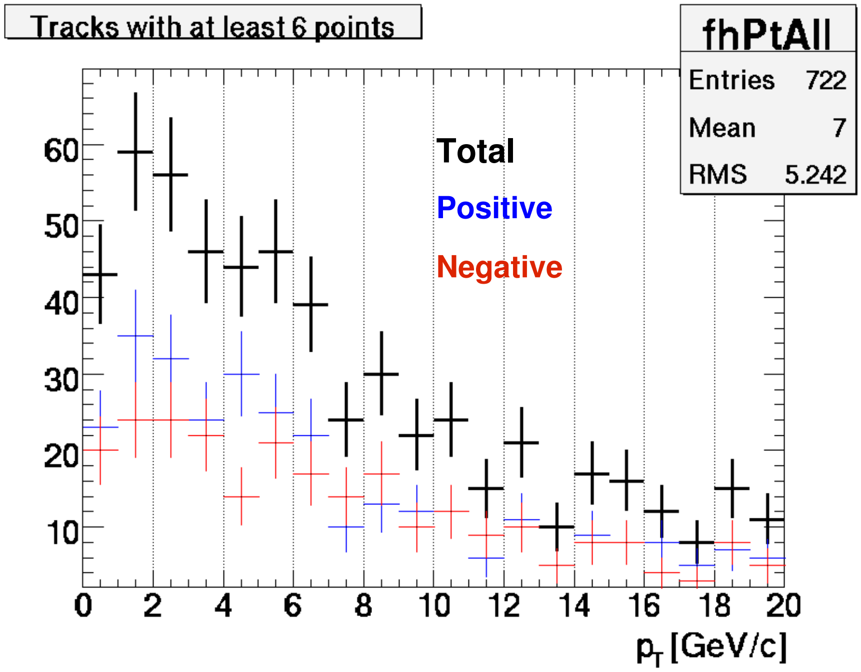

Figure 5.18: *Distribution in p_t of positive (blue), negative (red) and total (black) cosmic tracks for the events with $B = +0.5$ T in the ITS.*

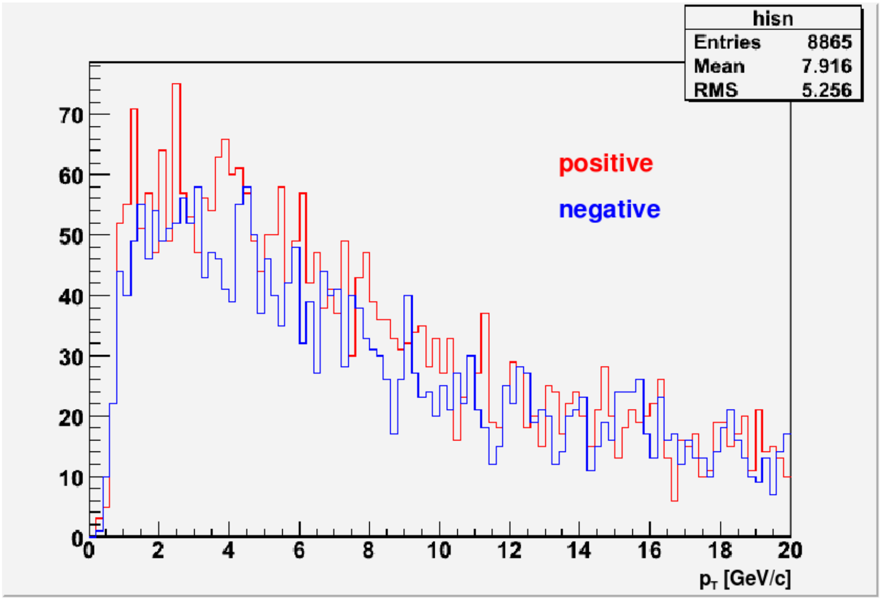

Figure 5.19: *Distribution in p_t of positive (red), negative (blue) cosmic tracks for the events with $B = +0.5$ T in the TPC. Taken from [182]*

tions obtained using the TPC. Fig. 5.20 shows the ratio. positive over negative tracks, as a function of the transverse momentum for the case of $B = +0.5$ T and Fig. 5.20 shows the same result for the case of $B = -0.5$ T. Combining the whole statistics a ratio of 1.11 ± 0.07 was obtained. This is compatible with the result obtained with the TPC (≈ 1.18).

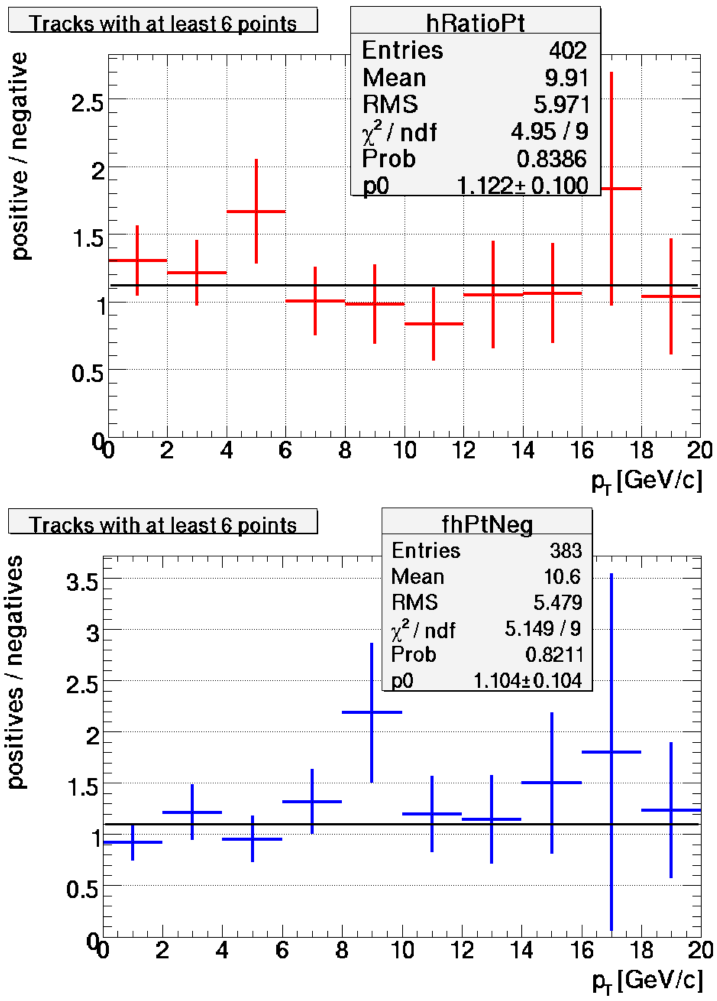

Figure 5.20: *Ratio of positive over negative tracks as a function of the transverse momentum for events with* $B = +0.5$ T *(top panel) and* $B = -0.5$ T *(bottom panel).*

Chapter 6

Beauty production measurement in the semi-electronic channel

In this Chapter a method for the extraction of the beauty cross section using electrons with a displacement from the primary vertex will be outlined. The idea is to use the good impact parameter resolution (provided by the ITS) and particle identification (provided by the TPC and the TRD) to separate the electrons coming from beauty semi-electronic decays from electrons coming from charm decays and other background electrons. The results will be shown for proton–proton and central Pb–Pb collisions. Moreover, for the case of proton–proton collisions the perspectives for the measurement in the first runs will also be discussed.

Since in the first runs the presence of the full TRD might be an issue (the expected number of TRD super modules for the 2009 run is of 8 over a total of 18), the possibility of using the same strategy but with particle identification from the TPC only has been explored. To make this approach feasible, the cuts in impact parameter and specific energy loss ($\mathrm{d}E/\mathrm{d}x$) have been optimised simultaneously.

The misalignment of the ITS (and more precisely, of the SPD) will play a critical role on the ability to reach the nominal resolution on the impact parameter. Since this is a crucial element for the beauty detection strategy, the impact of misalignment on the experimental errors for the extraction of the beauty cross section in proton–proton collisions will also be evaluated. On a side note, the first proton–proton collisions in 2009 will most probably be at a centre-of-mass energy of 10 TeV instead of the 14 TeV used for the results presented here.

The v_2 is an interesting experimental probe that provides information about the thermalization of the medium created in non-central Pb–Pb collisions. Given the interest on v_2, an estimate of the experimental error on the beauty v_2 was obtained using a simple "first approach" method. The results make use of the simulation done for the central $(0-5\%)$ Pb–Pb collisions rescaled to non-central $(20-60\%)$ collisions.

The BDMPS model for the partonic energy loss predicts a mass dependence due to the dead cone effect. The idea is that a parton travelling trough a dense medium loses energy by "emitting" gluons. However the gluon emission is suppressed, due to a quantum interference effect, in a cone around the forward direction with an angle $\Theta \approx \frac{m}{E}$ (where m and E are the mass and the energy of parton). This effect can be quite sizable for b quarks (given their large mass of about 5GeV/c).

Combining the results for proton–proton and Pb–Pb collisions, it is possible to evaluate the experimental error on the measurement of the nuclear modification factor for beauty. Moreover, using this estimate for the beauty R_{AA} together with similar results for the charm R_{AA} (e.g. [106]), it is possible to evaluate the experimental error on the ratio of the nuclear modification factors of beauty over charm ($R_{\mathrm{B/D}}$). The $R_{\mathrm{B/D}}$ has been shown (e.g. [71]) to be quite sensitive to the mass dependence of partonic energy loss.

6.1 Measurement of the beauty cross section

The simulation used in these studies were done using the AliROOT framework [186], PYTHIA [187] Monte Carlo generator, retuned on the MNR results [100] and HIJING [188] as a Monte Carlo generator for the Pb–Pb collisions. For the proton–proton case, the samples generated were equivalent to 5.4×10^8 proton–proton events with a $\mathrm{b\overline{b}}$ pair and 4.6×10^7 proton–proton events with a $\mathrm{c\overline{c}}$ pair. For the background, a sample of 6×10^6 minimum–bias proton–proton collisions at $\sqrt{s} = 14$ TeV was used. For the Pb–Pb case, 1.3×10^7 electrons from beauty decays (equivalent to about 7×10^6 Pb–Pb events) and 1.5×10^8 electrons from charm decays (equivalent to about 8×10^6 Pb–Pb events) were generated. For the non-charm background was generated a sample of 2×10^4 central Pb–Pb collisions at $\sqrt{s_{\mathrm{NN}}} = 5.5$ TeV using HIJING. To speed up the simulation process, a parametrised response of the TPC was used. Fig. 6.1 summarises the sources of electron "signals" for a proton–proton collision. Event reconstruction was performed using the standard Kalman filter tracking, tracks were required to have a point in each of the six ITS layers. The magnetic field was set to 0.4 T. For the

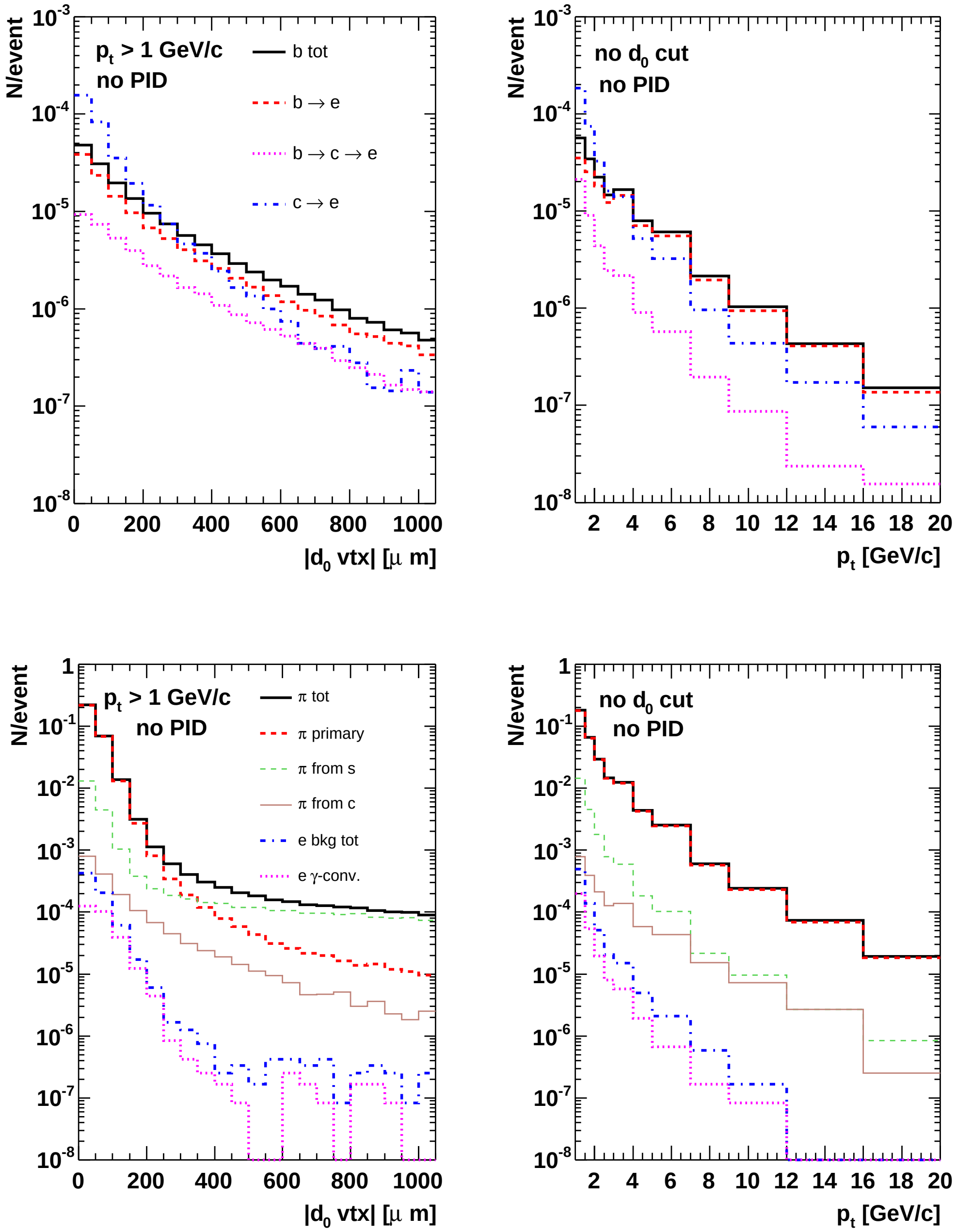

Figure 6.1: *Beauty and charm decay electrons (top), electrons from other sources and charged pions (bottom), as a function of* $|d_0|$ *(left) and* p_t *(right). The distributions are shown without any particle identification. In addition the distributions in* $|d_0|$ *are shown for* $p_t > 1$ GeV/c. *The plots are shown for the case of proton–proton collisions at 14* TeV.

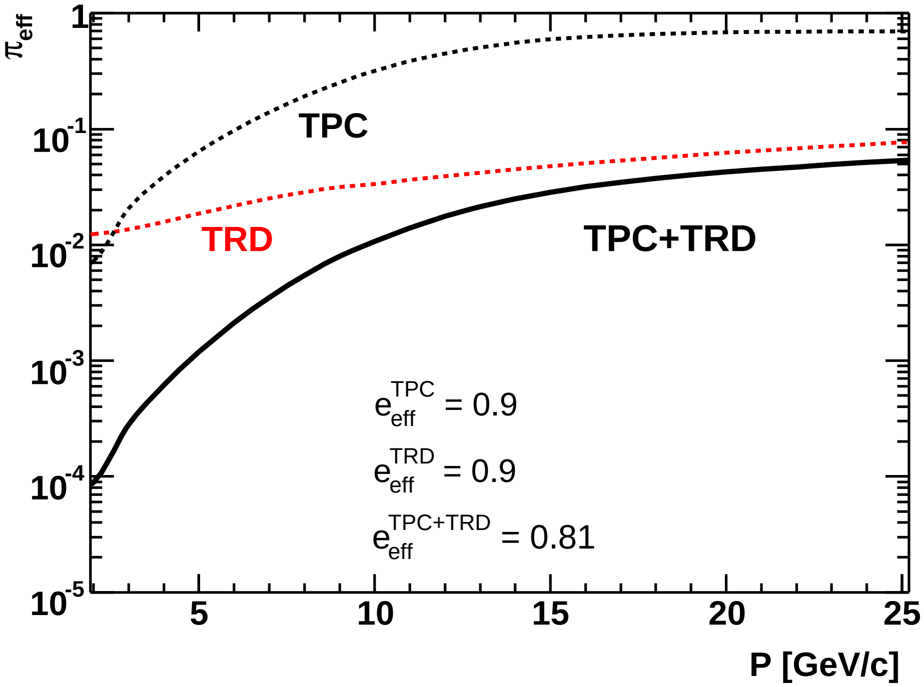

Figure 6.2: *Probability π_{eff} to misidentify a charged pion as electron, as a function of the momentum, with TRD only (red dotted line), with TPC only (black dotted line) and combining TPC and TRD (black solid line). PID cuts are set such that the probability e_{eff} for correct electron identification is* 90% *in each of the two detectors.*

data, the magnetic field will be set at 0.5 T. For the The detection strategy is based on three steps:

- *Electrons Identification*
  The PID strategy relies on a combined TPC-TRD technique. As shown in the TRD Technical Design Report [123] for $\mathrm{d}N_{\mathrm{ch}}/\mathrm{d}y = 6000$, is observed that, for an efficiency of electron identification $e_{\mathrm{eff}}^{\mathrm{TRD}} \simeq 0.90$, a contamination from pions $\pi_{\mathrm{eff}}^{\mathrm{TRD}} \sim 10^{-2}$ was expected at low momentum. These values were estimated from early beam tests.

- *Impact Parameter Cut*
  Beauty mesons are characterised by their large mean proper decay length

(of the order of 500 μm). This translates into a similarly large impact parameter for their decay electrons. Therefore, a cut on the minimum value of (projection of the impact parameter on the transverse plane) allows to reject a large part of the background electrons. Electrons from charm mesons, however, can also have rather large impact parameters.

- *Background subtraction*
  After the PID and the impact parameter cut the leftover background, estimated from charm and pion measurements, is subtracted.

6.1.1 Electrons identification efficiency

Electrons can be efficiently separated by combining the PID capabilities of the TPC, based on specific energy loss ($\mathrm{d}E/\mathrm{d}x$) and of the TRD, specifically devoted to electron identification via the transition radiation technique. Fig. 6.2 summarises the efficiency for pions and electrons given by the TPC alone, the TRD alone and the combined TPC and TRD, as a function of the momentum. Using the $\mathrm{d}E/\mathrm{d}x$ information from the TPC, the probability of pion misidentification is reduced by a factor $\approx 10^2$ at low momentum. As the momentum increases and charged pions approach the Fermi plateau in $\mathrm{d}E/\mathrm{d}x$, the additional pion rejection from the TPC decreases and becomes marginal at $p_\mathrm{t} \approx 10$ GeV/c. Combining the TPC and TRD capabilities, the pion contamination can be reduced by a factor $\approx 10^4$, at low momentum, and ≈ 20 at high momentum.

6.1.2 Selection of the impact parameter cut

After the electron identification, a p_t-dependent impact parameter cut is applied. For a given electron p_t interval, the value of the d_0 cut has been optimised in order to minimise the total error (statistical and systematic) on the number of beauty-decay electrons in the interval. The extraction of the electron-level cross section and the resulting errors are described in the following.

Extraction of the electron-level cross section

In a given p_t-bin, the number N of counted "electrons", is the sum of different contributions: $N = N_b$ (beauty) + N_c (charm) + N_{bkg} (bkg. e and misid. π). The cross section is obtained by the following procedure:

Table 6.1: *Selected cuts, in* $|d_0|^{MIN}$, *for proton–proton and central Pb–Pb collisions.*

p_{t} bin [GeV/c]	$|d_0|^{MIN}_{pp}$ [μm]	$|d_0|^{MIN}_{PbPb}$ [μm]
1.0-1.5	400	200
1.5-2.0	400	200
2.0-2.5	300	200
2.5-3.0	200	200
3.0-4.0	150	200
4.0-5.0	150	200
5.0-7.0	100	200
7.0-9.0	100	200
9.0-12.0	100	200
12.0-16.0	50	200
16.0-20.0	50	200

1. Subtraction of charm decay electrons, $N - N_c$. To estimate the charm contribution (N_c) will be used the cross section for D^0 mesons, measured in ALICE by reconstructing D^0 [192, 193] and D^+ [194] mesons.

2. Subtraction of the remaining background electrons and misidentified pions, $N - N_c - N_{bkg}$. The background contribution (N_{bkg}) will be estimated on the basis of a Monte Carlo simulation tuned on the measured light-flavour hadron production.

3. Correction of the number of beauty electrons for efficiency (tracking, electron identification, d_0 cut) and acceptance, $dN_b^{corr}/dy = (N - N_c - N_{bkg})/\epsilon$. The correction will be done via Monte Carlo techniques.

4. Normalisation of the corrected yield to the inelastic cross section, $d\sigma^{efromb}/dy = \sigma^{inel} \cdot dN_b^{ecorr}/dy$.

Experimental uncertainties

Each step of the outlined procedure introduces an error contribution.

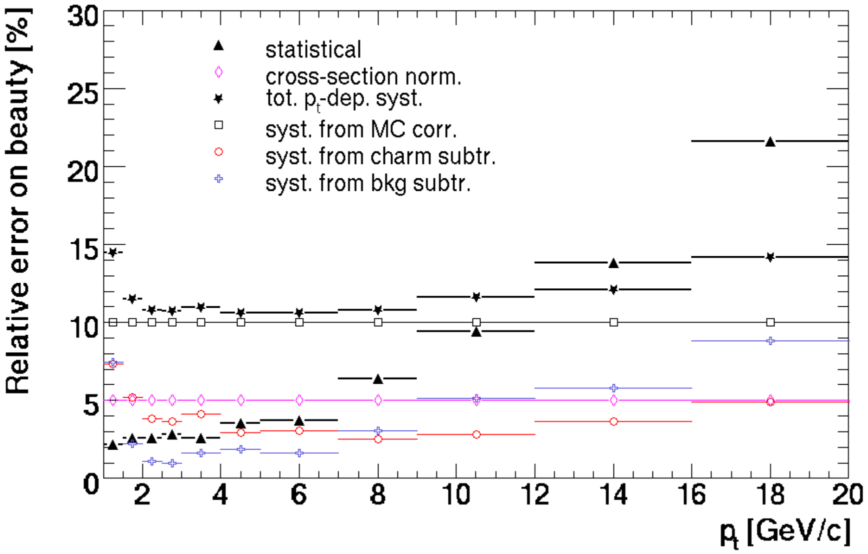

Figure 6.3: *Summary of the sources of errors as a function of* p_{t}*. The calculation are made assuming a statistics of* 10^9 *proton–proton events.*

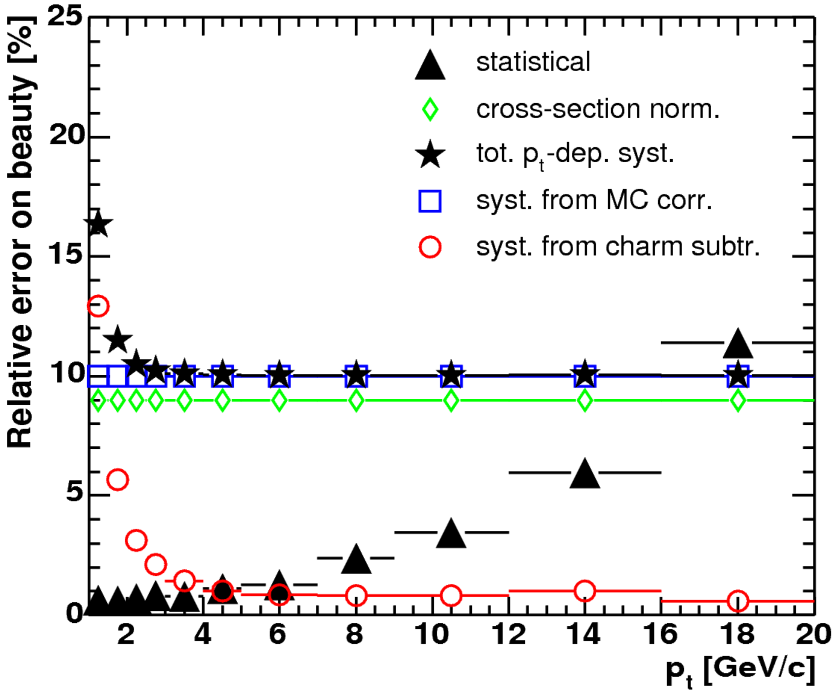

Figure 6.4: *Summary of the sources of errors as a function of* p_{t}*. The calculation are made assuming a statistics of* 10^7 *Pb–Pb events.*

- Statistical error. For a given p_{t}-bin with N_b electrons from beauty, N_c electrons from charm, N_{bkg} electrons from background, the relative statistical error on the beauty signal (N_b), after the subtractions in step 1 and 2, is:

$$\frac{\delta N_b}{N_b} = \frac{\sqrt{N_b + N_c + N_{bkg}}}{N_b} \, . \tag{6.1}$$

- Systematic error from Monte Carlo corrections. The error from Monte Carlo corrections was assumed to be 10% over the whole p_{t} range, although it is, in principle, p_{t}-dependent.

- Systematic error from uncertainties on charm and background subtractions. Once the relative errors on charm and background are known the two contributions to the final relative error are proportional to the fraction of charm/beauty and background/beauty, respectively:

$$\frac{\delta N_b}{N_b} = \sqrt{\left(\frac{\delta N_c}{N_c}\frac{N_c}{N_b}\right)^2 + \left(\frac{\delta N_{bkg}}{N_{bkg}}\frac{N_{bkg}}{N_b}\right)^2} \, . \tag{6.2}$$

  For a detailed description of the extraction of δN_c and δN_{bkg} can be found in [106].

- Systematic error on the inelastic cross section. A 5% error is expected on the measurement of the proton–proton inelastic cross section and a 9% error is expected on the measurement of the Pb–Pb inelastic cross section at LHC [107].

6.1.3 Beauty electrons cross section

Fig. 6.3 shows the summary of the expected errors on the measurement of the beauty decay electrons after the cuts, as measurable with a statistics of 10^9 proton–proton events. Fig. 6.4 shows the same result for 10^7 Pb–Pb events. The results for Pb–Pb events were obtained with the same strategy, optimised for the high-multiplicity environment of the Pb–Pb events. For each p_{t}-bin, the cut in impact parameter ($|d_0^{MIN}|$) that minimises the quadratic sum of statistic and systematic error was selected. In the lower p_{t}-bins the systematic error dominates, because such regions are dominated by electrons from charm decays and background, therefore enhancing the systematic contribution from charm and background subtraction. The result is that, at low p_{t}, the systematic error imposes

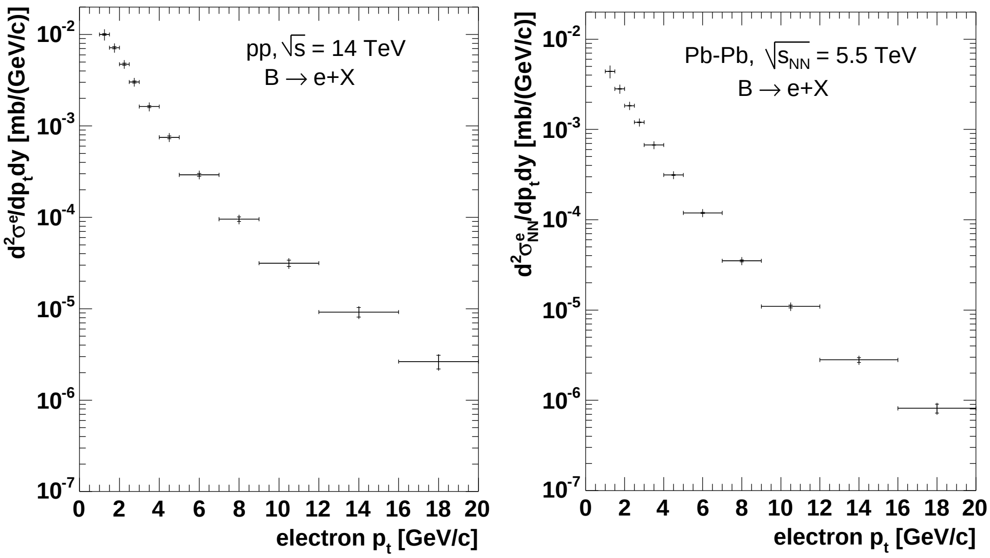

Figure 6.5: *Cross section for beauty electrons for proton–proton collisions (left) and Pb–Pb collisions (right). Statistical errors (inner bars) and quadratic sum of statistical and* p_t*-dependent systematic errors (outer bars) are shown.*

the value of $|d_0^{MIN}|$. In the higher p_t-bins the statistical error dominates because of the low number of electrons in such regions. The result is that, at high p_t, the statistical error impose the value of $|d_0^{MIN}|$. The summary of the selected cuts for proton–proton and Pb–Pb collisions is shown in Tab. 6.1. For the moment, the optimisation of the $|d_0^{MIN}|$ cut, according to the transverse momentum, was done only for the proton–proton. For the Pb–Pb case an average value of 200 μm was used.

Fig. 6.5 shows the cross section for electrons from beauty decays for 14 TeV proton–proton collisions (left) and 5.5 TeV Pb–Pb collisions (right) as obtained with this strategy.

6.1.4 Beauty mesons cross section in proton–proton collisions

The beauty cross section in proton–proton collisions at 14 TeV is a stringent test of pQCD. To compare the results of this study with the theoretical prediction, the cross section for beauty mesons is needed.

To extract the p_{t}^{min} differential cross section for beauty mesons, $\mathrm{d}\sigma^{B}(p_{\mathrm{t}} > p_{\mathrm{t}}^{min})/\mathrm{d}y$, from the electrons cross section a method similar to that developed by UA1 Collaboration [189] was used. The method, described in detail in Ref. [106, 190], is based on Monte Carlo simulation and it relies on the fact that the B meson decay kinematics, measured and studied in several experiments is well understood. It has been shown [190] (for the Pb–Pb case) that the systematic error introduced by this method is negligible with respect to the systematic uncertainties already present at the electron level. Fig. 6.6 presents the expected ALICE performance for the measurement of the p_{t}^{min}-differential cross section of B mesons, $\mathrm{d}\sigma^{B}(p_{\mathrm{t}} > p_{\mathrm{t}}^{min})/\mathrm{d}y$ vs. p_{t}^{min} averaged in the range $|y| < 0$. To illustrate the sensitivity compared to pQCD calculations, Fig. 6.6 reports the prediction and the uncertainty bands for three theoretical approaches: the collinearly-factorised FONLO (the baseline for this study), as implemented in the HVQMNR code [100], the FONLL [101] and the k_t-factorisation, as implemented in the CASCADE code [191]. It can be seen that the expected ALICE performance for 10^9 proton–proton events will provide a meaningful comparison with pQCD predictions.

Fig. 6.7 shows a comparison between the statistical error for the beauty cross section and the theoretical uncertainties, using different scenarios of statistic. One full ALICE nominal year of proton–proton collisions with the full detector set-up was estimated to correspond to 1×10^9 events [107] (black stars in the plot). One nominal month with the full detector corresponds to an equivalent statistic of 5×10^7 (blue squares). One nominal month with the expected TRD set-up for 2009 (8 modules out of 18) corresponds to an equivalent statistic of 2×10^7 (grey triangles). From the plot it can be seen that, even with less than the full nominal statistics, a meaningful comparison between the theory and ALICE experimental results is possible, even if in a smaller range of p_{t}^{min}.

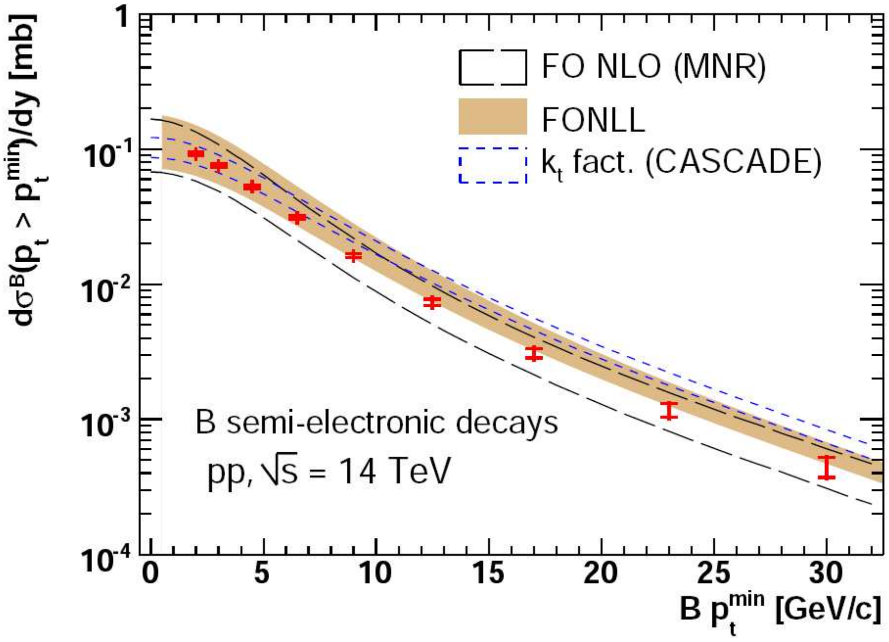

Figure 6.6: *Differential cross section for B mesons per proton–proton collision. Statistical errors (inner bars) and quadratic sum of statistical and* p_t*-dependent systematic errors (outer bars) are shown. The 5% normalisation error is not shown.*

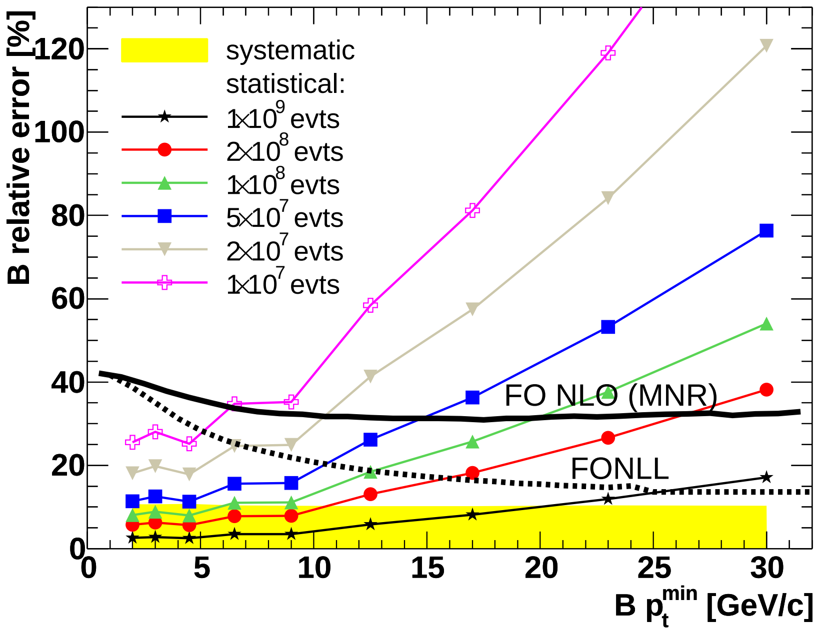

Figure 6.7: *Comparison between the statistical relative error on beauty hadron cross section as a function of* p_t^{min} *in different scenarios of statistics and theoretical uncertainties for FONLL and FONLO calculation. For more details on the different scenarios, see text.*

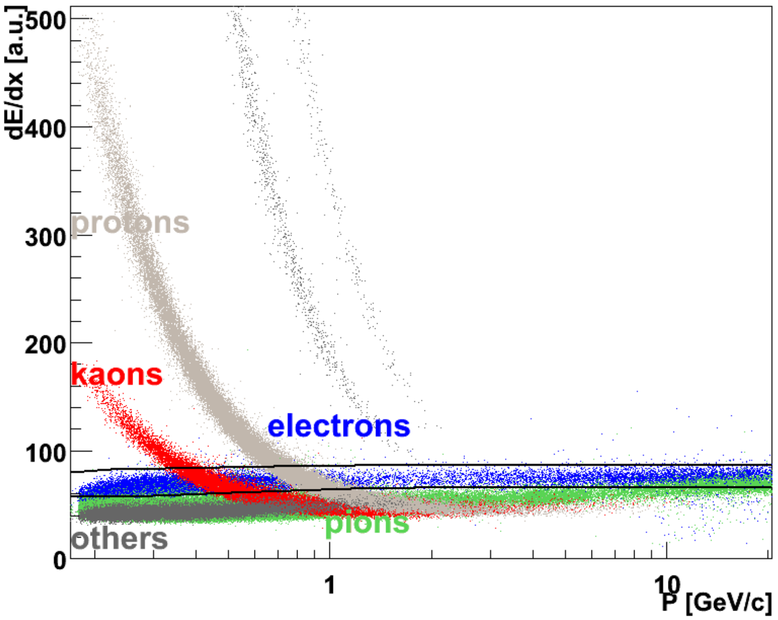

Figure 6.8: dE/dx *distributions in transverse momentum for different particles as measurable by the TPC.*

6.1.5 Cross section results with ITS+TPC only

The azimuthal angle coverage of the TRD for the 2009 runs will likely be 8/18. Therefore, to be able to use the full statistics a method to separate electrons from pions (the largest contribution to background) without the TPC was developed. The method relies on the simultaneous optimisation of the cut in $|d_0|$ and in the dE/dx value measured by the TPC. With the full central barrel set-up the particles are tracked from the TPC toward the ITS and then refitted from the ITS to the TRD. The track matching procedure between the TRD and the TPC has an efficiency of about 70% [107]. Using only TPC and ITS, the particles are tracked from the TPC to the ITS (and back). This means an increase in the statistics of about 30% that translates into a lower statistical error (about 15% less w.r.t the ITS+TPC+TRD case, see Eq. 6.1).

The original simulations (shown in Fig 6.1) were done with a parametrised particle identification. Since for this study a complete simulation of the TPC response was needed, the following strategy was used:

- A simulation with a fixed amount of electrons and charged pions was carried out. The simulation used a flat distribution in p_{t}.
- For each p_{t}-bin the distributions of electrons and pions in $\mathrm{d}E/\mathrm{d}x$ were rescaled according to the distributions shown in Fig. 6.1, in order to obtain the "correct" amount of pions and electrons.
- The N_b, N_c and N_{bkg} in Eq. 6.1 and 6.2 were drawn as functions of the cut in impact parameter ($|d_0|^{MIN}$) and of the cut in energy loss ($\mathrm{d}E/\mathrm{d}x^{MIN}$).
- Using the distributions of N_b, N_c and N_{bkg}, for every p_{t}-bin, the pair of cuts ($|d_0|^{MIN}$, $\mathrm{d}E/\mathrm{d}x^{MIN}$) that minimise the total error was chosen. An example for the 7.0-9.0 GeV/c p_{t}-bin is shown in Fig. 6.9.

Fig. 6.8 shows the $\mathrm{d}E/\mathrm{d}x$ in transverse momentum as measurable by the TPC. In Tab. 6.2 the chosen cuts for the $|d_0|$ and $\mathrm{d}E/\mathrm{d}x$ according to the p_{t}-bin are summarised. Fig. 6.10 shows the result for the various contributions to the relative error on beauty cross section using this set of cuts. While this is just a simple estimate, it seems to indicate that a measurement without the TRD is possible in the p_{t} range of $1.0 - 10.0$ GeV/c.

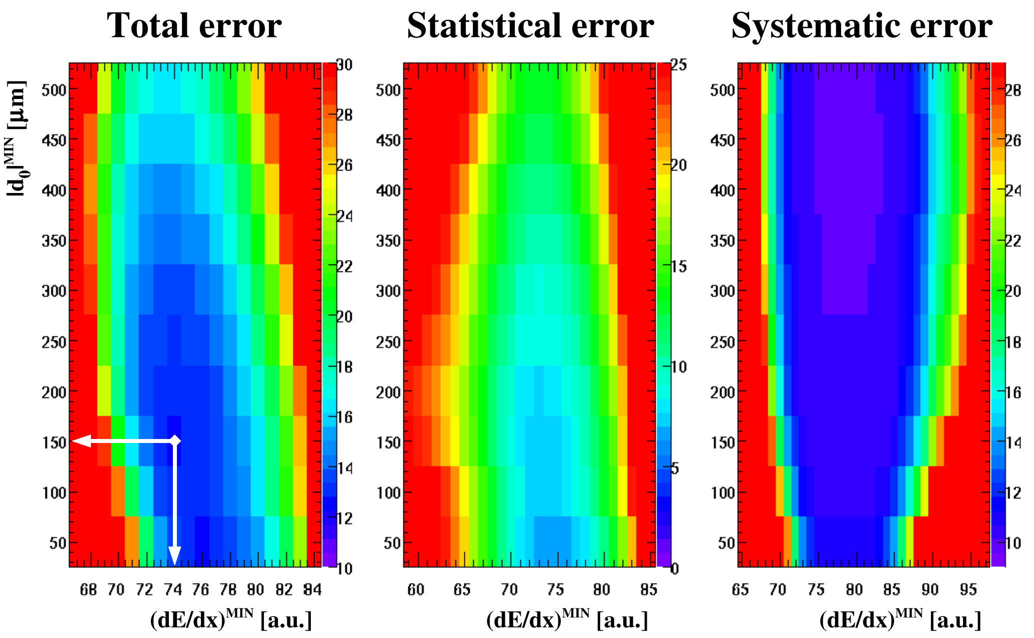

Figure 6.9: *Total, statistical and systematic relative error on the beauty electrons cross section for the* $7.0-9.0$ GeV/c p_t*-bin. The white arrows indicate the selected cuts for* $|d_0|^{MIN}$ *and* dE/dx^{MIN}.

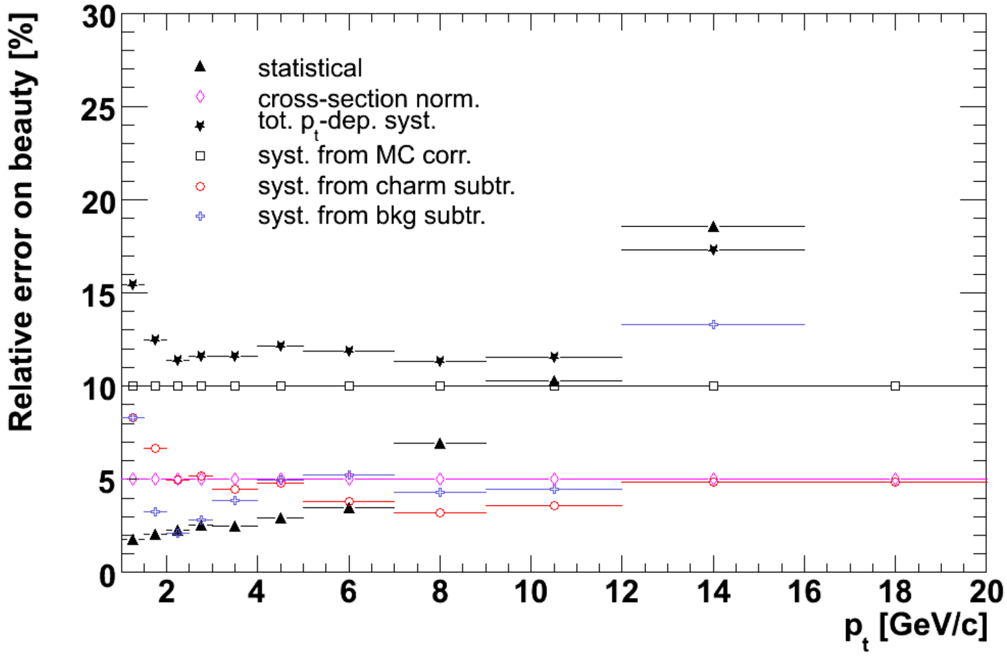

Figure 6.10: *Summary of the error contributions as a function of* p_t*. It is assumed a statistic of* 10^9 *proton–proton events and no TRD. The errors in the last* p_t*-bin are not shown since they are well above 50%.*

Table 6.2: *Selected cuts in impact parameter for the case of particle identification without the TRD.*

p_{t} bin [GeV/c]	$\vert d_0\vert^{MIN}$ [μm]	dE/dx^{MIN} [a.u.]
1.0-1.5	450	73
1.5-2.0	300	69
2.0-2.5	200	72
2.5-3.0	150	72
3.0-4.0	150	72
4.0-5.0	50	73
5.0-7.0	100	74
7.0-9.0	150	74
9.0-12.0	50	76
12.0-16.0	150	76
16.0-20.0	150	65

6.1.6 Cross section results including the expected misalignment

The results from the previous study were obtained using the ideal geometry (i.e. without misalignment). As it has been discussed in the previous chapters, this is not a realistic assumption.

To estimate the effect of the misalignment, the simulations shown in Fig. 6.1 were used with a Gaussian smearing applied "a posteriori" on the track impact parameter in order to reflect the estimated impact parameter resolution for the cases of "residual" and "full" misalignment (see Fig. 5.5 in Chapter 5).

Fig. 6.11 and 6.12 show the distributions in impact parameter of the electron signal for the different misalignment scenarios (for the p_{t} bin $5-7$ GeV/c). It can be seen that the misalignment introduces a smearing of the distributions. Since most of the statistics is at low values of impact parameter, the smearing translates into a broadening of the d_0 distribution. This in turn alters the fraction of charm over beauty (N_c/N_b) and of background over beauty (N_{bkg}/N_b), increasing them as more charm and background electrons pass the cut and reducing them when more beauty electrons pass the cut. Since the errors depend, on such fractions

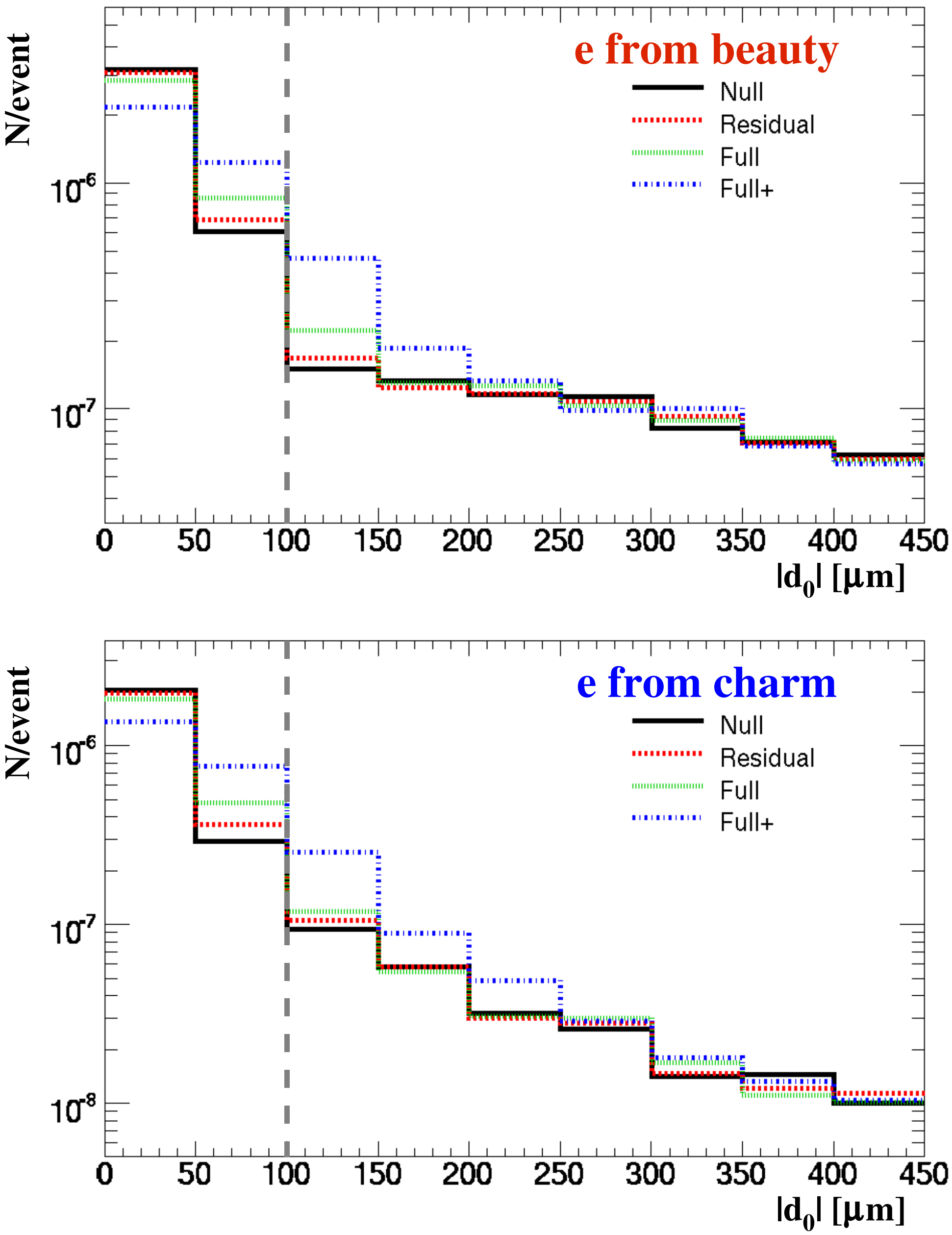

Figure 6.11: *Distributions in* $|d_0|$ *for different scenarios of misalignment* ($5 < p_{\mathrm{t}} < 7$ GeV/c)*. The vertical grey dotted line indicates the cut in impact parameter.*

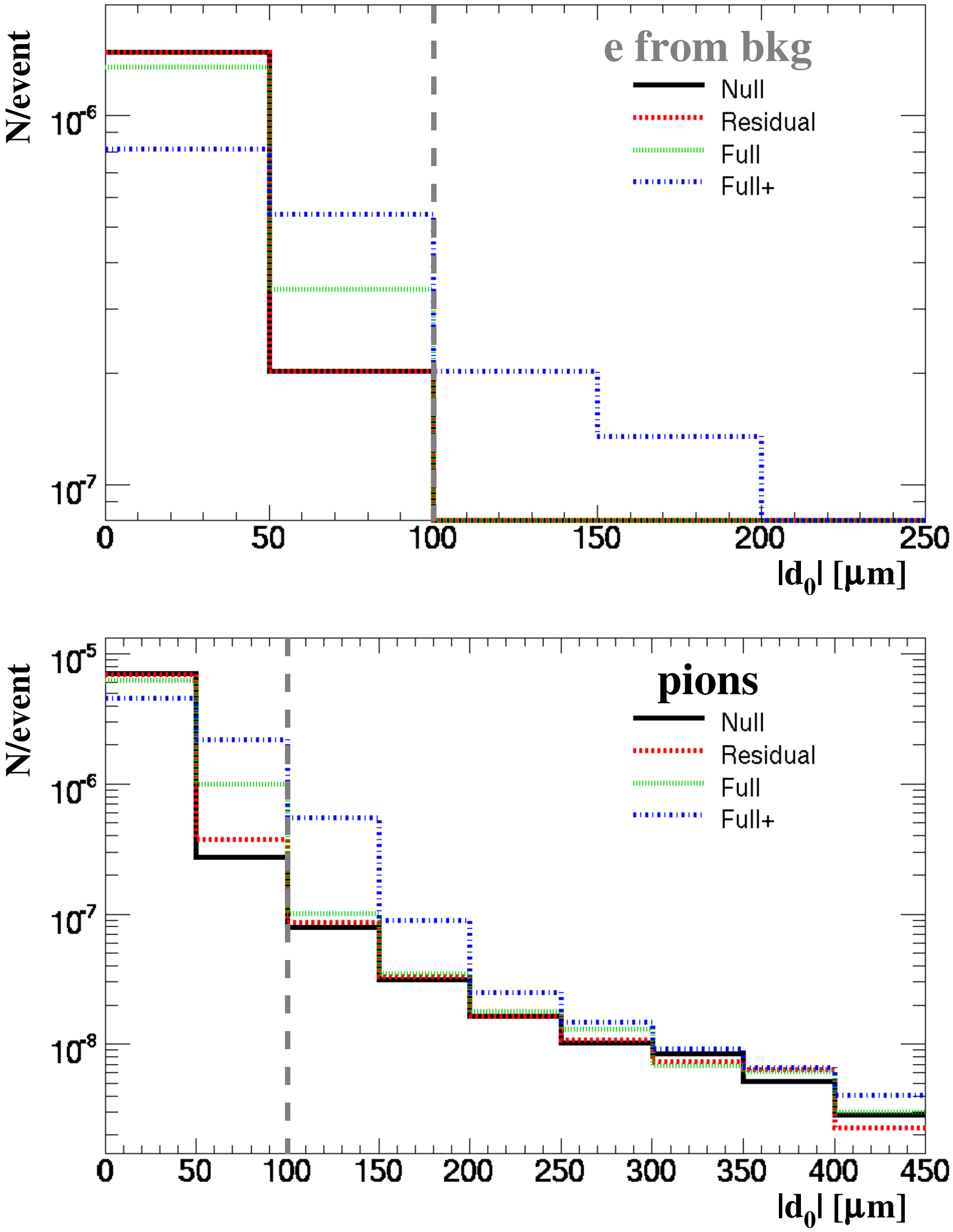

Figure 6.12: *Distributions in* $|d_0|$ *for different scenarios of misalignment* ($5 < p_{\mathrm{t}} < 7$ GeV/c)*. The vertical grey dotted line indicates the cut in impact parameter.*

(see Eq. 6.1 and 6.2), this effect translates into a change of the contributions of error to the measurement of the beauty electron cross section. This is shown in Fig. 6.13 for the four cases of misalignment.

The "null" misalignment case is shown as a reference. The "full+" is a worst-case scenario but it seems to already allow for a possible measurement (with 10^9 proton–proton events) of the cross section, but in a reduced p_t range. The increase of the total error is mostly due to the increase of the systematic contribution from background subtraction. This increase is due to the "d_0-broadening" of misidentified pions to higher bins of $|d_0|$. The "full" misalignment case seems to be already at the level of the errors for the case of "null" misalignment. This is mostly due to the fact that, for a moderate misalignment, the "d_0-broadening" affects all the sources approximately equally, therefore leaving the fractions unchanged. The errors for the "residual" misalignment scenario are almost the same for the "null" case. The last p_t-bin has a slight improvement: this is due to a higher "d_0-broadening" for the beauty electrons. However the statistics of the simulation for the last bin is quite low.

The "residual" misalignment scenario is the target of the realignment procedure and it has been reached for the SPD (see previous Chapter). For this case the errors on the measurement of the electron-level beauty cross section do not worsen significantly.

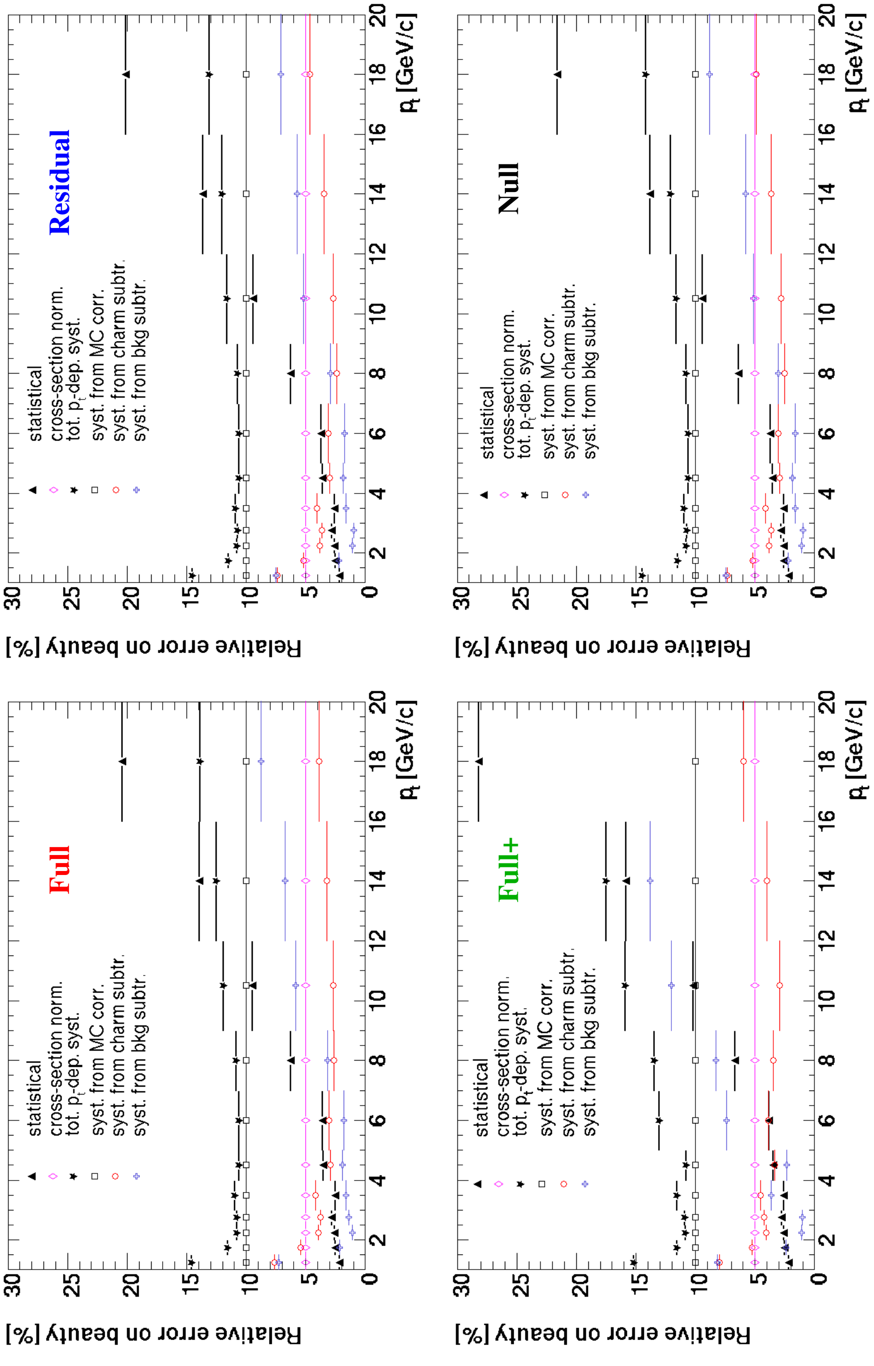

Figure 6.13: *Relative errors on beauty in different scenarios of misalignment.*

6.2 Strategy for the measurement of R_{AA}^{beauty} and $R_{\mathrm{B/D}}$

Using the results for proton–proton and Pb–Pb collisions presented here, it is possible to evaluate the experimental errors on the nuclear modification factor for beauty mesons. This is shown in Fig. 6.14. In the figure the theoretical calculation for the R_{AA} in the BDMPS framework of energy loss is also reported. The black line is the case for $\hat{q} = 0$ and it is shown as a reference. Initial-state effects (like shadowing) are responsible for the deviation from unity of the R_{AA} for $\hat{q} = 0$ in the kinematical region of p_{t} lower than ≈ 7 GeV/c. The two coloured bands are the theoretical predictions with (blue) and without (red) the effect of the beauty mass for the parton energy loss with $\hat{q} = 25$ GeV^2/fm (upper line) and $\hat{q} = 100$ GeV^2/fm (lower line). The case without the effect of the beauty mass was obtained by imposing $M_b = 0$ and it serves as a baseline for understanding the effect of the mass dependence for the parton energy loss. Since the suppression increases the statistical error, the Pb–Pb results were scaled to the yields for $\hat{q} = 50$ GeV^2/fm (an intermediate value between 25 and 100 GeV^2/fm). The results shown are the statistical error (black bars) and the systematic error (grey boxes). The systematic error (the grey boxes) is the convolution of the systematic error from the proton–proton and Pb–Pb results together with the theoretical uncertainty on the extrapolation from 14 TeV proton–proton collisions to 5.5 TeV (as for the Pb–Pb collisions). Comparing the two theoretical bands with the results of the simulations, one concludes that the measurement of R_{AA} for beauty mesons will allow to study the mass dependence of parton energy loss.

The size of the estimated errors ($\approx 15\%$ for the systematic and $< 10\%$ for the statistical error at $p_{\mathrm{t}} \approx 10$ GeV/c) seems to allow to estimate the mass dependence of the energy loss in the kinematical region $7 < p_{\mathrm{t}} < 14$ GeV/c.

Another interesting observable is the ratio of the R_{AA} for beauty electrons over the R_{AA} for charm electrons ($R_{\mathrm{B/D}}$). Energy loss may alter the $R_{\mathrm{B/D}}$ from unity because, according to the BDMPS model, the in-medium energy loss depends on the mass and colour charge of the propagating parton. Since charm and beauty are both quarks a deviation from unity for the $R_{\mathrm{B/D}}$ can only be due to the mass-dependence of the in-medium energy loss. Fig. 6.15 shows the expected performance for the measurement of $R_{\mathrm{B/D}}$. The errors were propagated from the results for the electrons from beauty shown here. The distribution of electrons

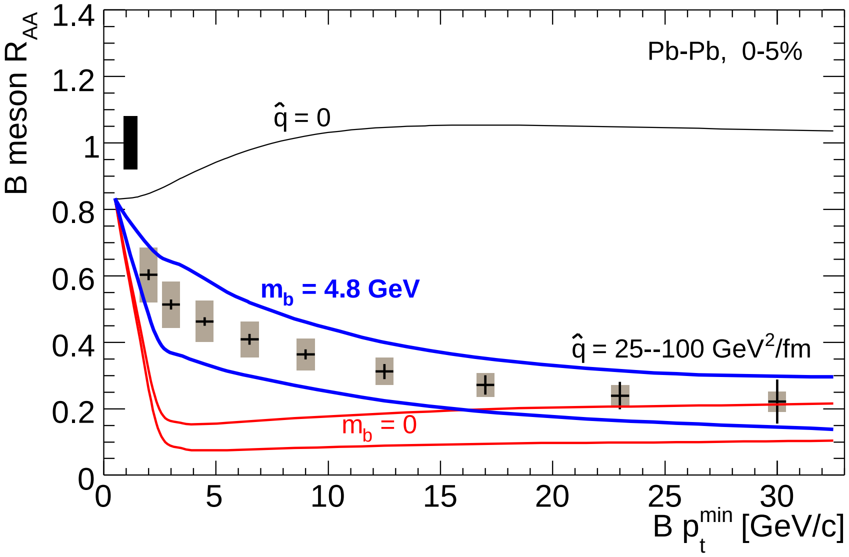

Figure 6.14: *R_{AA} for the beauty mesons. The theoretical predictions include shadowing and are drawn for $\hat{q} = 0$ (black line), $\hat{q} = 25 - 100$ GeV^2/c with massless beauty quark (red band), $\hat{q} = 25 - 100$ GeV^2/c with massive beauty quark (blue band). The results shown are the statistical error (black bars) and the systematic error (grey boxes). The normalisation error is the black box at $R_{\mathrm{AA}} = 1$.*

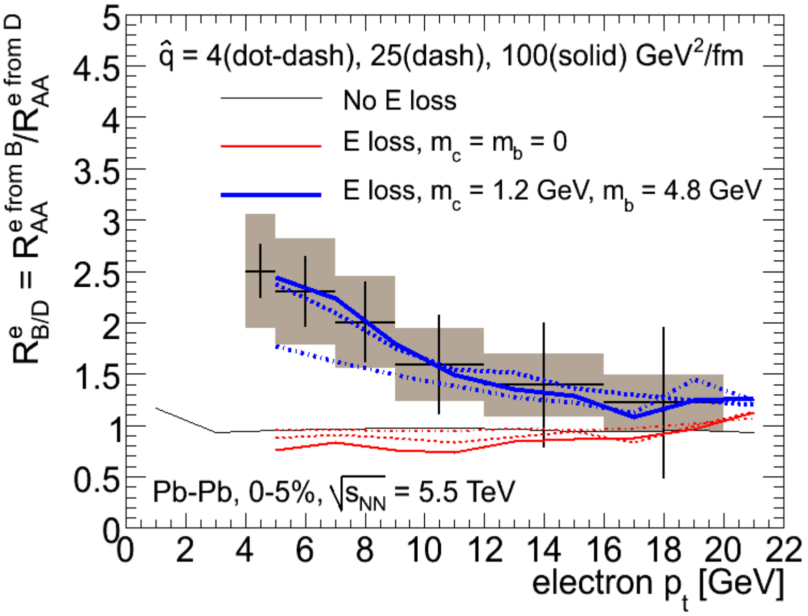

Figure 6.15: *Ratio of beauty electrons R_{AA} over charm electrons R_{AA}. The vertical bars represent the statistical error and the grey boxes represent the systematic error.*

from charm decays will be inferred from the distribution of charm mesons. The errors for the electrons from charm are obtained through a Monte Carlo technique (described in [190]). The results are compared with theoretical calculations taken from [71]. The solid black line is the case of no energy loss and it is very close to unity, as expected. Differences are due to the different effect of shadowing for c and b quarks (more for c, less for b). The red lines are for the cases of "massless heavy quarks", the masses for the heavy quarks were set to zero in the calculations to have a reference for the case of "massive heavy quarks" (blue lines). For both cases (massive and massless heavy quarks), the results are shown for a $\hat{q}$ of 4 $\mathrm{GeV}^2/\mathrm{fm}$ (dot-dashed), 25 $\mathrm{GeV}^2/\mathrm{fm}$ (dashed) and 100 $\mathrm{GeV}^2/\mathrm{fm}$ (solid). The calculations for the "massless heavy quarks" give a value of $R_{\mathrm{B/D}}$ close to unity for all the values of $\hat{q}$ and p_{t}. The theoretical lines for massive quarks have a large variation in $\hat{q}$ (a factor 25) but their corresponding $R_{\mathrm{B/D}}$ only varies a factor 1.4 (at most), thus confirming that the $R_{\mathrm{B/D}}$ is sensitive to the mass dependence of the energy loss. For values of p_{t} larger than ≈ 15 GeV/c, the cases for massive and massless heavy quarks converge. This is consistent with the general observation that the mass dependence of parton energy loss is a function of m/E and becomes negligible for $m/E < 0.1$ [197].

Such considerations allow to conclude that the $R_{\mathrm{B/D}}$ ratio, measured from Pb–Pb and proton–proton collisions at ALICE, provides an interesting test of the mass dependence of parton energy loss in a theoretically rather clean kinematical regime from $p_{\mathrm{t}} \approx 5$ GeV/c to $p_{\mathrm{t}} \approx 15$ GeV/c.

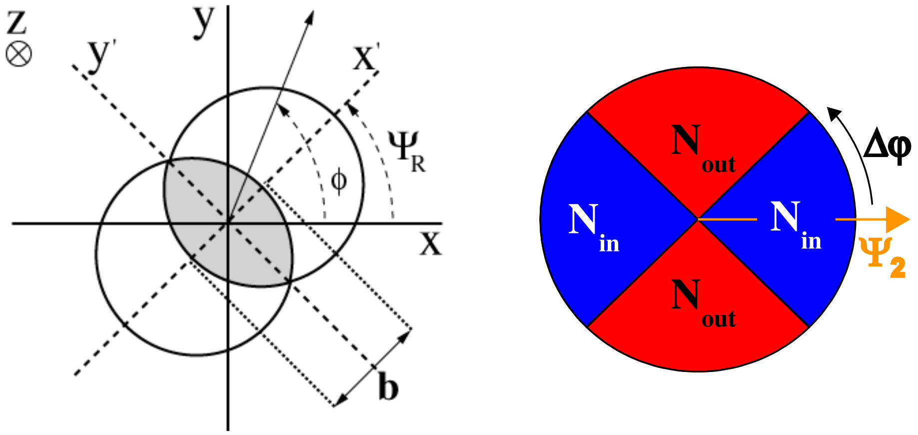

Figure 6.16: Left: *Definition of the reaction plane (in general* Ψ_R *or* Ψ_2 *for the case of* v_2*) between two nuclei with impact parameter* b. Right: *Scheme for the measurement of the* v_2. Ψ_2 *is the angle of the reaction plane and* $\Delta\Phi$ *is the azimuthal angle measured from the reaction plane* ($\Phi - \Psi_2$)*.*

6.3 Strategy for a measurement of the beauty elliptic flow

Another interesting variable that can be extracted from the beauty measurement is the elliptic flow coefficient, v_2. A first approach for the evaluation of v_2 would be to divide the azimuthal angle in two bins, as shown in Fig. 6.16, which shows the reaction plane of a heavy ion collision (left) and the definition of in-plane tracks ($\mathrm{N_{IN}}$) and out-plane tracks ($\mathrm{N_{OUT}}$). Neglecting higher order Fourier terms, the distribution of particles is:

$$\frac{dN}{d\phi} = N_0\,[1 + 2\,v_2\,\cos(2\,\phi)].$$

The value for $\mathrm{N_{OUT}}$ can be obtained as:

$$\begin{aligned}
\mathrm{N_{OUT}} &= \int_{\frac{\pi}{4}}^{\frac{3}{4}\pi} N_0\,[1 + 2\,v_2\,\cos(2\,\phi)]\,d\phi + \int_{\frac{5}{4}\pi}^{\frac{7}{4}\pi} N_0\,[1 + 2\,v_2\,\cos(2\,\phi)]\,d\phi \\
&= 2\,N_0\,[\phi + v_2\,\sin(2\,\phi)]_{\frac{\pi}{4}}^{\frac{3}{4}\pi} \\
&= N_0\,(\pi - 4\,v_2). \qquad (6.3)
\end{aligned}$$

Table 6.3: *Rescaling factors from events in the* $0-5\%$ *centrality bin to events in the* $20-60\%$ *centrality bin. The numbers were taken from [107].*

Centrality	$0-5\%$	$20-60\%$
Events	1×10^7	8×10^6
$\langle N_{coll}\rangle$	1616	419
$N^{\mathrm{c\overline{c}}}/ev$	115	31
$N^{\mathrm{b\overline{b}}}/ev$	4.6	1.3

The same calculations for $\mathrm{N_{IN}}$ give:

$$\mathrm{N_{IN}} = N_0\,(\pi + 4\,v_2)$$

This means that, for this case, v_2 can be written as:

$$v_2 = \frac{\pi}{4}\,\frac{\mathrm{N_{IN}} - \mathrm{N_{OUT}}}{\mathrm{N_{IN}} + \mathrm{N_{OUT}}}. \tag{6.4}$$

To evaluate the errors on such a measurement the results for beauty electrons in Pb–Pb collisions were used [190]. Since the simulation for Pb–Pb collisions were done for the $0-5\%$ centrality bin, the results have been rescaled for the $20-60\%$ centrality bin. The values used are summarised in Tab. 6.3. The total statistics was scaled by the number of events: in a nominal month of Pb–Pb collisions ALICE is expected to collect a sample of 1×10^7 central events and a sample of 2×10^7 minimum bias events. The 2×10^7 minimum bias events correspond to 8×10^6 events with a $20-60\%$ centrality therefore, the simulations must be scaled by a factor $8\times10^6/1\times10^7 = 4/5$. The background “electrons” were rescaled with the number of collision ($\langle N_{coll}\rangle$). The electrons from charm were rescaled according to the estimated number of $\mathrm{c\overline{c}}$ pairs ($N^{\mathrm{c\overline{c}}}/ev$). The electrons from beauty were rescaled according to the estimated number of $\mathrm{b\overline{b}}$ pairs ($N^{\mathrm{b\overline{b}}}/ev$).

The v_2 extracted from beauty electrons using 6.4 is actually the weighted sum of the v_2 of the various “electron” sources, as in:

$$v_2^{meas} = \frac{N_b\,v_2^b + N_c\,v_2^c + N_{bkg}\,v_2^{bkg}}{N_{tot}} \tag{6.5}$$

Therefore v_2 from beauty is calculated as:

$$v_2^b = \frac{N_{tot}\,v_2^{meas} - N_c\,v_2^c - N_{bkg}\,v_2^{bkg}}{N_{tot} - N_c - N_{bkg}} \tag{6.6}$$

where N_{tot}, N_b, N_c, N_{bkg} are the statistics, in each p_t-bin, for the total number of electrons, electrons from beauty decays, electrons from charm decays and background electrons, respectively. They were estimated from the previous studies rescaled as explained above. For the actual measurement, v_2^{meas} will be obtained using Eq. 6.4, v_2^c will be estimated from the measurement of charm (e.g. [194]) and v_2^{bkg} from pions. To estimate the experimental errors were used the predicted values for v_2^c and v_2^b from [195, 196]. As explained in 2.2.2, at low p_t (less then about 7 GeV/c) a non-zero v_2 is thought to arise from a collective behaviour due to early thermalization. Therefore, the predictions from [195], since they use a hydrodynamical model to calculate v_2, were used. At high p_t (greater then about 7 GeV/c) a non-zero v_2 is thought to arise from the in-medium path-length dependence of heavy-quark energy loss in the almond-shaped fireball (the average path-length is greater for particles travelling perpendicular to the reaction plane, see Fig. 6.16). Therefore the predictions from [196], since they use a model based on partonic energy loss to calculate v_2, were used. In the "overlap" region between the two regimes ($p_\mathrm{t} \approx 6 - 8$ GeV/c) an average value was used. In addition the following assumptions were made:

- $v_2^{bkg} = v_2^c$, this is a "working value" estimate since it does not contribute strongly to the total error.
- $\frac{\sigma_{v_2^c}}{v_2^c} = 0.25$, this was a "safe" assumption based on early results for the charm v_2 studies [194].
- $\frac{\sigma_{v_2^{bkg}}}{v_2^{bkg}} = 0.15$, this is a "rough" estimate based on the experience from previous experiments.

Propagating the errors from Eq. 6.6, the following error contributions are obtained:

- systematic from charm subtraction: $\frac{\sigma_{N_c}}{N_c}\frac{N_c}{N_b}\frac{v_2^b - v_2^c}{N_b}$
- systematic from charm v_2 estimation: $\frac{\sigma_{v_2^c}}{v_2^c}\frac{v_2^c}{v_2^b}\frac{N_c}{N_b}$
- systematic from background subtraction: $\frac{\sigma_{N_{bkg}}}{N_{bkg}}\frac{N_{bkg}}{N_b}\frac{v_2^b - v_2^{bkg}}{N_b}$
- systematic from background v_2 estimation: $\frac{\sigma_{v_2^{bkg}}}{v_2^{bkg}}\frac{v_2^{bkg}}{v_2^b}\frac{N_{bkg}}{N_b}$
- statistical from the v_2 measurement: $\frac{\sigma_{v_2^{meas}}}{v_2^{meas}}\frac{v_2^{meas}}{v_2^b}\frac{N_{tot}}{N_b}$

- statistical: $\frac{\sigma_{N_{tot}}}{N_{tot}} \frac{N_{tot}}{N_b} \frac{v_2^{meas}-v_2^b}{N_b}$

Using the assumption above and the results obtained for the measurement of the beauty cross section, the errors can be estimated. Fig. 6.18 summarises the systematic contributions to the total error. Fig. 6.19 summarises the statistical contributions to the total error.

The result is shown in Fig. 6.17. While the errors are quite large, it seems that a measurement is possible in the $2.0-7.0$ GeV/c range. For comparison, the measurement from PHENIX is in the $0.5-3$ GeV/c range (see Fig. 2.11).

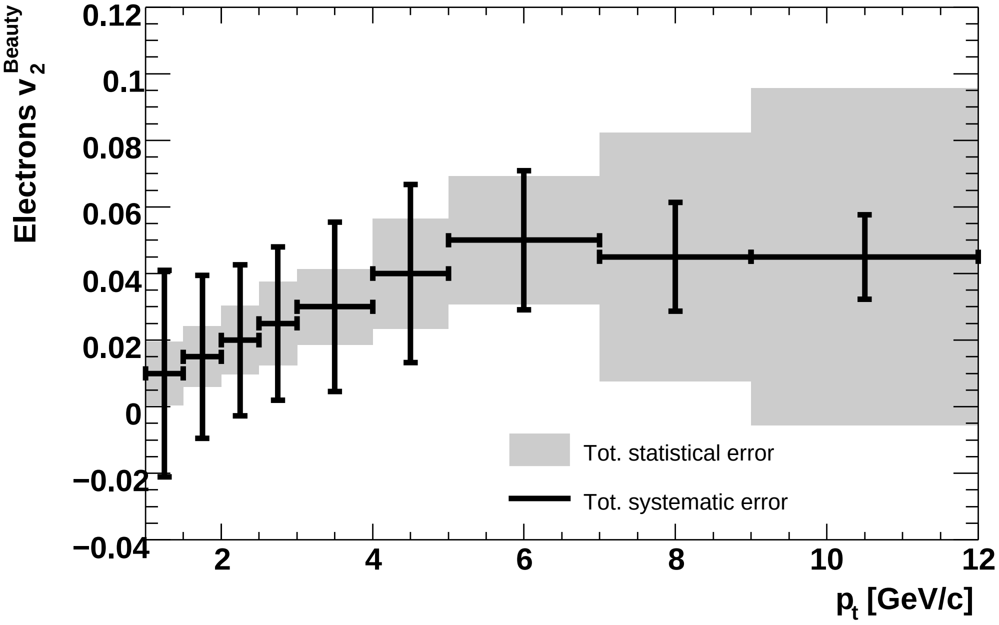

Figure 6.17: *Expected performance for the measurement of beauty decay electrons* v_2 *in Pb–Pb 20-60% semi-peripheral collisions at 5.5* TeV *(with* 8×10^6 *events).*

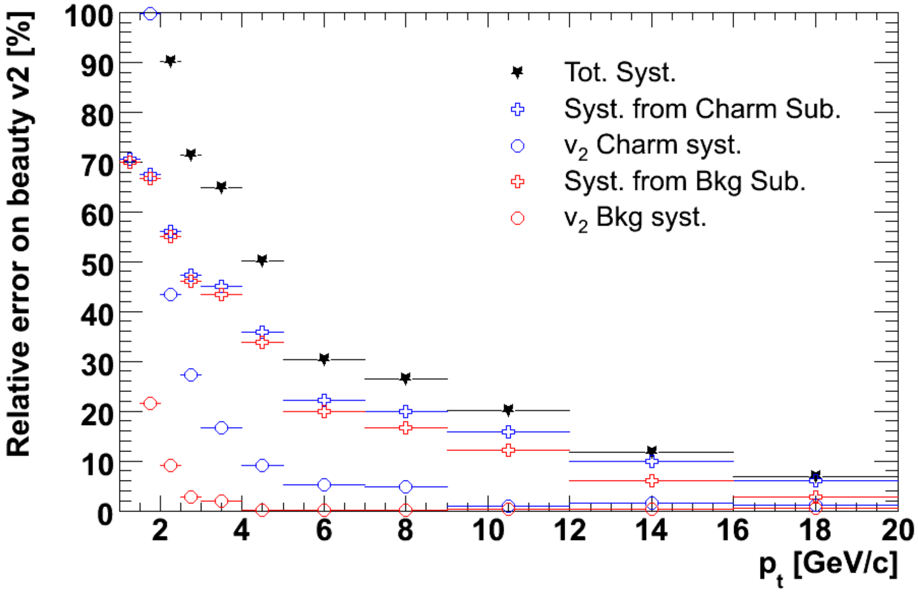

Figure 6.18: *Systematic contributions to the error for the measurement of beauty decay electrons* v_2.

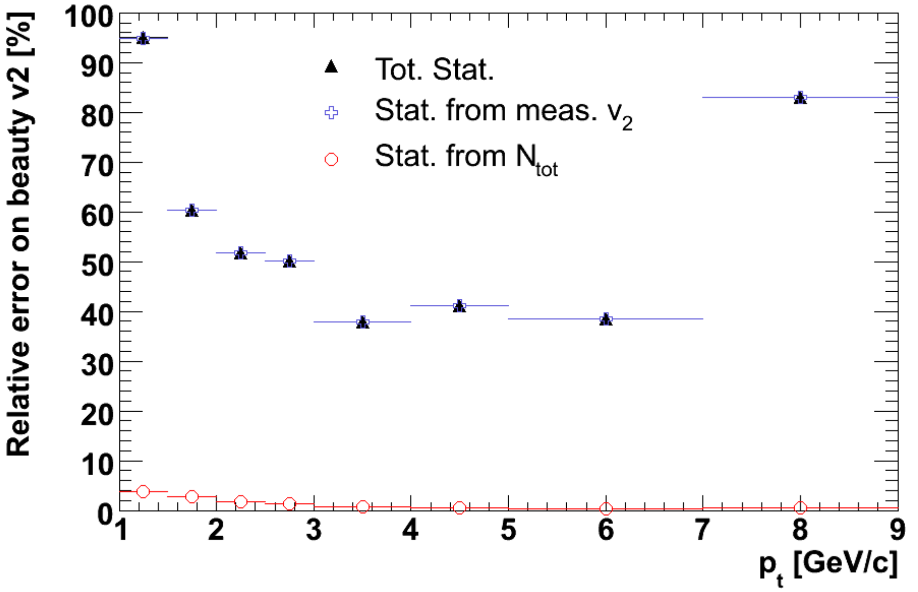

Figure 6.19: *Statistical contributions to the error for the measurement of the beauty decay electrons* v_2.

Conclusions

This work was aimed at assessing the capabilities of ALICE for the study of partonic energy loss using beauty quarks.

The semi-electronic channel was chosen for its high branching ratio. However, to separate beauty electrons from charm or background electrons a high precision tracker is needed. For ALICE, this task is performed by the ITS and, in particular, by the SPD.

The work presented here begins with the assembly of the sectors of the SPD. Since all the parts of the SPD were custom made for ALICE, the assembly required a careful tuning of the procedures to ensure a proper thermal contact with the cooling system and an alignment of the parts within the tolerances. The challenge was successfully met by the ALICE Padova and LNL Team with a delivery efficiency of 100%.

After the assembly was completed, the commissioning of the detector began. Therefore the work moved on from the assembly to the cooling system of the SPD. The power consumption and the constraint on radiation length make the cooling of the detector a challenging task that required several months to find a proper working point.

Once properly installed and functioning, the detector must be “aligned” before it can reach its full capabilities. To “align” a detector means to account, in the software, for the deviations of the actual apparatus from its design. However the alignment process must be monitored to identify and correct possible bugs and to assess the precision reached. This was done by developing a dedicated set of monitoring tools that helped the development and understanding of the alignment procedure.

The assembly of the sectors, the commissioning of the cooling system and the alignment of the detector were all performed successfully and the SPD is currently ready for the first proton–proton collisions.

Previous studies demonstrated the good capabilities of ALICE for the detection of beauty decays in proton–proton, as well as in Pb–Pb collisions using electrons with a large displacement from the primary vertex. They also showed that a measurement of the beauty electrons cross section is possible even with the reduced statistics of the first proton–proton runs. Using these studies as a starting point, three different observables were investigated.

A preliminary study on the feasibility of the extraction of the elliptic flow measurement for beauty electrons was done. The results seem to indicate that such measurement is possible in a kinematic region of $2 < p_{\mathrm{t}} < 7$ GeV/c. While the estimated errors are quite large, they are comparable with similar measurements from previous experiments although in a broader range of transverse momentum.

Combining the results obtained from the simulation studies for proton–proton and Pb–Pb collision it was possible to estimate the ALICE sensibility for the measurement of the beauty nuclear modification factor (R_{AA}). The expected precision for this measurement indicates that it will be a significant test of the mass dependence of partonic energy loss and therefore will be a testbed for the models of energy loss.

An even clearer observable to understand the mass dependence of partonic energy loss is the fraction of the beauty nuclear modification factor over the one for charm. The results for the beauty R_{AA} were combined with similar results for charm to evaluate ALICE capabilities for the extraction the $R_{\mathrm{B/D}}$. The estimated experimental uncertainties indicate that ALICE has a very good potential for the measurement of the $R_{\mathrm{B/D}}$ in the kinematic range of $5 < p_{\mathrm{t}} < 15$ GeV/c.

The aformentioned analyses allow to conclude that ALICE is well equipped for heavy flavour studies. This is due to the ALICE advanced design that fully exploits cutting-edge technologies (e.g. silicon pixel sensor), its careful construction and the long and thorough commissioning phase.

Bibliography

[1] I.Ya. Pomeranchuk, Dokl. Akad. Nauk. SSSR 78 (1951) 889.

[2] J.C. Collins and M.J. Perry, Phys. Rev. Lett. 34, 1353 (1975).

[3] F. Karsch et al., Phys. Lett. B478 (2000) 447.

[4] E.V. Shuryak, Phys. Rep. 61 (1980) 71.

[5] CERN Press Release, February 10, (2000), arXiv:nucl-th/0002042.

[6] T. Matsui and H. Satz, Phys. Lett. B 178 (1986) 416.

[7] L. D. McLerran, Lect. Notes Phys. 583 (2002) 291, arXiv:hep-ph/0104285.

[8] M. Lisa, S. Pratt, R. Soltz and U. Wiedemann, Ann. Rev. Nucl. Part. Sci. 55 (2005) 357.

[9] M. Cheng *et al.* [RBC-Bielefeld Coll.], Phys. Rev. D 77, 014511 (2008).

[10] Z. Fodorm, S.D. Katz, JHEP 0404 (2004) 050.

[11] S. Ejiri *et al.*, Prog. Theor. Phys. Suppl. 153 (2004) 118.

[12] M. Alford, K. Rajagopal and F. Wilczek, Phys. Lett. B422 (1998) 247.

[13] R. Rapp, T. Schäfer, E.V. Shuryak and M. Velkovsky, Phys. Rev. Lett. 81 (1998) 53.

[14] C. Alcock, *The Astrophysics and Cosmology of Quark-Gluon Plasma*, in Quark-Gluon Plasma, Springer-Verlag (1990).

[15] F. Karsch (2007), arXiv:0711.0661v1 [hep-lat].

[16] F. Karsch, Nucl.Phys. A698 (2002) 199, arXiv:hep-ph/0103314v1.

[17] J.D. Bjorken, Phys. Rev. D27 (1983) 140.

[18] B. Müller and J. Rafelski, Phys. Rev. Lett. 48 (1982) 1066.

[19] E.V. Shuryak, Phys. Rep. 61 (1980) 71.

[20] H. Beker *et al.*, NA44 Coll., Phys. Rev. Lett. 74 (1995) 3340;
I.G. Bearden *et al.*, NA44 Coll., Phys. Rev. Lett. 78 (1997) 2080;
I.G. Bearden *et al.*, NA44 Coll., Phys. Lett. B471 (1999) 6;

[21] G. Agakichiev *et al.*, NA45/CERES Coll., Phys. Lett. B422 (1998) 405;
B. Lenkeit *et al.*, NA45/CERES Coll., Nucl. Phys. A654 (1999) 627c;
B. Lenkeit *et al.*, NA45/CERES Coll., Nucl. Phys. A661 (1999) 23c;

G. Agakichiev *et al.*, NA45/CERES Coll., Eur. Phys. J. C41 (2005) 475.

[22] T. Alber *et al.*, NA49 Coll., Phys. Rev. Lett. 75 (1995) 3814;
H. Appelshäuser *et al.*, NA49 Coll., Eur. Phys. J. C2 (1998) 661;
F. Sikler *et al.*, NA49 Coll., Nucl. Phys. A661 (1999) 45c.

[23] E. Scomparin *et al.*, NA50 Coll., Nucl. Phys. A610 (1996) 331c;
M.C. Abreu *et al.*, NA50 Coll., Phys. Lett. B410 (1997) 337;
M.C. Abreu *et al.*, NA50 Coll., Phys. Lett. B450 (1999) 456.

[24] M. Masera *et al.*, HELIOS-3 Coll., Nucl. Phys. A590 (1995) 93c.

[25] R. Klingenberg *et al.*, NA52 Coll., Nucl. Phys. A610 (1996) 306c;
G. Ambrosini *et al.*, NA52 Coll., Phys. Lett. B417 (1998) 202;
G. Ambrosini *et al.*, NA52 Coll., New J. Phys. 1 (1999) 22.

[26] E. Andersen *et al.*, WA97/NA57 Coll., Phys. Lett. B449 (1999) 401;
F. Antinori *et al.*, WA97/NA57 Coll., Nucl. Phys. A661 (1999) 130c;
F. Antinori *et al.*, WA97/NA57 Coll., Eur. Phys. J. C14 (2000) 633.

[27] R. Albrecht *et al.*, WA98 Coll., Phys. Rev. Lett. 76 (1996) 3506;
M.M. Aggarwal *et al.*, WA98 Coll., Phys. Rev. Lett. 81 (1998) 4087; 82 (2000) 578;
M.M. Aggarwal *et al.*, WA98 Coll., Phys. Rev. Lett. 83 (1999) 926.

[28] G. Usai *et al.*, NA60 Coll., J. Phys. G34 (2007) S233;
S. Damjanovic *et al.*, NA60 Coll., J. Phys. G35 (2008) 104036.

[29] M.C. Abreu *et al.*, NA50 Coll., Phys. Lett. B477 (2000) 28.

[30] R. Arnaldi *et al.*, NA60 Coll., Nucl. Phys. A783 (2007) 261.

[31] K. Fanebust *et al.*, NA57 Coll., J. Phys. G28 (2002) 1607.

[32] S. Pratt, Phys. Rev. Lett. 53 (1984) 1219.

[33] P. Huovinen, P. F. Kolb, U. W. Heinz, P. V. Ruuskanen, S. A. Voloshin, Phys. Lett. B503 (2001) 58.

[34] J.D. Bjorken, FERMILAB-PUB-82-59-THY and Erratum (unpublished).

[35] R. Baier, D. Schiff, B.G. Zakharov, Annu. Rev. Nucl. Part. Sci. 50 (2000) 37.

[36] Xin-Nian Wang, Phys.Lett. B595 (2004) 165-170.

[37] S. Esumi, PHENIX Coll., Nucl. Phys. A715 (2002) 599.

[38] K.J. Eskola, K. Kajantie, P.V. Ruuskanen and K. Tuominen, Nucl. Phys. B570 (2000) 379.

[39] A.D. Martin, R.G. Roberts, W.J. Stirling and R.S. Thorne, Eur. Phys. J C4 (1998) 463.

[40] H.L. Lai *et al.*, CTEQ Coll., Eur. Phys. J. C12 (2000) 375.

[41] M. Gluck, E. Reya and A. Vogt, Eur. Phys. J C5 (1998) 461.

[42] V.N. Gribov, L.N. Lipatov, Sov. J. Nucl. Phys. 15 (1972) 438 and 675;
G. Altarelli, G. Parisi, Nucl. Phys. B126 (1977) 298;
Yu.L. Dokshitzer, Sov. Phys. JETP 46 (1977) 641.

[43] G. Altarelli, M. Diemoz, G. Martinelli and P. Nason, Nucl. Phys. B 308 (1988) 724.

[44] K.J. Eskola *et al.*, arXiv:hep-ph/0110348.

[45] K.J. Eskola, V.J. Kolhinen, C.A. Salgado, Eur. Phys. J. C9 (1999) 61.

[46] M. Hirai, S. Kumano and M. Miyama, Phys. Rev. D64 (2001) 034003.

[47] R. Vogt, Int. J. Mod. Phys. E12 (2003) 211, arXiv:hep-ph/0111271.

[48] C. Albajar *et al.*, Phys. Lett. B256 (1991) 121.

[49] F. Abe *et al.*, CDF Coll., Fermilab-Conf-94/134-E;
Fermilab-Conf-94/136-E; Fermilab-Conf-94/141-E;
K. Bazizi, D0 Coll., Fermilab-Conf-94/300-E.

[50] R.V. Gavai *et al.*, arXiv:hep-ph/9411438.

[51] M. Bedjidian *et al.*, *Hard Probes in Heavy Ion Collisions at the LHC: Heavy Flavor Physics*, arXiv:hep-ph/0311048.

[52] K.J. Eskola, V.J. Kolhinen and C.A. Salgado, Eur. Phys. J. C9 (1999) 61.

[53] V. Emel'yanov, A. Khodinov, S.R. Klein and R. Vogt, arXiv:hep-ph/9909427.

[54] Y. L. Dokshitzer and D. E. Kharzeev, Phys. Lett. B 519 (2001) 199.

[55] Z. w. Lin and R. Vogt, Nucl. Phys. B 544 (1999) 339.

[56] M. Gyulassy and X. n. Wang, Nucl. Phys. B 420 (1994) 583, arXiv:nucl-th/9306003.

[57] R. Baier, Y. L. Dokshitzer, A. H. Mueller, S. Peigne and D. Schiff, Nucl. Phys. B 483 (1997) 291, arXiv:hep-ph/9607355.

[58] R. Baier, Y. L. Dokshitzer, A. H. Mueller, S. Peigne and D. Schiff, Nucl. Phys. B 484 (1997) 265, arXiv:hep-ph/9608322.

[59] B. G. Zakharov, JETP Lett. 63 (1996) 952, arXiv:hep-ph/9607440.

[60] U. A. Wiedemann, Nucl. Phys. B 588 (2000) 303, arXiv:hep-ph/0005129.

[61] C. A. Salgado and U. A. Wiedemann, Phys. Rev. D 68 (2003) 014008, arXiv:hep-ph/0302184.

[62] M. Gyulassy, P. Levai and I. Vitev, Nucl. Phys. B 571 (2000) 197, arXiv:hep-ph/9907461.

[63] M. Gyulassy, P. Levai and I. Vitev, Phys. Rev. Lett. 85 (2000) 5535, arXiv:nucl-th/0005032.

[64] M. Gyulassy, P. Levai and I. Vitev, Nucl. Phys. B 594 (2001) 371, arXiv:nucl-th/0006010.

[65] A. Accardi, M. Gyulassy, Phys. Lett. B 586 (2003) 244, arXiv:nucl-th/0308029.

[66] A. Dainese, C. Loizides and G. Paic, Eur. Phys. J. C 38 (2005) 461, arXiv:hep-ph/0406201.

[67] M. G. Mustafa, D. Pal, D. K. Srivastava and M. Thoma, Phys. Lett. B 428 (1998) 234, arXiv:nucl-th/9711059.

[68] Y. L. Dokshitzer, V. A. Khoze and S. I. Troian, J. Phys. G 17 (1991) 1602.

[69] N. Armesto, C. A. Salgado and U. A. Wiedemann, Phys. Rev. D 69 (2004) 114003, arXiv:hep-ph/0312106.

[70] A. Dainese, J. Phys. G 31 (2005) S589, arXiv:hep-ph/0501292.

[71] N. Armesto, A. Dainese, C. A. Salgado and U. A. Wiedemann, Phys. Rev. D 71 (2005) 054027, arXiv:hep-ph/0501225.

[72] K. J. Eskola, H. Honkanen, C. A. Salgado and U. A. Wiedemann, Nucl. Phys. A 747 (2005) 511, arXiv:hep-ph/0406319.

[73] S. S. Adler *et al.*, PHENIX Coll., Phys. Rev. Lett. 91 (2003) 072303, arXiv:nucl-ex/0306021.

[74] S. S. Adler *et al.*, PHENIX Coll., Phys. Rev. C 72 (2005) 024901, arXiv:nucl-ex/0502009.

[75] J. Adams *et al.*, STAR Coll., Phys. Rev. Lett. 91 (2003) 172302, arXiv:nucl-ex/0305015.

[76] STAR Coll. BNL-73847-2005, Nucl. Phys. A 757 (2005) 102.

[77] M. Shimomura, PHENIX Coll., Nucl. Phys. A 774 (2006) 457, arXiv:nucl-ex/0510023v1.

[78] PHENIX Coll. BNL-73847-2005, Nucl. Phys. A 757 (2005) 184.

[79] A. Adare *et al.*, PHENIX Coll., arXiv:hep-ex/0609010.

[80] B.I. Abelev *et al.*, STAR Coll., arXiv:nucl-ex/0607012.

[81] M. Calderon de la Barca Sanchez *et al.*, STAR Coll., arXiv:nucl-ex/0608028.

[82] C. Zhong *et al.*, STAR Coll., arXiv:nucl-ex/0702014.

[83] A. Adare *et al.*, PHENIX Coll., arXiv:nucl-ex/0611018

[84] C. Albajar et al., UA1 Coll., Phys. Lett. B 186 (1987) 237; Phys. Lett. B 256 (1991) 121.

[85] P. Nason, S. Dawson, and R. K. Ellis, Nucl. Phys. B 303 (1988) 607.

[86] P. Nason, S. Dawson, and R. K. Ellis, Nucl. Phys. B 327 (1989) 49.

[87] F. Abe *et al.*, CDF Coll., Phys. Rev. Lett. 68 (1992) 3403.

[88] F. Abe *et al.*, CDF Coll., Phys. Rev. Lett. 69 (1992) 3704.

[89] F. Abe *et al.*, CDF Coll., Phys. Rev. Lett. 71 (1993) 500.

[90] A. D. Martin, R. G. Roberts, W. J. Stirling and R. S. Thorne, Eur. Phys. J. C 4 (1998) 463, arXiv:hep-ph/9803445.

[91] H. L. Lai *et al.*, CTEQ Coll., Eur. Phys. J. C 12 (2000) 375, arXiv:hep-ph/9903282.

[92] A. D. Martin, W. J. Stirling and R. G. Roberts, Phys. Rev. D 47 (1993) 867.

[93] F. Abe *et al.*, CDF Coll., Phys. Rev. Lett. 75 (1995) 1451.

[94] S. Frixione,M. L.Mangano, P. Nason and G. Ridolfi, Adv. Ser. Direct. High Energy Phys. 15 (1998) 609, arXiv:hep-ph/9702287.

[95] D. Acosta *et al.*, CDF Coll., Phys. Rev. D 65 (2002) 052005.

[96] D. Acosta *et al.*, CDF Coll., Phys. Rev. Lett. 91 (2003) 241804.

[97] S. Abachi *et al.*, D0 Coll., Phys. Rev. Lett. 74 (1995) 3548.

[98] S. Abachi *et al.*, D0 Coll., Phys. Lett. B 370 (1996) 239.

[99] B. Abbott *et al.*, D0 Coll., Phys. Lett. B 487 (2000) 264, arXiv:hep-ex/9905024.

[100] M. Mangano, P. Nason and G. Ridolfi, Nucl. Phys. B 373 (1992), 295.

[101] M. Mangano, P. Nason and R. Vogt, Phys. Rev. Lett. 95 (2005), 122001.

[102] R. Vogt, Eur. Phys. J. Special Topics 155 (2008), 213.

[103] S. Wicks, W Horowitz, M. Djordjevic, M. Gyulassy, arXiv:nucl-ex/0512076.

[104] H. van Hees and R. Rapp, Phys. Rev. C73 (2006) 034913.

[105] G.D. Moore and D. Teaney, Phys. Rev. C71 (2005) 064904.

[106] B. Alessando et al., J. Phys. G. Nucl. Part. Phys. 32 (2006) 1295.

[107] F. Carminati et al., J. Phys. G. Nucl. Part. Phys. 30(2004)1517.

[108] H.J. Specht, Experimental aspects of heavy ion physics at LHC energies. CERN 90-10-v-2; ECFA 90-133-v-2, p. 1236.

[109] J. Schukraft, A dedicated heavy ion experiment at the LHC. ECFA 92-146 p. 479.

[110] ALICE Coll., *Letter of Intent for a large ion collider experiment* CERN/LHCC 93-16; LoI Addendum 1 (Muon Spectrometer), CERN/LHCC 95-24.

[111] ALICE Coll. *Technical Proposal for a large ion collider experiment at the CERN LHC* CERN/LHCC/95-71.

[112] ALICE Coll. *Technical Proposal Addendum 1* CERN/LHCC/96-32.

[113] ALICE Coll. *Technical Proposal Addendum 2* CERN/LHCC/99-13.

[114] ALICE Coll. *Technical Proposal Addendum 3* CERN/LHCC/2006-14.

[115] ALICE Coll. *Technical Design Report of the High Momentum Particle Identification Detector* CERN/LHCC/1998-19.

[116] ALICE Coll. *Technical Design Report of the Photon Spectrometer* CERN/LHCC/1999-04.

[117] ALICE Coll. *Technical Design Report of the Zero Degree Calorimeter* CERN/LHCC/1999-05.

[118] ALICE Coll. *Technical Design Report of the Inner Tracking System* CERN/LHCC/1999-12.

[119] ALICE Coll. *Technical Design Report of the Forward Muon Spectrometer* CERN/LHCC/1999-22; Addendum CERN/LHCC/2000-046.

[120] ALICE Coll. *Technical Design Report of the Photon Multiplicity Detector* CERN/LHCC/1999-32; Addendum CERN/LHCC/2003-038.

[121] ALICE Coll. *Technical Design Report of the Time Projection Chamber* CERN/LHCC/2000-01.

[122] ALICE Coll. *Technical Design Report of the Time Of Flight Detector* CERN/LHCC/2000-12; Addendum CERN/LHCC/2002-016.

[123] ALICE Coll. *Technical Design Report of the Transition Radiation Detector* CERN/LHCC/2001-21.

[124] ALICE Coll. *Technical Design Report of the Trigger, Data Acquisition, High Level Trigger and Control System* CERN/LHCC/2003-062.

[125] ALICE Coll. *Technical Design Report of the Forward Detectors FMD, T0 and V0* CERN/LHCC/2004-025.

[126] ALICE Coll. *Technical Design Report of the Computing* CERN/LHCC/2005-018.

[127] S. Eidelmann *et al.*, Particle Data Group Coll., Phys. Lett. B 592 (2004) 1.

[128] A. Morsch and B. Pastircak, ALICE Internal Note, ALICE-INT-2002-028.

[129] F. Antinori *et al.*, Nucl. Instr. Meth. A360(1995)91,
G. Alexeev *et al.*, Nucl. Phys. A590(1995)139c.

[130] A. Kluge *et al.*, Proceedings of the 7th Workshop on Electronics for LHC Experiments, Stockholm, Sept 10-14, 2001.

[131] A. Kluge *et al.*, Proceedings of the PIXEL 2002 Workshop, Carmel, Sept. 2002.

[132] A. Kluge, Nucl. Instr. Meth. A560(2006)67.

[133] G. Aglieri Rinella *et al.*, JINST 2(2007)P01007.

[134] A. Rashevsky *et al.*, Nucl. Instr. Meth. A461(2001)133.

[135] D. Nouais *et al.*, Nucl. Instr. Meth. A450(2000)338.

[136] S.Beolé *et al.*, Nucl. Instr. Meth. A570(2007)236.

[137] D. Nouais *et al.*, ALICE INternal Note, ALICE-INT-2001-59.

[138] M. Germain *et al.*, Nucl. Instr. Meth. A482(2002)634,
M. Germain *et al.*, Nucl. Instr. Meth. A485(2002)121,
Rachevskaia *et al.*, Nucl. Instr. Meth. A530(2004)5964,
L. Bosisio *et al.*, Proceedings of the 2006 IEEE Nuclear Science Symposium Conference Record,
Rashevskaya *et al.*, Nucl. Instr. Meth. A572(2007)122124.

[139] J.R. Lutz *et al.*, Proceedings of the 5th Workshop on Electronics for LHC Experiments, Snowmass Colorado, 20-24 September 1999,
J.R. Lutz *et al.*, Proceedings of the 9th Workshop on Electronics for LHC experiments,
M. Bregant *et al.*, Nucl. Instr. Meth. A566(2006)18,
M. Bregant *et al.*, Nucl. Instr. Meth. A569(2006)29,
M. Bregant *et al.*, Nucl. Instr. Meth. A570(2007)312.

[140] C. Hu-Guo *et al.*, Proceedings of the 7th Workshop on Electronics for LHC Experiments, Stockholm, Sweden, September 2001,
C. Hu-Guo *et al.*, Proceedings of the 8th Workshop on Electronics for LHC Experiments, Colmar, France, 9-13 September 2002,
C. Colledani, C. Hu and J.D. Berst, HAL25 V3 User Manual v0.1, LEPSI-IN2P3-CNRS/ULP Strasbourg - France.

[141] A.P. de Haas *et al.*, Proceedings of the 5th Workshop on Electronics for LHC experiments, Snowmass Colorado, 20-24 September 1999,
V. Borshchov *et al.*, Proceedings of the 8th Workshop on Electronics for LHC experiments, Colmar, France, 9-13 September 2002.

[142] G.A. Feofilov *et al.*, Proceedings of the CERN Workshop on Advanced Materials for High Precision Detectors, September 1994,
A. van den Brink *et al.*, Proceedings of the 11th European Conference on Composite Materials, Rhodes, May 31 2004.

[143] O.N.Godisov *et al.*, Proceedings of the First International Workshop on Electronics and Detectors Cooling, Lausanne, Switzerland, 4-7 October 1994.

[144] A. van den Brink *et al.*, Proceedings of the 7th Workshop on Electronics

for LHC Experiments, Stockholm, Sweden, 10-14 September 2001.

[145] J. Manschot *et al.*, ALICE Internal Note, ALICE-INT-2003-021.

[146] R. Kluit *et al.*, Proceedings of the 7th workshop for LHC and future experiments, Stockholm, Sweden, 10-14 September 2001,
R. Kluit *et al.*, Proceedings of the 10th workshop for LHC and future experiments, Boston, USA, September 2004.

[147] M.J. Rossewij *et al.*, Proceedings of the 9th workshop on Electronics for LHC experiments, Amsterdam, Netherlands, 29 September-3October 2003.

[148] M. Oinonen *et al.*, Proceedings of the 11th Workshop on Electronics for LHC and Future Experiments, Heidelberg, Germany, 12-16 September 2005.

[149] C. Garabatos, Nucl. Instr. Meth. A535(2004)197.

[150] J. Wiechula *et al.*, Nucl. Instr. Meth. A548(2005)582.

[151] H. Stelzer *et al.*, ALICE Internal Note, ALICE-INT-2003-017.

[152] U. Frankenfeld *et al.*,ALICE Internal Note, ALICE-INT-2002-030.

[153] R. Campagnolo, Proceedings of the HEP-EPS 2005, Lisbon, PoS HEP2005:373, 2006.

[154] A. Akindinov *et al.*, Eur. Phys. J. C32S1(2004)165.

[155] A. Akindinov *et al.*, Eur. Phys. J. C45(2006)669.

[156] E. Cerron-Zeballos, I. Crotty, D. Hatzifotiadou, J. Lamas-Valverde, S. Neupane, M.C.S. Williams and A. Zichichi, Nucl. Instr. Meth. A374(1996)132.

[157] A. Akindinov *et al.*, Nucl. Instr. Meth. A456(2000)16.

[158] A. Akindinov *et al.*, Eur. Phys. J. C34(2004)s325.

[159] F.Q. Wang and N. Xu, Phys. Rev. C61(2000)021904.

[160] Y. Andres *et al.*, EPJdirect C, 4(S1)(2002)25.

[161] A. Rimai *et al.*, ALICE Internal Note, ALICE-INT-1997-23.

[162] R. Wurzinger, Y. Le Bornec and N. Willis, ALICE Internal Note, ALICE-INT-1997-10.

[163] D.K. Swoboda *et al.*, Proceedings of the 19th International Conference on Magnet Technology Genua, Italy, IEEE Trans. on Applied Superconductivity, June 2006.

[164] S. Moretto *et al.*, Journal of Physics: Conference Series 41 (2006) 361.

[165] A. Pepato *et al.*, Nucl. Instr. Meth. A565 (2006) 6.

[166] V. Manzari *et al.*, 2004 Proc. VERTEX 2004 Workshop.

[167] M. Cinausero *et al.*, Proceeding of the IMTC 2004 - Instrumentation and

Measurement Technology Conference Como, Italy, (2004) 1823.

[168] M. Lunardon *et al.*, Proceeding of the IMTC 2004 - Instrumentation and Measurement Technology Conference Como, Italy, (2004) 1817.

[169] F. Scarlassara *et al.*, ALICE Internal Note, ALICE-INT-2000-18.

[170] `http://tydes.web.cern.ch/tydes/doc/SPDMood/`

[171] C.Cheshkov, LHC Detector Alignment Workshop CERN Detector Description Overview (2006).

[172] R. Grosso, LHC Detector Alignment Workshop CERN ALICE Misalignment Framework (2006).

[173] V. Blobel and C. Kleinwort, Report DESY 02-077 (2002), arXiv:hep-ex/0208021

[174] A. Dainese, M. Lunardon, S. Moretto and A. Rossi, “ITS alignment with Millepede”, ITS alignment & offline Meeting, September 2008.

[175] A. Dainese, M. Lunardon, S. Moretto and A. Rossi, “First look at SDD alignment with Millepede”, ITS alignment & offline Meeting, December 2008.

[176] A. Dainese and A. Rossi, “ITS alignment with AliAlignmentTracks”, ITS alignment & offline Meeting, November 2008.

[177] C. Garcia, “SDD Time Zero from track-cluster residuals”, ITS alignment & offline Meeting, October 2008.

[178] F. Prino, “Update on SDD time zero calibration”, ITS alignment & offline Meeting, December 2008.

[179] P. Bilior, Nucl. Instrum. Methods 225 (1984) 352;
The code can be found here:
`http://aliceinfo.cern.ch/static/aliroot-new/STEER/AliTrackFitterKalman.cxx`

[180] The code can be found here:
`http://aliceinfo.cern.ch/static/aliroot-new/STEER/AliTrackFitterRieman.cxx`

[181] A. Dainese, M. Lunardon, S. Moretto and A. Rossi, “ITS alignment using Millepede and cosmics: status report”, ITS alignment & offline Meeting, June 2008.

[182] M. Ivanov, “Cosmic runs with magnetic field”, First Physics Meeting, .

[183] A. Badalà, R. Barbera, G. Lo Re, A. Palmeri, G.S. Pappalardo, F. Riggi, ALICE Internal Note ALICE-INT-2001-011 (2001).

[184] N. Bustreo, B.S. Nilsen, L. Vannucci, ALICE Internal Note ALICE-INT-2001-013 (2001).

[185] A. Dainese and M. Masera, ALICE Internal Note ALICE-INT-2003-027

(2003); the Note can be found at:
http://alice.pd.infn.it/OurPubs.html

[186] http://aliceinfo.cern.ch/Offline/

[187] http://home.thep.lu.se/ torbjorn/Pythia.html

[188] X. N. Wang and M. Gyulassy, Phys. Rev. D44 (1991)3501,
M. Gyulassy and X. N. Wang, Comput. Phys. Commun. 83 (1994) 307,
The code can be found at:
http://www-nsdth.lbl.gov/ xnwang/hijing/index.html

[189] C. Albajar *et al.*, UA1 Coll., Phys. Lett. B 213 (1988), 405;
C. Albajar *et al.*, UA1 Coll., Phys. Lett. B 256 (1991), 121.

[190] F. Antinori, A. Dainese, M. Lunardon and R. Turrisi, ALICE Internal Note ALICE-INT-2005-33 (2006).

[191] H. Jung, Comput. Phys. Commun. 143 (2002), 100, arXiv:hep-ph/0109102.

[192] N. Carrer, A. Dainese and R. Turrisi, J. Phys. G29 (2003), 575.

[193] A. Dainese, Ph.D. Thesis, Università degli Studi di Padova (2003), arXiv:nucl-th/0311004.

[194] E. Bruna, Ph.D. Thesis, Università degli Studi di Torino (2007).

[195] H. van Hees, V. Greco and R. Rapp, arXiv:0706.4456v2 [hep-ph].

[196] C. A. Salgado, N. Armesto, M. Cacciari, A. Dainese and U. A. Wiedemann, J. Phys. G: Nucl. Part. Phys. 35 (2008) 054001

[197] N. Armesto, C. Salgado, U. Wiedemann, Phys. Rev. D 69 (2004), 114003.